Coordination Chemistry Reviews 458 (2022) 213851

Contents lists available at ScienceDirect

Coordination Chemistry Reviews

journal homepage: www.elsevier.com/locate/ccr

Review

Coordination and organometallic precursors of group 10 and 11: Focused electron beam induced deposition of metals and insight gained from chemical vapour deposition, atomic layer deposition, and fundamental surface and gas phase studies

I. Utke [b,*], P. Swiderek [c,*], K. Höflich [d,e,*], K. Madajska [a], J. Jurczyk [b,f], P. Martinović [c], I.B. Szymańska [a,*]

[a] Nicolaus Copernicus University in Toruń, Faculty of Chemistry, Gagarina 7, 87-100 Toruń, Poland
[b] Empa - Swiss Federal Laboratories for Materials Science and Technology, Laboratory for Mechanics of Materials and Nanostructures, Feuerwerkerstrasse 39, CH - 3602 Thun, Switzerland
[c] Institute for Applied and Physical Chemistry (IAPC), Fachbereich 2 (Chemie/Biologie), University of Bremen, Leobener Str. 5 (NW2), 28359 Bremen, Germany
[d] Ferdinand-Braun-Institut gGmbH, Leibniz-Institut für Höchstfrequenztechnik, Joint Lab Photonic Quantum Technologies, Gustav-Kirchhoff-Str. 4, D - 12489 Berlin, Germany
[e] Helmholtz-Zentrum Berlin für Materialien und Energie, CoreLab Correlative Microscopy and Spectroscopy, Hahn-Meitner-Platz 1, D - 14109 Berlin, Germany
[f] AGH University of Science and Technology Kraków, Faculty of Physics and Applied Computer Science, Al. Mickiewicza 30, 30-059 Kraków, Poland

ARTICLE INFO

Article history:
Received 10 October 2020
Received in revised form 5 February 2021
Accepted 7 February 2021
Available online 5 January 2022

Keywords:
Group 10 and 11 elements
Volatile coordination and organometalic precursors
Focused electron beam induced deposition (FEBID)
Chemical vapour deposition (CVD)
Atomic layer deposition (ALD)
Nanofabrication
Electron-induced and surface reactions
Adsorption
Electron-induced dissociation
Desorption
Purification
Electron-enhanced ALD
Electron-enhanced CVD

ABSTRACT

Nanostructured materials made from group 10 (Ni, Pd, Pt) and group 11 (Cu, Ag, Au) elements have outstanding technological relevance in microelectronics, nano-optics, catalysis, and energy conversion. Processes that allow for the easy and reliable fabrication of such nanostructures are heavily sought after. Focused electron beam induced deposition (FEBID) is the only direct-write technique that can fabricate nanostructures with arbitrary shape and dimensions down to the sub-10 nm regime. However, the complex chemistry of FEBID involving electron-induced dissociation processes of metalorganic precursors molecules, surface kinetics, and thermal effects is poorly understood and far from being optimized.

Here, we review in a comparative manner the performance and the underlying chemical reactions of surface deposition processes, namely, chemical vapour deposition (CVD), atomic layer deposition (ALD), and FEBID itself. The knowledge gained in CVD and ALD as related surface deposition techniques will help us to understand the spatially selective chemistry occurring in FEBID. Fundamental surface and gas phase studies provide insight to electron-induced chemistry and desorption of precursor fragments. Specific emphasis is put on the type of the ligands and their different behaviour under thermal, surface-related, and electron-induced processes. The comprehensive overview of the current state of FEBID for group 10 and 11 metals includes reactive environments and purification approaches as these may provide valuable information on the design of novel precursors. The evaluation of the precursor and process performance is extended to include W, Co, Fe, Ru, Rh, and Ir to represent a general guide towards future developments in FEBID. These may not only rely on the design of novel compounds but also on optimized deposition strategies inspired by ALD and CVD.

Contents

* Corresponding authors.
E-mail addresses: Ivo.Utke@empa.ch (I. Utke), swiderek@uni-bremen.de (P. Swiderek), katja.hoeflich@fbh-berlin.de (K. Höflich), pola@umk.pl (I.B. Szymańska).

https://doi.org/10.1016/j.ccr.2021.213851
0010-8545/

1. Scope of the review

This article reviews the current state of processes for deposition of metals from groups 10 and 11 for all precursor molecules that have so far been applied or evaluated for focused electron beam induced deposition (FEBID). To provide a comprehensive overview of the chemistry involved in deposit formation, it includes a comparison with chemical vapour deposition (CVD) and atomic layer deposition (ALD) using the same precursors.

FEBID is a newly emerging method for fabrication of three-dimensional nanostructures. The process conceptually relies on chemical reactions of precursor molecules induced by electrons that are supplied by the focused electron beam of a scanning electron microscope (SEM) [1]. The precursors are typically complexes consisting of a metal core and of ligands that provide the compounds with a sufficient volatility so that they can be continuously fed to the area where the electron beam impinges on the surface. When adsorbed on the surface, the precursors are decomposed under the electron beam to produce a solid deposit that should, in the ideal case, contain only the metal while the ligands are converted to small volatile products that can desorb from the surface.

The reactions that underlie the formation of a deposit in FEBID occur via electronic states of the precursor different from the ground state. These may be accompanied by thermal surface processes, i.e. reactions proceeding in the electronic ground state, as predominant in ALD and CVD. Therefore, the research on FEBID was and still is inspired by the chemistry of CVD and ALD, leading to the use of similar or identical metalorganic precursors [1-7]. The second common line of FEBID, CVD, and ALD is the surface kinetics, involving adsorption of the precursors and the related surface reactions as well as desorption of reaction products. However, as will be detailed here, CVD and ALD precursors are not necessarily ideal for FEBID, calling for further developments for which this review is intended to serve as a reference.

In contrast to previous reviews, we will address these two common lines between CVD, ALD, and FEBID. We confine ourselves to the discussion of those volatile precursors from groups 10 and 11 for which FEBID experiments or fundamental surface or gas phase studies on the reactions occurring under electron irradiation have been reported. We thus exclude from our discussion liquid injection CVD or liquid phase FEBID where the solvent adds further complexity. This focus serves to highlight FEBID as selective and 3D deposition method, to show the complexity involved through thermal and non-thermal contributions in achieving pure metal deposits, and to understand how findings in ALD, CVD, and precursor synthesis can contribute to the goal of achieving well-controlled deposit composition in FEBID.

The review starts with an introduction on the fundamentals of the three deposition methods and on the fundamental surface and gas phase investigations involving electron irradiation of adsorbed and gas phase molecules, respectively. Chapters 3 and 4 continue with a detailed review of group 10 and 11 precursor families that were investigated in FEBID, ALD, CVD, and condensed film/gas phase studies. For each precursor family an introduction and 4 subsections provide available data in the respective fields. The introductory sections comprise all precursors with their structural formulae and naming. Alternative names are indicated when common in FEBID literature. Tables summarize the general properties of the compounds including sublimation and/or boiling points. The sublimation points serve for fast screening of the vapour pressure range and specify pressure and temperature for visible sublimation (often on a glass surface after a given time). Thermal decomposition data refer to experiments without catalytic surface effects. Where available, vapour pressure curves are provided that are measured under thermodynamically well-defined equilibrium conditions. Chapter 5 evaluates precursor and FEBID performance and summarizes implications for precursor design towards obtaining high metal contents in FEBID material. This chapter will also include FEBID precursors for W, Co, Fe, Ru, Rh, and Ir based on carbonyl, halogen, and alkyl compounds to generalize our findings. Chapter 6 discusses recent perspectives emerging from FEBID, ALD, and CVD.

2. Fundamentals of surface deposition processes

2.1. Thermal and electron-induced dissociation

Chemical vapour deposition dates back to around 1850 when Bunsen reported the deposition of iron oxide from iron chloride and water vapour [8]. Over the years it has developed into a thin film deposition technology relying on thermal dissociation reactions of precursor molecules. An increasing number of metalorganic precursors has been involved in CVD that was in turn named metalorganic chemical vapour deposition (MOCVD). The molecules employed in MOCVD span from true organometallic compounds with π or σ metal–carbon bonds as found for metal carbonyls and alkyls, to complexes having metal-nitrogen bonds, and metal–oxygen bonds such as metal-carboxylates and metal-β-diketonates, which are particularly relevant for this review (see chapters 3 and 4). Regardless of the type of metal–ligand bond, ideally the thermal dissociation reaction is assumed to break it leaving the non-volatile metal on the substrate while the volatile ligands are pumped away.

Typically, the gaseous precursor is introduced under laminar viscous flow conditions [9]. The gas forms a thin stagnant boundary layer through which the precursor molecules will diffuse to the substrate and their volatile thermal decomposition products return into the gas phase (Fig. 2.1a). Thermal dissociation reactions (pyrolysis) of the metalorganic molecules into non-volatile and volatile parts occur on the hot substrate surface as well as in the hot thin stagnant boundary layer above the substrate [3]. Of note is that gas phase reactions can be suppressed using high vacuum CVD (HVCVD) where the mean free path of molecules is large com-

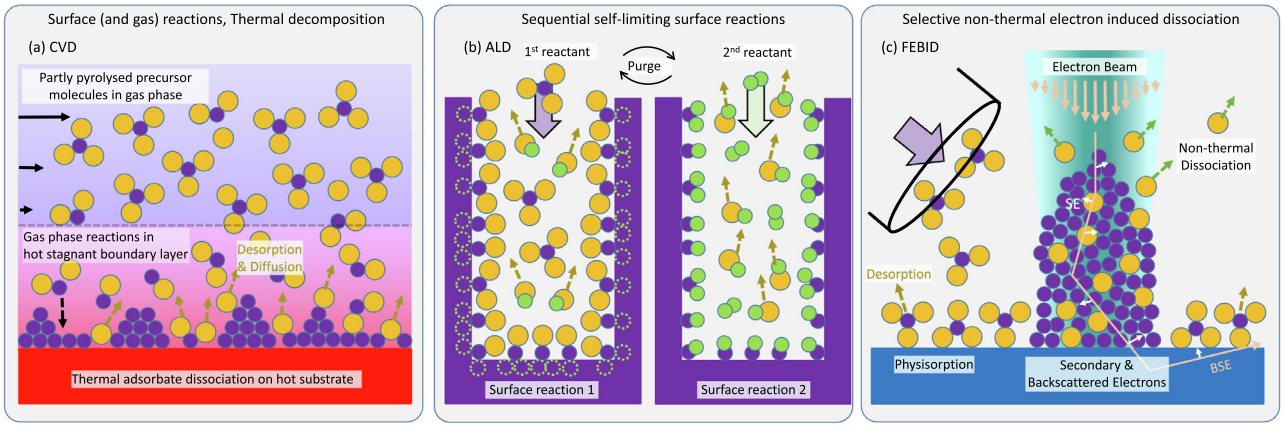

Fig. 2.1. Schematics of a) CVD, b) ALD, and c) FEBID. Note the different adsorbate dissociation mechanisms.

pared to the reactor dimensions. With appropriately directed gas inlets, a combinatorial screening of film compositions as function of impinging precursor fluxes can be performed in one deposition experiment by HVCVD [10]. Metal CVD processes have been comprehensively reviewed by Kodas & Hampden-Smith [2] and Jones & Hitchman [3].

Atomic layer deposition (ALD) as thin film deposition method was invented in the 1960s [11]. In contrast to CVD, ALD relies on sequential and self-limiting surface reactions of at least two precursor compounds [12-14]. For self-limiting surface reactions (Fig. 2.1b) multi-ligand metal compounds are a pre-requisite. The molecule dissociatively chemisorbs onto the moderately heated substrate losing one to several ligands which ideally thermally desorb to unblock the surface for further self-limiting surface reactions. At least one ligand needs to remain on the new monolayer surface to limit further chemisorption and physisorption of molecules from the gas phase. Evidently, to keep surface-triggered dissociation reactions the dominant mechanism as needed for ALD, the substrate must be kept in a temperature window lower than thermal decomposition of the adsorbates. To continue film growth within the concept of self-limiting surface reactions, the metal precursor excess needs to be purged from the reactor. A second reactant is introduced to form volatile products with the remaining ligands and to leave the desired surface groups. Then, the second reactant is purged and the cycle starts over again until the desired film thickness is reached. Due to the self-limiting surface reactions, ALD is the best suited deposition method for uniform films in open porosity materials as used for next generation energy conversion applications [15-20]. ALD reactors are run in several flow and exposure modes depending on the time the molecules need to diffuse and cover the entire surface. This can be minutes in bulk high aspect ratio structures, see [21–23] for analytical and numerical simulations, or milliseconds for planar substrates as realized in spatial ALD systems [24] for high throughput film growth. Metal ALD processes were comprehensively reviewed by Miikkulainen et al. [25], Emslie et al. [26], Hagen et al. [27], and Maina et al. [28]. Classification of metal ALD processes based on density functional theory insights was suggested by Elliot et al. [29].

FEBID is a relatively young research field compared to CVD and ALD; it dates back to 1976, when the residual gas in an electron microscope was used to pattern contamination-based etch masks [30]. Since then, understanding the adsorbate dissociation chemistry, being at the base of electron beam induced deposition, and searching for appropriate precursors is an ongoing challenge. In contrast to CVD and ALD, FEBID is a selective deposition method that performs outstandingly for additive 3D manufacturing at < 50 nm scale feature resolution with the world record of patterns being 1 nm-sized dots fabricated from $W(CO)_6$ [31]. An electron beam and the generated secondary electrons dissociate adsorbed precursor molecules by converting them into anionic, cationic, or neutral electronically excited states which subsequently decay into volatile and non-volatile moieties, the latter forming the deposit (Fig. 2.1c). The non-thermal dissociation on the surface makes the process selective as it can proceed only where electrons are present. This non-thermal nature of the process has to be understood in contrast to the thermal dissociation reactions in CVD and ALD. While FEBID proceeds at room-temperature and requires no external heat input per se, temperature still may play a crucial role, cf. Section 5. The mechanisms of this electron-induced dissociation have been reviewed previously [5,32,33]. Briefly, dissociation can proceed via dissociative electron attachment (DEA), dissociative ionization (DI), and dissociation into neutrals (ND). While DEA is a resonant process that occurs in a well-defined window of electron energies even below bond energies (< few eV), ND and DI have thresholds corresponding to the lowest electronic excitation (typically a few eV) and ionization energies (of the order of 10 eV), respectively. The dissociation reaction efficiencies of ionization and dissociation into neutrals increase monotonically with increasing electron energy as more excitation channels open and more excess energy needed for bond dissociation is available. However, a maximum is reached typically at around 70 eV above which the interaction time of the electron with a target molecule drops as consequence of its increasing velocity. Note that the electron energy spectrum involved in FEBID not only contains the high energy primary electrons (in the kiloelectron volt range) but also the energies from meV up to the primary electrons energy through their generated secondary and backscattered electrons [1]. Due to this continuous energy spectrum, DEA, ND, and DI all contribute to precursor fragmentation in FEBID such that bond selectivity inherent in particular dissociation channels is difficult to achieve. Of important note is that not only these initial electron-induced dissociation reaction steps determine the composition of FEBID materials. Simultaneously, the balance between desorption of the volatile dissociation products (ligands or their volatile fragments) and their concurrent surface reactions will determine the purity of the FEBID material. The corresponding electron-stimulated desorption (ESD) studies are mostly performed in UHV conditions irradiating cryogenically condensed films or surfaces of bulk material. Comprehensive reviews of FEBID are given by Utke et al. [1], Huth et al. [34], and Barth et al. [35].

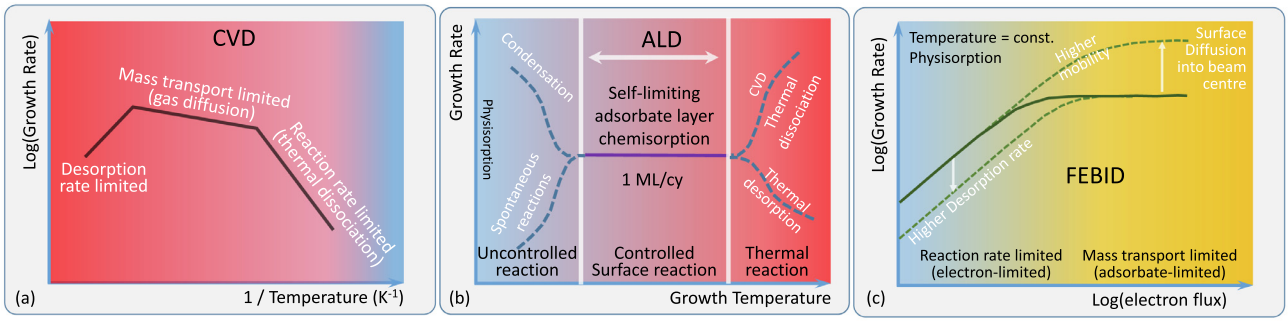

Fig. 2.2. Overview on typical growth regimes for (a) CVD, (b) ALD, and (c) FEBID. Note that for FEBID the electron flux varies on the horizontal axis while for CVD and ALD it is temperature. The log–log plot in (c) was chosen to cover several orders of magnitude in electron flux and growth rate.

2.2. Comparison of the growth regimes

Because of the different underlying dissociation mechanisms, the thermodynamic windows for CVD, ALD, and FEBID each show a different and characteristic dependence on the process parameters. Fig. 2.2 summarizes the generic growth rate graphs found in each of the three deposition processes.

For CVD, an Arrhenius plot (logarithmic growth rate versus inverse temperature) as shown in Fig. 2.2a, is marked by straight lines that represent three distinct growth regimes [36]. The growth rate in the lower temperature window is limited by the thermal dissociation rate. As this reaction depends exponentially on temperature, the growth rate changes by orders of magnitude with increasing temperature. When the temperature reaches a certain value, the thermal dissociation is fast compared to the molecule transport rate which becomes growth rate limiting. The smaller temperature dependence of this regime is due to pre-reactions happening in the stagnant layer. At even higher temperatures the thermal desorption rate of intact molecules is higher than the thermal dissociation rate and the growth slows down. Fig. 2.2b shows growth regimes and the ALD window. The ALD window is marked by a straight horizontal line with a nearly temperature independent growth rate per full ALD cycle. This is typical for self-limiting surface reactions. Deviations from this straight line indicate CVD or desorption contributions kicking in on the high temperature side or incomplete surface reactions and condensation on the low temperature side [37]. Fig. 2.2c shows growth regimes in FEBID as function of electron flux [1]. FEBID typically runs in the physisorption mode: without electrons no deposit would occur. The representation uses the electron flux instead of temperature which is kept constant in a FEBID process. At low electron flux, the growth is electron limited (reaction rate limited). At higher electron flux the growth rate saturates and is mass transport limited. This limitation is imposed by the rate of molecules impinging on the substrate or arriving by surface diffusion or by both of these transport processes.

These growth regimes have consequences for the lateral resolution [38] and shape control of three-dimensional deposits. Generally, the electron limited regime is preferred for uniform shapes but hard to realize in practice [39-41]. Therefore, growth parameters should optimally be adjusted such that each deposition event experiences similar precursor replenishment [42]. Fig. 2.3 shows examples of the unique resolution capabilities and shape flexibility of FEBID. The electron beam movement sequence for nanoprinting such complex 3D structures as shown in Fig. 2.3b-c is nowadays controlled via automated algorithms [39-44]. The mechanical properties of such FEBID structures were recently reviewed in [45] and in comparison to other nanoprinting techniques in [46]. Fields where FEBID materials and nanostructures are used comprise plasmonics [47-54], scanning probes and strain sensors [55-59], gas sensing [60,61], magnetics [44,62-68], superconducting devices [34,69-72], and single electron transport devices [73]. Some of the applications take advantage of the composite structure of typical FEBID deposits with the target metal embedded in a carbonaceous matrix [56,74], while others need high metal content [54,75]. FEBID is industrially integrated in photo mask repair [76,77] and scanning probe microscopy [59,78].

2.3. Surface adsorption and kinetics

In addition to the initial precursor dissociation event after adsorption - induced thermally (CVD), by reaction with specific

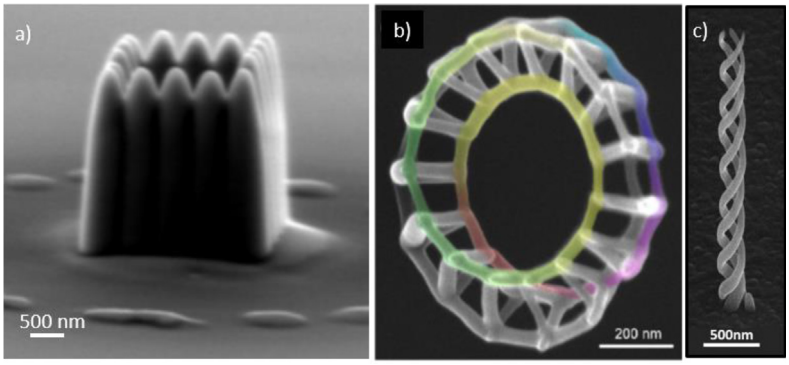

Fig. 2.3. Three-dimensional FEB grown architectures from group 10 and 11 precursors. a) Cu(hfac)VTMS, taken from Bret et al. [79]. b) Pt(η^5-CpMe)Me_3, reprinted from Winkler et al. [43] with the permission of AIP Publishing. c) Au(acac)Me_2, taken from Haverkamp [80]. Note the sub-50-nm resolution achievable for FEBID 3D nanoprinting in b).

surface sites that remove part of the ligands (ALD), or by impact of an electron beam (FEBID) - the deposit formation is influenced by the adsorption type and surface kinetics of the precursor fragments resulting after dissociation. Fig. 2.4 details the nature of the various chemical processes occurring for adsorbed precursor molecules. The initial event is a molecule impinging on the substrate. Depending on the nature and temperature of the substrate, the molecule can physisorb or chemisorb. Physisorption relies on weak van der Waals force interaction between approaching molecules and the substrate. The physics framework for this type of reversible adsorption was established by Langmuir for monolayer adsorption [81,82] and Brunauer-Emmet-Teller for multilayer adsorption [83] in the early 20th century. It has since then been modified for various intra-adsorbate interactions which resulted in different expressions for the balance of adsorption and desorption establishing the equilibrium adsorbate coverage for a given temperature and molecule gas pressure. Common to them is that the molecule resides for a given average residence time within the physisorption energy potential (of about 0.1 eV or 42 kJ/mol) before it can spontaneously thermally desorb again (Fig. 2.4a). Multilayer adsorption was recently discussed for FEBID with dicobalt octacarbonyl $Co_2(CO)_8$ [84].

An important dissociative adsorption mechanism employed for ALD is shown in Fig. 2.4b. This adsorption results in chemical bonds to the substrate while releasing part of the organic ligands, which then desorb from the moderately heated substrate. The ALD temperature range can vary largely depending on the molecule's reactivity but is always lower than the thermal decomposition temperature. This is needed to avoid the complete removal of organic ligands from the metal atom as the remaining ligands serve to prevent further reactions leading to continuous film growth (as in CVD for example). The incomplete dissociative chemisorption of the molecules is key for the self-limiting surface reaction employed in ALD that enables uniform coating of open porous structures, of high aspect ratio architectures, and obviously of planar geometries with atomic thickness control. Any mass flow related thin film growth contribution leading to film thickness inhomogeneity and thus premature blocking of open pores is by nature excluded. The chemical bond to the substrate ensures that the adsorbate cannot desorb anymore at growth temperature. The energies involved here are on the order of 1 eV or 418 kJ/mol.

Fig. 2.4c shows the (idealized) thermal decomposition of a gas phase molecule arriving on the strongly heated substrate. The growth temperature is chosen to thermally dissociate the adsorbate and to remove desirably all organic ligands by thermal desorption. As shown in Fig. 2.2a various thin film growth regimes in CVD can be addressed by still increasing the temperature. Within the reaction-limited regime, it is possible to also coat low aspect ratio architectures relatively uniformly. However, there is always a mass flow contribution [3], which is difficult to control and leads to thicker films where molecule supply is higher. Specific strategies were developed to extend CVD to infiltration into high aspect ratio architectures, like adding nucleation inhibitors or applying spatial temperature gradients in bulk porous material [85]. These CVD variants are material geometry and molecule specific in comparison to the generic ALD concept. They require very large efforts in flow or temperature control but there is a pay-off in growth speed for thickness variation tolerant applications.

Catalytic effects of the underlying surface can enhance the rate of dissociative thermal reactions. Suitable surfaces and metals can promote dissociation reactions at lower temperature than needed for thermal decomposition of the molecule. A special case is autocatalysis, in which metalorganic molecules dissociate catalytically

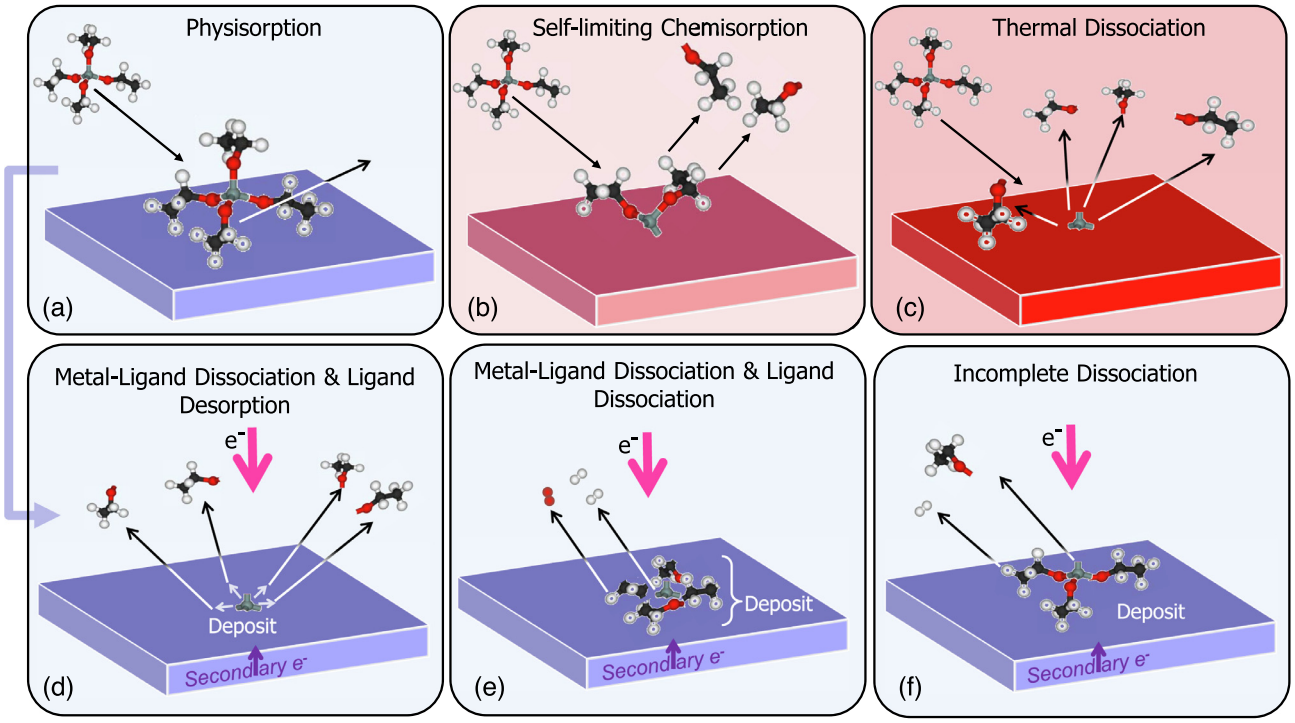

Fig. 2.4. Adsorption types and dissociation mechanisms. Note that the frames are not meant to represent the decay of a particular molecule but only to visualize schematically the possible outcome of adsorption on a surface. a) Physisorption, the molecule resides on the surface before desorbing intact. b) Dissociative chemisorption, the molecule fragments partly and establishes a chemical bond with the surface. c) Thermal dissociation upon adsorption, ideally the molecule loses all organic ligands to form a pure deposit. d-f) Non-thermal dissociation by the incoming primary electron beam or by secondary electrons released from the underlying surface under the impact of the primary electron. d) All organic ligands dissociate from the metal, reside as such on the surface and then desorb; a pure metal deposit is left. e) The organic ligands are further fragmented into volatile species and a carbonaceous residue. f) The molecule dissociates only incompletely, part of the ligands or fragments thereof remain attached to the metal. Scenarios e) and f) lead to a deposit in which the metal is typically embedded in a carbonaceous matrix.

below the thermal dissociation temperature into the metal and their volatile organic ligands, through contact with the previously deposited metal, which is also present in the precursor. For example, $Cr(CO)_6$ and $Fe(CO)_5$ show autocatalytic dissociation into metal and volatile carbon monoxide molecules and thus form a pure chromium and iron film, respectively [86]. This was employed in an electron beam induced surface activation (EBISA) process [87-89], where the focused electron beam acted as an 'invisible ink' that locally activated the surface for subsequent autocatalytic decomposition of arriving molecules. For FEBID of note is that after the initial substrate coverage the growing irradiated material itself represents the surface. In this situation the model assumption of a pure physisorption of molecules is most likely not valid anymore.

In general, by using a spatially confined energy input into the schemes of physisorption and partially dissociative chemisorption (both not leading to film growth by nature), area-selective film deposition and three-dimensional additive manufacturing can be obtained. In ALD, surface patterning is achieved by using inhibitors which make the surface inert to chemical reactions [90]. Photo-assisted CVD emerged as selective deposition technique where a laser provides the local energy input in terms of heat and photon energy. The involved pyrolytic and photolytic dissociation reactions of adsorbed molecules are limited in their spatial resolution for selective deposition by heat dissipation and wavelength, respectively [91]. However, these approaches are out of the scope of this review.

With an electron beam as spatially confined energy input, FEBID occurs as natural variant for selective deposition with highest lateral resolution. Furthermore, as the electron beam is focused over a large depth of view it provides for additive manufacturing at the nanoscale, acting as nanoprinting platform with nanometre scale printing resolution and rich 3D options.

Figs. 2.4d-f schematically show individual dissociation types relevant to FEBID and leading to different deposit composition. The point of origin here is a physisorbed molecule which is irradiated by primary electrons (purple arrow) as well as by the generated secondary electrons escaping the substrate (or growing film) surface. Fig. 2.4d represents the ideal situation where the electrons cleave the ligand–metal bonds with high efficiency. The ligands are supposed to desorb as they are volatile but will reside on the surface for a given residence time needed to overcome the physisorption potential. This scheme assumes that the ligands' own dissociation efficiency into non-volatile carbon moieties via surface reactions and via electrons is low and/or the ligand interaction with the substrate is small so that desorption is faster than further fragmentation. Fig. 2.4e shows the situation where the ligands cleaved off the metal are co-dissociated before they were able to desorb, converting them also to a non-volatile residue. In this case the intra-ligand dissociation rate is higher than the thermal desorption rate of the intact ligand. In case metal ligand cleavage dominates over ligand dissociation, the desorption of ligands can be favoured by reducing the electron flux. However, this reduces the deposition rate as now also the intact molecules can desorb before being dissociated. Finally, Fig. 2.4f shows the situation of incomplete dissociation which can occur when efficiencies of electron-induced dissociation of intra-ligand bonds are comparable to or higher than for metal–ligand bonds.

2.4. Elemental quantification

Special care has to be taken in the quantification of the deposit composition. In most studies standardless EDX is employed. It is of important note that EDX without a standard is not a quantitative technique, especially for the low acceleration voltages often used. Already for bulk samples large relative errors can occur [92]. In addition, the layered or 3D structure of many deposits leads to inconsistencies with the internally defined matrix factors that map the compositionally dependent interelement effects of electron scattering and energy loss, the expected X-ray self-absorption in the bulk and secondary X-ray emission following the self-absorption. Since these calculations assume a solid in which all elements are homogeneously distributed, the so-called 'geometric effects' can result in measured relative elemental intensities that deviate dramatically from the actual composition of the deposit [92]. In case of layered systems, these problems can partly mitigated by commercial algorithms. Still, the obtained stoichiometry can vary in the 5 at.% range as further input parameters like the layer thickness and the assumed mass density of the materials have to be provided. Using two different acceleration voltages to obtain two independent sets of data increases the certainty as the densities can serve as adjustment parameter to obtain the correct film thickness that can be measured independently. Yet, the variations in the calculated densities (compare e.g. the Supporting Information of [93]) indicate corresponding uncertainties in the quantification.

In this respect, the carbon content is especially difficult to quantify. In total three different carbon sources can be present during FEBID processing and EDX quantification, first the carbon content of the precursor molecule, second the residual hydrocarbons present in the vacuum background of the deposition chamber, and third the residual hydrocarbons present in the vacuum background of the EDX chamber. All these carbon sources are prone to variations not only between different experimental setups but also between different sessions at the same instrument, e.g. when this is a multi-user system or if the compounds experienced some aging. The carbon content of the locally supplied gas may increase significantly if the precursor partly decomposes in the crucible releasing excess ligands that are co-deposited, e.g. for $Pd(hfac)_2$ [94] or $Au(hfac)Me_2$ [95,96]. The hydrocarbons in the background of any high-vacuum chamber add further contamination to the deposit. During EDX quantification the carbon is not incorporated but added as a surface layer. As here large currents in the range of several nA have to be employed to achieve a sufficient signal-to-noise ratio, the influence of the residual hydrocarbons in the vacuum background can lead to significant overestimation of the carbon contents. EDX quantification of a fresh silver layer obtained by physical sputtering resulted in a measured carbon content of 15 at.% (cf. Supporting Information of [97]). The hydrocarbon background in HV conditions is the reason why even in deposits from carbon-free precursors like $Pt(PF_3)_4$ a substantial carbon content around 10 at.% may be measured [98]. The EDX generated carbon "background" can be measured on a place distant from the FEBID deposit and corrected for consequently.

Having regard to the issues discussed above one can conclude that EDX quantification does provide accuracies in the range of 1–5 at.% and tends to overestimate the carbon content. Nevertheless, the huge experimental basis for the well-established precursors shows a good overall agreement in deposit composition obtained by the different research groups. For tables and figures we rely here on the best obtained metal content under typical FEBID conditions, that are specified in the corresponding paragraphs.

2.5. Surface science tools and gas phase experiments for molecular level insight into surface deposition processes

The electron-induced fragmentation of a FEBID precursor is the first step in a sequence of reactions that, altogether, lead to formation of a deposit. Knowledge of the species resulting from this initial step is extremely helpful to shed light on the complex surface chemistry involved in FEBID [5]. The outcome of the initial electron-induced precursor fragmentation can be studied in the

gas phase as has been reviewed with respect to FEBID [5,99] and also for plasma processes applied in semiconductor etching [100]. Analysis of the fragmentation products is most conveniently done by mass spectrometry (MS) under single electron-molecule collision conditions [5,33,99]. These experiments, that typically employ a crossed electron and molecular beam setup, monitor either anionic species resulting from DEA or cationic species that are the result of DI. The yield of these charged particles can be monitored in dependence on the electron energy. For DEA, electron energies in the range of roughly 0–20 eV are usually sufficient to obtain a comprehensive picture while energies up to 100 eV are of interest when DI is studied. Together, this covers the typical energy distribution of secondary electrons (SEs) that are released in large numbers when an electron beam with energies of several keV, as applied in FEBID, impinges on a solid material [5,101]. Convoluting the energy dependent cross sections for formation of particular fragments with the energy dependent SE yield from the material on which a deposit grows can, in principle, provide an overview of the relevance of particular initiating electron-precursor interactions in FEBID [101]. In the absence of data on the energy dependence of electron-induced dissociation, however, a standard electron ionization MS (EI-MS) acquired with an electron energy of 70 eV, at which ionization cross sections typically have their maximal values, already yields an overview of the fragmentation channels in DI. Note furthermore that fragmentation by DEA and DI also produces complementary neutral fragments. Also, ND yields exclusively neutral species. The neutrals are difficult to assess experimentally [99] but possible neutral by-products of DEA and of DI can be estimated from thermodynamic arguments [33].

Detailed insight into surface reactions requires experiments that are performed under ultrahigh vacuum (UHV) conditions. Under these conditions, the adsorption rate from the residual gas in the vacuum chamber is small enough such that surfaces stay clean for sufficiently long periods of time. For instance, the kinetic theory of gases predicts that the rate of surface collision under high vacuum (HV) conditions ($\approx 10^{-6}$ mbar) is so high that a monolayer coverage is reached within a few seconds if all impinging molecules stick to the surface, whereas to reach the same coverage under UHV conditions ($\approx 10^{-10}$ mbar) requires several hours [102]. In a typical experiment, precursor molecules are adsorbed to a coverage of several monolayers on the surface held at cryogenic temperature. The cryogenic conditions are needed to keep a well-defined amount of precursor on the surface and, thus, allow to monitor its conversion to the deposit under electron exposure. The decomposition of the precursor can then be monitored by different surface analytical techniques [6,7,103]. X-ray photoelectron spectroscopy (XPS) and Auger electron spectroscopy (AES) provide information on the elemental composition of the pristine precursor layer and of a deposit that forms under electron irradiation or through surface reactions. The chemical shift of an XPS signal further reveals the oxidation state or binding situation of the metal and provides, for instance, evidence of the formation of elemental metal. The loss of organic ligands as consequence of electron irradiation can be monitored by reflection absorption infrared spectroscopy (RAIRS) [103–105]. Mass spectrometry (MS) is also a powerful approach to study electron-stimulated desorption (ESD) of fragments that occurs upon irradiation of the condensed precursor monolayers or bulk surfaces as well as to assess thermally driven desorption of volatile products upon heating [106,107]. Note that most experiments monitor ESD of neutral species by post-ionization in the mass spectrometer. Neutral fragments desorb much more easily than charged fragments [108], see also discussion in chapter 5. However, when an MS setup is equipped with ion extractors, it can also detect charged species [109,110]. In a FEBID study, MS cannot only monitor ESD of volatile species but also thermal reactions that occur when the deposit is exposed to a process gas. Furthermore, thermal desorption spectrometry (TDS), also refered to as temperature-programmed desorption (TPD), monitors the evolution of species from the surface as the temperature is increased. It detects products with lower volatility that remain in the deposit at cryogenic temperature or products that are formed through thermal reactions upon temperature increase [107]. TDS thus represents an important link between surface science experiments performed at cryogenic temperature and the actual FEBID process that is typically performed at or above room temperature.

The focused keV beam from an electron gun used for AES has also been applied to perform model FEBID experiments in UHV. In such experiments, the precursor is dosed onto a surface held at room temperature to prevent condensation of the molecules while the surface is continuously irradiated at typical energies of 1.5 keV or 3 keV [111–115]. This experiment allows to study deposit compositions without the influence of the typical residual gases present in an electron microscope operated under HV conditions. We also note that specialized electron microscopes may be operated under UHV conditions [87-89]. Such a setup has, however, not been applied to precursors of interest for this review.

Only few of these techniques are typically applicable in the technical FEBID process. For instance, electron microscopes are often equipped with AES or, alternatively, energy dispersive X-ray spectroscopy (EDX) for elemental mapping as the only analytical tool [87,103]. In contrast, an ALD reactor can be coupled to several in-situ observation techniques, like infrared spectroscopy of the film [116] or MS for monitoring the gas phase [106]. Transfer to a UHV chamber is needed for elemental XPS analysis of the film [117]. This adds to the importance of performing studies directly under UHV conditions. For an overview on in-situ studies on ALD surface reaction mechanisms, we refer to a tutorial of Bosch and Kessels [118] and to an in-depth review on quartz microbalance and infrared in-situ studies to Knapas and Ritala [119].

3. Group 10 precursors

3.1. Tetrakis(trifluorophosphine)M(0) complexes (M = Ni, Pt)

3.1.1. Introduction

As the incorporation of carbon constitutes a major obstacle in FEBID, carbon-free inorganic compounds may be an attractive choice to achieve pure deposits. The ligand trifluorophosphine (PF_3) is a particularly strong π-acceptor [120]. Group 10 complexes with PF_3 are thermally more stable than the corresponding carbonyls but still exhibit sufficiently high vapour pressures (cf. Fig. 3.1). The compound tetrakis(trifluorophosphine)nickel(0), $Ni(PF_3)_4$ has to be handled with care due to its high toxicity [121] and features a vapour pressure of 195 mbar at 21°C [122]. Tetrakis(trifluorophosphine)platinum(0), $Pt(PF_3)_4$ has a similarly high vapour pressure at room temperature [115]. The properties of the FEBID relevant group 10 tetrakis(trifluorophosphine)M(0) complexes are collected in Table 3.1 and Fig. 3.1 summarizes structural formulae and vapour pressure data.

3.1.2. FEBID

The only study concerned with electron beam induced deposition of nickel from $Ni(PF_3)_4$ led to moderate Ni contents of around 36 at.% [121], see also Table 3.2. The deposit contained most probably nickel oxide in addition to elemental nickel, even though oxygen was not present in the precursor molecule. The substantial amount of oxygen in the deposit was attributed to the residual water in the vacuum chamber. The main constituents of the vac-

Table 3.1
Properties of tetrakis(trifluorophosphine)M(0) complexes (M = Ni, Pt) discussed in this section.

compound	phase	appearance	melting point	boiling point	decomposition	stability	ref.
$Ni(PF_3)_4$	liquid	colourless	−55 °C	70.7 °C	150 °C	stable (water/air)	[123,124]
$Pt(PF_3)_4$	liquid	colourless	−15 °C	86 °C	> 90 °C	stable (light/air)	[125]

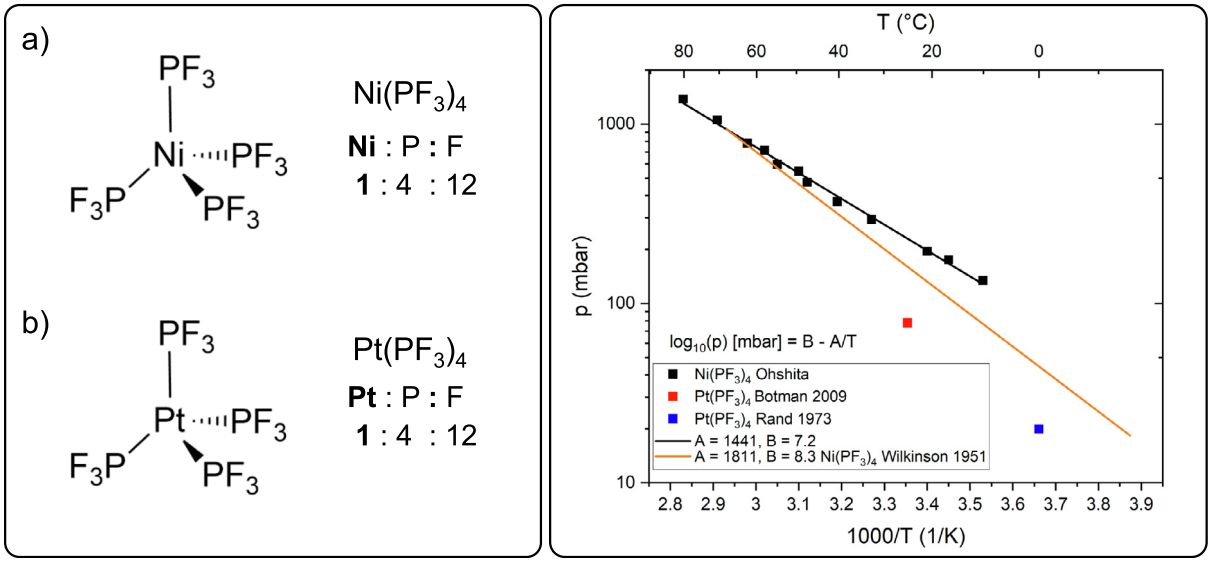

Fig. 3.1. Left: structural formulae and atomic ratios of nickel and platinum tetrakis(trifluorophosphine) complexes. Right: vapour pressure with fitted $\log_{10}(p)[mbar] = B - A/T[K]$ curves. Graphs were reproduced from [122,126,127,128].

uum background were H_2O, N_2, and O_2, respectively, which accounted for 60 %, 25 %, and 6 % of the total pressure measured using a residual gas analyser. That led to oxidation of the precursor molecules, presumed to form phosphorus oxide, hydrofluoric acid (HF), and their derivatives [121]. An oxygen (O_2) co-flow did not improve the nickel content but increased the oxygen content. Surprisingly a hydrogen (H_2) co-flow resulted in identical effects on the deposit composition which was traced back to an increased H_2O pressure during dosing of H_2 [121]. However, significantly increasing the beam current to 15 μA led to the formation of micrometre sized grains with 95 at.% Ni, the remaining 5 at.% being C, O, F, and P contamination. This was attributed to thermal effects in combination with the catalytic activity of nickel nanoparticles [121]. The carbon impurities can be probably attributed to residual gas hydrocarbons during EDX measurements, see Section 2.5.

The first deposition experiments using $Pt(PF_3)_4$ were carried out in an UHV setup equipped with an Auger spectrometer [115]. The internal electron beam source of the spectrometer was employed for electron beam induced deposition and resulted in spot deposit diameters of around 370 μm. The average film composition was 15 at.% Pt, 57 at.% P, 18 at.% C, and 9 at.% O in which the presence of carbon and oxygen was attributed to contamination from the residual H_2O and CO inside the vacuum chamber (cf. Table 3.2). The oxygen content is most likely incorporated in the matrix as phosphorus oxide [115]. Under co-dosing of O_2, the platinum content increased above 20 at.%. With in-situ substrate heating of 120 °C during electron irradiation but in the absence of added O_2, a platinum content of 70 at.% (neglecting oxygen and fluorine) could be achieved [115].

The focused electron beam induced deposition under high-vacuum conditions (HV) with a beam current of 41 nA resulted in a platinum content of 82.6 at.% where, however, elements other than those of the precursor have been neglected [129]. Another study found a deposit composition of 61 at.% Pt, 14 at.% P, 15 at.% O, and 10 at.% C, where the observed oxygen and carbon was attributed to residual gases during deposition but also during elemental analysis [98]. Table 3.2 displays the achieved deposit composition in relation to the precursor stoichiometry. In addition, the conductivity significantly improved for increasing beam currents, what can be attributed to thermal effects [129] and may be related to the loss of intact PF_3 ligands from surface-bound $Pt(PF_3)_3$ formed as intermediates [130] (see also Section 3.1.5). Correspondingly, also an in-situ substrate heating resulted in a platinum content of 58 at.% for a stage temperature of 100 °C [131].

Also a post-deposition treatment with low-temperature annealing at 100 °C and 200 °C under nitrogen (N_2) flow led to significant improvement in the conductivity in the deposits [132]. Here, the N_2 was supplied in an open environment such that the influence

Table 3.2
Normalized atomic ratios of nickel and platinum precursors with the corresponding *as-grown* deposit compositions. The *as-grown* deposit metal content is also summarized. The arrow terms read "atoms in precursor $\xrightarrow{e^-}$ atoms in FEBID material". The star denotes a fluorine content that was inferred from the 1 at.% missing in the deposit composition. The authors noted the missing fluorine explicitly [115].

complex	Ni/Pt	P	F	O	C	metal at.%	ref.
$Ni(PF_3)_4$	1	4→0.47	12→0.3	0→0.6	0→0.4	36	[121]
$Pt(PF_3)_4$	1	4→3.8	12→0.07*	0→0.6	0→1.2	15	[115] (UHV)
$Pt(PF_3)_4$	1	4→0.23	12→0	0→0.25	0→0.16	61	[98] (HV)

of ambient O_2 in the improvement could be neither confirmed nor excluded. Loss of phosphorus was observed but could not be quantified. While an independent experiment using EDX had yielded a P content of only 13.2 at.%, the observed volume shrinkage of about 40 % was taken as evidence of more residual P possibly due to a lower beam current during FEBID [132]. However, a significant contribution of carbon co-deposition may also have contributed to this result. Further post-treatments after deposition in an UHV SEM were carried out under vacuum. In a TEM, annealing and electron beam irradiation at 300 keV acceleration voltage and electron fluxes from 10^{-6} to 10^{-9} C/m^2 was performed. Both, annealing and electron beam irradiation resulted in the formation of crystalline platinum grains with the largest grain sizes achieved for annealing at ~ 127 °C [133]. In-situ TEM annealing at 250 °C proved again growth and coalescence of platinum nanoparticles in the deposit [98]. The beam sensitivity of deposits from $Pt(PF_3)_4$ was confirmed by in-situ post-deposition irradiation [134]. Further annealing procedures were performed at temperatures up to 400 °C in N_2 atmosphere and forming gas (5 % H_2 in N_2) with the latter breaking apart the deposit due to massive volume shrinkage and crystal formation [98]. In contrast, annealing at 400 °C under H_2O atmosphere avoided structural decomposition leading to pure platinum deposits [135]. Under HV conditions an autocatalytic growth of platinum from $Pt(PF_3)_4$ under co-dosing of XeF_2 can be achieved [136]. The growth proceeds from the region of high XeF_2 flux and occurs without electron beam impact after a conditioning period of 30 to 45 min of pure XeF_2 flow. However, electron beam prepatterning under XeF_2 flow and subsequent co-flow of $Pt(PF_3)_4$ and XeF_2 without electron irradiation resulted also in high purity platinum growth. Furthermore, pure platinum growth could be achieved by electron beam scanning at extremely low flux under co-flow of $Pt(PF_3)_4$ and XeF_2. The authors substantiated the hypothesis that platinum nucleation is induced by chemisorbed fluorine followed by rapid autocatalytic growth of platinum [136].

3.1.3. CVD

$Ni(PF_3)_4$ was used in a hot-wall-type CVD system in which the background pressure was 1.33 mbar. The precursor was evaporated at room temperature, while the deposition temperature was between 180 and 270 °C. Helium was used as the carrier gas. Deposits were placed on SiO_2/Si patterned substrates. Continuous Ni films were obtained. The amounts of residual impurity atoms such as F and P were <1 at.% (XPS) [122]. $Ni(PF_3)_4$ was also used to obtain $NiSi_x$ films. The pressure in the reactor was controlled to 50 mbar, the precursor evaporation temperature was 50 °C, while the deposition temperature was varied from 180 °C to 250 °C. Additionally, Si_3H_8 (1% diluted by 99% H_2) was introduced into the reactor chamber [137]. Moreover, deposition of active ^{63}Ni layers onto semiconductor silicon supports was conducted using $^{63}Ni(PF_3)_4$. A uniform crystalline nickel layer was formed at a substrate temperature of 400 °C and working pressure of 0.06–0.07 mbar [124].

$Pt(PF_3)_4$ was used to produced uniform, smooth, continuous, adherent layer of mirror-bright Pt on several types of substrates (e.g. Si, SiO_2, deposited Al_2O_3, GaAs). The complex was stored under dry N_2 in a saturator at 0 °C, at which temperature its vapour pressure was estimated to be 20 mbar. The best results were obtained by using H_2 and substrate temperature in the range of 200 – 300 °C. The Pt films contained small amounts of residual phosphorus (no quantitative data are available). The level of phosphorous impurities is four or five times higher if the deposition is carried out in nitrogen only [128]. The data is summarized in Table 3.3.

It should be noted that the presence of hydrogen improves the quality of the platinum deposit, but in the case of nickel precursor, its use was not necessary.

3.1.4. ALD

ALD studies have not yet been performed with these precursors.

3.1.5. Fundamental surface and gas phase studies

Not much is known about the fundamental electron-induced chemistry of $Ni(PF_3)_4$. The only available data is on electron attachment measured in a flowing-afterglow Langmuir-probe (FALP) apparatus [138]. This study has revealed that electron attachment to both $Pt(PF_3)_4$ and $Ni(PF_3)_4$ leads to loss of a single PF_3 ligand. However, in the case of $Ni(PF_3)_4$, nothing is known so far about the further fate of the resulting intermediate in a surface process.

The interaction of electrons with $Pt(PF_3)_4$ has been studied both in the gas phase [138–140] and for thin adsorbed surfaces layers formed under cryogenic conditions [141]. The results have been covered as prototypical case study in several reviews [6,7,101] and are thus summarized only briefly here. In the surface experiments, $Pt(PF_3)_4$ was adsorbed on a surface at cryogenic temperature and irradiated at an electron energy of 500 eV. XPS experiments [141] revealed that decomposition proceeds in two sequential steps, the first of which being a rapid loss of one PF_3 ligand by ESD forming a surface-bound $Pt(PF_3)_3$ intermediate. Further electron irradiation, however, leads only to slower cleavage of P-F bonds in the remaining ligands and presumably consequent desorption of F^- ion. This results in a deposit composed mainly of Pt and P. Annealing after completion of deposit formation does not remove further phosphorous. However, when the substrate temperature was increased step by step up to 295 °C after the initial regime of PF_3 loss, the Pt/P ratio of the final deposit continuously increased [6,130]. This gives evidence that thermal reactions of the $Pt(PF_3)_3$ intermediate dissociate further ligands from the metal, a reaction that is not possible anymore after the PF_3 ligands were dissociated by an electron-driven reaction (Fig. 3.2).

Gas phase studies have given insight into the nature of the dissociation event of the first reaction step. It was shown that cleavage of a single PF_3 ligand dominates by two orders of magnitude above all other fragmentations in DEA [140]. Notably, DI leads to loss of up to all four ligands [5]. This supports the view that the initial loss of one PF_3 ligand from adsorbed $Pt(PF_3)_4$ is predominantly initiated by DEA. In addition, a recent computational study [142] in combination with previous cross section data for electronic excitation [139] indicates that ND following electronic excitation is also a very relevant process. The calculations revealed that most of the multiple electronically excited potential energy surfaces are repulsive so that ND must occur as soon as electronic excitation has occurred [142]. The experimentally determined cross sections for electronic excitation, however, are even higher than the cross section for loss of PF_3 via DEA pointing to the relevance of ND [140].

Table 3.3
Summary of CVD data. The abbreviations mean: nq - 'not quantified', RT- room temperature, and nf - 'not found'.

compound	T precursor	T deposition	pressure	gases	film composition	ref.
$Ni(PF_3)_4$	RT	180–270 °C	1.33 mbar	He	> 99 at.% Ni	[122]
$Pt(PF_3)_4$	0 °C	200–300 °C	nf	H_2	Pt + P impurities (nq)	[128]

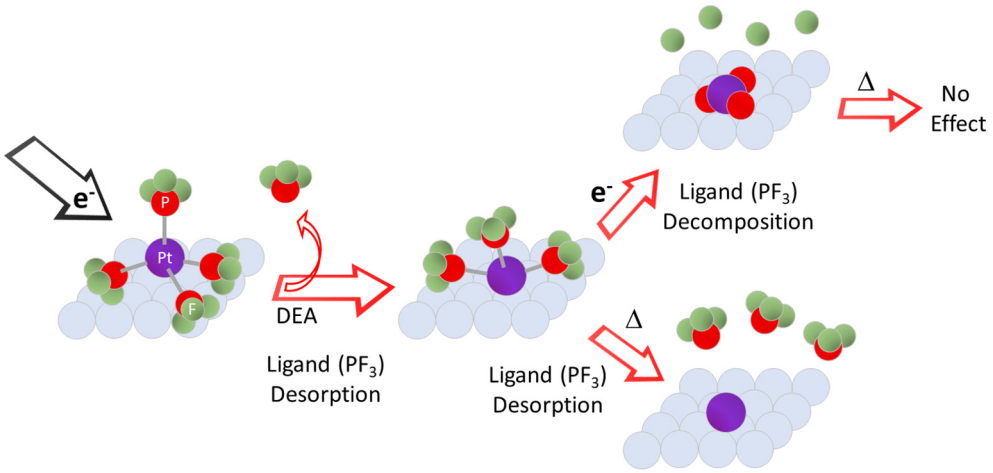

Fig. 3.2. Molecular level events during EBID from $Pt(PF_3)_4$ as deduced from surface studies under UHV conditions: The initial electron-induced dissociation leads to desorption of an intact PF_3 ligand and yields a surface-bound $Pt(PF_3)_3$ intermediate. Continued electron irradiation at cryogenic temperature up to room temperature then cleaves only P-F bonds leaving P in the deposit. Temperature increase (symbolized by Δ) leads to thermal desorption of more PF_3 and a higher Pt content of the deposit. Figure adapted by permission from Spencer et al. [6] Springer Nature, copyright (2014).

Table 3.4
Properties of cyclopentadienyl complexes (M = Ni, Pd, Pt) discussed in this section. The abbreviation nf stands for 'not found' and RT for room temperature.

compound	phase	appearance	melting point	sublimation point (T,p)	decomposition	stability	ref.
Ni(η^5-CpMe)$_2$	solid	dark green	34–36 °C	85–90 °C, 1.33 mbar	250 °C	air sensitive	[143]
Pd(η^3-allyl)(η^5-Cp)	solid	red crystal needles	60–62 °C	25 °C, p < 40 mbar	61 °C	air sensitive	[145,146]
Pt(η^5-Cp)Me$_3$	solid	colourless	108.5 °C	RT, in vacuo	140.5 °C	nf	[147]
Pt(η^5-CpMe)Me$_3$	solid	off-white	30–31 °C	23 °C, 0.071 mbar	≥ 300 °C	air & moisture sensitive	[148-151]

3.2. Cyclopentadienyl complexes of Ni(II), Pd(II), and Pt(IV)

3.2.1. Introduction

The cyclopentadienyl anion is a planar C-donor ligand that is highly stable due to its aromatic ring structure. For a group 10 metal complex the typical pentahapto (η^5-) bonding mode is observed. At room temperature, the bis(methylcyclopentadienyl) nickel(II) (Ni(η^5-CpMe)$_2$) is a solid [121] that melts around 36 °C and gradually decomposes in air [143]. The also air-sensitive (η^3-allyl)(η^5-cyclopentadienyl)palladium(II), Pd(η^3-allyl)(η^5-Cp) is solid at room temperature subliming under high vacuum conditions [144]. The very similar two compounds (η^5-cyclopentadienyl)(trimethyl)platinum(IV), Pt(η^5-Cp)Me$_3$ and (η^5-methylcyclopentadienyl)(trimethyl)platinum(IV)[1], Pt(η^5-CpMe)Me$_3$ are stable solids with melting points of 108.5 °C and 30–31 °C, respectively. Pt(η^5-Cp)Me$_3$ and Pt(η^5-CpMe)Me$_3$ feature similar vapour pressures.

The properties of the group 10 cyclopentadienyl complexes studied in FEBID are collected in Table 3.4; their structural formulae and vapour pressure data are collected in Fig. 3.3.

3.2.2. FEBID

There is only one study investigating a cyclopentadienyl complex for electron beam induced deposition of nickel. Ni(η^5-CpMe)$_2$ results in low nickel contents of around 12 at.% and a strong tendency of forming nickel oxide in the deposits (Table 3.5) [121].

Pd(η^3-allyl)(η^5-Cp) was used for electron beam induced deposition already in 1994 in a scanning tunnelling microscope (STM) under UHV conditions. The STM tip was employed as tightly confined source of electrons, which triggered deposition either on the substrate or the tip itself depending on the polarity. At 2.75 V positive bias, lines of 50 nm width with a palladium content > 95 at.% were obtained. The growth started from isolated grains that coalesced upon further scanning during deposition. The authors attribute this to an electron-excitation mechanism, i.e. an electron-induced dissociation. The growth of the grains can be explained by two mechanisms: i) by a catalytic activity of the first deposited Pd atoms and ii) by the enhanced field between the STM tip and these metallic seed deposits that led to focusing of electrons onto the seed and consequently faster growth [154]. Later experiments using Pd(η^3-allyl)(η^5-Cp) under typical FEBID conditions resulted in deposit compositions of 26 ± 5 at.% Pd and of 74 ± 5 at.% C (cf. Table 3.5) with the palladium content varying between 18 and 29 at.% for currents from 0.8 to 26 nA [144]. A post-deposition treatment with electron beam irradiation at high currents of around 26 nA under simultaneous flow of O_2 could improve the palladium content to ~ 60 at.% [144].

Platinum cyclopentadienyl complexes are standard compounds in commercial gas-injection systems and are, hence, ubiquitous in FEBID. First, Pt(η^5-Cp)Me$_3$ was employed [155,156] leading to platinum contents in the range of 4–13 at.% [155] while later 21.5 at.% were found for high aspect ratio deposits (Table 3.5) [157]. Interestingly, the very similar compound Pt(η^5-CpMe)Me$_3$ leads to deposits with a typical platinum content of about 15–17 at.% even though more carbon is present in its stoichiometry [131,158]. Later, also higher platinum contents around 22–25 at.% were reported [55,157-159], most probably related to in-operando purification by the residual water in the vacuum chamber [35]. While the background pressures in the range of $8{\cdot}10^{-7}$–$3{\cdot}10^{-6}$ mbar were comparable [55,131,158,160,161], it has to be noted, that in studies with higher Pt content relatively high currents around 1.6 nA were used along with the bad heat conductor SiO_2

[1] In FEBID literature commonly abbreviated as MeCpPt(Me)$_3$.

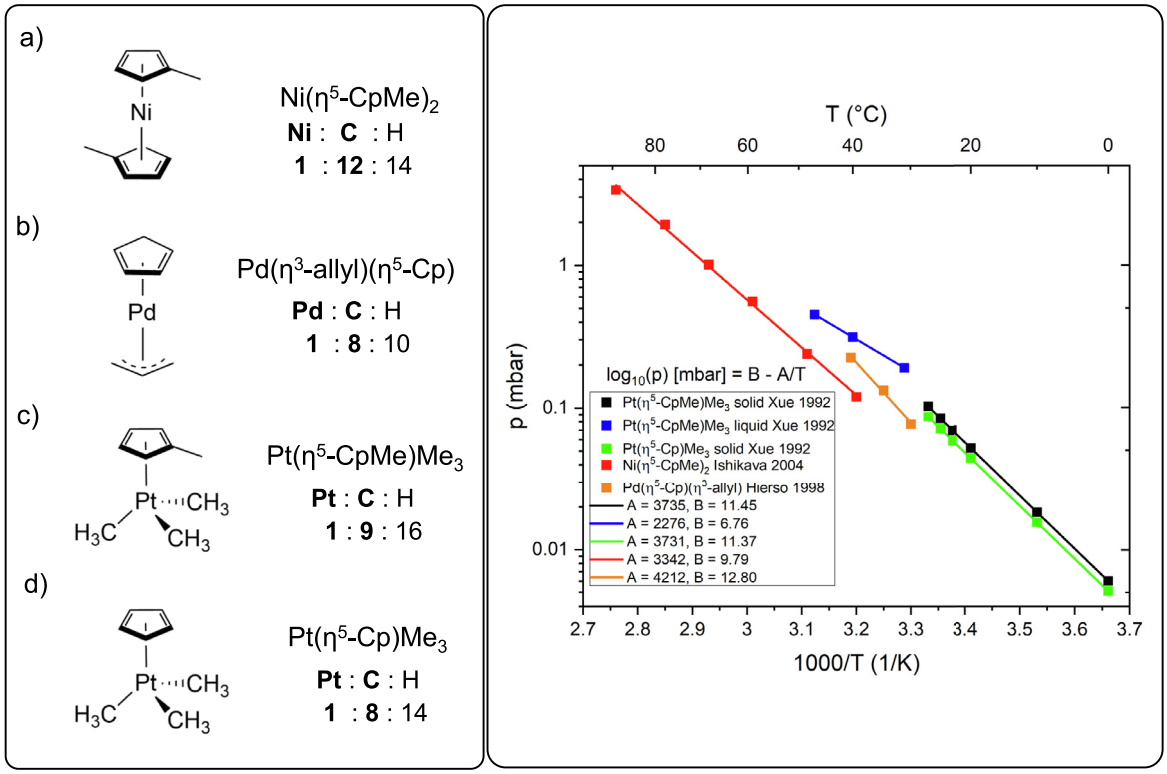

Fig. 3.3. Left: structural formulae and atomic ratios of cyclopentadienyl complexes of nickel, palladium, and platinum. Right: vapour pressure with fitted $\log_{10}$(p)[mbar] = B - A/T[K] curves. Graphs were reproduced according to Ni(η^5-CpMe)$_2$ [143], Pt(η^5-CpMe)Me$_3$ and Pt(η^5-Cp)Me$_3$ [152], and Pd(η^3-allyl)(η^5-Cp) [153].

as a substrate [55,160,161]. Studies of lower reported Pt content relied on a silicon substrate with native oxide [131,158,162-165]. Therefore, thermal effects may also play a critical role here (cf. Sections 3.4.5 and 5.4). Table 3.5 summarizes the obtained deposit composition normalized to metal content in relation to the precursor stoichiometry. Increasing the electron beam current used for nanopillar deposition leads to an increased platinum content up to about 28 at.% after which it decreases again [166]. In view of Section 2, the observed behaviour can be explained as a variation from i) incomplete dissociation and/or ligand co-deposition for low currents to ii) improved ligand desorption due to local heating for medium currents to finally iii) strong precursor depletion and ligand co-deposition for high currents. However, the corresponding regimes are strongly dependent on the local deposition conditions (precursor flow, beam profile, dwell and refreshment times) and on the local chemistry (dissociation cross-section, diffusion behaviour, and residence times of the compound as well as stability and residence time of the ligands). Hence, the deposition conditions have to be optimized for each specific compound in each specific experimental setting (cf. Section 6). Fortunately, this does not necessarily limit the potential of FEBID for three-dimensional nanofabrication. Instead of many a priori unknown parameters, the vertical growth rate may be employed as an empirical parameter for the calibration of growth models. Based on such models the required electron beam paths for the deposition of complex 3D shapes can be calculated (Fig. 3.4) [40,42,166,167].

The impressive results in the fabrication of complex nanostructures prove the extraordinary reliability of Pt(η^5-CpMe)Me$_3$ as precursor for direct electron beam writing. Pt(η^5-CpMe)Me$_3$ can be used for years without refilling the gas-injection system, heating the compound to 60–80 °C for several thousand times without any sign of thermal decomposition. However, exactly this thermal stability hampers the growth of pure platinum structures [170]. In contrast to other precursors (see e.g. Section 3.1 for the case of Pt(PF$_3$)$_4$ and Section 4.4 for the case of gold), heating of the substrate during the deposition process does not change the material composition [171]. This can be attributed to the fact that no stable intermediates are formed under electron beam induced

Table 3.5
Normalized atomic ratios of nickel, palladium, and platinum precursors and *as-grown* FEBID material compositions. The *as-grown* deposit metal content is also summarized. The arrow terms read "atoms in precursor $\xrightarrow{e^-}$ atoms in FEBID material". The hydrogen content is neglected. *Note that this element was not part of the precursor molecule and reflects co-deposition of contaminants from the substrate and background gas. The abbreviation nq stands for 'not quantified'.

complex	Pd/Ni/Pt	C	O	metal at.%	ref.
Ni(η^5-CpMe)$_2$	1	12→6.8	0→0.4*	12	[121]
Pd(η^3-allyl)(η^5-Cp)	1	8→2.8	0→0	26	[144]
Pt(η^5-Cp)Me$_3$	1	8→6.7	nq	13	[155]
Pt(η^5-Cp)Me$_3$	1	8→3.4	0→0.26*	21.5	[157] (pillars)
Pt(η^5-CpMe)Me$_3$	1	9→4.9–5.7	nq	15–17	[131,158]
Pt(η^5-CpMe)Me$_3$	1	9→3-3.5	nq	22–25	[55,157-159]
Pt(η^5-CpMe)Me$_3$	1	9→2.6	nq	28	[166] (pillars)

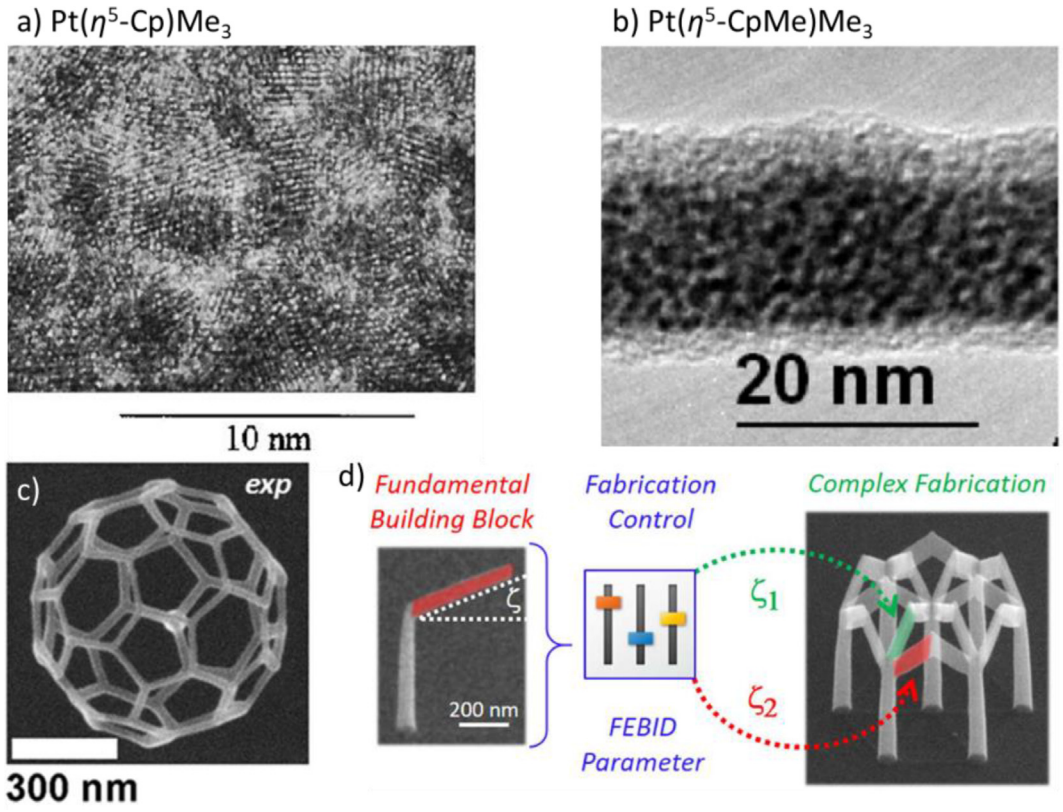

Fig. 3.4. a) & b) Transmission electron micrographs of platinum containing freestanding deposits from a) Pt(η^5-Cp)Me_3, reprinted with permission from Koops et al. [168], copyright (1995) American Vacuum Society. b) Pt(η^5-CpMe)Me_3, reprinted from Frabboni et al. [169], copyright (2007) with permission from Elsevier. c) Scanning electron micrograph of complex buckyball nanostructures fabricated using Pt(η^5-CpMe)Me_3 by computer-aided design relying on a hybrid Monte-Carlo continuum simulation, reproduced from Fowlkes et al. [39] copyright (2016) American Vacuum Society. d) Scheme of the computer-aided design approach, reprinted with permission from Winkler et al. [40] copyright (2018) American Chemical Society.

dissociation [130]. Also varying deposition conditions like beam energy, dwell time etc. shows no or only minor effects on the deposit composition [131,159,166]. Employing a pulsed laser to enhance the desorption of ligands after each deposition cycle improves the platinum content up to about 35 at.% [172] under preservation of the three-dimensional shape [165]. However, to remove the dominant carbon portion more efficiently, oxidizing agents have to be employed. This can be done in-situ e.g. by addition of H_2O vapour in an environmental SEM during deposition, resulting in 50 at.% platinum [173] or by a continuous flow of O_2 during deposition, resulting in 90 at.% of platinum [174]. However, most of the purification approaches are carried out as post-deposition treatments, like e.g. annealing strategies under oxidizing atmosphere [158,169]. This technique provides for platinum contents of above 70 at.% but reduces the shape fidelity. The same holds true for a combined approach with in-situ pulsed laser treatment under O_2 injection after deposition [175]. Much better results on shape preservation were achieved by providing the energy locally by electron beam irradiation [55,160,176]. However, without oxidizing agents the achievable platinum content was again limited to 35 at.% [176] matching the one of the in-situ laser treatment [172], cf. also Section 6.2. Upon addition of H_2O vapour [163] or O_2 [174] at room temperature or upon addition of O_2 at 50 °C substrate temperature [177,178] during the electron beam curing, pure platinum nanostructures could be realized under shape preservation. Interestingly, the O_2-assisted electron beam curing is a top down process, while the water-assisted curing is a bottom-up process. Results from modelling suggest, that bottom-up purification is a consequence of the efficient uptake of H_2O into the deposit in combination with a weak adsorption, while chemisorption of O_2 at the buried platinum surfaces controls the top-down purification [179]. In this respect, it should be noted that employing only pulses of O_2 at moderately increased temperatures of around 150 °C [180] led to comparably good purification. Here, the authors proposed an assistance of the process by the catalytic activity of platinum, that was also suggested for the combined laser-oxygen post-treatment [175]. Of note is that this is supported by ALD studies as well, cf. Section 3.2.4.

3.2.3. CVD

Ni(η^5-CpMe)$_2$ was used to deposit Ni films at substrate temperature of 120–600 °C and a chamber pressure of 0.13–13.3 mbar. The precursor was heated to 50–70 °C and introduced into the deposition chamber using hydrogen as the carrier gas. The deposited Ni reacted with the substrate Si resulting in $NiSi_2$ formation. Ni/C ratio of deposited films was 6 at 120 °C, 2 at 300 °C and 1 at 600 °C [143]. When the oxygen was used as reactive gas nickel oxide layers were grown [181].

Gozum et al. [182] described several Pd precursors for CVD among them the organometallic compound Pd(η^3-allyl)(η^5-Cp) that was also employed for FEBID (cf. Section 3.2.2). The formation of amorphous palladium films (up to 2 μm thick) contaminated with carbon (5 wt% C) was observed at 250 °C and $1.3 \cdot 10^{-4}$ mbar. Analysis of the gaseous products resulting from the thermolysis indicated a mixture of cyclopentadiene (about 43%), propene (about 38%), and only trace amounts of hexadienes (<1%) [182].

Crystalline palladium films with < 3 wt% of carbon were deposited using hydrogen (1% in helium) between 30 and 60 °C substrate temperature. Such considerable lowering of the deposition temperature indicates the catalytic nature of this process. The studies

Table 3.6
Summary of FEBID related CVD data for cyclopentadienyl complexes (M = Ni, Pd, Pt). The abbreviation nf stands for 'not found' and RT for room temperature.

compound	T precursor	T deposition	pressure	gases	film composition	ref.
$Ni(CpMe)_2$	50–70 °C	120–600 °C	0.13–13.3 mbar	H_2	Ni/C = 6, 2, 1 @120 °C, 300 °C, 600 °C	[143]
Pd(η^3-allyl)(η^5-Cp)	nf	250 °C	$1.3{\cdot}10^{-4}$ mbar	vacuum	95 at.% Pd, 5 at.% C	[182]
Pd(η^3-allyl)(η^5-Cp)	nf	30–60 °C	$1.3{\cdot}10^{-4}$ mbar	He + H_2 (1%)	>97 wt% Pd	[183]
Pt(η^5-Cp)Me_3	25 °C	180 °C	1013.25 mbar	Ar + H_2	>99 at.% Pt	[184]
Pt(η^5-Cp)Me_3	14 °C	90–180 °C	nf	He + H_2	>99 at.% Pt	[152]
Pt(η^5-Cp)Me_3	40–120 °C	250 °C	$1.3{\cdot}10^{-3}$ mbar	vacuum	74 at.%	[186]
Pt(η^5-CpMe)Me_3	23 °C	120 °C	1013.25 mbar	Ar + H_2	>99 at.% Pt	[185]
Pt(η^5-CpMe)Me_3	14 °C	90 – 180 °C	nf	He + H_2	>99 at.% Pt	[152]
Pt(η^5-CpMe)Me_3	10 °C	350 °C	2.7 mbar	Ar + O_2	resistivity: 10.5 μΩ cm (similar to the bulk metal)	[187]

of gaseous decomposition products suggest that the allyl ligand is mainly hydrogenated to propane [183].

Pt(η^5-Cp)Me_3 was vaporised at atmospheric pressure and 25 °C. Argon was used as carrier gas and the hydrogen was introduced as reactive gas. Glass slides and silicon wafers with (100) orientation were used as substrates. The deposition was carried out at 180 °C. The surface of the Pt film was highly contaminated with oxygen and carbon after several days of exposure to ambient conditions. Upon argon ion sputtering into the film, the oxygen content decreased below detection limits, while the carbon content decreased to <1 at.%. In the absence of H_2 much higher concentrations of carbon inside the film were detected [184].

In an experiment by Xue et al. [152], Pt(η^5-Cp)Me_3 and Pt(η^5-CpMe)Me_3 were evaporated at 14 °C. Deposition started by directing a helium gas flow over the organometallic source. Hydrogen was introduced into the reactor chamber and for deposition temperatures of 90 to 180 °C, the platinum films were pure (<1 at.% carbon, oxygen, and no other impurities).

Pt(η^5-CpMe)Me_3 was vaporised at atmospheric pressure in a stream of argon at 23 °C. H_2 was used as the reactive gas. Glass slides and oriented Si(100) substrates were heated to 120 °C. Analyses by XPS carried out after Ar^+ sputtering showed no detectable amount of carbon in the bulk of the platinum film [185]. The data is summarized in Table 3.6.

For completion we would like to note that cyclopentadienyls of Pd(II) [182,183] and Pt(IV) [152,182–185] could be deposited at low temperature but the metal CVD process required hydrogen presence. The post-deposition Ar^+ ion sputtering for the platinum deposit was useful for contamination removal.

Plasma CVD processes were found for Pd(η^3-allyl)(η^5-Cp) and Pd(η^5-Cp)Me_3 and are shown in Table 3.6a [188].

For palladium and platinum argon plasmas achieved pure metal films. The addition of oxygen plasma resulted in poorer platinum metal content. This is in line with oxygen plasma ALD experiments using the similar precursor Pt(η^5-CpMe)Me_3 [190,191], see Table 3.7, that observed the formation of platinum oxide at around 100 °C. Higher temperatures or addition of hydrogen to the plasma increased the platinum content to 100 at.%. Comparison with data from Table 3.6 shows that for Pd(η^3-allyl)(η^5-Cp), the plasma argon CVD resulted in pure palladium films, however, at 60 to 90 degrees higher hotter deposition temperatures compared to the He/hydrogen (1%) thermal process at 30–60 °C Pd [183].

3.2.4. ALD

Nickel film ALD was not attempted with Ni(η^5-CpMe)$_2$ but rather using nickelocene, Ni(η^5-Cp)$_2$, as the precursor. Triple precursor ALD processes with Ni(η^5-Cp)$_2$/H_2O/H-plasma at 165 °C [192] and Ni(η^5-Cp)$_2$/H_2O/H_2 at 330 °C [193] were employed. The role of water was shown to be important as hydrogen and hydrogen plasma alone proved not being able to form volatile moieties in reaction with the cyclopentadienyl. Using water alone gave mixed Ni/NiO films. Furthermore, water was assumed to form adsorption sites for Ni(η^5-Cp)$_2$.

Palladium ALD does not work with the combustion (oxidation) process [27]. Probably for this reason there is no report on ALD with cyclopentadienyl containing palladium precursors, including the Pd(η^3-allyl)(η^5-Cp) complex used in FEBID.

To deposit platinum films with a thermal ALD process, the precursor Pt(η^5-CpMe)Me_3 is most frequently used [194]. Water was found to be an inefficient co-reactant [195]. Thermal ALD at 300 °C with oxygen as a co-reactant results in uniform platinum films [196] by combustion of the platinum precursor. In this temperature range, molecular oxygen adsorbs dissociatively onto the platinum surface. Of note is that platinum acts as a catalyst for this surface reaction. The atomic oxygen remains at the surface during the purge pulse and reacts with the ligands of the platinum precursor in the following step. Due to the limited amount of adsorbed oxygen, the oxidation of the ligands may be incomplete. The unox-

Table 3.6a
Summary of plasma CVD data. The abbreviation nf stands for 'not found'.

compound	T precursor	T deposition	pressure	power density	gases	film composition	ref.
Pd(η^3-allyl)(η^5-Cp)	nf	120 °C	0.20 mbar	0.1 W/cm^2	Ar	100 % Pd	[188]
Pt(η^5-Cp)Me_3	40 °C	200 °C	0.25 mbar	0.44 W/cm^2	Ar	100 wt% Pt	[189]
Pt(η^5-Cp)Me_3	40 °C	25 °C	0.25 mbar	0.44 W/cm^2	Ar	99 wt% Pt	[189]
Pt(η^5-Cp)Me_3	40 °C	100 °C	0.25 mbar	0.22 W/cm^2	135 sccm Ar + 15 sccm O_2	87 wt% Pt	[189]

Table 3.7
Summary of FEBID related ALD data. The abbreviation RT stands for room temperature.

precursor	co-reactant	T deposition	film composition	ref.
Ni(η^5-CpMe)$_2$			No ALD report	
Pd(η^5-Cp)(η^3-allyl)			No ALD report	
Pt(η^5-CpMe)Me_3	O_2 (air)	300 °C	> 98 at.% Pt	[196–198]
Pt(η^5-CpMe)Me_3	O_2 plasma	100–300 °C	PtO_x for long plasma exposures and/or low T	[190,191]
Pt(η^5-CpMe)Me_3	O_2 plasma & H_2	RT	> 99 at.% Pt	[199]
	O_2 plasma & H_2 plasma			

idized ligands remaining after the purge react with the oxygen during the next pulse, resulting again in the starting configuration of a layer of oxygen atoms bond to a platinum surface [196]. The thermal ALD half reactions are shown in Fig. 3.5 and were summarized by Mackus et al. [197] and van Daele et al. [198].

The self-termination of the Pt(η^5-CpMe)Me_3 surface half-reactions on the platinum surface is obtained by the formation of a hydrocarbon monolayer blocking further adsorption of Pt(η^5-CpMe)Me_3 (see also Section 3.2.5). The oxygen half-reaction removes this hydrocarbon layer and terminates dissociative chemisorption by forming an oxygenated platinum surface.

In plasma ALD, oxygen radicals were introduced to the surface directly from the gas phase [191]. Pure platinum and platinum oxide were deposited, depending on the oxygen partial pressure, on the plasma exposure time, and on the deposition temperature [190,191]. At low temperatures, platinum oxide was preferably grown while pure platinum was achieved for higher temperatures (see Table 3.7). The platinum surface coverage with oxygen determined when a phase of platinum oxide formed on the top. To deposit pure platinum with good electrical properties, an additional hydrogen or hydrogen plasma step had to be introduced to reduce the deposited platinum oxide to pure platinum. With this, the temperature window could be lowered to room temperature [199].

Conformal pure platinum coatings on three dimensional carbonaceous FEBID structures with high shape fidelity were achieved by a triple precursor ALD process. The scanning electron micrographs in Fig. 3.6 a) and b) before and after ALD coating demonstrate the conformal coverage of complex geometries like the shown helix with three pitches. Three ALD steps were employed: Pt(η^5-CpMe)Me_3, remote oxygen plasma, and hydrogen plasma at 120 °C [80] with argon as the carrier gas. A deposition rate of 0.031 nm/cycle was observed. The resistivity was determined to 21 μΩ cm, being only two times higher than the bulk value of 10.6 μΩ cm.

The same ALD process initiates on Pt containing material as well as on carbonaceous material. Fig. 3.6 a)-c) show scanning electron micrographs of successful platinum coating of FEBID nanostructures that were deposited using Pt(η^5-CpMe)Me_3 as FEBID precursor while in Fig. 3.6 d) a carbon precursor was employed for FEBID, i.e. no initial platinum atoms were needed to start the process. The conformal coverage was also demonstrated for complex geometries like the shown helix with three pitches.

Further studies dealt with the island formation and evolution of Pt during ALD [200–204] which we do not discuss in the scope of this article. Table 3.7 summarizes the FEBID related ALD data.

3.2.5. Fundamental surface and gas phase studies

The only fundamental study performed on Ni(η^5-CpMe)$_2$ has been by ESD on adsorbed surface layers (at −173 °C) upon electron irradiation at 500 eV [103]. As only desorbing product, H_2 was observed, suggesting that C–H bond cleavage and subsequent crosslinking of the ligands occurs. This is in line with the low Ni content obtained in FEBID with this precursor (see Section 3.2.2). The electron-induced fragmentation of gaseous Pd(η^3-allyl)(η^5-Cp) by DI has been studied by MS for electron energies between 8 eV and 26 eV [205]. Threshold energies and relative abundances for the different positive ion fragments reveal that loss of allyl from the parent ion is slightly favoured above loss of the cyclopentadienyl ligand. Notably, the free metal cation Pd^+ was observed above 14 eV with relative abundance up to 4% which is higher than the yield of Pt^+ obtained from Pt(η^5-CpMe)Me_3 at 100 eV [206] pointing to a more efficient fragmentation of Pd(η^3-allyl)(η^5-Cp).

Studies on electron-induced surface reactions of Pd(η^3-allyl)(η^5-Cp) were not yet reported. The low thermal stability of cryogenically condensed Pd(η^3-allyl)(η^5-Cp) was noted in a surface study on the dissociative adsorption of the precursor on a clean Pd(1 1 1) surface. All other inner surfaces of the deposition apparatus needed to be covered by inert materials such as glass or Teflon to avoid unwanted decomposition by contact with metal parts [207]. While multilayer desorption occurred at −41 °C on SiO_2, condensed Pd(η^3-allyl)(η^5-Cp) in contact with the Pd(111) surface dissociated already at −101 °C, whereby the allyl ligand split from the precursor and interacted with the surface. Fragments released

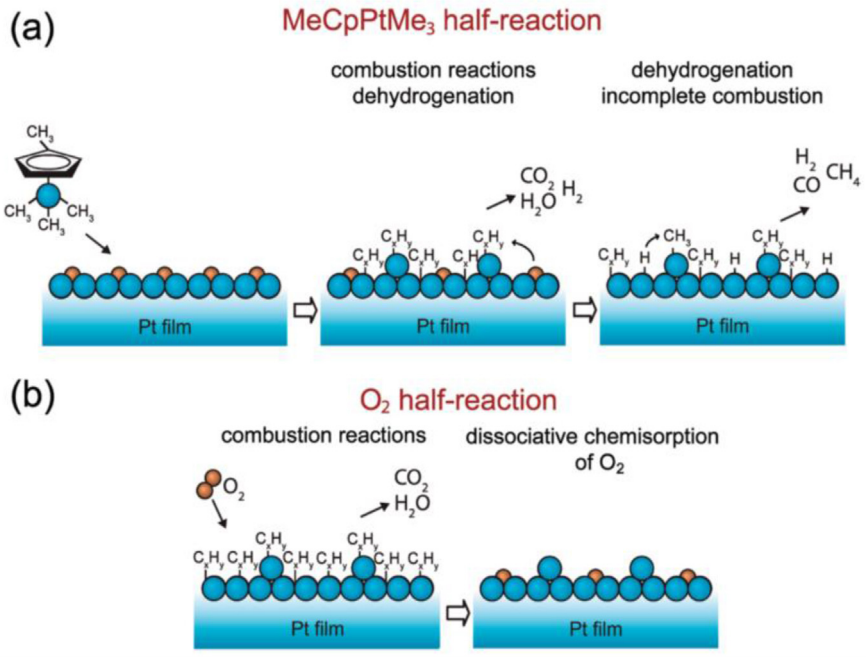

Fig. 3.5. Schematics of surface reactions during thermal ALD of Pt(η^5-CpMe)Me_3 (Me_3PtCpMe) and O_2 at 300 °C. Reprinted with permission from Mackus at al. [197], copyright (2012) American Chemical Society. a) Adsorption reactions of Pt(η^5-CpMe)Me_3 on oxygenated platinum surface. b) Adsorption reactions of oxygen on hydrocarbon terminated platinum surface. The purge steps between the half-reactions were omitted for clarity.

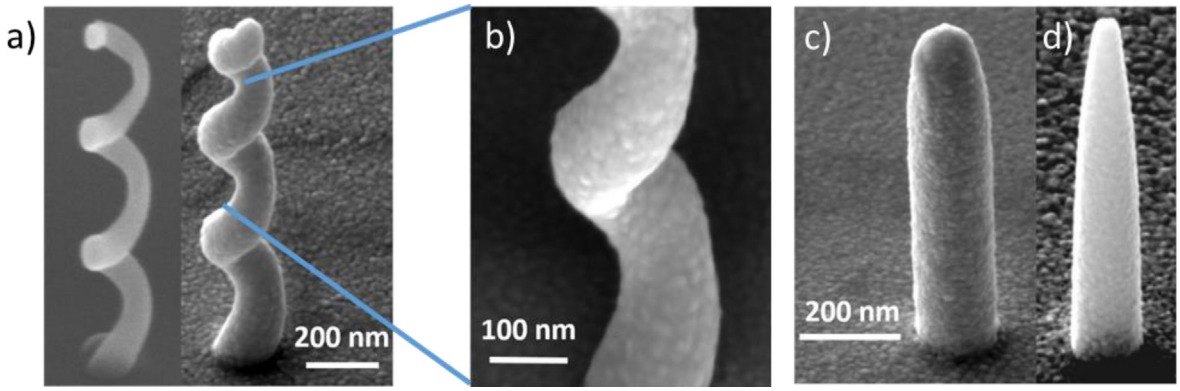

Fig. 3.6. Scanning electron micrographs of 3D FEBID structures. a) A FEBID helix using Pt(η^5-CpMe)Me_3 as precursor before and after conformal Pt ALD coating, and b) a close-up of this helix. c) A FEBID pillar deposited using Pt(η^5-CpMe)Me_3 as precursor, and d) a FEBID pillar deposited with the carbon precursor phenanthrene, both conformally coated with Pt ALD [80].

by this partial decomposition, presumably the allyl or products deriving thereof, reacted with precursor molecules in further top layers thus immobilizing them partly. At −38 °C, conversion of Pd(II) to Pd(0) occurred, indicating that all ligands were dissociated from the precursor then. However, most of the carbon content remained on the surface. It was also observed that this carbon content could not be removed by heating to 227 °C under an H_2 pressure of 10^{-5} mbar. The observed immobilization suggests that a high density of precursor on the surface counteracts the formation of high purity CVD layers because of crosslinking reactions of the ligands. The thermal deposition of Pd(η^3-allyl)(η^5-Cp) was also studied on differently pre-treated Si surfaces [208]. Decomposition of the precursor was most efficient on surfaces with Si-OH which can provide H needed to remove the ligands. The low thermal stability of Pd(η^3-allyl)(η^5-Cp) may also be responsible for the relatively high Pd contents as compared to Pt(η^5-CpMe)Me_3 observed in FEBID (see Section 3.2.2).

Owing to its very favourable vapour pressure already at room temperature and the fact that Pt(η^5-CpMe)Me_3 is a well-established commercial FEBID precursor, it has also been studied in depth at the fundamental level [206,209]. Pt(η^5-CpMe)Me_3 has, in particular, served as a prototypical case in previous reviews on the electron-induced chemistry of FEBID [5-7,101,103]. Briefly, it was shown by XPS that only one of the nine carbon atoms is lost upon irradiation of thin layers of the precursor condensed at cryogenic temperature leading to a composition of PtC_8 with unknown H content [209]. ESD revealed that H_2 and CH_4 are the only volatile products released from the surface under electron irradiation. ESD from Pt(η^5-Cp)Me_3 has been studied for comparison, showing the same result, which demonstrates that desorption of CH_4 relates to loss of a CH_3 ligand. A later study [107] has provided support for the initial hypothesis [209] that CH_4 was in fact formed in the precursor layer and not from reactions of CH_3 with hydrogen from the chamber walls. The exclusive desorption of CH_4 and absence of CH_3 further suggests that the conversion to CH_4 proceeds as an intramolecular reaction. This is of particular interest, as gas phase results on Pt(η^5-CpMe)Me_3 have revealed that DEA is by far dominated by loss of a single CH_3 and the most abundant fragments in DI are produced by loss of two or three CH_3 ligands both with and without loss of one or more hydrogen [206]. The initial electron-induced fragmentation of an isolated Pt(η^5-CpMe)Me_3 gas molecule thus always yields CH_3 radicals. This demonstrates that adsorption modifies the dissociation reactions of a precursor. Of important note is also that the deposit composition PtC_8H_x (x not measured but presence of H confirmed in [210]) formed through electron irradiation at 500 eV under cryogenic conditions (−93 °C) [209] does not quantitatively agree with the much lower carbon content of deposits obtained in FEBID processes ($PtC_{2.6\text{-}5.7}H_x$ see Table 3.5). Of note is also that $PtC_{<5}H_x$ compositions imply the partial removal of Cp that may be a consequence of the residual water in under HV FEBID conditions, see also Section 5.3.2. Even post-irradiation annealing of the condensed film to temperatures up to 367 °C did not change this composition [130]. This is in contrast to another surface study at cryogenic temperature which applied TDS to monitor the effect of temperature increase on a deposit produced from condensed Pt(η^5-CpMe)Me_3 at −168 °C by a comparable electron exposure but with an energy of 31 eV [107]. This study revealed that, although ESD of CH_4 was terminated, more CH_4 was released from the deposit through thermal reactions as the temperature was increased up to 177 °C without further electron irradiation. This indicates that the chemical nature of the deposit may vary with the applied electron energy, an effect that has not yet been studied in detail. Note again that post-deposition electron irradiation at 5 keV of deposits produced from Pt(η^5-CpMe)Me_3 in an actual FEBID process was shown to increase the Pt content up to 35 at.% for deposits with thickness below 50 nm [176]. It was suggested that this carbon removal involved small ligand fragments embedded in the growing deposit that can diffuse out of the deposit under post-deposition electron irradiation. This was supported by growth of the Pt nanograins which implies that the high-energy electron beam in fact induces a certain mobility of the deposit constituents that can influence the final composition. However, an alternative and very likely explanation for the removal of carbon in the SEM is that residual water impinges with around 1ML/s at 10^{-6} mbar on a surface in the SEM and etches away carbon under the electron beam [163].

Surface studies aiming at a fundamental understanding of ALD processes with Pt(η^5-CpMe)Me_3 also provide further information on the useful temperature range for deposition and demonstrate how ALD can profit from electron-induced chemistry. The thermal deposition on a Ni foil was found to be self-limiting at temperatures between 252 °C and 352 °C, but lead to multilayer deposition, i.e. a CVD-type process, at 402 °C [211]. Using XPS, a C:Pt ratio of 5:1 was deduced for the self-limiting regime, indicating that, under these conditions, the CH_3 ligands are lost upon activated bonding to the surface while the MeCp group remains coordinated to the adsorbed Pt atoms. Another recent study has shown that electron-impact excitation of Pt(η^5-CpMe)Me_3 in the gas phase leads to a more efficient uptake of the precursor on a silicon oxide surface [212]. This experiment used a nude ionization gauge pressure transducer operating at an acceleration voltage of 150 eV that was mounted out of sight of the sample for ionization of the precursor. This led to a typical C:Pt ratio around 6 on the surface, pointing again to loss of CH_3 ligands, this time prior to landing.

For further insight into the interaction of Pt(η^5-CpMe)Me_3 reference may also be given to a theoretical study that discusses how the precursor interacts with different defect sites on a graphene layer [213]. This may be relevant in terms of chemisorption on a typical FEBID deposit material composed of metal and a carbonaceous matrix, where the carbonaceous matrix material contains reactive sites due to electron irradiation.

3.3. M(II) β-diketonate complexes (M = Ni, Pd, Pt)

3.3.1. Introduction

The β-diketonates are an important class of volatile metal complexes and therefore widely used as precursors in CVD. The β-diketonate ligand can form a 6-membered ring enclosing the central metal ion as one of the hexagon corners [1]. The compounds have a relatively large vapour pressure (cf. Fig. 3.7) and the rigid chelate structure protects the central atom efficiently against chemical reactions. The only group 10 β-diketonate complex employed for FEBID so far is bis(hexafluoroacetylacetonate)-palladium(II), $Pd(hfac)_2$ due to its practical vapour pressure close to room temperature. The compound is stable and easily sublimates. To ensure a sufficiently large vapour pressure for FEBID only a temperature of 36 °C is required under high vacuum conditions [94]. All other compounds of Table 3.8 were not yet applied in FEBID but investigated in UHV studies, which may give further insight into the behaviour of β-diketonate complexes as relevant to FEBID.

Table 3.8 summarizes the properties of the reviewed group 10 β-diketonate complexes; the corresponding structural formulae and vapour pressure data are presented in Fig. 3.7.

3.3.2. FEBID

Depositions relying on gas phase FEBID using $Pd(hfac)_2$ and electron beam currents below 1 nA resulted in a dominant carbon portion within the deposit. The composition achieved was only 5.6 at.% of Pd, 81 at.% C, 12.6 at.% O, and 0.5 at.% F (cf. Table 3.9). Due to aging effects of the compound, the palladium content decreased further over time [94]. Later experiments of the same authors obtained palladium contents between 20 and 24 at.% for currents above 1 nA, what was attributed to the higher beam current and lower primary electron energies [144].

The Pd contents could be further improved to above 60 at.% by massive electron beam post-irradiation at currents of 26 nA under

Table 3.8
Properties of M(II) β-diketonate complexes (M = Ni, Pd, Pt) discussed in this section. These compounds are not light sensitive. The abbreviation RT stands for room temperature, nf for 'not found', and nq for 'not quantified'.

compound	phase	appearance	melting point	sublimation point (T, p)	decomposition	stability	ref.
$Ni(acac)_2$	solid	light green	230 °C	≈207 °C, 0.007 mbar	230 °C	stable (hygroscopic)	[215,216]
$Ni(hfac)_2$	solid	green	205 °C	100 °C, 1 atm	nf	stable	[214,217,218]
$Pd(acac)_2$	solid	canary yellow	190 °C	100–160 °C, p nq	190 °C	stable	[219]
$Pd(hfac)_2$	solid	yellow	100 °C	46–55 °C, p nq	230 °C	stable	[220–223]
$Pt(acac)_2$	solid	bright yellow	239.5 °C	150–180 °C, 0.067 mbar	248 °C	stable	[224–226]
$Pt(hfac)_2$	solid	orange crystals	~144 °C	65 °C, 0.133 mbar	nf	stable	[221,227]
Pd(η^3- allyl)(hfac)	solid	yellow crystals	nf	RT, HV 30–40 °C, 0.13 mbar	nf	air-sensitive	[183]

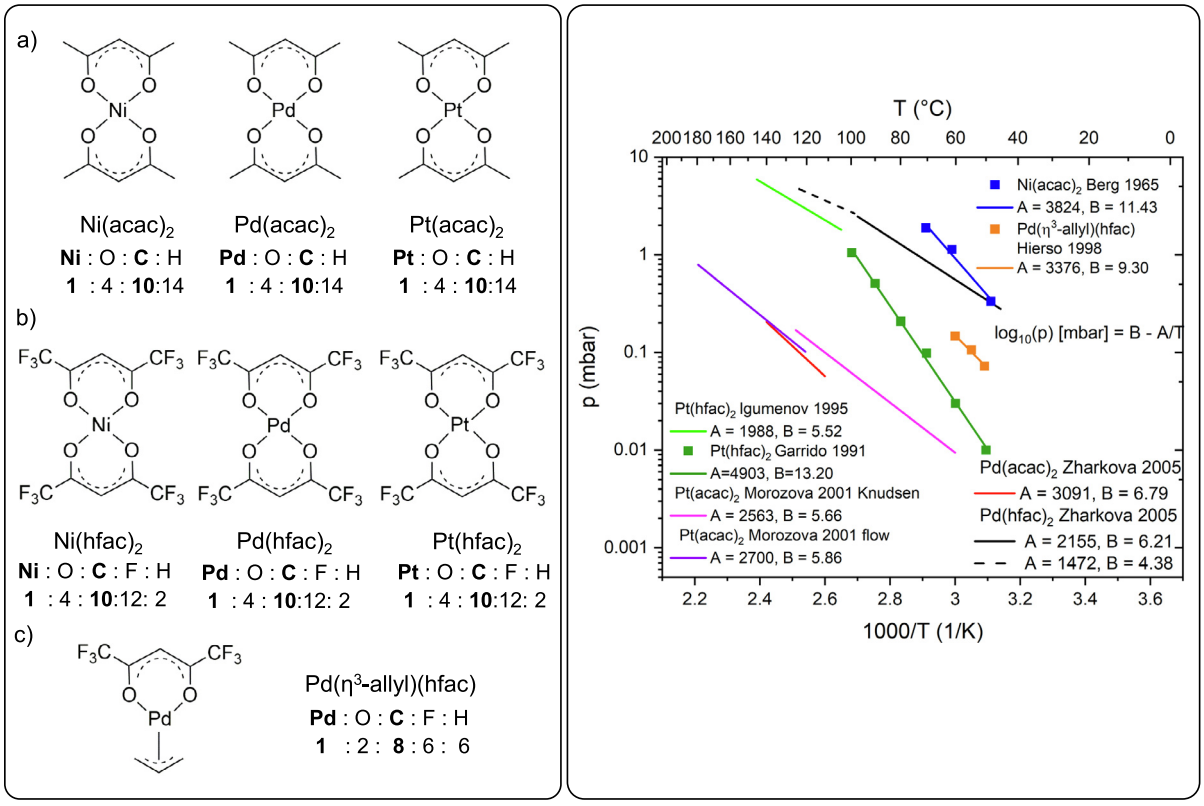

Fig. 3.7. Left: structural formulae and atomic ratios of M(II) β-diketonate complexes, where M = Ni, Pd, Pt. Right: vapour pressure with fitted $\log_{10}(p)$[mbar] = B - A/T[K] curves. Graphs were reproduced using: $Pd(acac)_2$ and $Pd(hfac)_2$ [228], Pd(η^3-allyl)(hfac) [153], $Pt(hfac)_2$ [229,230], $Pt(acac)_2$ [225], and $Ni(acac)_2$ [231].

Table 3.9
Normalized atomic ratios of the palladium precursor with corresponding *as-grown* deposit compositions. The *as-grown* deposit metal content is also summarized. The arrow terms read "atoms in precursor $\xrightarrow{e^-}$ atoms in FEBID material". Values higher than the initial carbon content indicate additional contamination. The hydrogen content is neglected.

Pd complex	Pd	C	O	F	metal at.%	ref.
$Pd(hfac)_2$	1	10→14.5	4→2.1	12→0.01	5.6	[94]
$Pd(hfac)_2$	1	10→2.1	4→0.3	12→0.8	24	[144]
$Pd(hfac)_2$	1	10→2	4→0.3	12→0.25	28	[232]

Table 3.10
Summary of CVD data. The abbreviation nf stands for 'not found' and RT for room temperature.

compound	T precursor	T deposition	pressure	gases	film composition	ref.
$Ni(acac)_2$	200–220 °C	250–350 °C	1013.25 mbar	$N_2 + H_2$	resistivity 8.1–13.3 μΩ cm; bulk metal: 6.8–7.5 μΩ cm	[233]
$Ni(hfac)_2$	100 °C	200–250 °C	1013.25 mbar	H_2	92 – 95 at.% Ni	[217]
$Pd(acac)_2$	140 °C	350–400 °C	10–15 mbar	$He + H_2$	>99 at.% Pd (XPS)	[235]
$Pd(hfac)_2$	65–75 °C	80–200 °C	nf	H_2	>99 at.% Pd (AES)	[236]
$Pd(hfac)_2$	77 °C	250 °C	500 mbar	He	Pd:C atomic ratio 0.65–0.75	[238]
$Pt(acac)_2$	150 °C	500–600 °C	$2.7–27{\cdot}10^{-5}$ mbar	vacuum	50 at.% Pt	[128]
$Pt(acac)_2$	170 °C	280 °C	5.3 mbar	$Ar + O_2$	>98 at.% Pt	[239]
$Pt(hfac)_2$	70 °C	325 °C, 350 °C	4 mbar	$Ar + O_2$	Pt + F (nq)	[240]
$Pd(\eta^3\text{-allyl})(hfac)$	30–50 °C	330 °C	66.7 mbar	$He + O_2$	>99 at.% Pd	[183,237]
$Pd(\eta^3\text{-allyl})(hfac)$	30–50 °C	45–60 °C	66.7 mbar	$He + H_2$ (1%)	>99 wt% Pd	[183,237]
$Pd(\eta^3\text{-allyl})(hfac)$	RT	410 °C	$1.3{\cdot}10^{-4}$ mbar	vacuum	78 at.% Pd	[237]

local supply of oxygen. Within the first 30 s a sudden decrease of the fluorine content from 27 at.% to 2.5 at.% and of the carbon content from 51 at.% to 18 at.% occurred, while the oxygen increased from 4 at.% to ~ 20 at.%. Characterizing the oxygen content in the deposits again several days after purification showed significantly reduced O/Pd ratio of about 0.2 suggesting that elemental palladium can be found in the deposit. When the curing FEB current was reduced to below 0.8 nA, the purification was as efficient, but less oxygen was incorporated and less shape deformations of the deposit occurred [144]. Using $Pd(hfac)_2$ as a precursor to deposit capping layers for atom probe investigation[2] leads to very similar palladium contents of 28 at.% [232]. Interestingly, the atom probe composition measurements found a reduced carbon content (35 at.% instead of 57 at.%) but a strongly increased oxygen content (44 at.% instead of 8 at.%) as compared to EDX. The authors attributed this to possible carbon contamination during the EDX measurements and residual oxygen-containing species in the atom probe chamber [232]. As shown in Table 3.9 relating the deposit composition to the precursor stoichiometry unveils the loss of 8 out of the 10 C atoms.

3.3.3. CVD

bis(acetylacetonate)nickel(II) was evaporated at a temperature of 200–220 °C at atmospheric pressure. The deposition temperature was in the range 250–350 °C. Under inert atmosphere no nickel film was obtained However, when hydrogen as the reactive gas and nitrogen as carrier gas was used, polycrystalline nickel films were deposited with resistivity close to that of bulk nickel on a borosilicate glass plate [233]. $Ni(acac)_2$ and $Ni(hfac)_2$ were also used in catalyst enhanced CVD on polymer surfaces (Teflon, polyimide, polysulfone). The substrate surface was modified by palladium compounds ($PdCl_2$, $Pd(acac)_2$) which caused a catalytic reaction and a decrease of the deposition temperature T_D. Depositions were conducted at atmospheric pressure with hydrogen as a carrier gas. The evaporation temperatures were in the range 160–180 °C and 100 °C and the substrate temperatures were in the range 220–270 °C and 200–250 °C, respectively. The purity of Ni films was about 90–95 at.% [217].

[2] In atom probe tomography a tip consisting of the material under investigation is set under high voltage (2 – 15 kV) in an UHV chamber at cryogenic temperatures. Additional voltage or laser pulses extract single atoms that are analysed in a time-of-flight ion detector.

$Pd(acac)_2$ was sublimated in helium at 140 °C. In the presence of even 1% hydrogen in helium the complex reduced to palladium metal even at room temperature [234]. $Pd(acac)_2$ was used to prepare membranes on porous substrates (Al_2O_3) at 350–400 °C. The system pressure during deposition was 10–15 mbar and hydrogen was used as reactive gas. No oxygen nor carbon impurities were incorporated into the metal film [235]. In another CVD experiment $Pd(hfac)_2$ was sublimed in the temperature range of 65–75 °C at a pressure of 0.067 mbar in the N_2 atmosphere. Pure palladium deposition was demonstrated over the temperature range of 80–200 °C on p-type silicon (100) with native oxide surface. The use of pure H_2 was necessary [236].

The hetero-ligand $Pd(\eta^3\text{-allyl})(hfac)$ complex was sublimed in the temperature range 30–50 °C and at a 66.7 mbar total pressure. Films with 99 at.% purity were obtained under different conditions: oxygen as carrier gas, deposition temperature 330 °C (glass substrate) and helium as the carrier gas with 1 % H_2 as the reactive gas, the deposition temperature in the range 45–60 °C. In contrast, the films contained 22 at.% carbon when this precursor was deposited under vacuum [183,237].

For CVD with $Pt(acac)_2$ a practical vapour pressure was achieved at about 150 °C. Deposition of Pt occurred at high temperatures of 500–600 °C on Si substrates in vacuum ($2.7–27{\cdot}10^{-5}$ mbar). However, electron beam microprobe analysis revealed heavy carbon contamination of about 50 at.% C [128]. Table 3.10 summarizes the data.

The presence of hydrogen during CVD with 10 group β-diketonates not only causes deposition or improves deposit purity but decreases also the deposition temperature.

3.3.4. ALD

Dual and triple precursor ALD processes with $Ni(acac)_2$ were reported by Utriainen [244]: the $Ni(acac)_2$-H_2 process resulted in nickel films on Al and Ti surfaces but not on SiO_2. On SiO_2 a film deposited only when a partial thermal decomposition of the precursors occurred. The $Ni(acac)_2$-O_3-H_2 process progressed via the formation of a nickel oxide layer by ozone and its subsequent reduction to nickel by molecular hydrogen and resulted in nickel films with some pinholes.

In case of palladium film ALD combustion reactions with molecular oxygen proved unsuccessful [27]. $Pd(hfac)_2$ needs atomic hydrogen to release the hfac ligand as Hhfac. Correspondingly,

Table 3.11
Summary of FEBID and surface science studies related ALD data.

precursor	co-reactant	T deposition	film composition	ref.
$Ni(acac)_2$	H_2	250 °C	surface oxidation upon ambient exposure	[244]
$Ni(hfac)_2$			No ALD	
$Pd(acac)_2$			No ALD	
$Pd(hfac)_2$	H_2	80–130 °C	Pd (XRD)	[241,242]
$Pd(hfac)_2$	formalin	200 °C	14 μΩ cm (11 μΩ cm bulk Pd)	[241]
$Pd(hfac)_2$	H_2 plasma	80 °C	C/Pd = 0.04 (on Ir); C/Pd = 0.06 (on W); C/Pd = 0.1 (on Si)	[243]
$Pt(acac)_2$	O_3 & H_2	120–130 °C	>98 at.%	[245]
$Pt(hfac)_2$			No ALD	
$Pd(\eta^3\text{-allyl})(hfac)$			No ALD	

Elam et al. [241] found that formalin (solution of formaldehyde HCHO in H_2O) is a powerful co-reactant and H donor to form pure palladium films by ALD with $Pd(hfac)_2$ on Al_2O_3 at 200 °C. The surface reactions involved are:

$Pd–H^*_x + Pd(hfac)_2 \rightarrow Pd–Pd(hfac)^*_{2-x} + xHhfac,$

$Pd–Pd(hfac)^* + HCHO \rightarrow Pd\text{-}Pd–H^* + Hhfac + CO.$

Here, the asterisk denotes surface species. In the first reaction, the H-terminated Pd surface reacts with $Pd(hfac)_2$ to release either one or two of the ligands as protonated Hhfac thereby reducing Pd either to Pd(I) in Pd–Pd(hfac)* or Pd(0) in Pd–Pd*. In the first case, the remaining Pd–Pd(hfac)* reacts with formaldehyde to release the second ligand and recover the H-terminated surface. Once a palladium seed layer was grown, the ALD temperature could be lowered to 100 °C and formalin could be replaced by molecular hydrogen for further growth. The observed low growth rate of 0.1 ML per ALD cycle was explained by the bulky hfac ligand remaining (slowly desorbing) on the Pd surface after the $Pd(hfac)_2$ exposure cycle and blocking the adsorption of additional $Pd(hfac)_2$ molecules.

Senkevich et al. [242] reported palladium ALD down to 80 °C on a palladium seed layer using $Pd(hfac)_2$ and molecular hydrogen. Instead of formalin, the hydrogen takes the role of H donor to release the hfac ligand. They indicated carbon contamination on iridium substrates to hamper adsorption of $Pd(hfac)_2$ and thus nucleation of palladium. Hydrogen plasma also serves as powerful reducing agent for $Pd(hfac)_2$ in ALD at 80 °C and was eliminating the need of noble metal substrates or palladium seed layers [243]. The precursor $Pd(\eta^3\text{-allyl})(hfac)$ was not yet investigated for ALD.

A triple precursor ALD process of $Pt(acac)_2$-O_3-H_2 was reported successful for depositing pure Pt films [243]. The molecular H_2 pulse after ozone in the pulsing sequence reduced platinum oxide to metallic Pt. The Pt films were highly oriented toward (111). Table 3.11 summarizes the FEBID and surface science studies related ALD data.

3.3.5. Fundamental surface and gas phase studies

A comprehensive study under cryogenic UHV conditions [246] has been performed on thin condensates of $Pd(hfac)_2$, and $Pt(hfac)_2$ and but included also $Cu(hfac)_2$ which is discussed in Section 4.1. The general trends during irradiation at 500 eV (Fig. 3.8) were independent of the metal except that F^- ions were retained on the surface only for $Cu(hfac)_2$ (see Section 4.1). During the initial stage of irradiation, a rapid loss of a significant fraction (≥50%) of O and F was observed by XPS after which only F continued to decline at a slower rate. In contrast, 80% of the initial C content remained in the deposit, in general agreement with the findings from FEBID. ESD revealed evolution of neutral species CO_2, CO, and some H_2 during the initial stage. Notably, desorption of F^- or F-containing fragments was not seen. Due to the high electron affinity, loss of F is thus most likely ascribed to C-F bond cleavage and desorption of F^- ions which, however, was not monitored. From these results, the reaction scheme shown in Fig. 3.8 was derived which represents the formation of the carbonaceous matrix the composition of which was also deduced from the FEBID results. Purification of the deposits was attempted by annealing of the deposit up to a temperature of 367 °C whereby the O content decreased further and the XPS binding energy of Pt4f approached the value of elemental Pt. In addition, the FEBID process was modelled under UHV conditions. In these experiments the precursors were continuously dosed onto a surface held at room temperature while the 3 keV electron beam of an Auger spectrometer was used for deposit formation yielding a qualitatively similar result as obtained from XPS.

Gas phase studies on the electron-induced fragmentation of $Pd(hfac)_2$ have provided a different perspective [247]. DEA is dominated by far by the formation of $hfac^-$ ions while in DI the bare Pd^+ ion is most abundant followed by the ionic fragments CF_3^+, $[Pd(hfac\text{-}CF_3)]^+$, and $[Pd(hfac)]^+$. The initial electron-induced fragmentation is thus favourable in the sense that the entire ligand can be split off. However, this does not translate to the surface process because the bulky hfac ligand apparently did not desorb but it converted to the carbonaceous matrix [246].

The electron-induced decomposition of $Ni(acac)_2$ was studied on a layer prepared by spray-coating from an alcoholic solution [248]. This layer was dried and then transferred in-situ to UHV for electron irradiation from the gun of a LEED (low energy electron diffraction) system and subsequent XPS analysis. By irradiation at

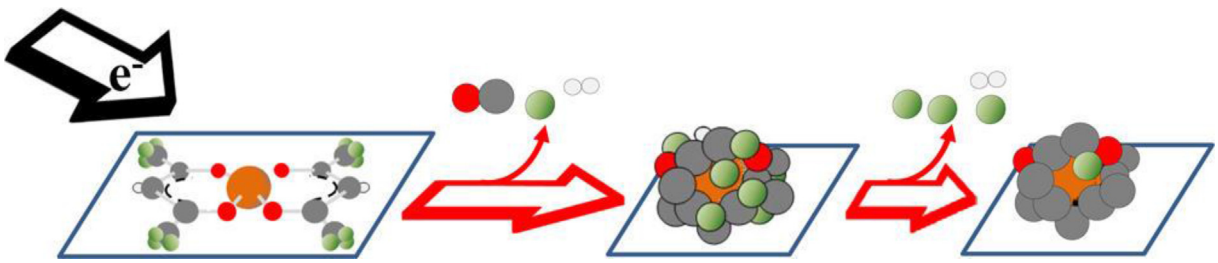

Fig. 3.8. Molecular level events during EBID of $Pd(hfac)_2$, $Pt(hfac)_2$, and $Cu(hfac)_2$ as deduced from surface studies under cryogenic UHV conditions: the initial electron-induced dissociation leads to partially reduced metal atoms in a carbonaceous matrix containing fluorine and oxygen. Continued electron irradiation then leads to slow further loss of fluorine. Reprinted with permission from Rosenberg at al. [246] copyright (2014) American Chemical Society.

500 eV, a C/Ni ratio of 0.13 was obtained which is in striking contrast to the results from the other metal-$(hfac)_2$ precursors [246]. However, Ni^0 only amounted to 59% of the Ni content showing that the metal could not be fully reduced by this process. DI gas phase data compare $Ni(acac)_2$ and $Ni(hfac)_2$ [249]. They show gradual differences in the fragmentation pattern but do not provide a mechanism for the extensive loss of C from $Ni(acac)_2$. This suggests that subsequent electron-induced processes in the deposit are more favourable in the case of the acac ligand as compared to hfac. Together with its relatively high vapour pressure it would be a good FEBID candidate.

Surface interactions of $Pt(acac)_2$ with different defect sites on a graphene layer were atomistically modelled [213]. This may be relevant to chemisorption on a carbonaceous (metal) deposit that contains reactive sites due to electron irradiation.

Finally, we note that some precursors may transfer their ligands to surface atoms of another metal. Such a redox transmetalation reaction has been reported for $Pd(hfac)_2$ that, when adsorbed on a Cu surface, can be converted to Pd(0) while Cu(0) is oxidized to Cu(II) yielding $Cu(hfac)_2$ [250]. This may be relevant for interface formation or the rate of production of seed layers.

3.4. Chlorido Pt(II) complexes

3.4.1. Introduction

Volatile metal halides are toxic and corrosive making them challenging in the FEBID implementation. However, halogen ligands are among the few possible monoatomic ligands and are thus anticipated to provide for high-purity deposits in FEBID [6]. The compound *cis*-dicarbonyldichloridoplatinum(II) (*cis*-$PtCl_2(CO)_2$) is solid at room temperature but sensitive to air and moisture. It has a convenient vapour pressure for FEBID when heated up to 80 °C [111]. An interesting, fully inorganic, alternative is the neutral complex *cis*-diamminedichloridoplatinum(II), *cis*-$PtCl_2(NH_3)_2$ (cisplatin) in which the carbonyl groups are replaced by NH_3 ligands and which is known as chemotherapeutic anticancer drug. Thermal analysis reported that thermal decomposition by loss of NH_3 and HCl occurs over the temperature range 235–385 °C. Cisplatin can be vaporised at least partially according to previously reported gas phase experiments [251], temperature-resolved thermal analysis [252], and in line with the successful sublimation of cisplatin in glassware by heating to 160 °C [104]. The needle-shaped solid shows a vapour pressure sufficient for gas phase FEBID at 165 °C [253].

Table 3.12 summarizes the properties of these two precursors Fig. 3.9 shows their structural formulae and vapour pressure data (as far as available).

3.4.2. FEBID

The compound *cis*-$PtCl_2(CO)_2$ is one of the first candidates that were suggested for FEBID based on mechanistic surface science studies [111] and quantum chemical modelling [254] (cf. Section 3.4.5). Electron beam induced deposition experiments were carried out in UHV with the internal electron source of an Auger spectrometer operated at 3 kV for steady state deposition and low electron flux with the substrate at room temperature. Corresponding to the expectation of efficient cleavage of CO ligands, the obtained deposit contained only minor amounts of carbon and oxygen. According to AES analysis, the deposit consisted of Pt (34.5 at.%) and Cl (63.8 at.%), roughly confirmed by subsequent EDX analysis as Pt (~37.6 at.%) and Cl (~ 58.7 at.%) [111], see Table 3.13. This translates to a deposit stoichiometry of ~ $PtCl_2$. The dominant Cl component is caused by the less efficient electron-stimulated desorption of Cl^- ions compared to the loss of CO from *cis*-$PtCl_2(CO)_2$ molecules [111]. Following this work, the obtained ~ $PtCl_2$ could be completely purified using electron beam curing under supply of atomic hydrogen radicals at room-temperature while curing without the reactant only occurred at the deposit surface which was ascribed to the limited escape depth of Cl^- ions [257].

In a very recent work, the performance of *cis*-$PtCl_2(CO)_2$ and *cis*-$PtBr_2(CO)_2$ was compared to that of the standard platinum precursor Pt(η^5-CpMe)Me_3 under UHV and HV (FEBID) conditions [258]. In sharp contrast to the UHV results confirming earlier work [111], deposition using *cis*-$PtCl_2(CO)_2$ under typical FEBID conditions (chamber pressure ~ $4{\cdot}10^{-6}$ mbar and high electron flux) leads to efficient loss of chlorine but a dominant carbon portion in the deposit of 55.4 at.% in combination with 20.1 at.% Pt [258]. Employ-

Table 3.12
Properties of $PtCl_2L_2$ complexes (L = NH_3, CO) discussed in this section. The abbreviation nf stands for 'not found'.

compound	phase	appearance	melting point	sublimation point (T, p)	decomposition	stability	ref.
cis-$PtCl_2(CO)_2$	solid	white/yellow needles	nf	80 °C, $1.3{\cdot}10^{-6}$ mbar	nf	air and moisture sensitive	[111,254]
cis-$PtCl_2(NH_3)_2$	solid	white to yellow	270 °C	160 °C, $5{\cdot}10^{-2}$ mbar	>235 °C	stable	[104,148,255]

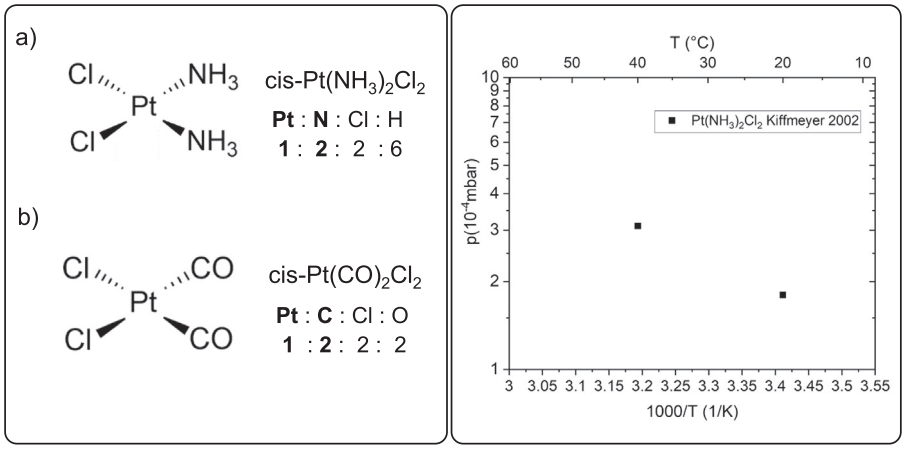

Fig. 3.9. Left: structural formulae and atomic ratios of $PtCl_2L_2$ (L = NH_3, CO) complexes. Right: vapour pressure data for *cis*-$PtCl_2(NH_3)_2$. Graphs were reproduced from [256].

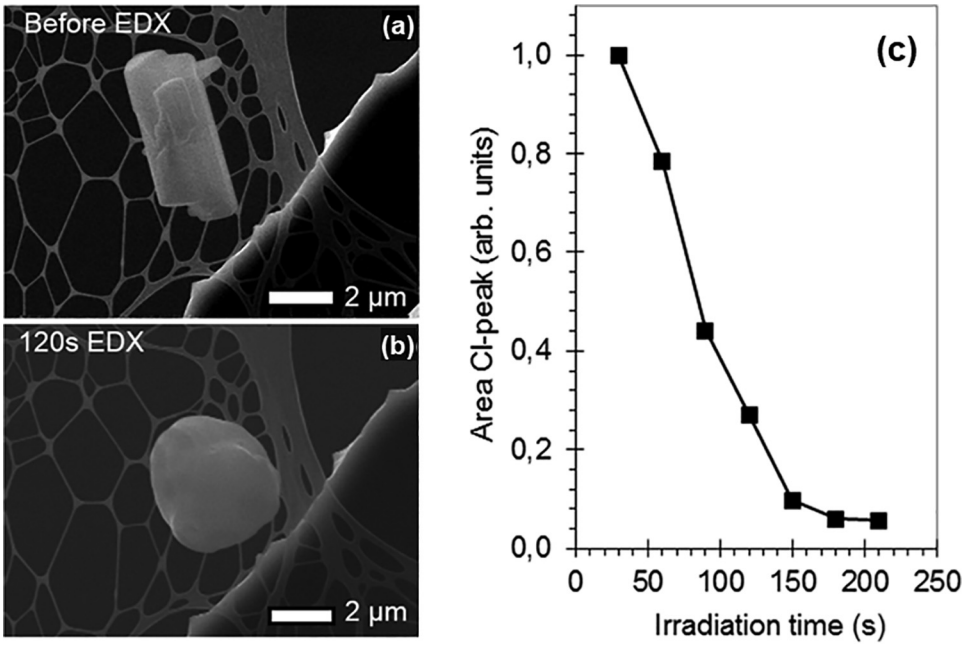

Fig. 3.10. (a) A SEM micrograph of a *cis*-$PtCl_2(NH_3)_2$ particle on a lacey carbon membrane. (b) The particle after complete decomposition to Pt by irradiation with an electron beam (20 keV, ~3 pA). (c) The integrated peak intensity of the Cl signal from EDX. Adapted with permission from Warneke at al. [253] copyright (2016) American Chemical Society.

Table 3.13
Normalized atomic ratios of platinum precursors with the corresponding *as-grown* deposit compositions. The *as-grown* deposit metal content is also summarized. The arrow terms read "atoms in precursor $\overset{e^-}{\rightarrow}$ atoms in FEBID material". The hydrogen content is neglected. *The compositions are given for deposition carried out after plasma chamber cleaning.

Pt complex	Pt	C	O/N	Cl/Br	metal at.%	ref.
cis-$PtCl_2(CO)_2$	1	2→≈0	2→≈0	2→1.6	37.6	[111] (UHV)
cis-$PtCl_2(CO)_2$	1	2→1.9	2→0.3	2→0.3	25.8	[258]*
cis-$PtBr_2(CO)_2$	1	2→5.9	2→0.9	2→0.6	11.3	[258]*
cis-$PtCl_2(NH_3)_2$	1	0→≈0	2→≈0	2→1	50	[253]

ing chamber plasma cleaning to remove hydrocarbons from the residual gases, a deposit composition of PtC_2 was obtained as the best stoichiometry. Table 3.13 summarizes the obtained compositions after chamber cleaning. The bromide complex[3] performed similarly under UHV conditions with a deposit composition of 35.9 at.% Pt and 54.9 at.% Br, but even worse than *cis*-$PtCl_2(CO)_2$ under FEBID conditions leading to a deposit stoichiometry of roughly PtC_6 (11.3 at.% Pt and 66.4 at.% C) after chamber cleaning [258]. While the efficient loss of halogens under HV conditions is known from other precursors, e.g. containing PF_3 groups (cf. Section 3.1.2), the huge carbon content is somewhat puzzling. The authors hypothesize that instead of the attempted cleavage of the intact CO groups, the residual water in the deposition chamber may have led to the formation of non-volatile formic acid and formaldehyde [258]. However, this explanation seems doubtful as both compounds are expected to be in the gas phase under these conditions. Even if the formaldehyde would have been thermally polymerized, it should have left more oxygen behind.

Based on a comparative surface science study with *cis*-$PtCl_2(CO)_2$ the similar compound *cis*-$PtCl_2(NH_3)_2$ (cisplatin) may enhance the loss of chlorine [104] (cf. Section 3.4.5). In a FEBID experiment *cis*-$PtCl_2(NH_3)_2$ was supplied with a home-built, short tube gas-injection system at 150 °C. Deposition was carried out for a beam current of 1 nA at a primary energy of 20 keV on native oxide silicon at room temperature [253]. This resulted in a composition of the deposit of 50 at.% Pt and 50 at.% Cl (cf. Table 3.13). The same study investigated electron beam irradiation of micrometre sized crystallites of *cis*-$PtCl_2(NH_3)_2$ placed on lacey carbon TEM membranes which resulted in the transformation to pure platinum, see Fig. 3.10. The authors attributed the very different behaviour to the different residence times of NH_3. In the irradiated precursor particles, the ligand NH_3 may remain trapped long enough to yield hydrogen upon decomposition. The hydrogen then volatizes the Cl^- ligands in form of HCl. In contrast, in a FEBID experiment, NH_3 may easily desorb from the adsorbed surface layer and leave a partly degraded cisplatin, containing less hydrogen for Cl^- ion removal. Hence, a complete reduction to platinum cannot be achieved [253]. However, the FEBID process and, in particular, thermal effects (especially on the poorly heat conducting lacey carbon films) may be worth revisiting in the light of a more recent UHV study that observed a complete removal of Cl from sub-100 nm sized sublimated cisplatin crystallites [104], cf. Section 3.4.5.

3.4.3. CVD

cis-$PtCl_2(CO)_2$ was investigated as precursor for Pt CVD with source temperatures in the 120–155 °C range and deposition temperatures varying between 187 °C and 600 °C [128]. Clean platinum films (>99%) were obtained in hydrogen (1013.25 mbar H_2). The highest purity was obtained on silicon substrates at a precursor vaporisation temperature of 145 °C and a deposition tempera-

[3] Please note that *cis*-$PtBr_2(CO)_2$ is discussed only in the FEBID section due to the novelty of the results.

Table 3.14
Summary of CVD data.

compound	T precursor	T deposition	pressure	gases	film composition	ref.
cis-$PtCl_2(CO)_2$	145 °C	300 °C	1013.25 mbar	H_2	>99 at.% Pt	[128]
cis-$PtCl_2(NH_3)_2$				no CVD		

ture of 300 °C. The formation of HCl was found to be crucial for deposit purity. However, the process was judged unattractive due to difficulties in handling the precursor and to poor adherence of the deposited film to the substrates [128]. CVD results for *cis*-Pt$(NH_3)_2Cl_2$ complex have not yet been reported. Table 3.14 summarizes the data.

3.4.4. ALD

ALD with $PtCl_2(CO)_2$ and *cis*-$PtCl_2(NH_3)_2$ has not yet been attempted.

3.4.5. Fundamental surface and gas phase studies

In fundamental studies with regard to FEBID, a sufficient precursor flux of *cis*-$PtCl_2(CO)_2$ could be established by sublimation at 80 °C to deposit a thin adsorbed layer for surface studies [111] and at 85 °C to produce an effusive molecular beam for gas phase experiments which produced a chamber pressure of $1\text{-}2\cdot10^{-7}$ mbar [254]. The vapour pressure was also sufficient to perform a model FEBID experiment in UHV (see Section 3.4.2). Studies under UHV conditions were performed using an electron flood gun operated at 500 eV as electron source while the precursor was leaked into the chamber and adsorbed on the cooled substrate at −90 °C. ESD and XPS revealed that, after rapid loss of CO, prolonged electron irradiation can further remove the Cl content [111], see Fig. 3.11.

However, the electron doses needed to remove Cl were two orders of magnitude larger than those needed to desorb the CO ligands. Gas phase results [254] are in line with this result and also point to the persistence of the anionic Cl^- ligands. They show that DEA to *cis*-$PtCl_2(CO)_2$ occurs at electron energies near 0 eV and leads predominantly to loss of CO thus producing $[PtCl_2(CO)]^-$ and $[PtCl_2]^-$ as the dominant fragments. DI at 70 eV yields the parent cation as the most abundant product followed by the bare Pt^+ cation but again points to a facile loss of the more weakly bound CO.

The gas phase experiments on cisplatin applied temperatures in the range 164–172 °C to obtain a background vapour pressure of 10^{-7} mbar when forming the molecular beam [251]. Thermal analysis reported, however, that thermal decomposition by loss of NH_3 and HCl occurs at higher temperatures over the range 235–385 °C [252]. The gas phase experiment on cisplatin [251] revealed DEA at electron energies between 0 eV and 2 eV leading predominantly to loss of atomic Cl or Cl^- ions and, to a minor extent, also to loss of both Cl atoms as Cl_2^- due to the cleavage of Pt-Cl bonds. The complementary DEA products $[PtCl(NH_3)_2]^-$ and $[Pt(NH_3)_2]^-$ were observed near 0 eV suggesting that, in contrast to *cis*-$PtCl_2(CO)_2$, electron attachment at these low energies leaves the neutral ligands, namely, NH_3 bound to the metal. Earlier reports indicated that electron irradiation of NH_3 adsorbates at electron energies above roughly 8 eV leads to production of N_2 and supplies hydrogen that acts as a reducing agent [259]. This suggested that the same reaction should also decompose the NH_3 ligands of cisplatin and assist in the removal of the Cl content, which is not efficiently removed as Cl^- ions due to the low desorption probability of ionic species [108] despite the fact that these are indeed produced by DEA [251].

A more comprehensive surface study on cisplatin sublimates by use of ESD, RAIRS, and XPS [104] revealed, in fact, that electron irradiation at 500 eV leads to ESD of N_2, NH_3, and HCl (Fig. 3.12). N_2 is produced by releasing atomic hydrogen from NH_3 which then removes the Cl ligands via formation of volatile HCl. Additionally, RAIRS revealed the formation of NH_4^+ cations indicating another reaction pathway in which NH_3 is ionized and transfers a proton to Cl^- to again yield HCl. According to XPS, these reactions lead to elementary Pt. The conversion was much slower at a primary electron energy of 50 eV suggesting that secondary electrons which are released in larger numbers at a primary electron energy of 500 eV drive the decomposition [104].

Comparison of *cis*-$PtCl_2(CO)_2$ and cisplatin for an electron energy of 500 eV showed that the electron-induced loss of Cl ligands from cisplatin is significantly faster. This supports the view that the reducing action of NH_3 enhances the removal of chlorine ligands [104]. The enhancing effect of atomic hydrogen has also been demonstrated within a post-purification protocol which converted deposits with approximate stoichiometry $PtCl_2$ produced from *cis*-$PtCl_2(CO)_2$ to pure, yet porous Pt [257].

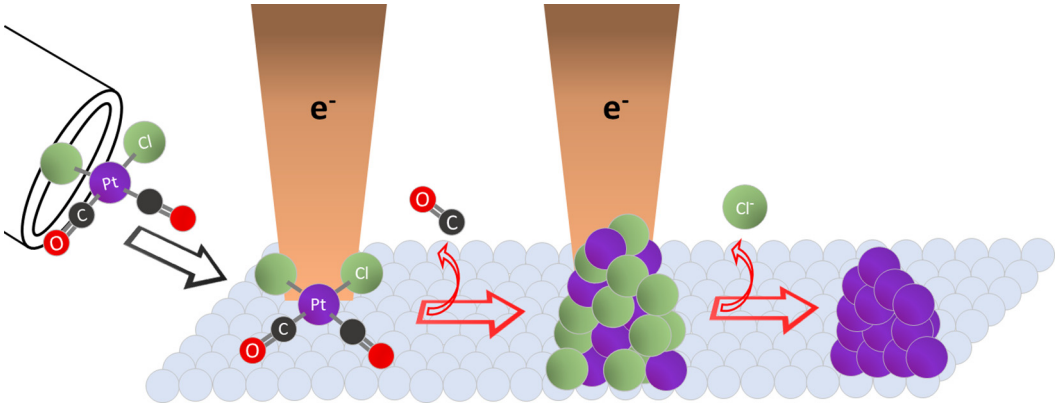

Fig. 3.11. Molecular level events during EBID of *cis*-$PtCl_2(CO)_2$ as deduced from surface studies on electron exposure of cryogenically condensed layers of the precursor under UHV conditions: The initial electron-induced dissociation leads to rapid loss of CO leaving behind a deposit with approximate stoichiometry $PtCl_2$. Continued electron irradiation then leads to slow loss of anionic Cl^-. Figure adapted from Spencer et al. [111].

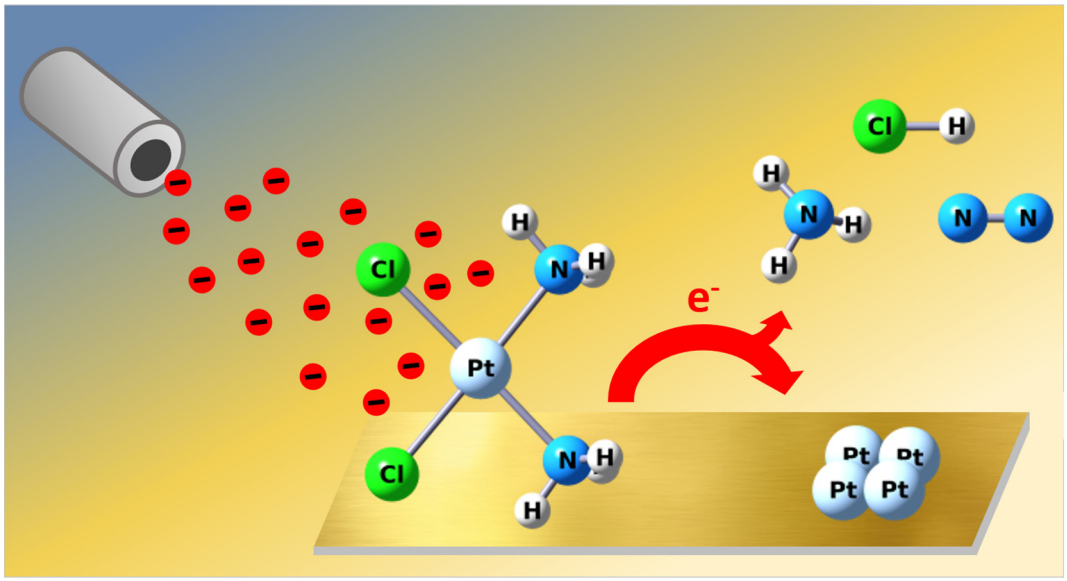

Fig. 3.12. Electron-induced decomposition of *cis*-$PtCl_2(NH_3)_2$ leads to removal of both types of ligands. NH_3 either desorbs or is fragmented to release N_2 and atomic hydrogen or H^+ that both convert the Cl^- ionic ligands to volatile HCl. Figure adapted from Rohdenburg et al. [104].

4. Group 11 precursors

4.1. Cu(II) β-diketonate and β-ketoesterate complexes

4.1.1. Introduction

Two complexes, namely bis(hexafluoroacetylacetonato)-copper (II), $Cu(hfac)_2$, and bis(*tert*-butylacetoacetato)copper(II), $Cu(tbaoac)_2$, were used in FEBID. $Cu(hfac)_2$ was mainly used as monohydrate $Cu(hfac)_2{\cdot}H_2O$, which is a green powder turning dark purple when losing the water at around 70 °C. bis(acetylacetonate) copper(II) $Cu(acac)_2$ [260] has not been considered for FEBID as its low vapour pressure would require heating of the gas injection system. The β-ketoesterate complex $Cu(tbaoac)_2$ was synthesised more recently by Devi et al. [261]. An increase of the sublimation rate was achieved without having to rely on fluorinated ligands. At the same time, the *tert*-butyl ester group on one end of the ligand causes an asymmetric electron density that weakens the Cu–O bond on that side of the precursor and leads to a lower pyrolysis temperature as shown by comparison with an acac-type compound. It was proposed that this effect is related to a thermodynamically favourable thermal fragmentation pathway yielding CO_2 and acetone upon pyrolysis [262]. The precursor properties of this section are summarized in Table 4.1.

Fig. 4.1 Summarizes the structural formulae and vapour pressure data. For $Cu(hfac)_2{\cdot}H_2O$ and $Cu(hfac)_2$ above 95 °C, the vapour pressures of all the literature sources cited in Fig. 4.1 give comparable values although with slightly different slopes. With decreasing temperature, Widmer's [267] measurements indicate a stronger decrease of vapour pressure for $Cu(hfac)_2$ than for the monohydrate $Cu(hfac)_2{\cdot}H_2O$. At room temperature, $Cu(hfac)_2{\cdot}H_2O$ and $Cu(hfac)_2$ have an extrapolated vapour pressure of around 0.01 mbar and 0.004 mbar, respectively. These pressures are still practical for FEBID when using a GIS inside the SEM chamber with short tubing < 1 cm. Alternatively, the precursor $Cu(hfac)_2{\cdot}H_2O$ can be heated but simultaneous water co-evaporation is taking place (witnessed by a colour change to deep purple crystals) during a certain time which may lead to non-reproducible results. Hence, for reproducibility in FEBID experiments one should ideally start with the dehydrated species as the water will be slowly released under high-vacuum conditions. The vapour pressure of $Cu(tbaoac)_2$ was deduced from sublimation rate measurements to be about 0.027 mbar at 100 °C [261].

4.1.2. FEBID

Although not explicitly noted, the monohydrated, green coloured, crystalline $Cu(hfac)_2{\cdot}H_2O$ was the starting compound for investigations in the studies of Luisier et al. [272], Szkudlarek et al. [273], and Puydinger et al. [274]. The deposits obtained by Luisier et al. [272] with a beam current of 500 pA contained 14 at.% copper, 75 at.% carbon and 5 at.% of oxygen while Szkudlarek et al. found higher carbon contents in the deposits and a significant amount of oxygen for similar deposition conditions, see Table 4.2. This difference may be due to the undefined co-evaporation of crystal water from the monohydrate upon transition to the anhydrous compound. Resistivity values of as-grown FEBID lines varied between 10^4 Ω·cm (as-grown) and 0.1 to 1 Ω·cm (after annealing up to 180 °C) [273].

Table 4.2 shows that the 12 fluorine atoms in the homoleptic precursor are always completely removed (below noise level of 1 at.%) from the initial fluorinated precursor molecules. Oxygen is less efficiently removed and seems to depend on the electron expo-

Table 4.1
Properties of copper(II) β-diketonate and β-ketoesterate complexes discussed in this section. The abbreviation nf stands for 'not found'.

compound	phase	appearance	melting point	sublimation point (T, p)	decomposition	stability	ref.
$Cu(hfac)_2{\cdot}H_2O$	solid	green crystals	133–136 °C	70 °C, 0.067 mbar	230 °C	air-stable, hygroscopic	[263]
$Cu(hfac)_2$	solid	purple	95–98 °C	nf	nf	air-stable	[242,263]
$Cu(acac)_2$	solid	blue	279–283 °C	140–190 °C, 133–400 mbar	>230 °C	air-stable	[264-266]
$Cu(tbaoac)_2$	solid	green, thin plates	110 °C	95 °C	190 °C	air-stable	[261]

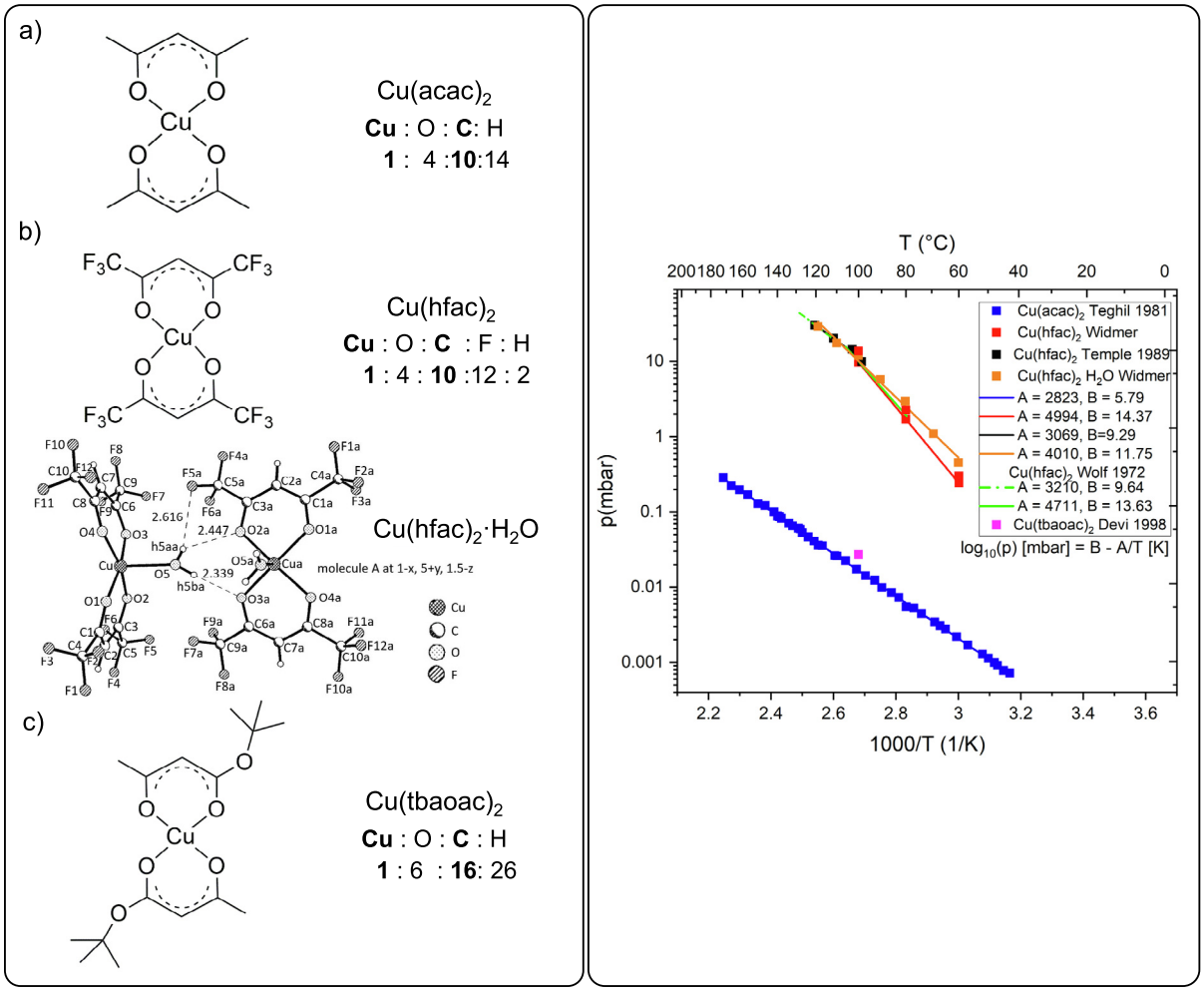

Fig. 4.1. Left: structural formulae and atomic ratios of Cu(II)(β-diketonate)$_2$ complexes and the ketoesterate complex Cu(tbaoac)$_2$. Top right: vapour pressure with fitted $\log_{10}$(p)[mbar] = B − A/T[K] curves. The [Cu(hfac)$_2$]·H$_2$O X-ray crystal structure was taken from [268] and represents only one of the possible configurations. Graphs were reproduced using: Cu(acac)$_2$ [269], Cu(hfac)$_2$ [267,270,271], and Cu(tbaoac)$_2$ [261].

Table 4.2
Normalized atomic ratios of copper(II) precursors with the corresponding *as-grown* deposits and the *as-grown* deposit metal content. The arrow terms read "atoms in precursor $\xrightarrow{e^-}$ atoms in FEBID material. Note that we do not include the crystal water into the atomic ratios. The hydrogen content is neglected.

Cu complex	Cu	C	O	F	metal at.%	ref.
Cu(hfac)$_2$·H$_2$O	1	10→5.4	4→0.4	12→0	14	[272]
Cu(hfac)$_2$·H$_2$O	1	10→6.4	4→2.5	12→0.1	10	[273]
Cu(tbaoac)$_2$	1	16→2.3	6→0.5	–	26	[93]

sure conditions as the two distinctly different values for Cu(hfac)$_2$·H$_2$O indicate.

The copper content can be further increased by applying in-situ H$_2$-Ar microplasma. The reactive atomic hydrogen will chemically reduce the carbon content in the deposit avoiding the oxidation of the metal [275]. When applied as a post-treatment under negative substrate bias, the copper content increased from 11 to 27 at.% while the carbon content was reduced from 62 to 41 at.%. The O and F contents did not change considerably. As pure Ar plasma post-treatment did not change the composition, thermally driven purification effects could be excluded [275]. However, the negative substrate bias of few eV accelerates Ar^+ ions towards the deposit to break C–C bonds. The cleaved bonds may be terminated by atomic hydrogen radicals to form volatile hydrocarbons [275]. Applying the plasma in-operando during FEBID, this plasma-assistance further increases the copper content up to 41 at.% with a remaining carbon portion of 45 at.% under negative bias. Remarkably, the oxygen content decreased as well to 13 at.% while F became undetectable [275]. Unfortunately, the spatial selectivity of FEBID was impeded by formation of a significant halo. The halo extension matched that of the microplasma (several hundred micrometre) and was formed due to the dissociation of adsorbed precursor molecules by impinging plasma radicals [275].

Post-growth annealing of deposits from Cu(hfac)$_2$·H$_2$O in vacuum either by stage heating or by an infrared laser irradiation did not improve the overall copper content in the deposit. However, starting at 150 °C substrate temperature, a morphological change of the deposit from amorphous to nanocrystalline could

be observed [273]. Most of the copper (~95 %) precipitated as pure copper nanocrystals on the deposit surface [273]. This was confirmed in a later comparative study leading to the conclusion that no volatile carbon containing species were formed during annealing under vacuum [274].

Under UHV conditions, a FEBID process was modelled in an Auger spectrometer by continuously dosing $Cu(hfac)_2$ onto a surface held at room temperature while the 3 keV electron beam of the Auger spectrometer was used for deposit formation [246]. In line with the precursors $Pd(hfac)_2$ and $Pt(hfac)_2$ discussed in Section 3.3.5, the $Cu(hfac)_2$ also resulted in large carbon content material by FEBID.

In the case of $Cu(hfac)_2$, the UHV FEBID approach was also used to demonstrate a process for purification that is capable of removing the majority of carbon contamination from the deposit. In this process, the deposit was first exposed to atomic oxygen to etch away the carbon matrix followed by treatment with atomic hydrogen to reduce back the formed metal oxide to the metallic state [246].

In contrast to $Cu(hfac)_2$, $Cu(tbaoac)_2$ does not contain any fluorine but the by far largest amount of carbon in the initial molecule for all FEBID Cu precursors, including the heteroleptic complexes of Cu(I) described in Section 4.2. Despite the high carbon content, the compound achieves the best copper content in the FEBID material of all copper(II) compounds with 24–26 at.% [93]. These values compare well to the best copper content of copper(I) compounds (see Section 4.2.2) and Cu(II)-carboxylates (see Section 4.3.2), however, the first having issues with thermal and vacuum stability and the latter having a small FEBID temperature window. Furthermore, it is of note that deposits from $Cu(tbaoac)_2$ are conducting. While the resistivity (1.26 MΩ) was six orders of magnitude larger than the value for bulk copper, it was the first evidence for conductive FEBID copper deposits without post-treatment [93].

4.1.3. CVD

The thermal decomposition of Cu(II) complexes containing β-diketonates requires substrate temperatures of 200 °C or higher and additional reactive gases to obtain pure copper deposits in CVD [2]. In contrast, β-ketoesterate ligands are generally easier to remove in CVD [261]. For the application of Cu(II) CVD precursors, the additional reducing agent such as hydrogen is used most often.

The importance of water or hydrogen in CVD was pointed out by LeCohier [276]. Hydrogen is provided to the hfac ligand for desorption as H(hfac) to obtain clean copper films. The protonated ligand H(hfac) was seen as reaction product in the gas phase [277]. Interestingly, desorption was not seen in UHV studies, likely due to the recombination of the hydrogen atoms to molecular hydrogen [278]. The hydrogen coverage was concluded to be quite low under UHV conditions due to the absence of a hydrogen gas phase for surface replenishment [2]. This is an important limitation of UHV studies to keep in mind.

Chemical vapour deposition of pure copper films was performed using $Cu(acac)_2$ on SiO_2/Si substrates by evaporation at 180–200 °C and decomposition of this copper complex at low temperatures (225–250 °C) in H_2-Ar (1:1) or pure hydrogen as a carrier gas at 1013.25 mbar. The nucleation rate and the growth rate of copper films decrease when the hydrogen pressure increases [264]. $Cu(hfac)_2$ was heated between 30 °C and 60 °C and introduced into the CVD reactor in pure hydrogen atmosphere. High quality, high purity (~99 %), uniform copper films were obtained in the temperature range 250–350 °C [279].

$Cu(tbaoac)_2$ as precursor was sublimed over the temperature range 90–150 °C and CVD was conducted at a reactor pressure of 13 mbar using argon as the carrier gas. Pyrolysis of $Cu(tbaoac)_2$ on thermally oxidized silicon(100) substrates leads to the formation of copper films at 225 °C. XPS analysis revealed the presence of 13 at.% carbon and 13.5 at.% oxygen [261]. In another process, copper films were grown on thermally oxidized Si wafers by evaporation of $Cu(tbaoac)_2$ at 135 °C using again argon as the carrier gas. Deposition at 285 °C and low pressures of 13 mbar led to well connected films with a smooth surface and relatively low resistivity [280]. No significant changes in morphology were observed when the deposition temperature was varied over the range 225–285 °C. Growth at temperatures higher than 285 °C yielded films with significantly greater carbonaceous contamination and higher resistivity [281]. Table 4.3 summarizes the data.

Table 4.3a summarizes the plasma CVD data. Plasma CVD was reported (Table 4.3a) for $Cu(hfac)_2$ [282,283] and $Cu(acac)_2$

Table 4.3
Summary of CVD data. The abbreviation nf stands for 'not found'.

compound	T precursor	T deposition	pressure	gases	film composition	ref.
$Cu(acac)_2$	180–200 °C	225–250 °C	1013.25 mbar	Ar + H_2	>99 at.% Cu	[264]
$Cu(hfac)_2{\cdot}H_2O$	90 °C	250 °C	nf	Ar + H_2	>99% Cu	[277]
$Cu(hfac)_2$	30–60 °C	250–350 °C	$1.3{\cdot}10^{-3}$ mbar	pure H_2	99 at.% Cu	[279]
$Cu(hfac)_2$	30–60 °C	250–350 °C	$1.3{\cdot}10^{-3}$ mbar	Ar/10% H_2	70 at.% Cu	[279]
$Cu(hfac)_2$	120 °C	340–390 °C	1013.25 mbar	Ar	100 at.% Cu	[271]
$Cu(tbaoac)_2$	90–150 °C	225 °C	13 mbar	Ar	74 at.% Cu (XPS)	[261]
$Cu(tbaoac)_2$	135 °C	285 °C	13 mbar	Ar	resistivity 4.3 μΩ cm; bulk copper: 1.6 μΩ cm	[280]

Table 4.3a
Summary of plasma CVD data. The abbreviation nf stands for 'not found'.

compound	T precursor	T deposition	pressure	power density	gases	film composition	ref.
$Cu(hfac)_2$	75–100 °C	150–250 °C	0.67–2.67 mbar	75–100 W, 1.5–2.2 W/cm^2	H_2	No impurities detected, 1.9–2.0 μΩ cm	[282]
$Cu(hfac)_2$	nf	100 °C	0.25–0.27 mbar	50 W	Ar/H_2 flow [sccm]: 75/78	100 wt% Cu6.2–7.4 μΩ cm	[283]
$Cu(hfac)_2$	nf	160 °C	0.25–0.27 mbar	20 W, ca. 0.05–0.06 W/cm^3	Ar/H_2 flow [sccm]: 10/15	99,7 wt% Cu1.8–4.0 μΩ cm	[283]
$Cu(hfac)_2$	nf	150 °C	0.25–0.27 mbar	80 W, 0.05–0.06 W/cm^3	Ar/O_2 flow [sccm]: 75/62	77.3 wt% Cu	[283]
$Cu(acac)_2$	170 °C	200 °C, 300 °C	1–10 mbar	0.28 W/cm^2	H_2	98 at.% Cu	[285]
$Cu(acac)_2$	170 °C	300 °C	1–10 mbar	0.28 W/cm^2	He	85 at.% Cu	[285]
$Cu(acac)_2$	100 °C	nf	$6.7{\cdot}10^{-4}$–$1.4{\cdot}10^{-2}$ mbar	radio-frequency bias voltage of − 50 V	Ar:H_2 1:10	>99.5 at.% Cu	[284]

[283,284]. The $Cu(hfac)_2$ and Ar/H_2 plasma CVD process [283] resulted in pure copper films at 100 °C deposition temperature. In comparison to thermal CVD, see Table 4.3, the deposition temperature with plasma was 150 to 190 degrees lower. The argon/hydrogen plasma CVD processes at 100 °C with $Cu(acac)_2$ resulted in > 99.5 at.% Cu film content [284]. Compared to thermal CVD the growth temperature was about 100 degrees lower. A sole helium plasma CVD process at 300 °C gave only 85 at.% Cu in the film. This underlines the role of atomic hydrogen species, which facilitate the efficient removal of hfac, and acac ligands at considerably lower deposition temperatures.

4.1.4. ALD

$Cu(hfac)_2{\cdot}xH_2O$ was used in a triple precursor thermal ALD process at 230 to 300 °C on silicon oxide, TaN, TiN, and Ta at $6.7{\cdot}10^{-3}$ mbar [286]. Molecular hydrogen bubbled through water was used as the carrier gas for the $Cu(hfac)_2{\cdot}xH_2O$ molecules heated at 75 °C. The authors suggested a two-step mechanism of Cu-ALD. When $Cu(hfac)_2{\cdot}xH_2O$ reaches the surface in excess of water, it adsorbs dissociatively into hfac ligands and $Cu(hfac)_2{\cdot}yH_2O$ (with y < x) followed by reaction to volatile Hhfac and copper oxide. The reactions proceed until the surface is saturated with copper oxide, hfac, and $Cu(hfac)_{2-z}{\cdot}yH_2O$. After the nitrogen purge, a reducing alcohol (methanol, ethanol, isopropyl alcohol = IPA) or formalin (approximately 37 % formaldehyde in 10–15 % methanol and water) was delivered. This was proposed to transfer hydrogen to $hfac^-$ to form volatile Hhfac and to reduce copper oxide. The films contained about 3 at.% carbon and 4 at.% oxygen when using methanol as reductant. Formalin and IPA gave the lowest impurity level, 1.5 at.% carbon with only traces of oxygen and hydrogen bonds. Fluorine was detected at the substrate film interface with around 0.25 at.%. The film resistivity was very close to bulk copper resistivity for thicknesses above 50 nm. The use of formaldehyde and IPA also resulted in "acceptable" copper films on glass, Si, and TaN coated Si substrates using argon instead of hydrogen as carrier gas. The self-limiting character of above proposed ALD reactions was not proven by exposure time or pulse time variations so that CVD contributions cannot be excluded.

An in-situ infrared reflection absorption spectroscopy (IRAS) study was performed of hydrogen plasma-assisted ALD with $Cu(hfac)_2{\cdot}xH_2O$ on Al_2O_3 at 80 °C and an operating pressure between $4{\cdot}10^{-2}$ and 0.27 mbar [287]. No carrier gas was used and the $Cu(hfac)_2{\cdot}xH_2O$ precursor was evaporated at 130 °C from a stainless steel cylinder. In contact with the Al_2O_3 substrate, it chemisorbed dissociatively on Al-O-Al surface bond bridges in a self-saturating manner leaving Cu(hfac), hfac, and probably some H_2O on the surface. Hydroxyl surface groups were not present on the substrate. Purging of thirty seconds with Ar/H_2 did not alter the surface, indicating that molecular hydrogen does not react at this temperature to form volatile Hhfac. The hydrogen plasma cycle completely removed the hfac ligands. Once a closed copper film forms, surface reactions need to continue on copper chemisorption sites. Copper hydrate species as dissociative chemisorption sites for $Cu(hfac)_2{\cdot}xH_2O$ were proposed but their characteristic bands were masked by other signals in the IRAS measurements.

To summarize, $Cu(hfac)_2{\cdot}xH_2O$ has a water content that changes during vacuum exposure time and with temperature. This will influence the oxidation of copper and protonation of the hfac to more volatile Hhfac. Atomic hydrogen would be needed in FEBID to desorb the "sticky" $hfac^-$ ion as Hhfac. This may be produced by the electron-induced dissociation of water, see Section 5.3.2. (Fig. 5.11), present in varying quantity as part of the molecule. H_2 as additional gas during FEBID would have a comparable electron-induced dissociation efficiency as water (Fig. 5.11) but is supposed to have a very short residence time (no dipole moment) as co-reactant on the surface. Furthermore, H_2 will not dissociate thermally on copper into atomic hydrogen. It therefore seems very likely that pure copper FEBID deposits are hampered by the co-dissociation/deposition of the "sticky" ionic $hfac^-$ ligands and that an atomic hydrogen source is needed, probably in a very specific temperature window, to desorb them.

For $Cu(tbaoac)_2$ no ALD process could be realized [288]. One reason may be the relatively low temperature for thermal decomposition starting at about 190 °C and relating to a thermal reaction pathway involving the facile loss of the thermodynamically stable CO_2 as driving force of the reaction [261], see also Section 4.1.1.

A triple precursor thermal ALD process below 200 °C for copper films employs cycles of $Cu(acac)_2$ with H_2O yielding Cu_2O which is then reduced to Cu by supercycles of hydroquinone [289]. Table 4.4 summarizes the FEBID and surface science studies related ALD data.

4.1.5. Fundamental surface and gas phase studies

Gas phase studies on the electron-induced fragmentation have shown that $Cu(hfac)_2$, in striking contrast to $Pd(hfac)_2$, predominantly forms the parent anion $[Cu(hfac)_2]^-$ upon electron attachment at 0 eV and some $hfac^-$ ions by DEA between 0 and 4 eV [247]. This does not reflect the loss of O and F observed in the case of the adsorbed precursor [246] considering that the anionic ligand is unlikely to desorb. However, fragmentation upon DI is more pronounced as exemplified by the dominant fragment m/z = 201 ($[Cu(CF_3)_2]^+$ or $[Cu(hfac)\text{-}CF_3]^+$) and the presence of a Cu^+ signal [247,290] suggesting that DI contributes to deposit formation. Note that the gas phase electron-induced fragmentation is less pronounced for $Cu(acac)_2$, both in DEA where $[Cu(acac)_2]^-$ dominates even more above the free ligand $acac^-$ [291] compared to $Cu(hfac)_2$ [247] and in DI [247,290]. In line with the possible enhancement of halide removal by protonating process gases [292], electron irradiation in presence of H_2O or NH_3 might offer the perspective to remove $acac^-$ by converting it to the more volatile Hacac under electron exposure (see also Section 5.3.2). This, however, has not yet been experimentally assessed.

Cohen et al. proposed from their adsorption measurements that $Cu(hfac)_2$ adsorbs as intact molecule on SiO_2 surfaces at room temperature [293]. On clean metal surfaces the same molecule adsorbs dissociatively above −73 °C [278,294]. The two hfac ligands migrate away from their original copper atom and adsorb on the metal surface. The hfac ligands prove very "sticky", meaning that upon heating above 100 °C [294,295] they do not desorb intact but rather left carbon, oxygen, and fluorine residues in a series of step-wise thermal decomposition reactions.

Table 4.4
Summary of FEBID and surface science studies related thermal ALD data. IPA stands for isopropyl alcohol. Note that formalin is a solution of formaldehyde, methanol, and water.

precursor	co-reactant	deposition	film composition	ref.
$Cu(hfac)_2{\cdot}xH_2O$ (carrier gas H_2 bubbled through H_2O)	methanol, ethanol, IPA, formalin (H_2 carrier gas)	260 to 300 °C	3 at.% C, 4 at.% O (methanol), 1.5 at.% C, < 0.25 at.% F (IPA)	[286]
$Cu(hfac)_2{\cdot}xH_2O$ (carrier gas Ar)	IPA, formalin (carrier gas Ar)	260 to 300 °C	"acceptable"	[286]
$Cu(acac)_2$	H_2O & hydroquinone	160 to 200 °C	~2 – 5 μΩ cm @ RT (1.7 μΩ cm bulk Cu)	[289]

Notably, a study on the adsorption of $Cu(acac)_2$ on Ni(1 1 0) and Cu(1 1 0) single crystal surfaces has shown that thermal surface reactions leading to desorption of an entire ligand from the surface occur already below −73 °C and the reduction to metallic Cu was observed below room temperature [296]. The loss of carbon was thus much higher than observed in FEBID and its model studies on $Cu(hfac)_2$. This indicates that thermal reactions would be favourable to the deposit purity in a FEBID process and that the balance between these and the inherent electron-induced chemistry should critically determine the deposit composition. Details of these thermal reactions as well as surface reactions with H_2O were also studied by computational methods [297] and may serve as reference for future studies on FEBID processes using $Cu(acac)_2$. Of similar relevance may be a DFT theoretical and experimental study on reactions of $Cu(hfac)_2$ on pristine highly ordered pyrolytic graphite (HOPG) and HOPG with –COOH and –OH defect sites [298]. While on HOPG-COOH and HOPG-OH the growth of Cu-nanoparticles is preferred at surface defect sites, the edges of the basal planes are preferred on pristine HOPG. Although these are idealized systems, such sites may also play a role when $Cu(hfac)_2$ adsorbs on the carbonaceous matrix of a previous FEBID deposit.

4.2. Cu(I) β-diketonate complexes with neutral π-donor ligands

4.2.1. Introduction

Cu(I) organometallic compounds used in FEBID are composed of a β-diketonate anion and a neutral π-donor ligand (Lewis base) [29]. Here, hexafluoroacetylacetonate (hfac) complexes are considered, in which the replacement of hydrogen atoms by fluorine atoms decreases the stability of the Cu(I)-O bonds. In order to improve the stability and volatility, unsaturated ligands can be used e.g. alkenes like vinyltrimethylsilane (VTMS) and 3,3-dimethylbutene (DMB), and also enynes like 2-methyl-1-hexen-3-yne (MHY) [2,299]. Table 4.5 summarizes the properties of the precursors in this section.

The investigated compounds Cu(hfac)VTMS, Cu(hfac)DMB, and Cu(hfac)MHY are liquid with vapour pressures sufficient for evaporation under high vacuum conditions without heating the compounds [272,300–305]. However, the implementation in FEBID is hampered as compounds of Cu(I) are extremely sensitive to air and moisture and decompose easily. Therefore, the use and storage of these compounds requires special attention. According to their decomposition temperatures, the compounds may be sorted with respect to their thermal stability as Cu(hfac)MHY > Cu(hfac)DMB > Cu(hfac)VTMS [272]. Their structural formulae and vapour pressure data are summarized in Fig. 4.2.

4.2.2. FEBID

The first FEBID experiments on Cu(I) β-diketonate complexes with neutral ligands were performed using Cu(hfac)VTMS as precursor. An electron beam current of 600 pA in an environmental SEM resulted in copper contents of 8–11 at.% and complete loss of fluorine (<1 at.%) [307]. As mentioned in Section 4.1.2, a comparative study investigated the compounds Cu(hfac)VTMS, Cu(hfac)MHY, and Cu(hfac)DMB with the obtained compositions for 500 pA electron beam current noted in Table 4.6 [272]. All obtained deposits were non-conducting.

Table 4.6 shows the lower copper contents from [272] as the authors mentioned that the high copper contents were probably an artefact of selective/preferential argon ion sputtering during depth profiling in their AES measurements. The six fluorine atoms in these heteroleptic precursors are usually completely removed

Table 4.5
Properties of β-diketonate Cu(I) complexes with neutral π-donor ligands. * colour caused by Cu(II) impurities [300]. The abbreviation nf stands for 'not found'.

compound	phase	appearance	melting point	boiling point (T,p)	decomposition	stability	ref.
Cu(hfac)VTMS	liquid	green*	−20 °C	50 °C, 66.5 mbar	63 °C	air-sensitive	[300,301]
Cu(hfac)DMB	liquid	yellow	nf	35 °C	88 °C	air-sensitive	[302-304]
Cu(hfac)MHY	liquid	yellow	13 °C	207.2 °C	207 °C	air-sensitive	[272,305]

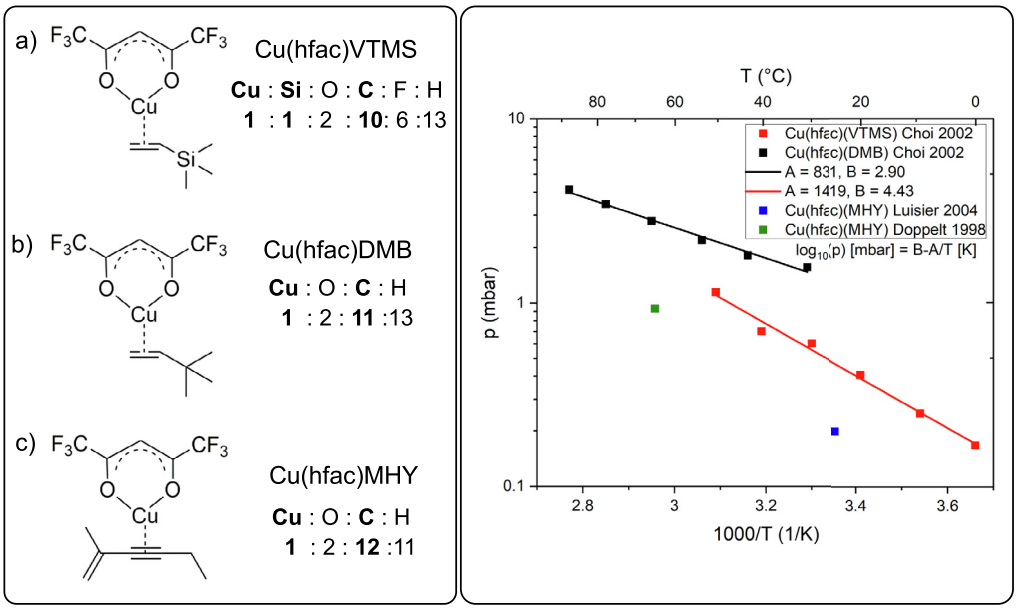

Fig. 4.2. Left: structural formulae and atomic ratios of β-diketonate Cu(I) complexes with neutral π-donor ligands. Right: vapour pressure with fitted $\log_{10}(p)$[mbar] = B - A/T [K] curves. Graphs were reproduced using: Cu(hfac)VTMS [306], Cu(hfac)DMB [306], Cu(hfac)MHY [272,299].

Table 4.6
Normalized atomic ratios of copper precursors with the corresponding *as-grown* deposit compositions and the *as-grown* deposit metal content. The arrow terms read "atoms in precursor $\overset{e^-}{\mapsto}$ atoms in FEBID material". Note that this table contains the lower copper content and correspondingly the higher carbon content from [272]. Hydrogen is excluded as it was not quantified in any of the studies. *The numbers are calculated from the stoichiometries given by the authors. **Heat-assisted FEBID.

Cu complex	Cu	C	O	F	Si	Cu at.%	ref.
Cu(hfac)VTMS	1	10→5	2→0.5	6→ < 0.1	1→3	11	[307] (ESEM)
Cu(hfac)VTMS	1	10→3.5	2→0.4	6→0	1→0.1	20	[272]
Cu(hfac)VTMS	1	10→5	2→1	6→0	1→0.3	≈14*	[308]
Cu(hfac)VTMS	1	10→5	2→1	6→1	1→1	≈11*	[309] 3D
Cu(hfac)VTMS	1	10→0	2→0	6→0	1→0	100 **	[310] pillar
Cu(hfac)MHY	1	11→6.3	2→0.2	6→0	–	13	[272]
Cu(hfac)DMB	1	11→2.4	2→0.6	6→0	–	25	[272]

from the initial fluorinated precursor molecules. The complex Cu(hfac)VTMS with the metal Cu and the semimetal Si in the ligand is interesting in so far as there is a preference in depositing copper with up to ten times higher efficiency than silicon. Alternatively, the fluorine which is released in the electron driven dissociation can also form the very volatile SiF_4 compound and thus etch away the otherwise deposited silicon [311,312]. Luisier et al. had a precursor flux of Cu(hfac)VTMS that translated to a local pressure above the surface of 0.013 mbar [272]. In contrast, under high-pressure conditions in an environmental SEM with the precursor pressure being 1.6 mbar, the silicon deposition was three times more efficient than copper deposition [307]. Further studies using Cu(hfac)VTMS obtained varying Cu:Si ratios but overall similar Cu:C ratios [308,309]. Especially for three-dimensional structures a reliable quantification via EDX correcting for the silicon signal of the substrate is challenging [309].

Pure FEBID copper deposits were reported by Utke et al. [310] for Cu(hfac)(VTMS). The deposited freestanding rods and pillars underwent a transition from ambient temperature FEBID deposits with a dominant carbon portion to pure crystalline copper via heat-assisted FEBID [310]. Due to the low heat conductivity of the freestanding structure with low copper content the temperature at the growth front increased with increasing length of the freestanding rod. The thermal decomposition of Cu(hfac)VTMS where disproportionation proceeds (see Sections 4.2.1 and 4.2.3) is around 120 °C and this temperature was most likely reached when the tips turned rough in morphology and formed pure nanocrystals of copper. This was remarkable in so far that also already deposited carbon-, fluorine-, oxygen-rich material converted into copper, meaning that the already deposited carbonaceous matrix was still volatile enough to be removed by combined thermal and electron energy input (electron stimulated desorption), see Fig. 4.3. As also the Si peak disappeared, one may hypothesize that the VTMS ligand was deposited still largely intact and removed by beam heating through thermal desorption.

4.2.3. CVD

In the chemical vapour deposition process based on copper(I) compounds, the disproportionation reaction occurs and copper(0) and volatile Cu(II) by-products (Cu(II) β-diketonates described in Section 4.1.) are formed:

2 Cu(β-diketonate)L → Cu(0) + Cu(β-diketonate)$_2$ + 2L

Therefore, Cu(hfac)VTMS reacts with or without hydrogen at temperatures from 130 to 235 °C [313]. The growth behaviour of copper film from Cu(hfac)VTMS was affected by temperature, flow rate, and the type of carrier gas (noble gases). The Auger profiles revealed that the impurities are nearly undetectable. The resistivity of deposited copper was lower for higher deposition temperature and is practically constant in the temperature range of 200 to 250 °C [314]. Cu(hfac)DMB was vaporised at 35 °C and carried to the reactor by argon. Total pressure in the CVD reactor was adjusted at 0.4 mbar. Films were deposited on a Si wafer coated with sputter deposited titanium nitride (TiN). The Cu film deposited at 150 to 200 °C had a resistivity of 2.0–2.2 μΩ cm which is close to the bulk copper [303]. Cu(hfac)MHY was introduced to the CVD reactor at 55 °C, 1.3 mbar pressure and water addition (0.3 sccm in 150 sccm N_2). The substrate temperature was 190 °C. In the case of this precursor, water addition is a critical point. It permits improved uniformity and resistivity [315].

Table 4.7 summarizes the CVD data.

4.2.4. ALD

ALD with copper(I) β-diketonate complexes used in FEBID was not reported presumably due to their thermal instability, i.e. decomposition in vacuum at low temperatures.

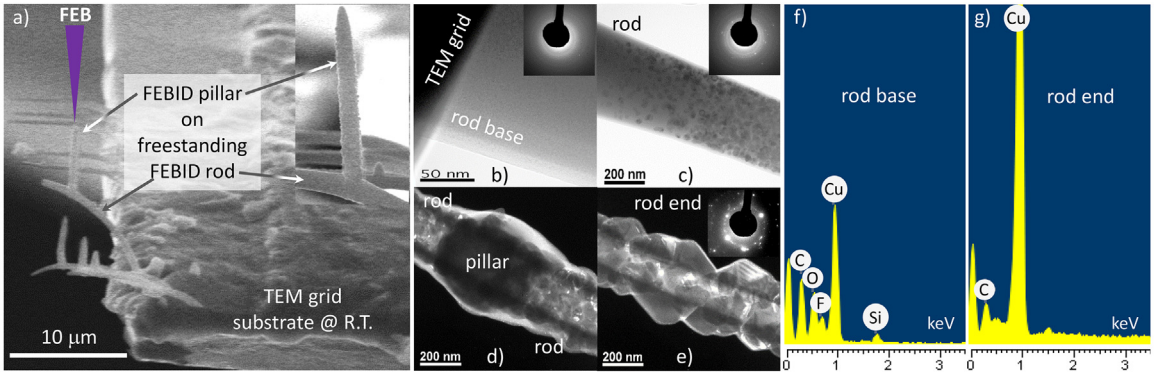

Fig. 4.3. Electron beam heating on low heat dissipating frestanding structures from Cu(hfac)VTMS. a) Scanning electron micrographs showing verticalpillar deposits on horizontal rods. Note the rough surface of the pillar due to copper nanocrystal formation. Corresponding transmission electron micrographs: b) base part close to the substrate with 2–5 nm copper nanocrystals dispersed in an amorphous carbonaceous matrix, c) rod region approaching the vertical pillar deposit with increased nanocrystal size 20–40 nm, d) dark-field TEM of rod region with pillar showing advanced coalescence of nanocrystals, e) example of facetted rod with large nanocrystals. Corresponding EDX analysis of f) base part and g) facetted rod shown in middle figure d). Note the disappearance of the ligand element Si and the reduction of the O, F, and C signals. Modified from [310].

Table 4.7
Summary of CVD data related to FEBID.

compound	T precursor	T deposition	pressure	gases	film composition	ref.
Cu(hfac)VTMS	40 °C	200–250 °C	8 mbar	noble gas	>99 at.% Cu (AES)	[314]
Cu(hfac)DMB	35 °C	150–200 °C	0.4 mbar	Ar	resistivity: 2.0 μΩ cm (bulk copper: 1.6 μΩ cm)	[303]
Cu(hfac)MHY	55 °C	190 °C	1.3 mbar	N_2	resistivity: 2.5 μΩ cm (bulk copper: 1.6 μΩ cm)	[315]

Table 4.8
Properties of Cu(II) and Ag(I) carboxylate complexes. The abbreviation nf stands for 'not found'.

compound	phase	appearance	melting point	sublimation point (T,p)	decomposition	stability	ref.
$Cu_2(\mu\text{-}O_2CC_2F_5)_4$	solid	blue	nf	nf	nf	stable	[316]
$Cu_2(^tBuNH_2)_2(\mu\text{-}O_2CC_2F_5)_4$	solid	blue	nf	nf	nf	stable	[317]
$Ag_2(\mu\text{-}O_2CC(Me)_2Et)_2$	solid	white	nf	nf	150 °C	light sensitive	[318,319]
$Ag_2(\mu\text{-}O_2C^tBu)_2$	solid	white	nf	nf	155 °C	light sensitive	[319]
$Ag_2(\mu\text{-}O_2CC_3F_7)_2$	solid	white	292–294 °C	nf	320 °C	light sensitive	[319,320]
$Ag_2(\mu\text{-}O_2CC_2F_5)_2$	solid	white	~241 °C	150 °C (10^{-1} mbar)	182 °C	light sensitive	[321,322]
$Ag_2(\mu\text{-}O_2CCF_3)_2$	solid	white	257–260 °C	nf	257–260 °C	light sensitive	[323]

4.2.5. Surface science studies

So far, fundamental studies with respect to FEBID of Cu(hfac)VTMS, Cu(hfac)DMB, and Cu(hfac)MHY do not exist. However, we note that the DFT theoretical and experimental study on reactions of $Cu(hfac)_2$ with different HOPG surfaces also included a comparison with Cu(hfac)VTMS [298] and may again serve as model system to supply insight into the adsorption of the precursor on a carbonaceous matrix as typically produced in FEBID. The study concluded, however, that the interactions of Cu(hfac)VTMS with the edges of the HOPG sheet as well as with HOPG with –COOH and –OH defect sites is weaker than for $Cu(hfac)_2$. Furthermore, the adsorption of Cu(hfac)VTMS on single crystal Cu surfaces was investigated under UHV conditions which revealed that VTMS dissociates from the complex and similar surface species as in the case of $Cu(hfac)_2$ were formed [294]. It was concluded that the bimolecular disproportionation that is proposed to drive CVD of Cu from Cu(hfac)VTMS (see Section 4.2.3) is slow at such low pressures because of low surface coverage, whereas this reaction becomes suitable at higher pressures relevant to CVD.

4.3. Cu(II) and Ag(I) carboxylate complexes

4.3.1. Introduction

Carboxylate group 11 complexes were recently investigated for FEBID to address the need for pure silver and copper nanoscale direct printing, especially for plasmonic applications of silver and local electronic circuit repair and testing in semiconductor industry [324,325]. Carboxylates are ligands, which can form interesting mono-, di-, and multinuclear structures because they are able to coordinate to metals monodentate, as chelates, and bridging. The applied secondary ligands in heteroleptic complexes enable influencing physicochemical parameters of the obtained compounds. Due to the extraordinarily long systematic names of the complexes, here we employ the chemical formulae.

The precursor properties of this section are collected in Table 4.8 and their structural formulae are summarized in Fig. 4.4. No vapour pressure data is available yet.

The copper(II) $Cu_2(\mu\text{-}O_2CC_2F_5)_4$ complex (also named $Cu_2(pfp)_4$) is one of the Cu(II) carboxylates $Cu_2(\mu\text{-}O_2CR)_4$ used as substrates for synthesis of many CVD precursors such as $Cu^I_2(PR_3)_2(\mu\text{-}O_2CR)_2$, $Cu^I_2(\text{-VTMS})_2(\mu\text{-}O_2CR)_2$ [327], and $Cu^{II}_2(^tBuNH_2)_2(\mu\text{-}O_2CR)_2$ [317,326]. However, the $Cu_2(\mu\text{-}O_2CR)_2$ carboxylates themselves did not seem promising in this role, because they contain copper(II) and would probably need the presence of hydrogen for pure deposit formation in Cu CVD. On the other hand, the thermal analysis (TG-IR) of the $Cu_2(^tBuNH_2)_2(\mu\text{-}O_2CR)_4$ (R = CF_3, C_2F_5, C_3F_7, C_4F_9) has indicated that copper carriers are formed even at atmospheric pressure (Fig. 4.5). This fact seems advantageous for Cu CVD (cf. Section 4.4.3.) [326].

Silver carboxylate complexes are stable in ambient atmosphere and start to evaporate at practical FEBID amounts at temperatures around 150 °C. Vapour pressures of these precursors are not known. Vacuum TGA measurements [328] for the silver carboxylates and inert ambient pressure gas TGA for $Cu_2(\mu\text{-}O_2CC_2F_5)_4$ are shown in Fig. 4.4. Jurczyk et al. [328] compared ambient pressure TGA versus vacuum TGA of the silver carboxylates. They found the evaporation temperature onsets in vacuum TGA around 120–130 °C lower than for ambient pressure TGA. The fluorinated compounds evaporated almost completely without residues. The evaporation temperature of the non-fluorinated silver carboxylates in vacuum was lower by about 30–40 °C than in ambient pressure TGA and these complexes left silver residues. The residual mass was close to the stoichiometry content of silver so that it was concluded that the complex decomposes thermally. As local silver FEBID deposition was successfully proven with the non-fluorinated silver compounds [97] a window of evaporation of intact molecules must exist at the onset temperature region. From Fig. 4.5. the thermal stability of the precursors can be classified as $Ag_2(\mu\text{-}O_2CC(Me)_2Et)_2 \approx Ag_2(\mu\text{-}O_2C^tBu)_2 < Ag_2(\mu\text{-}O_2CC_2F_5)_2 < Ag_2(\mu\text{-}O_2CCF_3)_2 \approx Ag_2(\mu\text{-}O_2CC_3F_7)_2$.

4.3.2. FEBID

Deposition experiments with a beam current of 460 pA using the copper(II) carboxylate complex $Cu_2(\mu\text{-}O_2CC_2F_5)_4$ resulted in about 23 at.% Cu content only [324]. Still, it is remarkable that this number already entails the removal of three out of the four ligands from the complex as can be derived from Table 4.9. Berger et al. [324] suggested the dissociation path shown in Fig. 4.6 based on post-growth composition measurements of the FEB deposited material. In addition to copper, a carbonaceous matrix containing fluorine and oxygen was deposited. In regions of higher electron flux, oxygen was removed and fluorine and carbon formed the matrix in which the copper was embedded. In contrast to the silver carboxylate FEBID, low electron fluxes did not improve the removal of carbon and fluorine. Keeping the deposits for longer time at ambient conditions turned out to oxidize the copper nanocrystals in the matrix. A post-FEBID annealing at 250 °C in oxygen to remove the carbon followed by forming gas reduction of the copper oxide led to the formation of pure copper [324].

For silver carboxylates, the reservoir temperature was kept around 150–180 °C for sufficient evaporation of intact binuclear

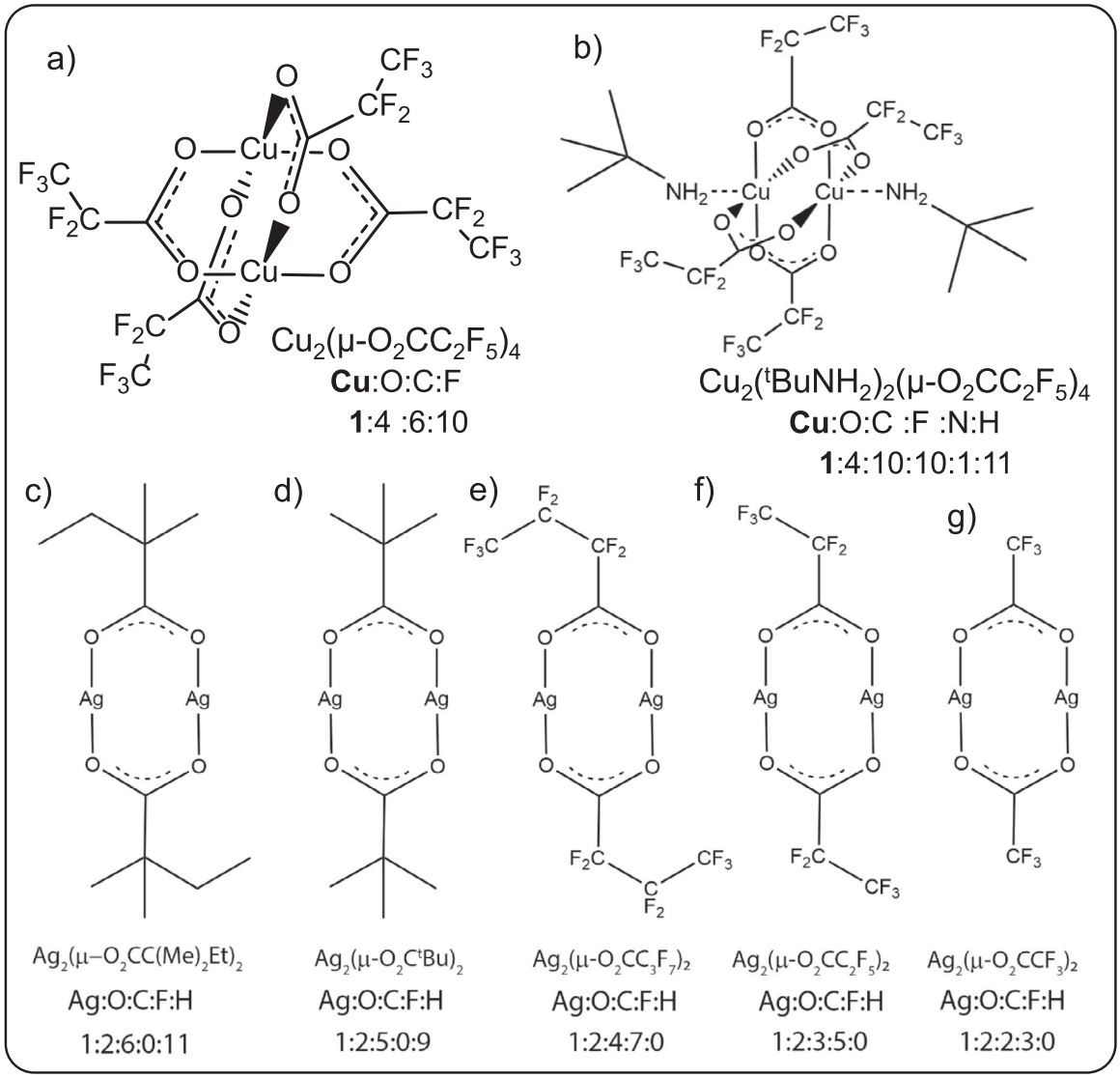

Fig. 4.4. Structural formulae and atomic ratios of Cu(II) and Ag(I) carboxylate complexes [324-326].

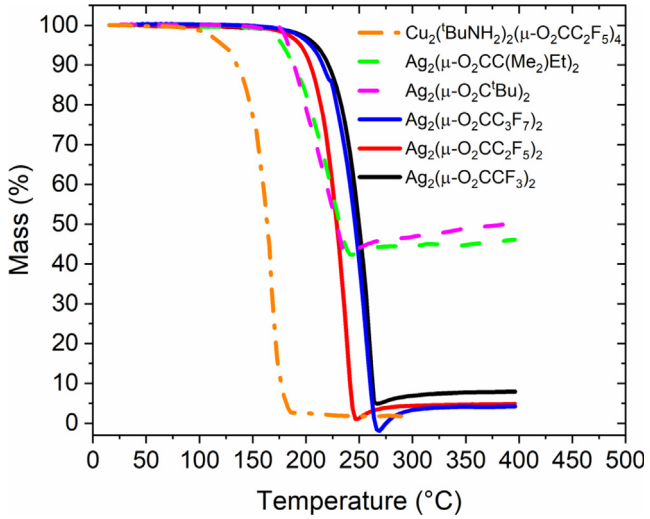

Fig. 4.5. Vacuum TGA of the silver carboxylates $Ag_2(\mu\text{-}O_2CR)_2$ and ambient pressure inert gas TGA for the Cu(II) carboxylate complex with *tert*-butylamine $Cu_2(^t\text{-}BuNH_2)_2(\mu\text{-}O_2CC_2F_5)_4$. Reproduced from Jurczyk et al. [328] under CC BY license.

molecules through the gas injection system. The substrate temperature was kept in the same range to avoid condensation or thermal decomposition of the molecules. In a comparative study [325], the highest silver content of deposits from the fluorinated carboxylates changed from about 75 at.% to 57 at.% with increasing carbon chain length of the ligand, see Fig. 4.4 c-e and Table 4.9. The non-fluorinated silver carboxylates showed around 50 at.% silver content independent of the number of carbons in the ligand. Furthermore, the oxygen content in deposits from all silver carboxylates was below 5 at.% and carbon was removed by 89 % from the initial precursor molecule. Of note is that an optimum of 76 at.% silver was achieved for $Ag_2(\mu\text{-}O_2CC_2F_5)_2$ [329] while the optimum for $Ag_2(\mu\text{-}O_2CC(Me)_2Et)_2$ was very similar with 73 at.% of silver [97]. For all carboxylates precise temperature control was vital to avoid condensation and thermal decomposition of the precursor on the substrate.

To explain the observed compositional variations in silver spot deposits, an electron beam flux dependent ligand co-deposition mechanism was proposed as illustrated in Fig. 4.7 for the $Ag_2(\mu\text{-}O_2CC(Me)_2Et)_2$ [97]. Of note is that no autocatalytic reaction leading to growth without electron irradiation was observed. As discussed in the introduction section, see Fig. 2.4.e, the desorption

Table 4.9
Normalized atomic ratios of copper and silver carboxylate precursors with the corresponding *as-grown* deposit compositions together and the *as-grown* deposit metal content. The arrow terms read "atoms in precursor $\overset{e^-}{\rightarrow}$ atoms in FEBID material". From [325] the best achieved atomic ratios are taken. The hydrogen content is neglected.

complex	Cu/Ag	C	O	F	metal at.%	ref.
$Cu_2(\mu\text{-}O_2CC_2F_5)_4$	1	6→1.5	4→0	10→2	23	[324]
$Ag_2(\mu\text{-}O_2CC(Me)_2Et)_2$	1	6→0.5	2→0.1	0→0	59	[325]
$Ag_2(\mu\text{-}O_2CC(Me)_2Et)_2$	1	6→0.3	2→0.04	0→0	73	[97]
$Ag_2(\mu\text{-}O_2C^tBu)_2$	1	5→0.6	2→0.1	0→0	57	[325]
$Ag_2(\mu\text{-}O_2CC_3F_7)_2$	1	4→0.5	2→0	7→0.22	57	[325]
$Ag_2(\mu\text{-}O_2CC_2F_5)_2$	1	3→0.3	2→0.04	5→0.1	70	[325]
$Ag_2(\mu\text{-}O_2CC_2F_5)_2$	1	3→0.26	2→0.01	5→0.04	76	[329]
$Ag_2(\mu\text{-}O_2CCF_3)_2$	1	2→0.3	2→0.02	3→0.03	74	[325]

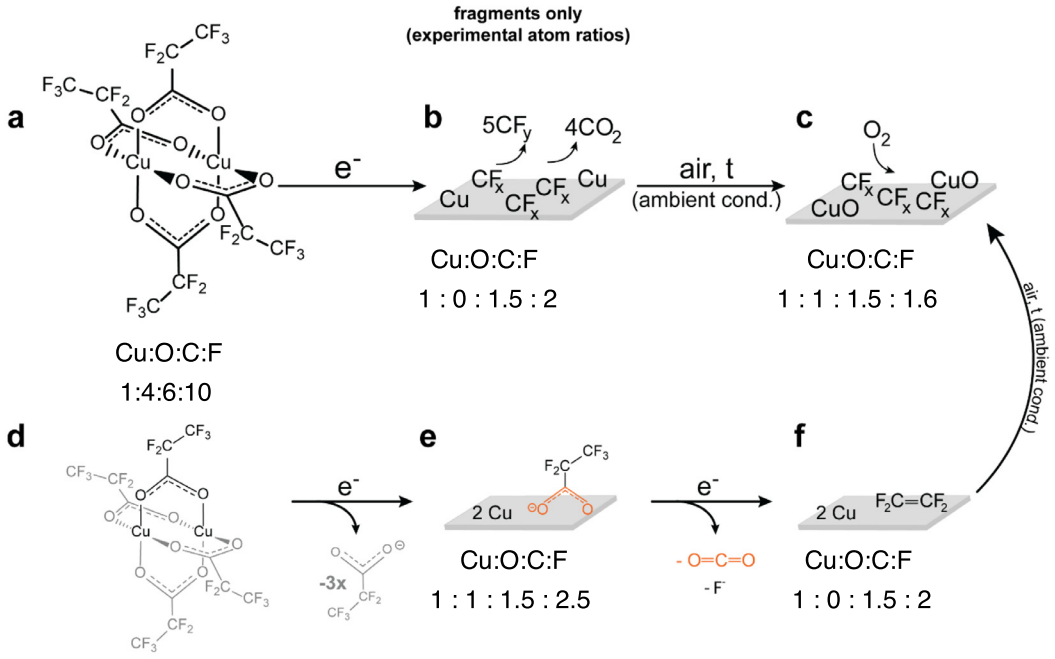

Fig. 4.6. Proposed dissociation paths of $Cu_2(\mu\text{-}O_2CC_2F_5)_4$ as concluded from the final FEBID deposit composition. Modified from Berger et al. [324]. a-c) Show the fragment scheme. d-e) Shows the entire ligand dissociation scheme. The determination of the exact dissociation species would require in-situ mass spectrometric measurements.

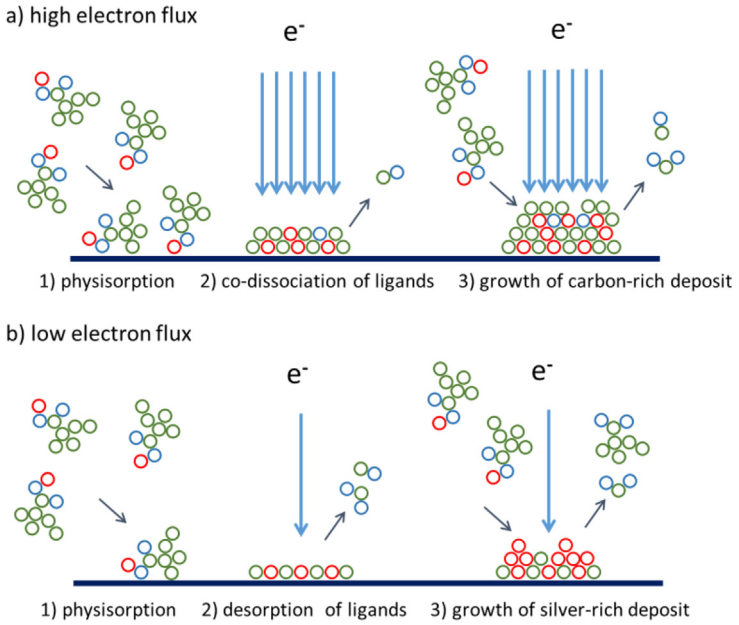

Fig. 4.7. Electron beam flux dependent ligand co-deposition for $Ag_2(\mu\text{-}O_2CC(Me)_2Et)_2$. Red circles symbolize silver atoms while the colours signify elements of the organic ligand. a) At high electron flux electron beam induced co-dissociation of ligands leads to the growth of carbon-rich deposits; and b) at low electron flux efficient desorption of ligands leads to growth of silver-rich deposits. Adapted with permission from Höflich et al. [97].

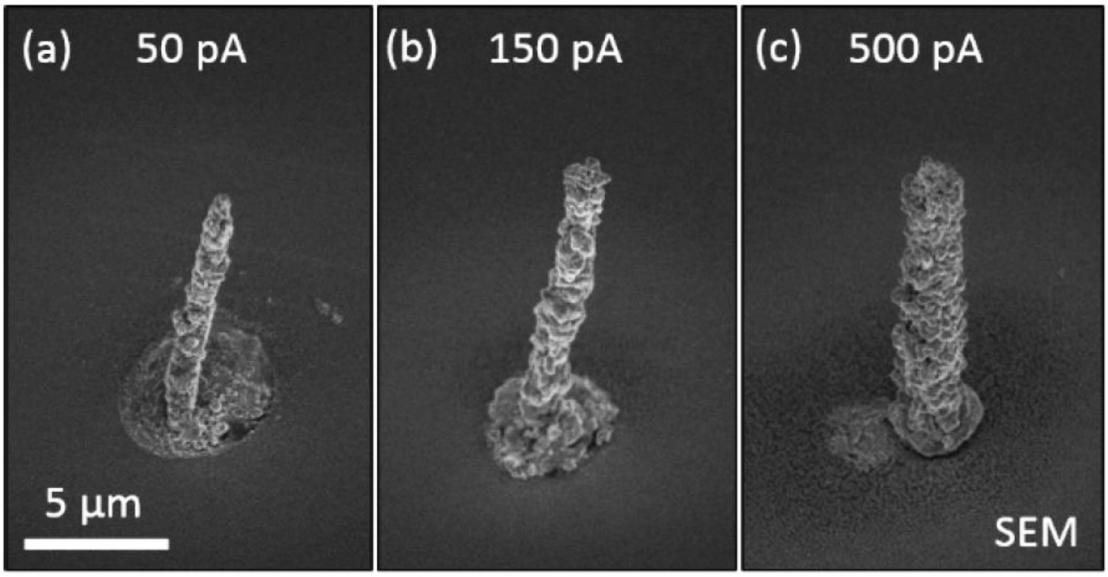

Fig. 4.8. Tilt scanning electron micrographs of single silver pillars obtained from continuous spot irradiation for (a) 50 pA, (b) 150 pA, and (c) 500 pA beam current using $Ag_2(\mu\text{-}O_2CC_2F_5)_2$ as FEBID precursor. Reproduced from Höflich et al. [330], CCBY license, Beilstein-Institut.

rate of the intact ligand must be larger than its fragmentation rate to obtain a pure metal deposit. Otherwise, its non-volatile fragments will be co-deposited and form a part of the deposit. The transition from ligand desorption to ligand fragmentation, i.e. from no ligand co-deposition to ligand co-deposition, occured over at least one order of magnitude change of electron flux. Fig. 4.7 represents a simplified picture of co-deposition, see Sections 5.2.2. and Section 5.2.3 for a more detailed discussion on the thermodynamically favoured dissociation channels and electron-induced co-deposition.

Fig. 4.8 shows three-dimensional pillar deposits obtained from $Ag_2(\mu\text{-}O_2CC_2F_5)_2$ continuous spot deposits [330]. An evident feature of these deposits is the formation of large silver crystals. However, it is interesting to note that the achievable silver content for the pillar deposits is smaller than for planar deposits (~50 at.% vs. 76 at.%). The high electron flux in the beam centre may lead to ligand co-dissociation what in turn increased the volume deposition rate sufficiently to enable vertical growth for $Ag_2(\mu\text{-}O_2CC_2F_5)_2$ in contrast to the case of $Ag_2(\mu\text{-}O_2CC(Me)_2Et)_2$.

4.3.3. CVD

The CVD experiments for perfluorinated copper(II) carboxylates $Cu_2(\mu\text{-}O_2CR)_4$ have not yet been carried out. However, their derivatives with *tert*-butylamine of the general formula $Cu_2(^tBuNH_2)_2(\mu\text{-}O_2CR)_4$, where R = CF_3, C_2F_5, C_3F_7, C_4F_9, C_5F_{11}, C_6F_{13} were used in CVD process in argon only and metallic copper layers were obtained. It should be noticed that no additional reducing agent such as hydrogen was needed what is unusual for copper(II) CVD precursors [326].

On the basis of MS EI and variable temperature infrared spectroscopy (VT IR) spectra analysis the transport mechanism of copper in the gas phase comprising two pathways was proposed [317]. The first one is the formation of copper(II)-carboxylate species $Cu_2(\mu\text{-}O_2CR)_4$ (see Section 4.3.2. – the complex $Cu_2(\mu\text{-}O_2CC_2F_5)_4$ was used in the FEBID process) in the condensed phase over 30–100 °C temperature range:

$Cu_2(^tBuNH_2)_2(\mu\text{-}O_2CR)_4$ (s) → $2\,^tBuNH_2$ (g) + $Cu_2(O_2CR)_4$ (s)

In the next step, the Cu(II) carboxylate generates Cu(I) carboxylate species that are more stable in the gas phase. These latter can be one of the types of the metal carriers in the CVD process, e.g. for R = C_2F_5:

$Cu_2(O_2CC_2F_5)_4$ (s) → $Cu_2(O_2CC_2F_5)_2$ (g) + $2CO_2$ (g) + C_4F_{10} (g)

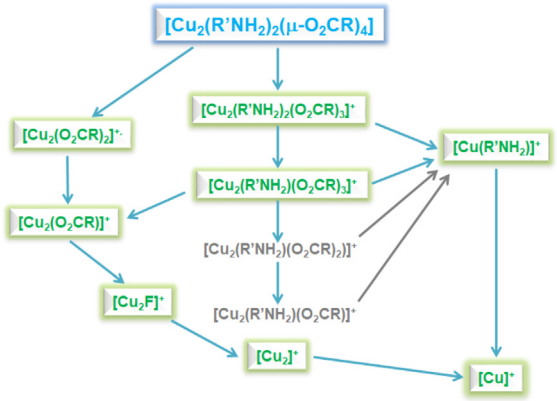

Fig. 4.9. The main pathways of fragmentation for copper(II) carboxylate compounds with simple amines $Cu_2(R'NH_2)_2(\mu\text{-}O_2CR)_4$, where R'=Et, ^sBu, ^tBu and R = C_2F_5; R'= ^tBu and R = C_nF_{2n+1}, n = 1, 3–6. Suggested on the base of metal containing ions in electron-induced MS and DI experiments in [326,334].

Table 4.10
Summary of CVD results.

compound	T precursor	T deposition	pressure	gases	film composition	ref.
$Cu_2(^tBuNH_2)_2(\mu\text{-}O_2CR)_4$	162–200 °C	350–460 °C	1.5 mbar	Ar	>98.5 at.% Cu	[326]
$Cu_2(\mu\text{-}O_2CC_2F_5)_4$			No CVD			
$Ag_2(\mu\text{-}O_2CCF_3)_2$	300 °C	600 °C	26.7 mbar	H_2	>99 at.% Ag (XRD, AES)	[332]
$Ag_2(\mu\text{-}O_2CC_2F_5)_2$	240 °C	270–350 °C	4 mbar	Ar	59–80 at.% Ag	[322]
$Ag_2(\mu\text{-}O_2C^tBu)_2$			No CVD			
$Ag_2(\mu\text{-}O_2CC(Me)_2Et)_2$			No CVD			

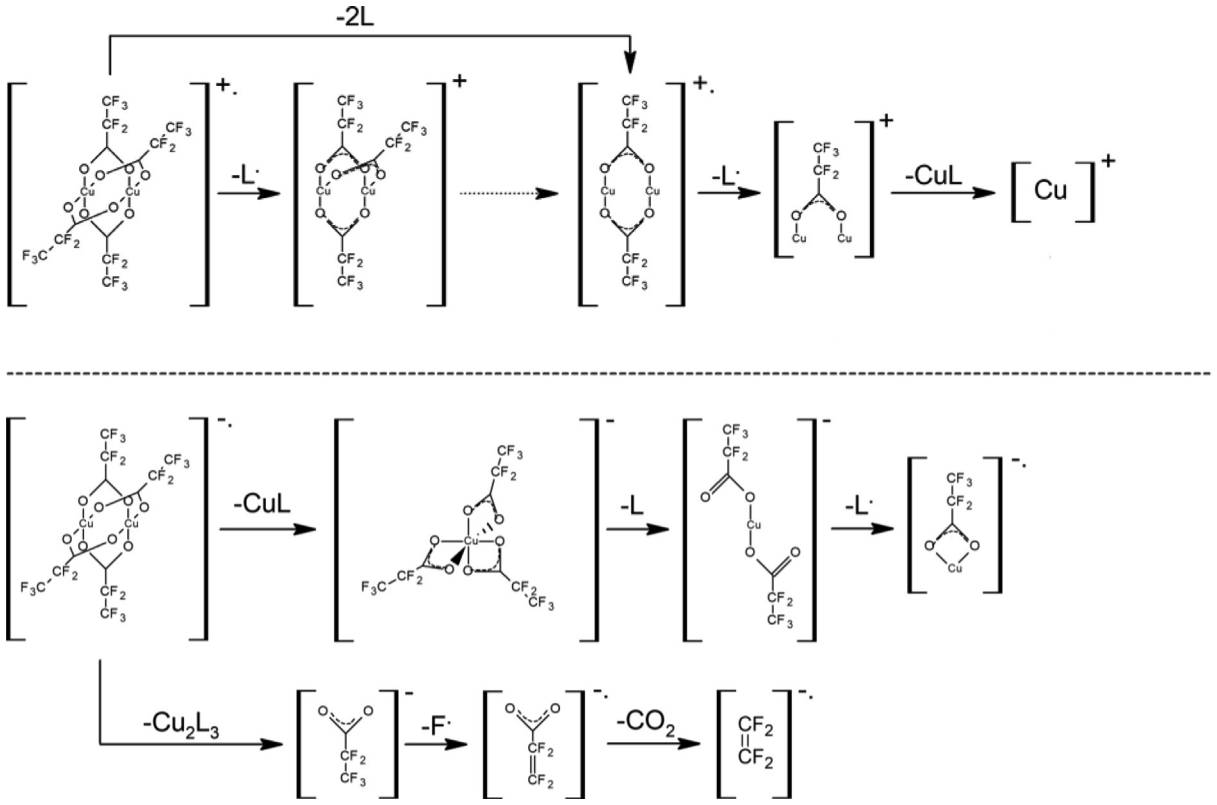

Fig. 4.10. The fragmentation pathways for $Cu_2(\mu\text{-}O_2CC_2F_5)_4$, L in the figure means $O_2CC_2F_5^{-}\bullet$. Top: Dissociative Ionization (DI). Bottom: Dissociative Electron Attachment (DEA). On the base of [334].

Table 4.11
Mass spectrometry data of FEBID tested silver(I) carboxylates $Ag_2(\mu\text{-}O_2CR)_2$. The symbols *m*/*z* stand for ionic fragment mass over charge and I for intensity in the mass spectrum [318,331,335]. a) The data is reported for the most intensive line in the pattern: $^{107}Ag^{109}Ag$ isotope compositions. b) The temperatures were chosen at the local maxima of the total ion current curve (TIC). c) $[CH_3CH_2CH_2]^+$ 43 (100%). d) $[C_2F_4]^+$ 100 (100%).

R	CF_3	C_2F_5 [a]	I [%] [b]		C_3F_7 [d]	CMe_3	CMe_2Et [a]
	***m*/*z* (I%)**	***m*/*z***	**180 °C**	**220 °C**	***m*/*z* I(%)**	***m*/*z* I(%)**	**197 °C**
$[CO_2]^+$	44 (39)	44	15	42	44 (32)	44(11)	44 (23)
$[R]^+$	69 (100)	119	100	100	169 (8)	57 (100)	71(64)
$[RCO]^+$	97 (20)	147	35	23	–	85 (3)	–
$[Ag]^+$	107 (26)	107	6	64	107 (65)	107 (5)	107 (2)
$[AgCO_2]^+$	151 (1)	–	–	–	151 (2)	–	–
$[Ag_2]^{+\cdot}$ [a]	214 (10)	216	2	2	214 (20)	214 (8)	216 (10)
$[Ag_2O]^{+\cdot}$	230 (2)	–	–	–	230 (3)	–	–
$[Ag_2F]^+$ [a]	233 (2)	235	–	<1	–	–	–
$[Ag_2(O_2CR)]^+$ [a]	327 (21)	379	12	11	427 (39)	315 (17)	331(38)
$[Ag_2(O_2CR)R]^+$	–	–	–	–	–	373 (<1)	–

The second pathway is the sublimation of entire $Cu_2(^tBuNH_2)_2(\text{-}\mu\text{-}O_2CR)_4$ molecules and this is the second type of the copper carriers [317]:

$Cu_2(^tBuNH_2)_2(\mu\text{-}O_2CC_2F_5)_4$ (s) → $Cu_2(^tBuNH_2)_2(\mu\text{-}O_2CC_2F_5)_4$ (g)

Over the 200–280 °C temperature range, both types of copper carriers can deposit the metal. The differences in a Cu(I)/Cu(II) carriers mixture ratio and the species stability were observed in a group of the studied complexes. Both factors influence the copper layer formation [317].

Silver carboxylates were discussed as CVD precursors by Grodzicki [331]. Using $Ag_2(\mu\text{-}O_2CC_2F_5)_2$ deposition, silver layers with some carbon impurities were obtained. The precursor was heated at 240 °C. Argon was used as carrier gas and the total pressure was 4 mbar. Using $Ag_2(\mu\text{-}O_2CC_2F_5)_2$, films were grown on glass or silicon substrates heated to 270–350 °C. The best material, containing 80% of silver, was deposited at 290 °C. The impurities (C, O) were localized on the surface of the Ag layers [322]. When $Ag_2(\mu\text{-}O_2CCF_3)_2$ was used as the CVD precursor, the best silver films were obtained at 600 °C with hydrogen flow on various fibres and on flat polycrystalline Al_2O_3 substrates. No impurity phases or elements in the films were detected [332].

$[Ag_2(\mu\text{-}O_2C^tBu)_2]_n$ was summed up as not so successful CVD precursor to 2005 [331], because it required a relatively high sublimation temperature (230–510 °C under 0.01 mbar) and gives a low yield in the CVD process (≤0.2% at temperatures above 540 °C). These results were related to a polymeric chain structure of this compound. Kuzmina et al.[4] wanted to limit the formation of the polymeric chain and used a secondary ligand $^iPr_2NH$. The sil-

[4] N. Kuzmina, S. Paramonov, R. Ivanov, V. Kezko, K. Polarno, S. Troyanov, Silver pivalate as a new volatile precursor for thin film deposition, J. Phys. IV Fr. 9 (1999) 923–928, https://doi.org/10.1051/jp4:19998116.

ver complex $Ag(O_2C^tBu)(^iPr_2NH)_2$ was obtained. Unfortunately, in TGA experiments the formation of the primary polymeric silver carboxylate $[Ag_2(\mu\text{-}O_2C^tBu)_2]_n$, by imine $^iPr_2NH$ detachment, was observed. Therefore, CVD deposition parameters for $Ag(O_2C^tBu)(^iPr_2NH)_2$ were the same as for $[Ag_2(\mu\text{-}O_2C^tBu)_2]_n$[4]. However, the deposition temperature was decreased to 180-200°C when PMe_3 or PEt_3 were applied as a secondary ligand for $Ag(O_2C^tBu)(PMe_3)$ and $Ag(O_2C^tBu)(PEt_3)$ [331].

In the case of $[Ag_2(O_2CC(Me)_2Et)_2]_n$, TGA-IR and VT IR of vapours studies revealed no silver carriers at atmospheric and reduced pressure (0.01 mbar) [318]. For the $Ag_2(O_2CC_3F_7)_2$ and $[Ag_2(O_2CC(Me)_2Et)_2]_n$ complexes no CVD experiments have been yet reported. Table 4.10 summarizes the CVD data.

4.3.4. ALD

No atomic layer deposition experiments were reported so far on Cu(II) and Ag(I) carboxylate complexes.

4.3.5. Fundamental surface and gas phase studies

For surface science studies, two complexes $Cu_2(EtNH_2)_2(\mu\text{-}O_2CR)_4$, where R = C_2F_5, C_3F_7 were chosen among the copper(II) perfluorinated carboxylates with amines due to their gel like form. They could be placed directly on the studied surface [333]. On the base of IR, high-resolution electron energy loss spectroscopy (HREELS), and ESD experiments, partial amine detachment at room temperature under vacuum was observed. Complete removal of this ligand could be achieved by heating or low-energy electron irradiation. Interactions with these electrons also caused dissociation of the carboxylate ligands what seemed promising for FEBID. For silver carboxylates, surface UHV studies are not yet available.

Studies in the gas phase have been started from simple electron impact mass spectrometry and the results indicated the high stability of the $Cu_2(^tBuNH_2)_2(\mu\text{-}O_2CR)_4$ compounds in the gas phase (cf. Fig. 4.9). That was advantageous for vapour deposition methods, such as e.g. CVD. Moreover, the reduction reaction of Cu(II) to Cu(I) was confirmed by the detection of ions $[Cu_2(O_2CR)]^+$ and $[Cu_2(O_2CR)_2]^+$. It was also worth noting the high intensity of the $[CO_2]^+$ ion (vide infra).

In the next step, the copper(II) pentafluoropropionate complexes $Cu_2(R'NH_2)_2(\mu\text{-}O_2CC_2F_5)_4$, where R'=Et, ^{s}Bu, ^{t}Bu; and $Cu_2(\mu\text{-}O_2CC_2F_5)_4$ were studied in electron collision experiments [334]. The dissociation pathway in the positive ion mode revealed a successive loss of the carboxylate and/or the amine ligands from the molecules (cf. Fig. 4.9 and Fig. 4.10). The Cu^+ ion was observed with high intensity for $Cu_2(\mu\text{-}O_2CC_2F_5)_4$ and weakly for $Cu_2(EtNH_2)_2(\mu\text{-}O_2CC_2F_5)_4$ as well, which may be of interest for the FEBID process. All main DEA anions, dinuclear $[Cu_2(O_2CC_2F_5)_4]^{-\bullet}$ and mononuclear $[Cu(O_2CC_2F_5)_3]^-$, $[Cu(O_2CC_2F_5)_2]^-$, and $[Cu(O_2CC_2F_5)]^{-\bullet}$, were formed close to 0 eV and have been the same for all studied compounds (cf. Fig. 4.10) [334].

Collecting and managing of EI MS data for silver carboxylates is not a trivial issue due to transmetallation process (between Ag(I) and Cu(0)), which can occur in some mass spectrometers, containing copper elements [335]. However generally, the main signals in EI MS were attributed to $[Ag_2(O_2CR)]^+$, $[Ag_2(O_2CR)(O_2C)]^+$, $[Ag_2(O_2CR)_2]^+$ (cf. Table 4.6) as in the case of the Cu(I) carboxylates [331]. Their stability depends on the length of aliphatic chain (C_xH_{2x+1} or C_xF_{2x+1}), or the presence of bulky groups (e.g. ^{t}Bu). However, for FEBID tested silver carboxylates only monocarboxylate fragments $[Ag_2(O_2CR)]^+$ were detected that suggests the decarboxylation process is important for the metal deposit formation. The direct metal–ligand M–O bonds are broken with the formation of gaseous CO_2 (Table 4.6). Moreover, the efficiency of $[Ag]^+$ and $[Ag_2]^+$ fragments formation correlates with FEBID results (cf. Table 4.11).

4.4. Dimethyl(β-diketonate)gold(III) complexes

4.4.1. Introduction

Commercially available precursors for gold deposition are based on β-diketonate ligands (cf. Section 3.3.1.). Due to their stability, the thermal decomposition of dimethyl(acetylacetonate)gold(III), $Au(acac)Me_2$ under fragmentation and release of ethane occurs only above 200 °C [2]. The compound $Au(acac)Me_2$ is solid with a

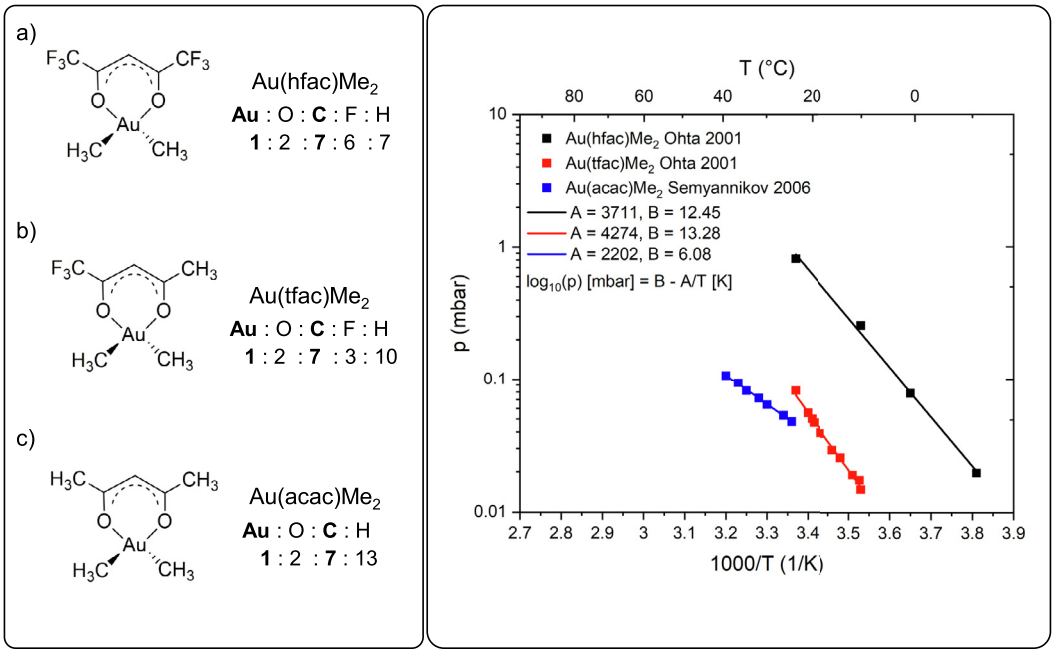

Fig. 4.11. Left: structural formulae and atomic ratios of β-diketonate Au(III) complexes. Right: vapour pressure with fitted $\log_{10}(p)$[mbar] = B - A/T[K] curves. Graphs were reproduced using: $Au(hfac)Me_2$ and $Au(tfac)Me_2$ [336], and $Au(acac)Me_2$ [339].

melting point around 80 °C and starts to sublime already at room temperature. Replacing the hydrogen in one or both of the methyl groups by fluorine further increases the vapour pressure for dimethyl(trifluoroacetylacetonate)gold(III), Au(tfac)Me_2 and even more for dimethyl(hexafluoroacetylacetonate)gold(III), Au(hfac)Me_2 [336], cf. Fig. 4.11. While the tfac complex is a relatively stable solid, the liquid compound Au(hfac)Me_2 is unstable under high vacuum conditions and therefore challenging in the FEBID implementation (cf. also Table 4.12). The properties of the Au(III) β-diketonate precursors in this section are summarized in Table 4.12. In case of Au(acac)Me_2 and Au(tfac)Me_2, vapour pressure and stability allow for easy implementation of the gas-injection into the vacuum chamber and for reliable deposition under the focused electron beam. However, this comes at the cost of a dominant carbon contamination in the deposit.

Fig. 4.11 summarizes their structural formulae and available vapour pressure data.

4.4.2. FEBID

First experiments on the electron beam induced deposition of gold in 1988 using Au(tfac)Me_2 resulted in a gold content of 4 at.% in the deposit (given as 40 wt% by the authors) [340]. Later experiments found values in the range of 3–10 at.% (~27 – 65 wt.%) [341], where the gold content increased with increasing electron beam currents and saturated around 1 nA at the expected value of the precursor stoichiometry. Increasing the substrate temperature showed a further slight improvement [341,342]. Furthermore, Au(acac)Me_2 was tested and mentioned to show negligible differences in the deposit composition as compared to Au(tfac)Me_2 [341].

The most volatile compound Au(hfac)Me_2 showed promise as a precursor for focused ion beam induced deposition [344]. However, due to its limited stability only little data is available for direct electron beam writing. It was used in an environmental SEM, where the addition of a reactive gas like oxygen or water significantly increased the gold content of the deposits up to 50 at.%. This was especially remarkable as deposition under HV conditions in the same chamber resulted in a gold content lower than expected from stoichiometry, around 2–3 at.% [95,96]. However, the most widely used gold precursor is Au(acac)Me_2 as it is stable and readily available for commercial gas-injection systems. The achieved gold contents vary from author to author, depending on the respective deposition conditions. Under typical HV deposition conditions with currents in the range of 0.1–1 nA, gold contents around 8–12 at.% are obtained for planar deposits [158,345] mainly reflecting the gold-to-carbon ratio of 1:7 in the precursor stoichiometry plus a potential carbon co-deposition from the residual hydrocarbons in the vacuum chamber (cf. Table 4.13). For large beam currents around few nA as well as high-aspect-ratio deposit geometries, local heating leads to significantly higher gold contents around 28 at.% (cf. Fig. 4.12) [75,346]. In the same manner, an elevated stage temperature can support the desorption of the ligands

Table 4.12
Properties of dimethyl(β-diketonate)gold(III) complexes. The abbreviation nf stands for 'not found' and RT for room temperature.

compound	phase	appearance	melting point	sublimation/boiling point (T, p)	decomposition	stability in air/light	ref.
Au(acac)Me_2	solid	colourless	81–82 °C	~25 °C, 0.013 mbar	nf	air-sensitive	[337,338]
Au(tfac)Me_2	solid	colourless	nf	RT (HV)	nf	air-sensitive	[337]
Au(hfac)Me_2	liquid	yellow	nf	RT	nf	unstable	[336,337]

Table 4.13
Normalized atomic ratios of gold precursors with the corresponding *as-grown* deposit compositions and the *as-grown* deposit metal content. Atomic ratios of gold precursors and FEB deposits normalized to gold content. The arrow terms read "atoms in precursor $\xrightarrow{e^-}$ atoms in FEBID material". The hydrogen content is neglected. *Only C and Au are monitored in these studies. The abbreviation nq stands for 'not quantified'.

Au complex	Au	C	O	F	Au at.%	ref.
Au(acac)Me_2	1	7→~7–11	2→nq	–	8–12	[158]* [345]
Au(acac)Me_2	1	7→2.2	2→0.1	–	30	[171] (stage heating)
Au(tfac)Me_2	1	7→2.5	2→0.5	3→nq	20	[351] (planar)
Au(tfac)Me_2	1	7→2	2→0.3	3→nq	30	[343] (lines)
Au(tfac)Me_2	1	7→1.6	2→0.6	3→nq	39	[353] (reactive surface)
Au(hfac)Me_2	1	7 →≫7	2→nq	6→nq	≪12.5	[95]*

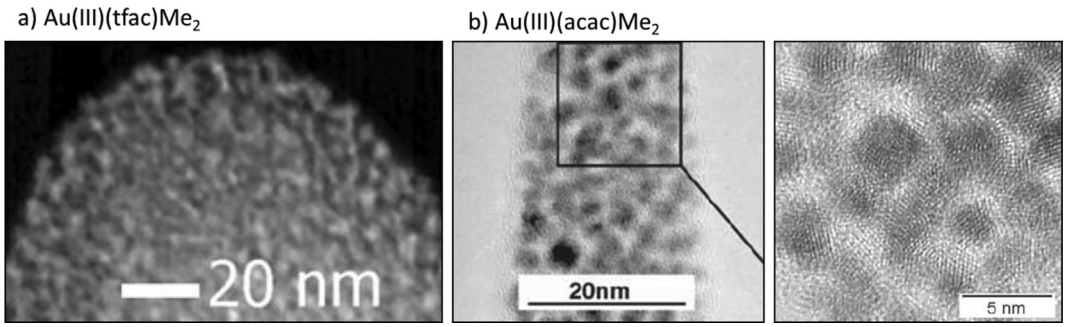

Fig. 4.12. Transmission electron micrographs showing the inner structure of FEBID material from gold(III) β-diketonates using the precursors a) Au(tfac)Me_2, reproduced from Utke et al. [343] with permission from The Royal Society of Chemistry, and b) Au(acac)Me_2, reproduced from [75]. Gold nanocrystals are embedded in a carbonaceous matrix.

[1] and leads to similar values in the gold content of around 30 at.% for a substrate temperature of 130–150 °C [171]. Also for Au(tfac)Me_2, co-injection of H_2O during deposition increased the achievable gold contents to 91 at.% [347]. High-aspect ratio deposits from Au(acac)Me_2 fabricated in an environmental SEM under 1.1 mbar H_2O pressure showed a core–shell structure with even a solid gold core [348]. Furthermore, the oxidative removal of the carbon matrix may be carried out after deposition, either by annealing in an oxidising atmosphere [75,158,345,349], electron beam irradiation in a water atmosphere [54] or using oxygen plasma [50] possibly combined with electron beam irradiation [350]. Optimally, the purification temperature is kept as low as possible, not above room temperature to preserve the 3D shape [50,54,75]. Still, without any thermal or chemical assistance, Au(tfac)Me_2 provides the best gold-to-carbon ratio of the three β-diketonate gold(III) complexes of around 15–39 at.% (cf. Fig. 4.12) [343,346,349-351]. As can be seen from Table 4.13, 30 at.% of gold in the deposit corresponds to a loss of 5 of 7 carbon atoms, where it has to be noted that fluorine was not detected [343]. 39 at.% gold content were achieved for thermally decoupled substrate that was pre-treated with Ga ion milling through a SiO_2 layer [353]. It is therefore not clear if the substantial amount of oxygen (23.1 at.%) measured via EDX was incorporated into the deposit as a consequence of the reactive surface or if part of the signal stems from the oxygen in the close vicinity (cf. Table 4.12).

4.4.3. CVD

Dimethyl(β-diketonate)gold(III) complexes are well-known as precursors for chemical vapour deposition [354,355]. Au(acac)Me_2, Au(tfac)Me_2, and Au(hfac)Me_2 were used as CVD precursors at room temperature and flow of argon carrier gas. In all runs, the substrate temperature was 300 °C and the chamber pressure was 0.67 mbar. The rates of deposition obtained under these conditions for each complex on SiO_2 are 13, 140, 940 Å/min, respectively. No carbon, oxygen, or fluorine contamination was observed for gold films obtained from Au(tfac)Me_2 and Au(hfac)Me_2, while gold layers obtained from Au(acac)Me_2 contained 15 at.% of carbon [356]. Table 4.14 summarizes the CVD data.

Plasma CVD processes using Ar, oxygen, and hydrogen as plasma gases were reported for Au(acac)Me_2 [357]. They are summarized in Table 4.14a.

The striking difference to thermal CVD data of Table 4.14 is that deposition temperatures down to room temperature gave pure gold films. Also of note is that Ar plasma achieved the purest gold films while oxygen plasma was not effective. Adding hydrogen and oxygen together in the plasma improved the metal content again.

4.4.4. ALD

ALD reports using β-diketonate gold(III) complexes are not available to the best of our knowledge. As discussed for platinum and palladium metal ALD in Section 3.3.4, this could be due to the fact that molecular oxygen and hydrogen cannot dissociatively adsorb on gold, which was a prerequisite for the self-limiting adsorption and combustion surface reactions creating Pt-O* adsorption sites and volatile CO_x. In the same manner, the dissociative adsorption of molecular oxygen and hydrogen into atomic oxygen and hydrogen is required for the self-limiting adsorption and reduction surface reactions creating Pd-H* adsorption sites and volatile Hhfac for palladium ALD, see Section 3.3.4. respectively. Hagen et al. [27] also pointed out in their review on metal ALD that thermal stability of these precursors was problematic.

4.4.5. Fundamental surface and gas phase studies

Fundamental studies for this class of compounds have been reported only for Au(acac)Me_2 condensed as thin layer on a Ag foil or an amorphous carbon substrate held at −113 °C [112]. This temperature prevented the adsorption of H_2O which is relevant because electron irradiation in presence of H_2O is known to cause removal of carbon [347]. In line with the substantial amounts of remaining carbon found in FEBID with Au(acac)Me_2 (see Section 4.4.2.), decomposition of the precursor by electron irradiation at 520 eV led to a change of the Au:C:O stoichiometry from 1:7:2 to 1:6:0.8 [112]. H_2, CH_4, and CO as well as smaller quantities of C_2H_6 were monitored as volatile products in ESD while larger species indicative of desorption of the acac ligand were not observed. According to XPS, Au was reduced to the metallic state indicating that the metal was embedded in a dehydrogenated carbon matrix. The conversion was studied at electron energies between 40 eV and 1500 eV and was most rapid at 175 eV. However, due to the lack of gas phase studies on the electron-induced fragmentation of Au(acac)Me_2, insight into the underlying initial dissociation channels does not exist so far.

Notably, a higher C:Au ratio of 2.9 was observed in the deposit, when deposition was performed in a steady state experiment in UHV by leaking Au(acac)Me_2 onto a substrate held at room temperature and decomposing the precursor under the 3 keV electron beam of an AES [113]. This indicates that more of the ligand material has desorbed in this case and may relate to the lower surface density and shorter residence time of decomposition products as compared to the experiment under cryogenic conditions [112]. These two effects counteract the crosslinking of the ligands under electron irradiation. Note also that deposits produced from Au(acac)Me_2 could be converted to pure Au in UHV according to XPS by sequential treatment with atomic oxygen to combust the

Table 4.14
Summary of CVD data. The abbreviation RT stands room temperature.

compound	T precursor	T deposition	pressure	gases	film composition	ref.
Au(acac)Me_2	RT	300 °C	0.67 mbar	Ar	85 at.% Au	[356]
Au(tfac)Me_2	RT	300 °C	0.67 mbar	Ar	>99 at.% Au	[356]
Au(hfac)Me_2	RT	300 °C	0.67 mbar	Ar	>99 at.% Au	[356]

Table 4.14a
Summary of plasma CVD processes. The abbreviation RT stands for room temperature.

compound	T precursor	T deposition	pressure	power density	gases	film composition	ref.
Au(acac)Me_2	RT	25 °C	0.25 mbar	0.22 W/cm^2	Ar	100 at.% Au	[357]
Au(acac)Me_2	RT	200 °C	0.25 mbar	0.13 W/cm^2	Ar	100 at.% Au	[357]
Au(acac)Me_2	RT	75 °C	0.25 mbar	0.13 W/cm^2	O_2	40 at.% Au	[357]
Au(acac)Me_2	RT	30 °C	0.25 mbar	0.33 W/cm^2	O_2, H_2	94 at.% Au	[357]

carbon content and atomic hydrogen that removed remaining surface oxygen species and returned the Au to 100% back to the metallic state [114].

4.5. Au(III) and Au(I) complexes with small ligands

4.5.1. Introduction

Following an intuitive paradigm in focused electron beam induced deposition, precursors with as small as possible ligands and as little as possible carbon may lead to deposits of higher purity. Therefore, inorganic compounds may be attractive alternatives compared to the carbon-rich β-diketonates.

One interesting inorganic candidate is trifluorophosphine (PF_3) as it is an excellent donor–acceptor ligand (cf. also Section 3.1.1.) PF_3 makes metal complexes even more stable than the corresponding carbonyls [1]. The inorganic precursor chlorido(trifluorophosphine)gold(I), $AuCl(PF_3)$ has a vapour pressure of 10^{-4} mbar that is sufficient to sublime at room temperature [358]. Unfortunately, this complex is light sensitive and unstable in air. This holds also true for the alternative precursor chlorido(carbonyl)gold(I), AuCl(CO) that has similar appearance and properties [359] containing carbon only in the carbonyl group. Therefore, it should not be dried under vacuum as the loss of the thermodynamically stable CO is facile and promotes decomposition of the material [360].

Sacrificing the strict limitation to inorganic ligands, the stability of the gold complexes may be improved by replacing phosphine and carbonyl groups with methyl groups. Three of such organometallic compounds were investigated regarding their potential for electron beam induced deposition, namely di-μ-chlorido-bis[dimethylgold(III)], $Au_2Me_4(\mu\text{-}Cl_2)$, methyl(trimethylphosphine)gold(I), $AuMe(PMe_3)$, and chlorido(dimethylsulfide)gold(I), $AuCl(SMe_2)$ [361].

Recently, isocyanides were introduced as ligands to replace carbonyls and phosphines what may realize a sufficient stability while being volatile enough for use in FEBID. Isocyanides are isoelectronic with carbonyl, but are also stronger σ-donors relative to CO and PF_3 [113]. The investigated trifluoromethyl alkylisocyanide complexes $Au(CF_3)(CNMe)$ and $Au(CF_3)(CN^tBu)$ have sublimation onset temperatures of 51 °C and 39 °C, respectively at 0.17 mbar. Thermal decomposition sets in at 80 °C for the $Au(CF_3)(CNMe)$ and at 126 °C for the $Au(CF_3)(CN^tBu)$ [113]. Note that several similar Au precursors with small ligands have been evaluated for their volatility but not yet tested in any deposition process [362].

The properties of gold precursors in this section are collected in Table 4.15; their structural formulae and available vapour pressure data are summarized in Fig. 4.13.

4.5.2. FEBID

$AuCl(PF_3)$ was the first inorganic gold precursor that was successfully employed for electron beam induced deposition. Due to its instability, precursor loading of the gas-injection system had to be carried out under an inert atmosphere. Apart from that, no special care was taken to avoid carbon contamination. Still, the deposition of pure gold crystals could be demonstrated (cf. Fig. 4.14) [352,372]. Even vertical growth could be demonstrated [352], although the shape flexibility and fidelity was limited due to crystal formation and possibly thermodynamic effects like Ostwald ripening upon beam-induced substrate heating.

In the same manner, the carbonyl complex AuCl(CO) allowed for the deposition of pure gold (cf. Fig. 4.14) [359]. Here, the vapour pressure was so large, that the precursor had to be used at a reduced temperature of 9 °C. The gas flow in the vacuum chamber is dominated by the release of CO with the precursor pressure being only 0.05 % of the total pressure. However, the beam-induced dissociation of the carbonyl complex was extremely efficient, becoming apparent by the occurrence of tiny gold particles tens of microns away from the primary beam [359].

The investigation of the gold(III) complex $Au_2Me_4(\mu\text{-}Cl_2)$, and the gold(I) complexes $AuMe(PMe_3)$ and $AuCl(SMe_2)$ started by determining their composition in high vacuum by EDX spectroscopy [361]. The complex $Au_2Me_4(\mu\text{-}Cl_2)$ is volatile subliming in vacuum at room temperature with a determined composition showing some excess carbon and silicon grease from the synthesis. A similar behaviour is observed for $AuMe(PMe_3)$. In contrast, $AuCl(SMe_2)$ does not sublime but the smallest crystals decompose to pure gold upon electron beam impact suggesting it may be a promising candidate for electron beam induced deposition [361].

In the following FEBID experiment, the $Au_2Me_4(\mu\text{-}Cl_2)$, $AuCl(SMe_2)$, and $AuMe(PMe_3)$ complexes show a very different deposition behaviour under electron beam impact (cf. Fig. 4.14) [361]. $Au_2Me_4(\mu\text{-}Cl_2)$ leads to successful deposition with a gold content of 29–41 at.% being largest for higher beam currents. The chlorine is removed almost completely and the grainy structure for the higher beam current of 0.4 nA resembles the one obtained from the inorganic precursors. In contrast, no gold is found in deposits from $AuCl(SMe_2)$. This is consistent with the X-ray photoelectron spectroscopy (XPS) results on condensed precursor where no gold signal could be detected either. Most probably, the precursor molecules are not volatile and thermally decompose in the crucible under release of SMe_2 and Cl_2. Finally, $AuMe(PMe_3)$ proves successful for FEBID with a gold content in the range of 19–25 at.% independent from the beam current in the range of 0.1–13 nA and a smooth surface of the deposit. However, some oxygen is detected in the deposit, most probably arising from oxidation of the air-sensitive PMe_3 ligands [361].

A recent surface science study of $Au(CF_3)(CNMe)$ and $Au(CF_3)(CN^tBu)$ [113] investigated the deposition in UHV under steady state conditions in an Auger spectrometer. In case of $Au(CF_3)(CNMe)$, electron beam induced deposition with a beam energy of 3 keV results in 22 at.% gold, similar to that of the commercial precursor $Au(acac)Me_2$ when being used for deposition under the same conditions. The obtained gold content from $Au(CF_3)(CN^tBu)$ is 14 at.%. Table 4.16 summarizes the obtained deposited compositions in relation to the precursor stoichiometries of the studied Au complexes.

Table 4.15
Properties of Au(I) and Au(III) complexes with small ligands. The abbreviation nf stands for 'not found' and RT for room temperature.

compound	phase	appearance	melting point	sublimation point (T, p)	decomposition	stability in air/light	ref.
$AuCl(PF_3)$	solid	white/colourless	nf	RT (CVD)	45 °C	air, light sensitive	[363,364]
AuCl(CO)	solid	colourless	247–253 °C	RT, HV	253 °C	unstable	[360,365,366]
$Au_2Me_4(\mu\text{-}Cl_2)$	solid	nf	nf	RT, HV	nf	unstable in HV	[361]
$AuMe(PMe_3)$	solid	nf	70–71 °C	53 °C, 1.3 mbar	130 °C	stable in HV	[361,368-370]
$AuCl(SMe_2)$	solid	off-white	160 °C	nf	ca. 100 °C (TGA)	unstable	[113,369,371,372]
$Au(CF_3)(CNMe)$	solid	colourless needles	65 °C	51 °C	80 °C	unstable	[113,369]
$Au(CF_3)(CN^tBu)$	solid	white	nf	39 °C	126 °C	unstable	[113]

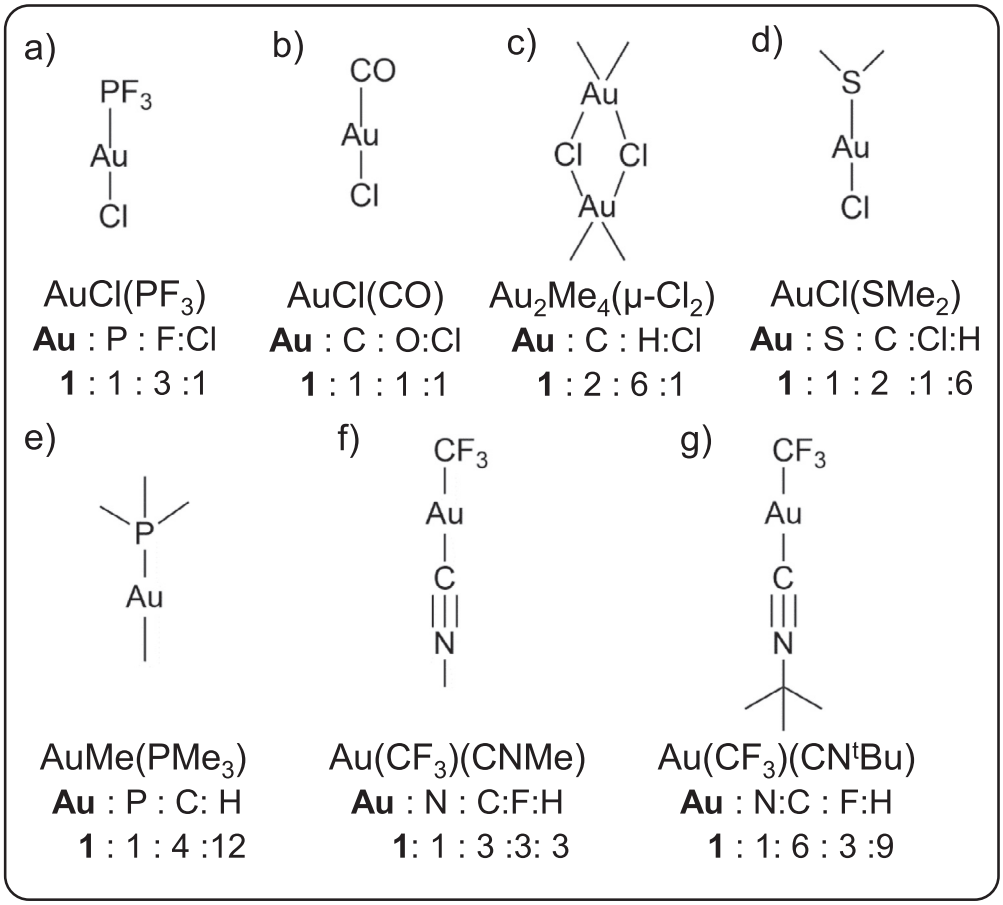

Fig. 4.13. Structural formulae and atomic ratios of Au(I) a), b), d) to g) and Au(III) c) complexes with small ligands.

4.5.3. CVD

Gold metallic thin-film deposition using $AuCl(PF_3)$ was conducted on SiO_2/Si (thermal 100 nm of SiO_2 on Si(100) wafers) and Ta/TaN/SiO_2/Si substrates. During deposition experiments, the precursor was kept at room temperature, while the substrate temperature was 200 °C and the total pressure in the reactor was held at 0.27 mbar. Electron spectroscopy for chemical analysis (ESCA, same as XPS) revealed that this film contained C, O, Cl, F,

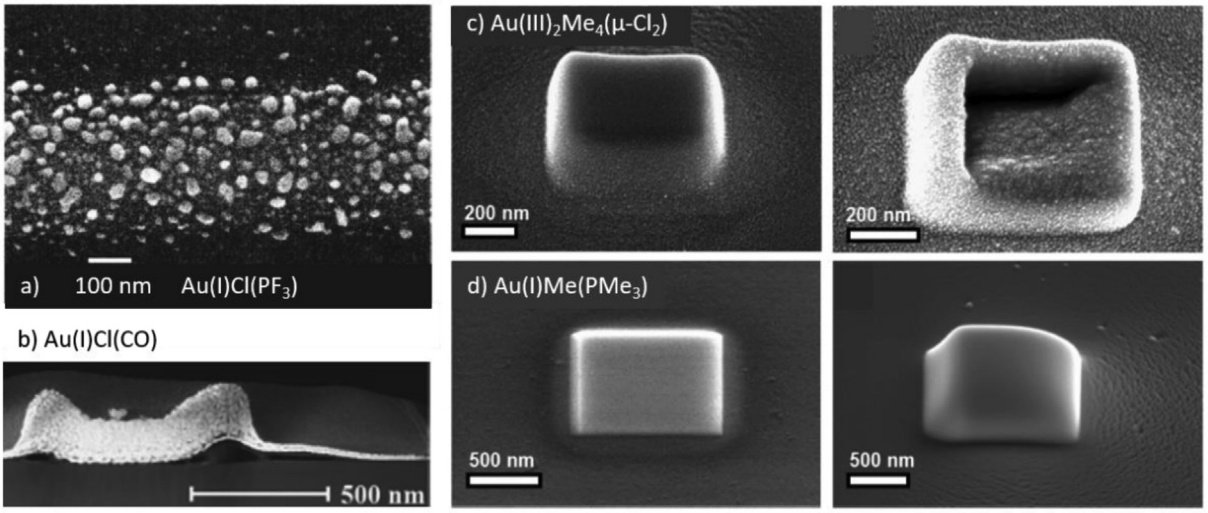

Fig. 4.14. Scanning electron micrographs of successful electron beam induced depositions using small ligand gold complexes a) $AuCl(PF_3)$, reprinted with permission from Utke et al. [352], copyright (2000), American Vacuum Society. b) AuCl(CO) reproduced from Mulders et al. [359] © IOP Publishing. Reproduced with permission. All rights reserved. c) & d) $Au_2Me_4(\mu\text{-}Cl_2)$ and $AuMe(PMe_3)$ [361] deposited with beam current of 0.1nA (left) and a higher current of 0.4nA for $Au_2Me_4(\mu\text{-}Cl_2)$, and 1.6nA for $AuMe(PMe_3)$ (right). Adapted with permission from [359] copyright (2014) American Chemical Society.

Table 4.16
Normalized atomic ratios of gold precursors with corresponding *as-grown* deposit compositions and with the *as-grown* deposit metal content. The arrow terms read "atoms in precursor $\xrightarrow{e^-}$ atoms in FEBID material". Hydrogen is excluded as it was not quantified in any of the studies. *From the given range the highest gold contents together with the lowest carbon contents are taken.

Au complex	Au	C	O	F/Cl	P/N	Au at.%	ref.
$AuCl(PF_3)$	1	0→0	–	3/1→0	1→0	100	[352]
AuCl(CO)	1	1→<0.05	1→0	1→0	–	>95	[359]
$Au_2Me_4(\mu\text{-}Cl_2)$	1	2→1.3	–	1→~0.15	–	41	[361]*
$AuMe(PMe_3)$	1	4→2.2	0→~0.2	–	1→~0.6	25	[361]*
$Au(CF_3)(CNMe)$	1	3→2.8	0→<0.05	3→0.04	1→0.6	22	[113]
$Au(CF_3)(CN^tBu)$	1	6→5.7	0→<0.07	3→0	1→0.4	14	[113]

and P near the surface. Nevertheless, a single argon ion sputter was sufficient to completely remove these impurities, leaving essentially pure Au metallic film [364].

For the CVD of the $Au(CF_3)(CNMe)$, the reactor with the reservoir containing the gold complex has been warmed to 60–70 °C and the glass or silicon substrate was held at 260 °C. The volatile by-products were identified as C_2F_6, MeNC, and MeCN. Analysis of the film by XPS, after argon ion sputtering, showed that the film contained > 99 % gold with <1 % carbon impurity and no detectable impurities of fluorine or nitrogen. The low catalytic activity of gold in this process was confirmed [373].

For the $Au(CF_3)(CN^tBu)$ compound no application in the classic CVD method was found.

The CVD data is summarized in Table 4.17.

4.5.4. ALD

Good purity gold films with > 90 at.% Au were achieved with a three precursor ALD process employing $AuMe(PMe_3)$, oxygen plasma, and water at around 120 °C (close to the thermal decomposition of the gold precursor at 130 °C) [374]. The water was needed to remove the P_2O_5 reaction product converting it into volatile phosphoric acid H_3PO_4. No ALD growth was observed for $AuMe(PMe_3)$ with molecular hydrogen, hydrogen plasma, molecular oxygen, and ozone, because these were not reactive enough below the thermal decomposition temperature.

Adsorption studies of $AuMe(PMe_3)$ on SiO_2 at 100 °C [375] showed many surface reaction species, gold(III) trimethylphosphine, reduced gold phosphine, trimethylphosphine oxide, and graphitic carbon. The coverage of $AuMe(PMe_3)$ on SiO_2 was measured to about 10 % of all available hydroxyl sites and attributed to steric hindrance by the molecule. The authors further hypothesized that the role of the oxygen plasma was to complete oxidation of any surface phosphine ligands. The water takes two roles, forming volatile H_3PO_4 which desorbs, as well as to create some hydroxyl surface groups on the growing gold surface to continue growth.

4.5.5. Fundamental surface and gas phase studies

The design of precursors for Au with small ligands has been discussed extensively in previous reviews [6,7] and in recent original work [113,361]. In contrast, fundamental insight into their electron-induced chemistry is relatively sparse. While a library of precursors, namely $Au_2Me_4(\mu\text{-}Cl_2)$, $AuCl(SMe_2)$, $AuCl(PMe_3)$, and $AuMe(PMe_3)$ has been synthesised and their sublimation or decomposition behaviour in vacuum has been characterized by XPS and MS [361], the electron-induced decomposition was not investigated by these techniques. However, a study of DEA to $AuCl(SMe_2)$ has very recently appeared [376].

In addition to the deposition experiments under steady-state conditions at room temperature (see Section 4.5.2.), the electron-induced decomposition of $Au(CF_3)(CNMe)$ was also studied with XPS by condensing a thin layer of the precursor onto graphite and Au substrates held at -148 °C and exposing them to increasing doses of 500 eV electrons [113]. While charging effects hampered a detailed analysis of the composition, the data confirmed that decomposition predominantly leads to loss of F indicating again that C-F bond cleavage is the dominant fragmentation pathway in the adsorbate. Notably, mass spectrometry both in positive and negative ion mode gave evidence of a stronger fragmentation in the isolated molecule. In positive ion mode, loss of CF_3 was the dominant channel for $Au(CF_3)(CNMe)$ while a fragment $[AuCN + H]^+$ was the most intense signal in the case of $Au(CF_3)(CN^t\text{-}Bu)$ pointing to additional loss of an olefin deriving from the ^{t}Bu group. The alkyl group was lost in the predominant fragmentation channel in negative ion mode for both precursors [113]. It is likely that in the adsorbate, radicals produced by loss of F reacted with the triple bond of the CN unit of an adjacent $Au(CF_3)(CNR)$ leading to a polymerization reaction that produces a strongly crosslinked and thus non-volatile material.

5. Evaluation of precursor and process performance

This chapter will summarize the findings of the previous chapters and attempt to illustrate relations across the different precursors discussed above. To see tendencies more clearly, this chapter will discuss ten more compounds used in FEBID for metals of Ru, W, Pb, Co, Fe, Ir, and Rh to include carbonyl, halogen, and alkyl ligands. Hydride compounds of semimetals will not be included (neopentasilane Si_5H_{12} [377,378], Ge_2H_6 [379]) as the FEB deposited materials were not measured for their hydrogen content (however, judged pure due to formation of nanocrystals). For these and more carbonyl compounds, we refer to a recent review by Barth et al. [35]. Fig. 5.1 summarizes the ranges of metal atomic content obtained in FEBID as detailed in the tables of the previous FEBID sections and table S1 from the supporting information. It shows a large scatter in the experimental FEBID metal content data that we attribute to the wealth of additional reactions sometimes (obscurely) involved in FEBID. Minimum metal content data shown in Fig. 5.1 were obtained without extra stage heating, modest beam currents below a few hundred picoampere, and mostly for flat planar deposits on well heat and electrically conducting substrates. The latter is important for efficient dissipation of heat and charge

Table 4.17
Summary of CVD data. For Au(CO)Cl, $Au_2Me_4(\mu\text{-}Cl_2)$, $AuMe(PMe_3)$, $AuCl(SMe_2)$, and $Au(CF_3)(CN^tBu)$ no CVD was performed. The abbreviation RT stands for room temperature.

compound	T precursor	T deposition	pressure	gases	film composition	ref.
$AuCl(PF_3)$	RT	200 °C	0.27 mbar	H_2	>99 at.% Au	[365]
$Au(CF_3)(CNMe)$	60–70 °C	260 °C	$1.3{\cdot}10^{-2}$ mbar	vacuum	>99% Au	[374]

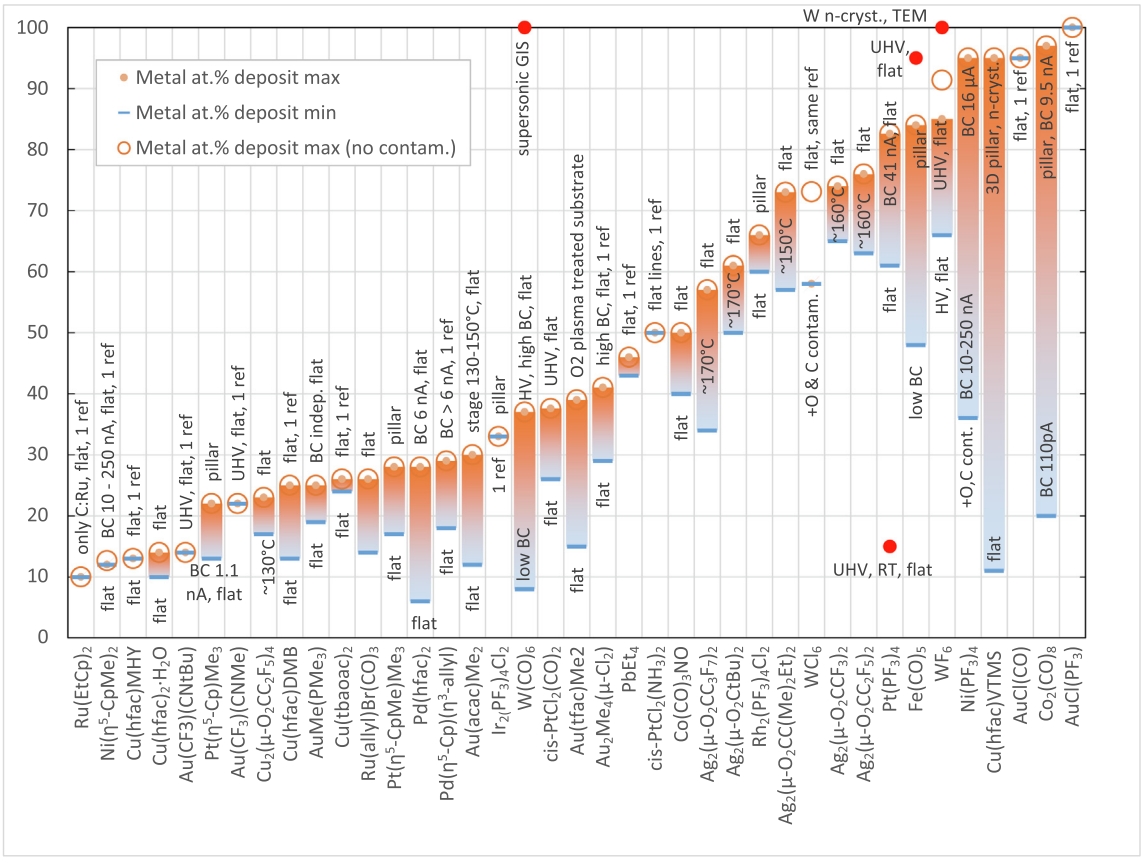

Fig. 5.1. Summary of FEB deposit metal content ranges obtained with various precursors. The data is arranged in the order of increasing maximum metal content. The lowest values usually refer to flat deposits and to heat and charge dissipating substrates. The highest values were obtained under conditions that often involve pillar structures, high beam currents (BC), or UHV conditions. No range signifies that only one reference (1 ref) was available giving one value. Circles indicate the metal content without chamber or substrate contamination (e.g. O and C in deposits of WCl_6 and WF_6). The red points signify non-typical FEBID conditions.

implanted by the focused electron beam. Native oxide, doped silicon as the typical substrate in most FEBID experiments fulfills these demands. The maximum metal content values include mostly exceptions to the previous list of conditions - stage heating, UHV, 3D pillars, TEM membranes, and high beam current. The three latter conditions entail a heat accumulation due to restricted heat dissipation (3D vs. 2D and 1D) and increased implanted power, respectively. Individual legends of the data points detail these conditions.

The formation of a deposit in FEBID is a complex chemical transformation that comprises multiple reactions, both electron-induced and thermal. These reactions depend not only on electron beam parameters such as electron energy, current density, dwell time, and others, but also on the nature of the surface on which a given precursor is adsorbed and on the presence of other molecular species during the deposition process. Overall, the process comprises first the adsorption of the precursor on a surface which is typically the growing deposit, then an electron-induced fragmentation reaction, and finally the desorption of the fragmented ligands or concurrent reactions that convert this material to non-volatile residues. An overview of these elementary processes is given in Fig. 5.2 which also attempts to categorize their possible outcomes with respect to the aim of producing a pure metal deposit. These elementary processes constitute the outline of this section. First, the precursor adsorption process is discussed in Section 5.1. This aspect has not been comprehensively considered in FEBID research so far and knowledge gained from CVD and ALD processes can provide some inspiration and guidance. Section 5.2 discusses the actual electron-induced fragmentation and its dependence on the design of the precursors. This has received considerable attention previously and we refer the reader to the earlier reviews [5-7,35,94]. Here, we widen the scope to energetic arguments that drive fragmentation as well as to the role of temperature on precursor fragmentation, which is particularly relevant to some of the less volatile compounds. In Section 5.3 we consider the fate of ligands or fragments and discuss their desorption from the surface as well as chemical reactions that counteract this desired volatility of the organic material. In addition, we emphasize the mechanisms of reactions with process gases that can assist the deposition process. Overall, we thus aim at inspiring novel strategies towards the development of optimized processes in the world of thermal and non-thermal mechanisms governing FEBID.

5.1. Molecule adsorption: non-dissociative versus dissociative

When a precursor adsorbs on a surface, it will be bound either by intermolecular forces, a process which is named physisorption and is non-dissociative, or it will establish stronger bonds to the surface through chemisorption which is often a dissociative adsorption process. During chemisorption, ligands can dissociate from the metal atom and the fragments establish new chemical bonds to the substrate. The FEBID process ideally requires precursor molecules to adsorb in a physisorbed state because dissociative adsorption on the underlying surface would counteract the spatial selectivity of deposition. There are two exceptions. (i) The chemisorption is self-limiting after one (or very few) monolayers as employed in ALD so that further non-selective growth without

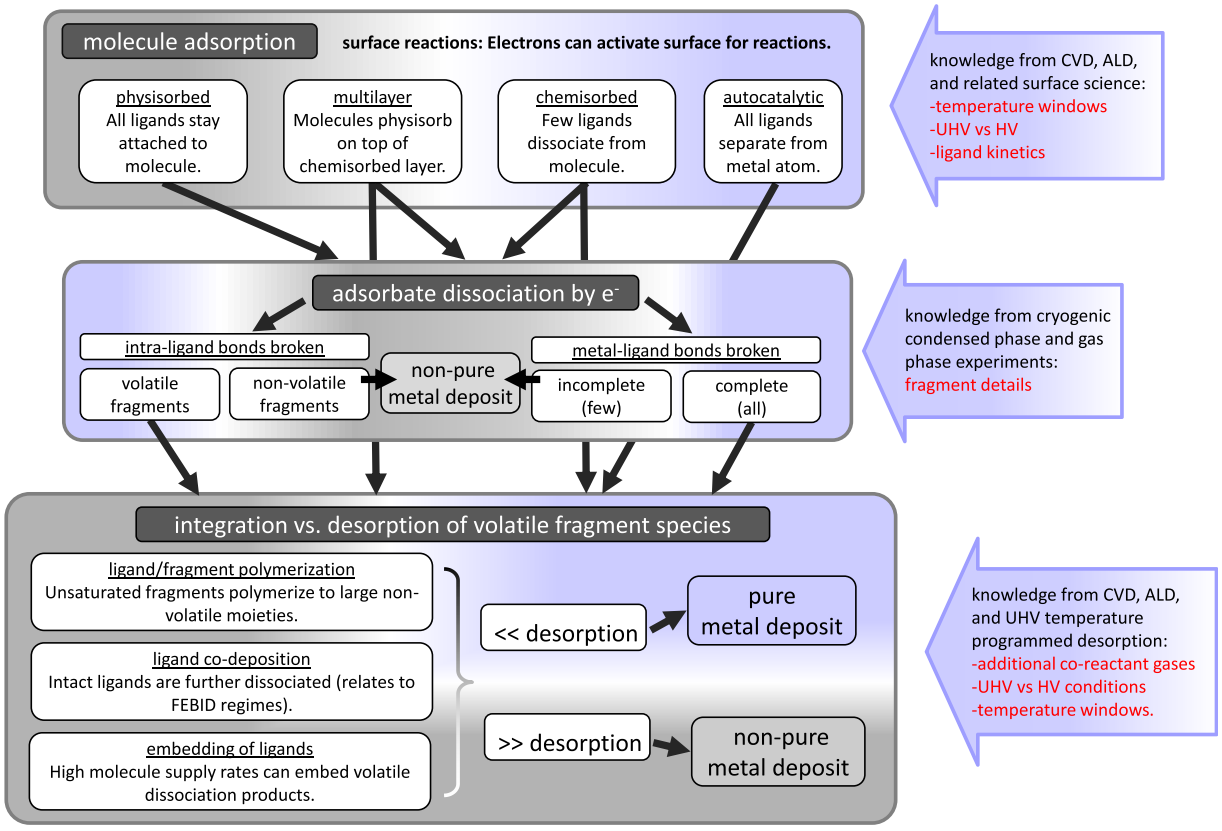

Fig. 5.2. Overview of mechanisms and reactions that a precursor molecule can endure during the electron-induced deposition process. Note that molecule adsorption and fragment desorption depend strongly on the composition and coverage of the *growing* surface. Depending on the time scale of volatile fragment desorption, incorporation reactions may dominate the final FEBID material purity. The blue shading intends to illustrate the potential of each mechanism for clean metal deposits.

electron irradiation is suppressed (these first monolayers can be removed by gentle etching after FEBID if needed). (ii) Dissociative adsorption occurs selectively on the growing FEB deposit. Dissociative adsorption can occur when the energy required to break part of the bonds in the precursor is balanced or exceeded by the energy gained through formation of new bonds between the resulting fragments and the underlying surface. Therefore, dissociation on reactive surfaces can occur at lower temperatures than dissociation upon uptake of heat in isolated molecules.

5.1.1. Adsorption schemes in FEBID studies

The investigation of adsorption schemes in HV FEBID is rare. Bishop et al. [380] investigated tetraethyl orthosilicate $Si(OC_2H_5)_4$ (TEOS) for FEBID of SiO_2. This precursor is also used in plasma and thermal CVD and in thermal ALD (using NH_3 as catalyst and H_2O at 27 °C) to obtain thin films of SiO_2 [381]. The material composition they obtained by room-temperature FEBID was carbon rich with a ratio of C:O ≈ 0.25 and confirmed results of previous room-temperature studies [382,383]. Their interesting move was to increase substrate temperature into regions were the adsorption type changes (see Fig. 5.3a). Increasing temperature decreased the FEBID rate by an order of magnitude at around 130 °C (see Fig. 5.3b). This is due to the exponential increase in desorption rate with temperature of the physisorbed TEOS molecule. Further increasing the temperature to around 280 °C activated the self-limiting dissociative adsorption of TEOS:

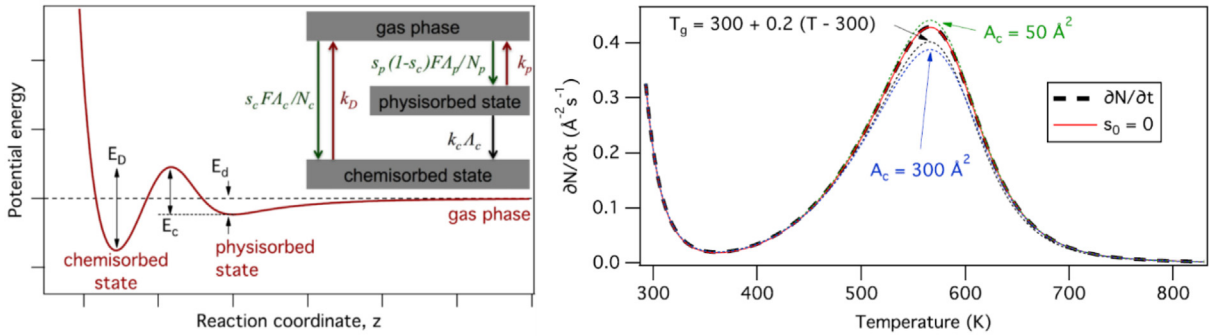

Fig. 5.3. a) Energy levels for physisorption and chemisorption related adsorption (green) and desorption (red) terms. Note the energy barrier E_c between the physisorbed and chemisorbed state and their varying desorption energies E_d and E_D. b) FEBID rate variation with temperature. The peaks at room temperature and 297 °C correspond to physisorption and chemisorption schemes, respectively. Reprinted with permission from Bishop et al. [380] copyright (2012) by the American Physical Society.

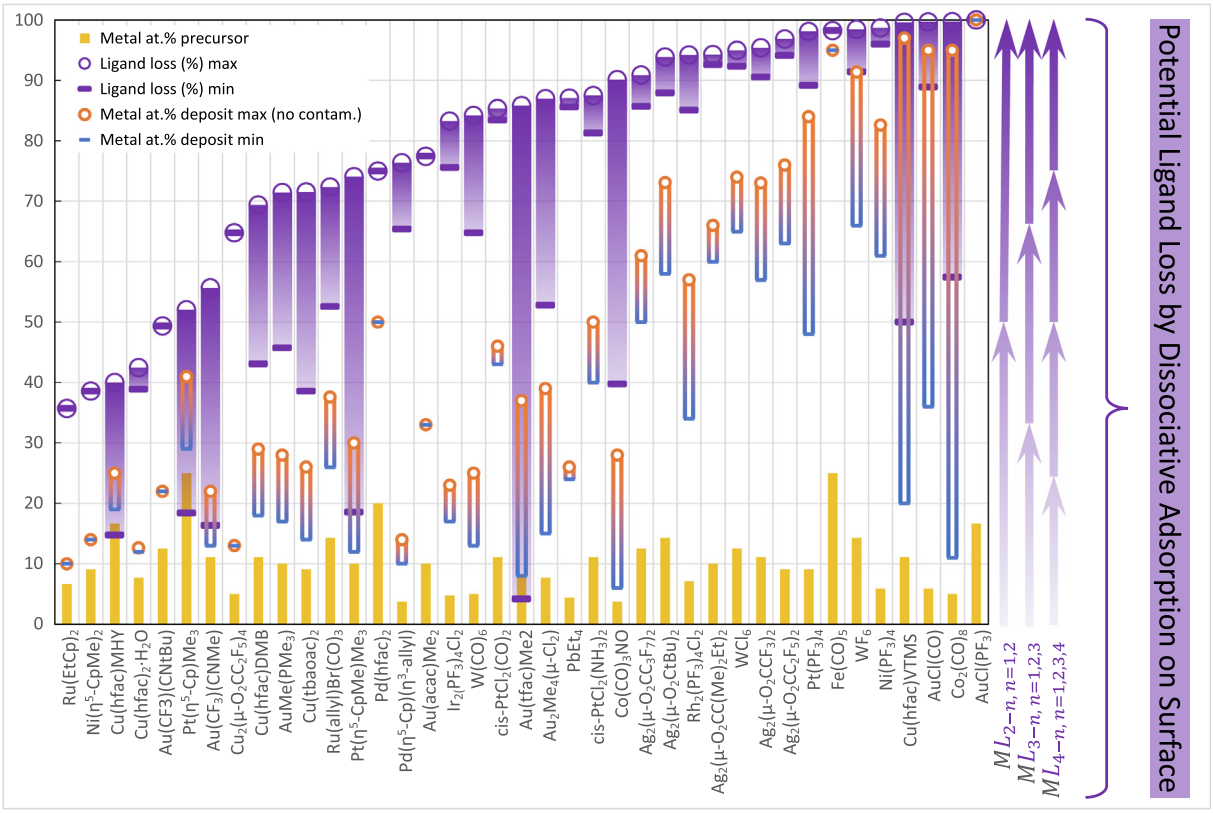

Fig. 5.4. Summary of ligand loss range derived from FEBID experiments (purple bars). Right side: The potential contribution of thermal dissociative surface adsorption is exemplified for homoleptic precursors ML_m with m one atom ligands (M is the metal, L the ligand atom) when they release n ligand atoms. For heteroleptic precursors and multi-atom ligands, the number of elements leaving per ligand modifies the loss (arrow length). Yellow bars signify the metal content in the pristine precursor and framed bars the metal content ranges observed in the FEB deposit.

SiO_2*+ $Si(OC_2H_5)_4$ → SiO_2-$Si(\text{-}OC_2H_5)_{4-x}$* + $x(OC_2H_5)$ in the irradiated area, where the asterisk denotes the surface species and x signifies the number of removed ethoxy ligands upon surface adsorption, varying between 1 and 2. This surface reaction would self-limit at approximately one adsorbed monolayer without any second reactant. The role of the second reactant was taken by the electrons as in the irradiated regions an increase of FEBID rate by again an order of magnitude was observed. The material deposited at this temperature was much cleaner with a ratio of C : O ≈ 0.05 (carbon reduction by a factor of 50) indicating an efficient-desorption of electron-triggered dissociation fragments in addition to the removal of the ethoxy ligands by thermally stimulated dissociative adsorption. The second role of the electrons was to activate the surface for dissociative adsorption. Further increasing the temperature to 530°C again decreased the FEBID rate by an order of magnitude, probably due to the exponentially increased thermal desorption rate of the intermediate $Si(\text{-}OC_2H_5)_{4-x}$ compared to the electron induced dissociation reaction leading to non-volatile SiO_2.

The partial removal of the organic ligands by dissociative chemisorption and their thermal desorption can in fact be helpful in improving the deposit purity as long as the temperature is low enough to suppress complete thermal dissociation (CVD). The carbon content of a chemisorbed FEBID "precursor" is always lower than in its physisorbed state, compare to Figs. 2.4.a & b. However, electron irradiation conditions must be also tuned such that the dissociated ligands desorb readily instead of being co-deposited by further intra-ligand dissociation through the electrons. The higher temperature naturally involved in (partial) dissociative chemisorption plays in favor of high desorption rates of thermally produced ligands as well as of the volatile electron-triggered dissociation fragments.

Fig. 5.4. illustrates how thermal dissociative adsorption on the surface would potentially contribute to increase the metal content of the adsorbed species by ligand loss prior to electron beam irradiation (arrows). The ligand losses ΔL were obtained from the calculated initial atomic metal content x in the metal–ligand precursor molecule M_xL_{1-x} and the published atomic metal contents y in the metal-"ligand" deposit M_yL_{1-y} as $\Delta L = (y - x)/((1 - x)y)$. Here, x and y are atomic fractions <1. The wide span of ligand losses for the same molecule observed for FEBID in Fig. 5.4 indicates that thermal reactions may have played, so far yet unnoticed, a role in specific FEBID conditions or deposit shapes. This may not only include the adsorption mechanisms summarized in Fig. 5.2 but also the thermal desorption of ligands which will be discussed in Section 5.3. Fig. 5.4 also includes the related metal content range (same as in Fig. 5.1) and the metal content in the pristine molecule. It highlights that for many molecules impressive ligand losses are in fact observed for FEBID. Yet, one remaining ligand or just one atom of that last remaining ligand reduces the metal content already down to considerably smaller 50 at.% or 50 at.%, respectively. It is an astounding fact that ligand losses are impressively high for many molecules. One needs to investigate what makes the last ligand, ligand fragment or ligand atom to stay on the surface and what inhibits them leaving the metal atom just like their former companion ligands and atoms did.

Multilayer adsorption in the FEBID process was theoretically studied by Sanz-Hernandez et al. [84]. The difference to monolayer adsorption (Langmuir scheme) is shown in Fig. 5.5 where the

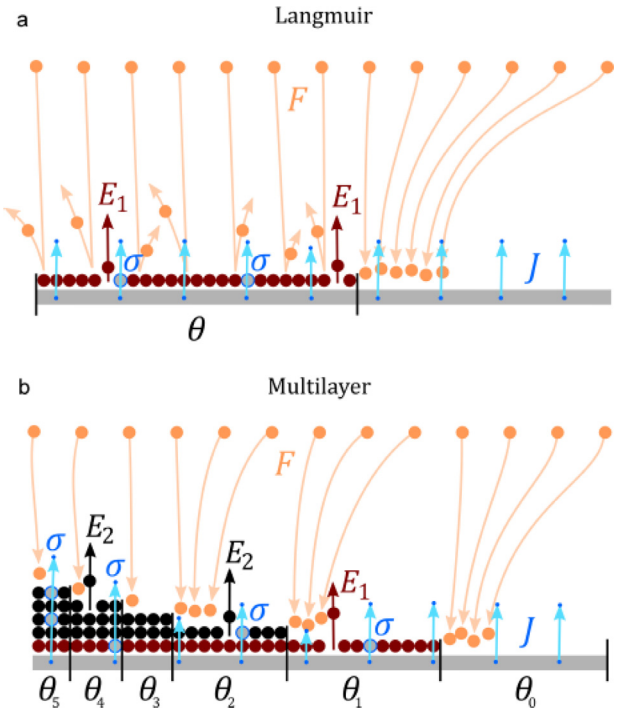

Fig. 5.5. Langmuir (a) vs. multilayer adsorption (b). The light blue colored circles signify electron-induced dissociation events within the first layer (red circles) and the multilayers (black circles). Note that volatile dissociation fragments in buried multilayers need to diffuse towards the surface before desorption. Orange circles denote impinging gas molecules and dark blue points emitted secondary electrons (primary electrons were omitted). For symbols see Sanz-Hernandez et al. [84] from which this figure was reproduced, CCBY license, Beilstein-Institut.

adsorption is illustrated with varying numbers of multilayers. This type of adsorption can be described within the Brunauer-Emmett-Teller (BET) [83] framework. The situation shown in Fig. 5.5. resembles in principle the situation in studies of condensed phase described in chapters 3 and 4, except that temperatures now reflect room-temperature conditions prevailing typically in FEBID of flat materials. We recall that condensed phases or multilayers imply that volatile electron-induced reaction products may stay buried instead of desorbing and thus may react with their vicinity neighbor moieties. This may include catalytic reactions within the film around free metal centers (including autocatalytic decomposition of the adsorbed precursor layers yielding pure metal deposits) or polymer forming reactions of reactive ligand fragments (yielding carbon rich deposits), see Section 5.3 for more details.

Autocatalytic reactions in FEBID in the sense of precursors self-decomposing into metal and volatile ligands upon contact with the same metal were invoked for $Co_2(CO)_8$, AuCl(CO), $Fe(CO)_5$, and $AuCl(PF_3)$ [1]. Such reactions require that an initially pure metal surface is created by FEBID. The situation then resembles more correctly a selective (local) autocatalytic CVD yielding high metal content with the deposit shape driven by mass transport considerations and thermal reaction schemes instead of FEB control. This was indeed observed for cauliflower structures with $Co_2(CO)_8$ [384] and for "baseball bat" structures with $Fe(CO)_5$ [385] showing facetted metal nanocrystals. To regain shape control by electron-induced reactions, the local heat generated in the interaction volume by the electrons depending on the beam current, energy, and beam size must be dissipated efficiently.

5.1.2. Insights from ALD and CVD

ALD and CVD by nature rely on dissociative adsorption of molecules on surfaces. They result in metal-rich material and their thermal reactions are thus attractive concepts to include into FEBID, provided the shape control of electron-induced reactions is not compromised. The temperatures and gas additives reported in the CVD and ALD sections in chapters 3 and 4 may be adapted to a certain degree into FEBID approaches to obtain purer metal structures. However, care must be applied not to lose the spatial selectivity.

In CVD, the growing hot metal surface is often beneficial in lowering the thermal dissociation temperature below the gas phase thermal decomposition temperatures of the molecules (compare tables of the introductory and CVD sections of chapters 3 and 4). A CVD process that leads to autocatalytic growth of pure metal films without the assistance of further process gases can be consulted to identify the temperatures needed to decompose a given precursor in a thermal surface reaction. However, supply of heat from the surface at typical CVD temperatures is not large enough to lead to fragmentation should the growing surface not be catalytically active. To underline this, the average thermal energy per vibrational degree of freedom kT at 300 °C is around 50 meV. Taking $Fe(CO)_5$ as an example, vibrational Fe-CO stretching frequencies as the degrees of freedom that would lead the molecule towards loss of CO are between 400 and 500 cm^{-1}, i.e. 50–70 meV [386]. In contrast, the energy required to dissociate the first Fe-CO bond is around 1.8 eV [387] and thus not in reach by mere statistical influx of heat under CVD conditions.

A prominent example of a molecule for autocatalytic metal HV-CVD and UHV-CVD is $Fe(CO)_5$ with growth temperatures of 100 °C and 25 °C, respectively. Kunz et al. [86] performed iron and chromium CVD experiments in HV at temperatures of 100 °C and 100–300 °C using $Fe(CO)_5$ and $Cr(CO)_6$ and pressures of around $7.5{\cdot}10^{-5}$ mbar and 0.045 mbar, respectively. The activation energies for autocatalytic CVD were determined to be 0.14 eV and 1.06 eV for $Fe(CO)_5$ and $Cr(CO)_6$, respectively, and are considerably lower than the first bond dissociation energies for metal carbonyls ranging from 1.6 to 2.4 eV [86]. Marbach et al. [87] demonstrated selective UHV-CVD for $Fe(CO)_5$ and $Co(CO)_3NO$ at room temperature [388]. $Fe(CO)_5$ resulted in the spatially selective autocatalytic growth of iron metal nanocrystals with high iron purity, while $Co(CO)_3NO$ resulted in granular, oxygen, carbon, and nitrogen-containing material (on iron seeds). Interestingly, both groups used electron beams to initiate the metal CVD growth non-thermally on the surface of a silicon wafer by forming seed nuclei that initiated autocatalytic growth of elemental metal. Of note is the temperature difference needed to sustain autocatalytic CVD with $Fe(CO)_5$: in HV it is 100 °C and in UHV autocatalysis performs at room temperature. As a rule of thumb, a background pressure of $1{\cdot}10^{-7}$ mbar (good HV) corresponds roughly to about one monolayer per second residual gas impinging on the substrate (about 10^{14} molecules/cm^2s). These gases, depending on their residence time until desorption, can occupy the reactive sites on the metal surface and thus prevent precursor molecules from being decomposed by the surface. The residence time is exponentially dependent on temperature. UHV (around > $1{\cdot}10^{-9}$ mbar) was an important prerequisite to produce the clean iron surface at room temperature as it strongly reduced the flux of residual gases onto the surface. Performing CVD in high (and ultra-high) vacuum also eliminates gas interactions and diffusion issues (specifically ligand removal) through the stagnant precursor layer. Absence of these mechanisms leads generally to lower deposition temperatures. High vacuum CVD can deliver important details on the surface reaction kinetics and especially their related time scales. This was exemplified for titanium dioxide deposition using titanium isopropoxide and water [389]. The desorption kinetics of ligands was also studied in a low temperature barium titanate HV-CVD process [390]. It was observed that the surface was passivated by hfac ligands upon

exposure to barium hexafluoroacetylacetonate. These ligands desorbed slowly and blocked adsorption for further precursor molecules. In a FEBID process this mechanism would translate to large carbon content in FEBID material via ligand co-deposition as will be discussed in Section 5.3. Of significant note is that hfac ligands belong to the β-diketonate "family", which constitute a large amount of FEBID precursors discussed in this article. Within this precursor group FEBID metal contents are below 30 at.% with only two exceptions for Cu(hfac)VTMS and Au(tfac)Me_2 which can be attributed to thermal contributions and surface treatments, respectively, see also Fig. 5.1 and the respective FEBID sections for these details.

In ALD, temperatures are lower, so that only a part of the ligands is dissociated while one or several remaining ligands are compulsory to self-terminate the surface reaction towards further molecules arriving from the gas phase. The ALD tables in chapters 3 and 4 give an indication of the minimum temperature needed for (incomplete) thermal dissociative adsorption of the molecule and specify the reactant gas necessary to remove the remaining ligands. The extent to which the electrons can replace the reactant ALD gas efficiently and remove the remaining ligands via electron stimulated desorption needs still to be studied in more detail. Encouraging results were achieved for electron beam assisted ALD were electron-stimulated desorption was integrated as an ALD sequence for certain molecules and materials (Co, Si, and nitrides) as will be discussed in Section 6.3. In addition, initial Pt (C) FEBID seeding for selective Pt ALD [197,199,203] and Ru ALD [391] was shown successful. The systematic integration and study of ALD and CVD schemes into *3D nanoprinting* FEBID, however, is still in its infancy.

For completion we would like to note that room temperature ALD processes are known for highly exothermic reactions, for instance for Al_2O_3 [392] with trimethylaluminum/water and ZnO [393] with diethylzinc/water, witnessing the principal possibility of room-temperature dissociative adsorption. However, these are limited to metal oxides presently.

5.1.3. Insights from surface science adsorption studies

These kinds of studies have often been performed to elucidate thermal mechanisms in ALD and CVD processes and were discussed in the previous related sections. However, they are presently confined to a few molecules and surfaces but fundamental research to this subject is widening as the importance of surface reactions becomes more evident. The energy balance for dissociative adsorption of a given precursor is delicate and depends on the nature of the surface, which implies not only the type of elements that the surface is composed of (see for example [394]) and its atomistic structure such as steps or defects (see for instance [298]). On top of this, co-adsorbed species can interfere with the adsorption of a precursor and drive the reactions to even different products as seen, for instance, when atomic oxygen adsorbed on a Pt surface decomposes Pt(η^5-CpMe)Me_3 in an ALD process [197]. However, depending on the surface temperature, dissociative adsorption may not occur even if it is energetically favourable. This is because the transition from the physisorbed adsorption state to a chemisorbed dissociated state may be subject to an activation barrier which relates to the fact that bonds are broken in order to form new ones [395], see also Figure 5.3. The temperature at which a transition from the physisorbed state to dissociative adsorption occurs depends again on the underlying material (see for example [394]). An example is Cu(hfac)$_2$, which adsorbs molecularly on SiO_2 surfaces at room temperature but dissociatively on metal surfaces above −73 °C [278,293]. Surface analysis of the adsorbate under UHV conditions is required to obtain detailed mechanistic insight and has also been performed for some precursors with respect to ALD (see the respective ALD and surface studies sections in this review). Of note for surface science studies dedicated to metal ALD is that they mostly measure the dissociative adsorption at ALD growth temperature (which is more elevated than for FEBID) and specifically on surfaces treated by the co-reactant. This latter is typically a reducing or oxidizing agent that cleans the metal from the organic ligand to very low contamination levels. Surface catalysis will be more pronounced on clean metals than on FEBID materials that are often contaminated by a carbonaceous matrix up to now, but will be of increasing importance on the way for developing FEBID processes with high metal purity.

On the other hand, surface science experiments dedicated to FEBID usually omit studies on dissociative adsorption of precursors in the absence of an electron beam [103] because it is the physisorbed state that is usually considered relevant to FEBID. Also, for reasons of sensitivity, the studies typically involve multilayer adsorbates that only condense to the surface at cryogenic temperatures. However, even should dissociation of precursor molecules not occur on typical surfaces used in FEBID, the situation can change under electron irradiation. This was demonstrated by the electron beam induced surface activation (EBISA) studies by the Marbach group which have revealed that diverse surfaces ranging from oxides and adsorbed layers of large organic molecules to coordination polymers can be activated by the electron beam to then decompose precursors such as $Fe(CO)_5$ or $Co(CO)_3NO$ [88,89,396]. Such dissociative adsorption may also contribute to the growth of a deposit in FEBID at locations where the electron beam impinges and produces reactive species through activation of the underlying surface. Also, when dissociation of the precursor leads to fragments that are integrated in the deposit, the resulting crosslinked material may become reactivated by the electron beam and react with further impinging precursor molecules. Detailed insight into such surface reactions of FEBID precursors is extremely sparse with rare exceptions mainly from computational chemistry. Here, work has particularly focused on silica surfaces starting from the hypothesis that electron irradiation removes part of the surface hydroxyl groups and the precursors then adsorb dissociatively on the resulting undercoordinated Si sites [397-399]. In contrast, the actual growing FEBID deposit surface is typically highly complex and chemically ill-defined (yet representing the real world situation!) because it often contains carbonaceous matrices or contaminations of other elements as we exemplified in the FEBID sections of this review. Therefore, information on the mode of adsorption on an elemental or even single crystalline metal surface is typically not representative of the situation encountered on a growing FEBID deposit. More detailed surface science studies performed in UHV that focus on the precursor adsorption on a previously formed deposit, also after reactivation by the electron beam, are needed to shed light to these questions and to unravel or to underpin their relation to the reaction mechanisms that underlie ALD.

5.1.4. Vacuum and thermal stability of the precursors

Thermal reactions of a solid or liquid precursor may already occur in the reservoir. Here, dissociation of ligands from the precursor can be driven by formation of new bonds in the reaction products. As a prominent example, transition metal carbonyl complexes such as $Co_2(CO)_8$ and others tend to convert to larger, i.e. multinuclear metal clusters by loss of CO [400]. This conversion is reversible and an increased CO partial pressure drives the equilibrium to the smaller complexes that have a higher CO:metal ratio. However, when CO is pumped off in a vacuum system, the equilibrium shifts towards the larger clusters. As an example, this reaction occurs already at room temperature in the case of $Co_2(CO)_8$ and must be carefully considered for each individual precursor. For instance, the precursor AuCl(CO) also loses CO when placed in vacuum [360]. Similar vacuum stability problems (varying in intensity) are known for AuCl(PF_3), Cu

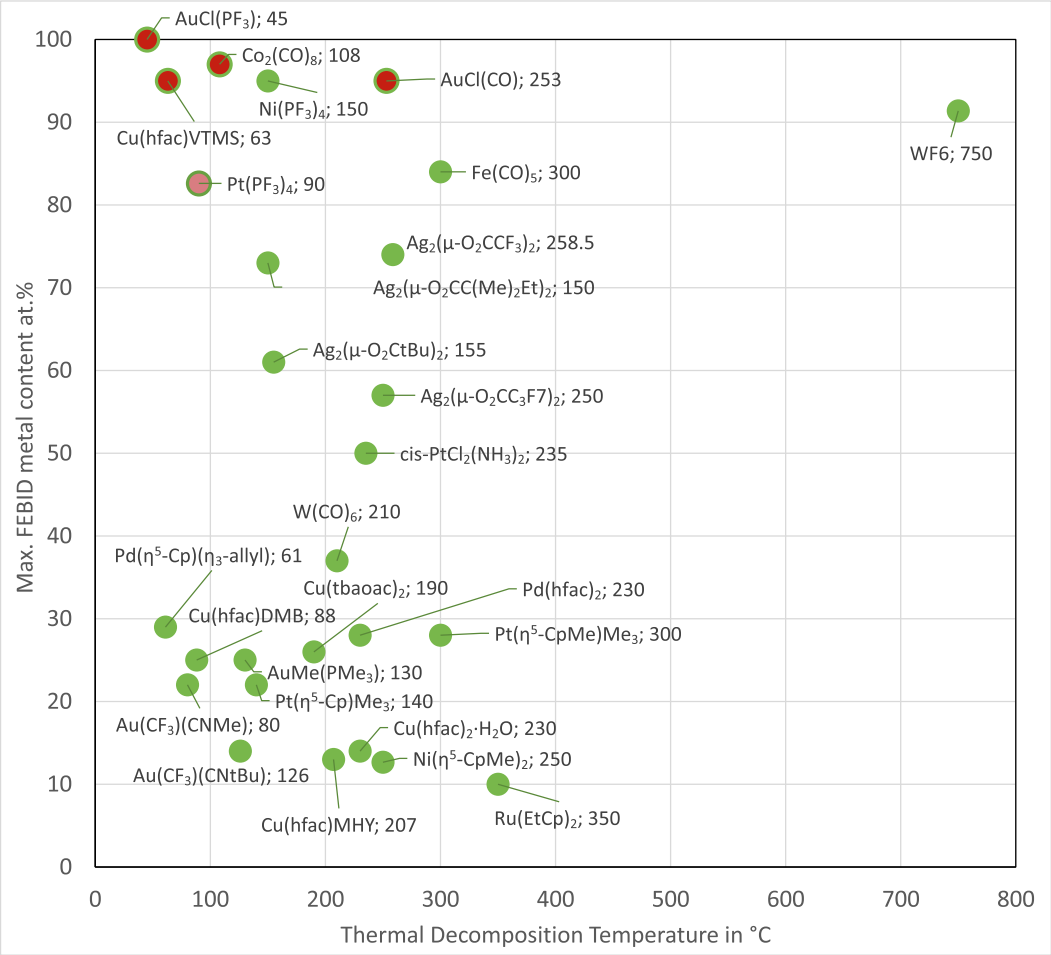

Fig. 5.6. Maximum FEBID metal content vs. thermal decomposition of precursor molecules for which data were available. Red circles mark vacuum instable precursors.

(hfac)VTMS, and $Pt(PF_3)_4$ under moderate heating [139]. Fig. 5.6 shows that these precursors are among the ones which yielded > 90 at.% FEBID metal content.

Fig. 5.6 furthermore shows that there is no correlation between gas phase thermal decomposition temperature (see values in tables of introductory sections in chapters 3 and 4) and metal content in FEBID material. This is due to the role of the surface immanent in any growth process. As discussed in Section 5.1.1, dissociative adsorption is driven by the energy gain that occurs by formation of new bonds with the underlying surface. This renders the dissociation on a reactive surface more favourable than the dissociation of an isolated precursor molecule in the gas phase where it would require an exceedingly high influx of heat by molecular collisions.

5.2. Electron-induced adsorbate dissociation

In contrast to the thermally initiated dissociative adsorption schemes discussed in the previous section, the electron-induced adsorbate dissociation occurs via electronically excited states and is a non-thermal mechanism, which assures the spatial selectivity of FEBID. The initial reaction step on the way to a deposit in FEBID is an electron-induced fragmentation of the physisorbed or potentially partially dissociated adsorbed precursor.

5.2.1. Insights from surface science and gas phase studies

As discussed previously, knowledge of individual electron-precursor interactions as studied in the gas phase is an important starting point to understand the further chemistry that occurs during deposit formation [5,99]. Popular gas phase studies, however, do not capture any intra-fragment reactions, which may consequently happen in the adsorbed state. The initial electron precursor interaction either leads to dissociation of entire ligands from the precursor or, as common in the case of larger ligands, to their fragmentation. In the actual deposit formation on a surface, the fragments released by electron-precursor interaction can interact with other molecular species in their environment or with the surface of the growing deposit in more complex reaction sequences. Surface science studies performed in UHV on the electron-induced decomposition of various FEBID precursors have been reviewed before and we refer to those [6,7,101,103]. The current state of insight into these processes in the case of group 10 and 11 FEBID precursors has been summarized in Sections 3 and 4. We will refer to these studies in the following to discuss underlying principles that govern the performance of particular precursors and FEBID processes. Fig. 5.7 shows a summary of metal contents observed in condensed phase UHV electron irradiation experiments under cryogenic conditions as well as after temperature-programmed desorption (TPD) experiments. Cryogenic studies may capture intra-fragment reactions over proportionally as thermal desorption of certain volatile ligands and fragments is low at these temperatures. Interestingly, the majority of the cryogenic condensed phase metal contents corresponds to the lower range values of metal contents found in FEBID experiments. In reverse, this fact suggests that the lower values of metal ranges correspond

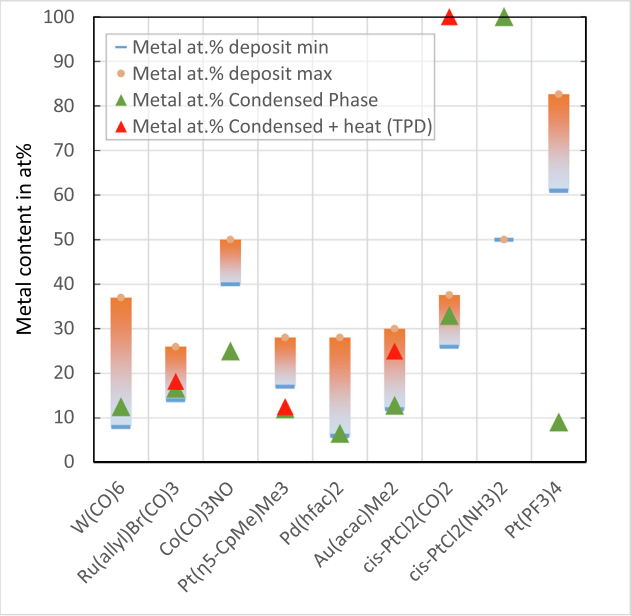

Fig. 5.7. Metal contents obtained from condensed phase electron irradiation studies in comparison to FEBID metal contents (taken from Fig. 5.1). Green triangles symbolize cryogenic conditions and red triangles temperature-programmed desorption (TPD) experiments. See respective fundamental surface studies in chapters 3 and 4 for references.

to non-favourable desorption conditions for volatile ligands or their volatile fragments.

5.2.2. Favorable electron induced dissociation channels and link to thermodynamics

Thermal factors as discussed in the case of dissociative adsorption of precursor molecules (see Section 5.1) can also enhance their fragmentation upon electron-precursor interaction. This does not only result from the fact that bonds are often weakened when a molecule is promoted into an electronic state other than the ground state. In particular, it is important to realize that attachment of an electron to a precursor or its fragments often provides an additional amount of energy on top of the available electron kinetic energy. Fig. 5.8 gives an overview of the relevant energy contributions.

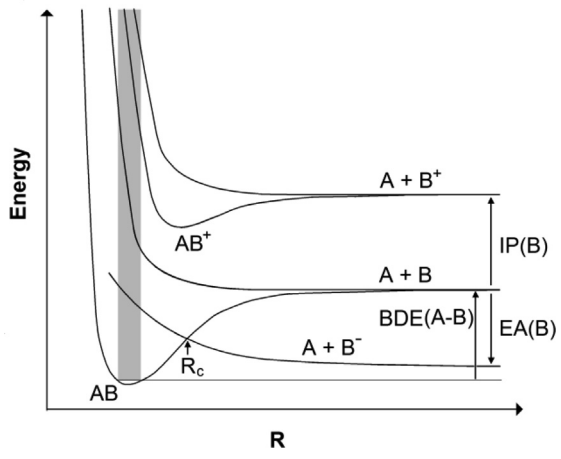

Fig. 5.8. Potential energy diagram for a molecule AB representing a cut through the electronic potential energy surface along the A–B bond direction. Included are typical potential energy curves for bound and unbound states of the neutral AB molecule and the cation, as well as an unbound state of the anion. IP(B) is the ionization potential of the B fragment, EA(B) the electron affinity of B, and BDE(A–B) is the A–B bond dissociation energy. Typical orders of magnitude for these energies are around 10 eV for IP, up to roughly 4 eV but often lower for EA, and a few eV for BDE. Reproduced by permission of The Royal Society of Chemistry from Boehler et al. [33].

A particularly instructive example is the release of CN^- from formamide ($HCONH_2$) and other molecules by DEA [33,401]. This process was observed at electron energies around 2 eV which is surprisingly low considering the extensive amount of energy needed to dissociate four covalent bonds (BDE(C–H) ≈ 4.3 eV, BDE(C=O) ≈ 7.7 eV, and two times BDE(N–H) ≈ 4 eV) as required to release the CN fragment. The low energy threshold for formation of CN^- is only partially explained by the formation of a stronger triple bond between C and N and the high electron affinity of CN (EA(CN) = 3.86 eV), i.e., the energy that is gained when the impinging electron is attached on the CN fragment. In addition, the simultaneous formation of a stable neutral byproduct, H_2O in the case of formamide, out of the dissociated atoms delivers the amount of energy relating to dissociation of two O–H bonds, i.e. an energy of 2 × BDE(O–H). The formation of CN^- at an electron energy around 2 eV is thus explained by the following reaction:

$$e^- + HCONH_2 \rightarrow (HCONH_2)^{\bullet -} \rightarrow CN^- + H_2O + H^\bullet$$

Based on tabulated thermodynamic data, this reaction brings the energy required to form CN^- upon DEA down to 2.33 eV, in close agreement with the experimental result (see [401]). Note that similar considerations also apply to dissociation following electron impact ionization, i.e., dissociative ionization processes. For instance, when propanol ($CH_3CH_2CH_2OH$) is ionized, a fragment $C_3H_6^{\bullet +}$ requires only a few tenth of an eV more energy than the energy IE($CH_3CH_2CH_2OH$) for formation of the parent radical cation, again rationalized by formation of the byproduct H_2O [402].

A particularly large amount of energy is gained when DEA leads to formation of HF as neutral fragmentation product with a bond energy of 5.9 eV. In consequence, DEA to hexafluoroacetylacetone leads to the predominant formation of an ion $[M–HF]^-$ where M stands for the parent molecule [247]. However, by comparing with other fluorinated compounds, it was argued that the molecular structure must allow for an intramolecular approach of the F towards one of the H atoms to enable formation of HF. With F being located in the periphery of a rigid structure, such a rearrangement is not possible in the hfac complexes as shown for the cases $Cu(hfac)_2$ and $Pd(hfac)_2$ [247].

As noted in a very recent review [35], a thermodynamic driving force was also suggested as reason why $Cu(tbaoac)_2$ performed better than β-diketonates in CVD [261]. In contrast to acac, tfac, and hfac ligands and as a result of the ester linkage, the tbaoac ligand may undergo bond rearrangement that leads to stable and volatile small molecules, among them the particularly stable CO_2. This probably contributes to the facile decomposition of the complex.

The examples suggest a strategy towards the design of good precursor molecules for FEBID. This strategy should aim at a structure that can form thermodynamically favourable decomposition products under electron irradiation that are, at the same time, volatile enough to exhibit a high desorption rate. The high metal content observed in FEBID with Ag carboxylates (see Section 4.3 and Fig. 5.1) is probably related to this effect. As was shown in fundamental studies on non-volatile carboxylates of Cu(II), namely, copper oxalate (CuC_2O_4) and the metalorganic framework HKUST-1 (a coordination polymer consisting of Cu(II) dimers bridged in 3D by a trivalent benzene carboxylate), electron irradiation leads to highly efficient desorption of CO_2 [105,403]. This can be rationalized by a mechanism in which ionization of the carboxylate group leads to cleavage of the C–C bond between the carboxylic group and the carbon chain of the ligand according to

$$R\text{-}CO_2^- + e^- \rightarrow R\text{-}CO_2^{\bullet} \rightarrow R^\bullet + CO_2.$$

If the radical R• is a hydrocarbon fragment, it may stabilize subsequently by expulsion of atomic hydrogen to again exhibit a reducing action on the metal.

We note that thermodynamic effects may also contribute to the retention of fluorine in deposits obtained from $Cu(hfac)_2$ [246] or $Cu_2(\mu\text{-}O_2CC_2F_5)_4$ [324] in contrast to the results for $Ag_2(\mu\text{-}O_2CC_2F_5)_2$ [329] (see Section 4.3). The standard enthalpy of formation for solid CuF_2 is more than twice as large as for solid AgF (–542.7 kJ/mol vs. –204.6 kJ/mol) [404]. This may drive the incorporation of F in the deposit as was seen in XPS measurements in the case of $Cu(hfac)_2$ [246]. As pointed out recently [35], the lower thermodynamic stability of the metal fluoride phases of Pd and Pt as compared to Cu can also explain why F^- is incorporated in a deposit produced from $Cu(hfac)_2$ but not in the case of the analogous precursors $Pd(hfac)_2$ and $Pt(hfac)_2$ [246].

5.2.3. Thermal assistance of electron-induced dissociation

By definition, a chemical reaction that occurs in the electronic ground state of a system is considered as thermal reaction. In a FEBID process, the electron-induced precursor fragmentation is a non-thermal reaction. However, a number of thermal reactions can occur during all other steps involved in deposit formation.

As discussed in Section 5.1, the purely thermal dissociation of a precursor requires high temperatures. In contrast, as summarized in Section 5.2.2, electron-induced bond dissociation via non-thermal pathways is accessible at ambient temperature and may even be energetically more favourable than thermal reactions. This fact was used recently in electron-enhanced ALD to grow nitrides and cobalt films at low process temperature, see Section 6.3. Furthermore, the temperature can have a pronounced effect on electron-induced dissociation processes [405]. A strong effect is expected in the case of DEA where a dissociative anion state can cross into the manifold of vibrational states in the neutral ground state, see Fig. 5.9. The transition from the ground state to the anion potential energy curve upon electron attachment occurs vertically, i.e., upon preservation of the ground state bond length. This is related to the fact that electron attachment is much more rapid than the atomic movement. Consequently, the anion state is populated with a bond length that corresponds to the position where the amplitude of the vibrational wave function of a given level is maximal via transitions indicated by the red vertical arrows. The system then evolves down the anion potential towards increasing bond length and thus dissociation. As a concurrent process, the electron can detach again bringing the molecule back to the ground state. This, however, can only happen as long as the critical bond length R_C has not been exceeded. Beyond this point, the anion state lies below the ground state so that energy would be needed to detach the electron.

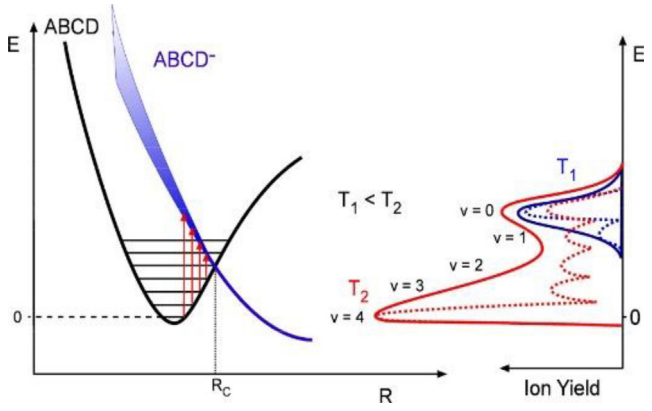

Fig. 5.9. Schematic potential energy curves for the neutral ground state (ABCD) and a repulsive anionic state ($ABCD^-$) and of transitions between them by electron attachment. The red vertical arrows indicate the transition to the anionic state at threshold for the lowest vibrational levels. The resulting DEA intensities are shown schematically on the right side for two different temperatures. A strong effect can occur when higher vibrational levels become thermally populated as described by the Boltzmann equation when the relative position of ground and anion state is appropriate. The distance between vibrational levels varies between a few ten meV up to around 400 meV, depending on the type of molecular vibration. While many such levels must be excited to reach the dissociation threshold thermally in the ground state, only a few vibrational levels may need to be populated to observe an increase of DEA cross section. Reprinted from from Bald et al. [405] with permission from Elsevier.

In the situation depicted in Fig. 5.9 increasing the temperature has a pronounced effect on the fragmentation via DEA. When higher vibrational levels are populated, electron attachment occurs at lower electron energies as seen from the decreasing length of the red arrow. Also, the anion potential energy curve is reached nearer to R_C. This increases the probability that the anion survives beyond this distance leading to a higher DEA cross section. However, when the vibrational energy is too high, a transition to the anion curve is not possible anymore and the DEA cross sections will drop. This effect has not yet been investigated in FEBID precursors so that we refer to the examples of molecules discussed in [405]. However, as large precursors typically also have DEA processes occurring at near-thermal energies [5], an effect of the temperature on the fragmentation probability should be considered. Note that this effect must be carefully distinguished from temperature dependences that occur through thermal reactions of labile surface intermediates that result from the initial electron-induced precursor fragmentation. This latter process was discussed in detail, for instance, for the case of $Pt(PF_3)_4$ where a higher deposit purity at higher temperature was observed and ascribed to thermal decomposition by loss of further PF_3 from surface-bound $Pt(PF_3)_3$ intermediates [130].

5.3. Integration versus desorption of ligands or ligand fragments

In this section we turn to the mechanisms which compete with desorption of the ligands or ligand fragments that were formed as a result of thermal surface reactions (see Section 5.1) or of electron induced dissociation reactions (see Section 5.2). This aspect is crucial as it will finally decide about the purity of FEBID material, which underwent complete metal–ligand dissociation and/or dissociation of ligands into volatile fragments, compare to Fig. 5.2. Desorption of entire ligands following electron-induced dissociation of a precursor is the most desirable case, however, differs for various ligand types (charged vs. neutral, light vs. heavy, tendency to polymerize). Firstly, due to Coulomb and polarization forces charged ligands, like $CpMe^-$, Cp^-, $allyl^-$, CH_3^-, CF_3^-, $acac^-$, $tfac^-$, $hfac^-$, RCO_2^-, and also simple F^- and Cl^-, interact more strongly with their surrounding material than neutral ligands, such as PF_3, CO, NH_3, VTMS, DMB, MHY, CNR, SMe_2, and PMe_3. Consequently, they have a much lower tendency to desorb [108]. Secondly, ESD experiments on different FEBID precursors observed that light species have a higher probability to desorb at a given temperature while heavier dissociation products are usually not detected [6,7,103]. Thirdly, ligands may be dissociated either by a catalytically active surface or under the impact of the electron beam to produce reactive species that bind to the growing deposit and even induce further reactions, for instance, crosslinking of organic ligand material.

Overall, the ability of ligands or their fragments to desorb depends on the combination of the metal to be deposited, the nature of the ligands, as well as the structural details of the growing deposit, properties that are intimately linked to each other. Added process gases open up more reaction pathways that can have a favorable effect on deposit purity. By relating to results from ALD and CVD where appropriate, we discuss typical chemical reactions

for different types of ligands that can be anticipated in the growing deposit following an initial electron-induced dissociation (see Section 5.3.1) as well as the influence of process or residual gases on the deposit (see Section 5.3.2).

5.3.1. Deposit formation without added reactants

Intuitively, one can expect that desorption should be most efficient for small, neutral ligands. Regarding the precursors discussed herein, CO, PF_3, but also NH_3 are the most prominent examples of this type of ligand. CO, in particular, is an outstanding model compound in surface chemistry and its adsorption, akin to the binding in the carbonyl complexes, has been studied on various metal surfaces [406]. Already in this well-investigated case, the interaction with an underlying material, i.e., the binding strength and thus the temperature at which desorption will occur is challenging to predict for a deposit produced from FEBID that may not be crystalline but contains a lot of defects and impurities. The same applies to other ligands. A simple example reveals the problem. While PF_3 desorbs from a single crystal Pt(111) surface at 150 °C, it requires temperatures of 350 °C to desorb from a polycrystalline Pt surface on which defect sites exist, where the adsorbate typically binds more strongly than on a smooth surface [115]. Note also, that dissociative adsorption may occur in particular for ligands or ligand fragments generated by electron-induced dissociation (see for example the wealth of data on CO in [406]). Therefore, a detailed atomistic picture of how the precursor fragments are adsorbed on a realistic model of a deposit would be required to make precise predictions. This has been tackled only rarely so far, see for example [398].

Despite the potential variations in binding strength to a growing FEBID deposit, CO is a prime example of a ligand that is easy to desorb by electron irradiation [6,7,103]. In contrast, small anionic ligands desorb much less efficiently. The example of cis-$PtCl_2(CO)_2$, where removal of Cl^- required a much higher electron exposure than desorption of CO illustrates this effect most clearly (see Section 3.4.5). Small anionic fragments may also result from fragmentation of larger ligands. In the case of the different M $(hfac)_2$ complexes (M = Pt, Pd, Cu), XPS and ESD results led to the conclusion that F^- was released by DEA but retained in the deposit in significant amounts only in the case of Cu$(hfac)_2$ [246]. This indicates a larger binding strength of F^- to the deposited Cu and consequently a lower desorption probability than is the case for Pd and Pt, as discussed in terms of thermodynamic stability of the resulting solid in Section 5.2.2.

In the case of the large anionic ligands acac, tfac, and hfac, desorption is even more difficult to achieve. These ligands have a certain tendency to dissociate from the complex as such, both in dissociative adsorption on metal surfaces, where the ligand then coordinates to the surface metal, and upon DEA (see Section 4.1.5). The adsorbed ligands then require elevated temperature beyond the typical working range in FEBID to detach from the surface and to be converted to volatile species [407]. Furthermore, it has been reported that CH_3 fragments tend to react with protonated Hacac, thus leading to less volatile organic residues [408]. These processes rationalize the large amount of carbon remaining in the FEBID deposits when using precursors with acac and related β-diketonate ligands. This is a typical example of how surface and side reactions of fragments resulting from electron-induced dissociation can compromise the purity of a deposit. The contrary situation as encountered, for instance, in $Pt(PF_3)_4$, where thermal treatment can desorb further PF_3 ligands from a surface bound Pt $(PF_3)_3$ intermediate resulting from electron-induced dissociation of the first ligand from the complex (see Section 3.1.5 and [130]).

The higher desorption efficiency of the neutral ligand CO in FEBID as compared to ionic ligands does not necessarily translate to larger neutral ligands. The CVD data reveal that, due to a facile disproportionation reaction, Cu(hfac)L complexes with neutral ligands L = VTMS, DMB, MHY have a lower thermal decomposition temperature than Cu$(hfac)_2$ (see Sections 4.1.3 and 4.2.3). However, this does not lead to an increased purity of deposits in FEBID (Sections 4.1.2 and 4.2.2). First, if disproportionation should proceed at the lower FEBID process temperature, the resulting Cu $(hfac)_2$ probably again has a substantial residence time and its fragmentation will again be incomplete. Second, it is known that ionization of organic molecules with double bonds can lead to polymerization as shown in Fig. 5.10. We propose that such reactions can also be initiated in the double or triple bonds of the neutral ligands VTMS, DMB, and MHY, thus contributing to the formation of less volatile species that become integrated in the deposit. They very likely also play a role in the case of CNR ligands as used in Au(I) precursors that yield very low losses of carbon in FEBID (see Section 4.5).

The widely used cyclopentadienyl ligands Cp and derivatives as well as allyl$^-$ are also notorious for producing carbonaceous deposits. While an electron-induced reaction as proposed in Fig. 5.10 is conceivable in the neutral protonated form (see Section 5.2), an electron-induced C–H bond cleavage leading to cross-linking between the ligands is also a very likely scenario that contributes to the retention of ligands in deposits produced from cyclopentadienyl precursors. The H recombines to desorb as H_2, as was in fact observed during electron irradiation of Ni(η^5-CpMe)$_2$ (see Section 3.2.5 and [103]). Such a reaction is known from self-assembled surface monolayers of biphenylthiol and other aromatic molecules where they yield a mechanically extremely stable carbon layer [409].

As noted in Section 5.2.2, the thermodynamic stability of dissociation products can drive a surface or electron-induced reaction in a specific direction. In the case that these stable products are highly volatile, they should desorb easily to yield a deposit with high purity. Although CVD using Cu$(tbaoac)_2$ yields only 74 at.% of Cu content (see Section 4.1.3), it performs surprisingly well in FEBID despite its bulky ligands (see Section 4.1.2). Along the same line of argumentation, the efficient decomposition of carboxylate precursors relates to the expulsion of CO_2 under electron irradiation (see also Section 5.2.2). In the case of the Ag carboxylates, high purity is achieved even for a carbon rich side-chain as encountered in $Ag_2(\mu\text{-}O_2CC(Me)_2Et)_2$ (see Section 4.3.2). The hydrocarbon group of the ligand remains behind as radical $Et(Me)_2C^\bullet$ when CO_2 is released. As a reactive species, it may recombine with other radicals to yield a volatile species (like e.g. octane derivatives) or to

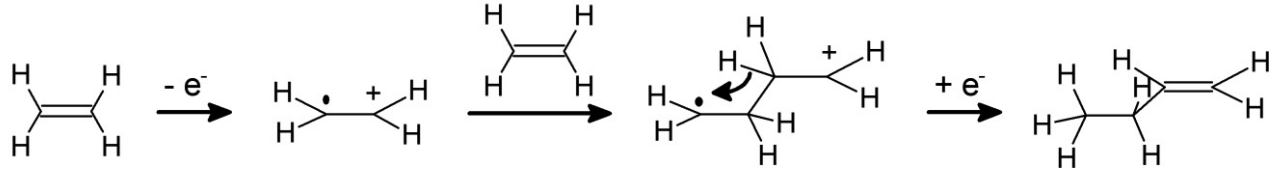

Fig. 5.10. Single step of a polymerization reaction of an organic molecule with a double bond initiated by electron impact ionization. The cation is attracted to the electron-rich double bond of a second molecule leading to bond formation. This reaction can be terminated by recombination with a thermal electron followed by energy dissipation (last reaction) or it can continue [259]. All polymerization products are less volatile and will lead to larger carbon contents in FEBID material.

yield a less volatile material. However, in the absence of such a reaction partner, it may also convert to a stable volatile hydrocarbon molecule by loss of atomic H, whereby a new double bond is formed, and desorb from the deposit. We propose that this may be the case at sufficiently low precursor coverage and electron flux, a hypothesis that nonetheless requires further experimental verification.

We note as a final comment that it is also conceivable that volatile species can be embedded in a deposit due to high precursor flux. In this case, a post-treatment with higher temperature should volatize these species.

5.3.2. Deposit formation in presence of added or residual gases

In CVD, gases are often added to enhance the deposition process. In particular, molecular hydrogen (H_2) is used as a reducing agent in thermal CVD. It can be activated when it adsorbs dissociatively on the growing surface to yield atomic hydrogen. The effect in the reaction is twofold: (i) metals that are contained in a precursor in a positive oxidation state can be reduced to the elemental form when atomic hydrogen transfers its electron to the metal and (ii) the resulting H^+ can protonate negatively charged ligands L^- to convert them to more volatile neutral species HL. This anion protonation is the most straightforward approach to transform them to neutral compounds such as HCp, Hhfac, Htfac, Hacac, Htbaoac, HCl and thus weakens their interaction with the surface leading to a higher desorption rate. Of importance is that atomic hydrogen is available on the surface. At elevated temperatures, the metal surface can act as catalyst for the dissociative adsorption of molecular hydrogen into adsorbed atomic hydrogen according to $H_2 \rightarrow 2\,H_{ads}$. This concerns mostly the CVD and ALD reactions for metal β-diketonates and cyclopentadienyl complexes discussed in the previous chapters. As ALD performs at lower temperature, where the catalytically driven dissociative adsorption of H_2 performs less efficiently on some metal surfaces, hydrogen plasma needs to be employed. Note that hydrogen would also be needed to convert ionic ligands or fragments of intraligand dissociation reactions such as CH_3^- or CF_3^- into neutral species.

Atomic hydrogen prepared by passing H_2 over a heated filament has also been used for post-deposition purification of FEBID deposits (see Section 3.4.5). However, the purification efficiency was shown to depend on the type of precursor [246,257]. While atomic hydrogen was not effective in removing carbon from deposits produced from Pt(η^5-CpMe)Me_3, Pt$(hfac)_2$, and Pt$(PF_3)_4$ (in the latter case carbon must stem from impurity gases), Cl was efficiently removed from deposits produced by electron irradiation of Pt$(CO)_2Cl_2$. This difference is related to the different nature of the deposit. In FEBID, Pt(η^5-CpMe)Me_3 yields deposits that contain elemental Pt particles, i.e., metal that has already been reduced by the electron beam, a reaction that is not possible in CVD. This results in a crosslinked carbonaceous matrix which is not cracked by atomic hydrogen. In contrast, Pt$(CO)_2Cl_2$ yields the ionic material $PtCl_2$ by loss of CO. In this case, atomic hydrogen reduces the Pt to its elemental form and the resulting H^+ converts Cl^- to volatile HCl. Note that these reactions have been discussed in depth in [257].

Insight from ALD shows that instead of atomic hydrogen, atomic oxygen is needed to convert carbonaceous materials to volatile oxidized species such as CO_2 and CO (see Section 3.2.4). This is in fact a thermodynamically favourable conversion [257] although the elemental nature of the metal is decisive for the success of this process which may be accompanied by oxidation of the metal. As studied in depth for the case of Pt ALD from Pt(η^5-CpMe)Me_3, O_2 dosed onto a pure Pt surface adsorbs dissociatively to produce surface-bound atomic oxygen (see Section 3.2.4). This atomic oxygen, which is a very reactive species, then oxidizes the ligands of subsequently dosed precursor to remove them completely. In analogy, atomic oxygen delivered from an atom source onto a surface has been used for the purification of FEBID deposits [246,257]. However, it was shown that while both carbon and fluorine are etched away from deposits produced from Cu$(hfac)_2$, Cu was also oxidized during atomic oxygen treatment. This required for an additional atomic hydrogen step to reduce the metal back to its elemental state. FEBID processes that use either co-dosing of O_2 [121] or post-deposition purification by electron irradiation in the presence of O_2 [178,410] very likely also rely on the action of atomic oxygen. Here, electron-induced fragmentation can contribute to the dissociation of O_2 besides dissociative adsorption on the growing deposit. However, again, the conditions are harsh and often lead to oxidation of the metal. These examples show that the range of metals that are not oxidized by atomic oxygen is limited to noble metals Pt and Au [170]. In addition, oxides of Ag can be reduced to elemental Ag by mere electron irradiation [411]. Overall, we can conclude that thermodynamic arguments regarding potentially formed metal oxides are important to predict the outcome of a purification process that applies oxygen either as O_2 or directly as atomic oxygen.

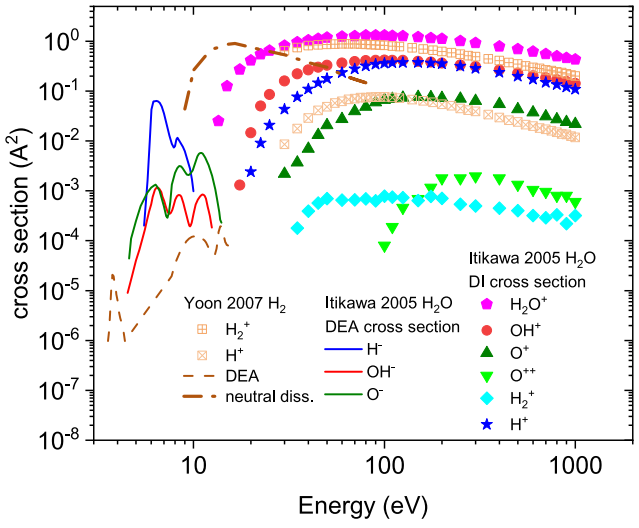

Fig. 5.11. Electron induced dissociation of gaseous H_2O and H_2 as function of electron energy [412,413].

Atomic hydrogen is also produced by electron triggered dissociation of H_2. However, the residence time of molecular H_2 on a surface is probably very short (non-polar molecule) which would entail a low hydrogen dissociation rate and hence low formation rate of atomic hydrogen. Locally generated atomic hydrogen via the focused electron beam would be very helpful in establishing surface reactions leading to locally cleaner metal deposition. Atomic hydrogen was exploited in several metal ALD plasma processes, see the ALD sections in chapters 3 and 4, as well as in a few metal plasma CVD processes with $Cu(hfac)_2$ and $Au(acac)Me_2$ [188,189,280-283,357], discussed in the related CVD sections. When using hydrogen plasma, generally film growth could be performed at lower temperature sometimes including room temperature.

In contrast, H_2O as dipolar molecule adsorbs strongly in comparison to H_2 and contributes to the chemical reactions in FEBID. H_2O is not only particularly relevant because within most SEMs high vacuum conditions prevail and about half of the background residual gas is composed of water molecules. The diffusion constant of water on hydrophilic surfaces is roughly one order of magnitude larger than diffusion constants of typical precursors. Hence, the efficient diffusive replenishment of water will result in an overabundance of water molecules during FEBID [35]. The cross sections for electron-induced dissociation of gas phase H_2O [412] is shown together with data for H_2 [413] in Fig. 5.11. As a side-product to the charged fragments represented in Fig. 5.11, neutral atomic hydrogen is also produced in these gas phase processes. However, when H_2O aggregates, as will typically occur on surfaces, or can interact with precursor molecules, the reaction channels are altered. Under these conditions, ionization through electron impact induces predominantly an intermolecular proton transfer according to $H_2O^{+\bullet} + H_2O \rightarrow H_3O^+ + OH^\bullet$ [414] or, when an anionic ligand is involved, to $H_2O^{+\bullet} + L^- \rightarrow HL + OH^\bullet$. Similarly, when H^- or $O^{\bullet-}$ are formed by DEA, they will react according to $H^- + H_2O \rightarrow H_2 + OH^-$ and $O^{\bullet-} + H_2O \rightarrow OH^\bullet + OH^-$ [415]. Therefore, electron irradiation in adsorbed H_2O yields not only H^+ as needed for conversion of ligands to the protonated neutral form but several reaction channels open up that yield $OH^\bullet$ radicals which are again oxidizing reagents. Both $H_2O^{+\bullet}$ as well as $OH^\bullet$ radicals can add, for instance, to double bonds in a carbonaceous structure which is the first step that eventually leads to conversion of the carbon content to CO [107]. These reactions are relevant to the chemistry that underlies the purification of FEBID deposits produced from Pt(η^5-CpMe)Me_3 by electron irradiation in presence of H_2O [163]. The same types of reactions are likely to be involved also in other cases such as the deposition of Au by co-dosing of $Au(tfac)Me_2$ and H_2O [347]. Note, however, that proton transfer to yield HL (HMeCp in the case of Pt(η^5-CpMe)Me_3) will not lead to volatile species anymore once the ligands have been transformed to a crosslinked carbonaceous structure. Protonation may thus only be considered as a possible contribution in a process that simultaneously dosed the precursor and an excess of H_2O.

The implication for precursor design from the protonation's point of view would be to design metalorganic molecules which contain water, like the hydrate $Cu(hfac)_2{\cdot}H_2O$ (see Section 4.1), which would act as built-in proton donor when activated by an ionization event. However, as visible from Fig. 5.11 and discussed for Pt(η^5-CpMe)Me_3, reactive oxygen species and the $OH^\bullet$ radicals produced by electron-induced proton transfer from $H_2O^{+\bullet}$ can also oxidize the metal. This oxidation was very pronounced for nickel FEBID which resulted in nickel oxide FEBID although there was no oxygen contained in the precursor molecules but incorporated from the background residual gas in the SEM chamber at 10^{-6} - mbar, (see Sections 3.1.2 and 3.2.2). However, for the more noble metals Au and Pt, oxidation (or combustion) of remaining carbon residuals in the deposit via electron irradiation and reaction with H^2O or O_2 does not lead to metal oxidation as exemplified by the cases of Pt(η^5-CpMe)Me_3 [163] (see Section 3.3) and $Au(tfac)Me_2$ [347] (see Section 4.4).

Beside these fragmentation reactions that may be enhanced even by residual H_2O in the SEM chamber, there are always competitive ligand-codeposition reactions occurring such as intraligand dissociation (see Fig. 2.4) and ligand or ligand fragment polymerization, for example. When the rate of such ligand co-deposition reactions is comparable to or larger than the desorption rate of the ligands then ligand elements will be incorporated in the FEB deposited material. For instance, even if proton transfer from ionized H_2O to a CpMe ligand would yield a volatile CpMeH molecule, this latter contains double-bonded carbon which makes it prone to undergo polymerization when it becomes itself ionized under electron impact before it can desorb (see also Section 5.3.1).

An electron-induced proton transfer or release of atomic hydrogen is also relevant for NH_3 present as ligand in cisplatin (*cis*-$PtCl_2(NH_3)_2$, see Section 3.4). In this case, both reactions contribute to the complete removal of Cl during electron irradiation [104]. NH_3 acts as the ideal case of a reducing agent integrated in the precursor architecture although it is not favourable with respect to volatility. It would be desirable to identify alternative ligands that can act as a source of hydrogen under electron irradiation but do not exhibit this latter disadvantage.

5.4. Implications for precursor design

As detailed in the previous sections of this chapter, there is large potential for FEBID of pure metals moving away from room temperature and HV condition typically applied and adapting temperature and additional gas schemes from CVD and ALD. Many surface science aspects would change accordingly, as a cleaner growing metal surface will imply different interactions with the adsorbates, including precursor and fragments.

Fig. 5.12 illustrates that the number of successful high metal content FEBID processes under HV and room temperature conditions is very small. Reproducible, operator independent, high metal contents > 90 at.% are so far limited to FEBID with iron and cobalt carbonyls. Similar high metal content FEB deposits of Au already have limited reproducibility due to $AuCl(PF_3)$ and AuCl(CO) precursor stability problems discussed in Section 5.1.4 and do not qualify for wide-spread FEBID use unless stabilizing agents can be found.

Shifting the paradigm to more process chemistry implies an increasing complexity of the setup and number of parameters to control (temperature, gas ambience) in a scanning electron microscope. For this reason, FEBID precursor design was looking so far for precursors performing well at HV and room temperature conditions but should consider in future improving precursors with respect to the mechanisms developed previously in this chapter:

(i) dissociative adsorption,
(ii) autocatalysis,
(iii) ability to fragment upon irradiation into volatile moieties within ligands (e.g. CO_2),
(iv) contain in-built purification moieties (proton donors) within ligands (e.g. H_2O, NH_3),
(v) easy ligand desorption,
(vi) "inertness" to intra-ligand fragment product polymerization.

Most of these mechanisms depend heavily on temperature and on catalytic activity of the growing metal surface (depending on cleanliness and metal element) under electron irradiation. Generalization or classification of certain precursors according to ligand properties (neutral vs. ionic, mono- vs. multi-dentate) or metals

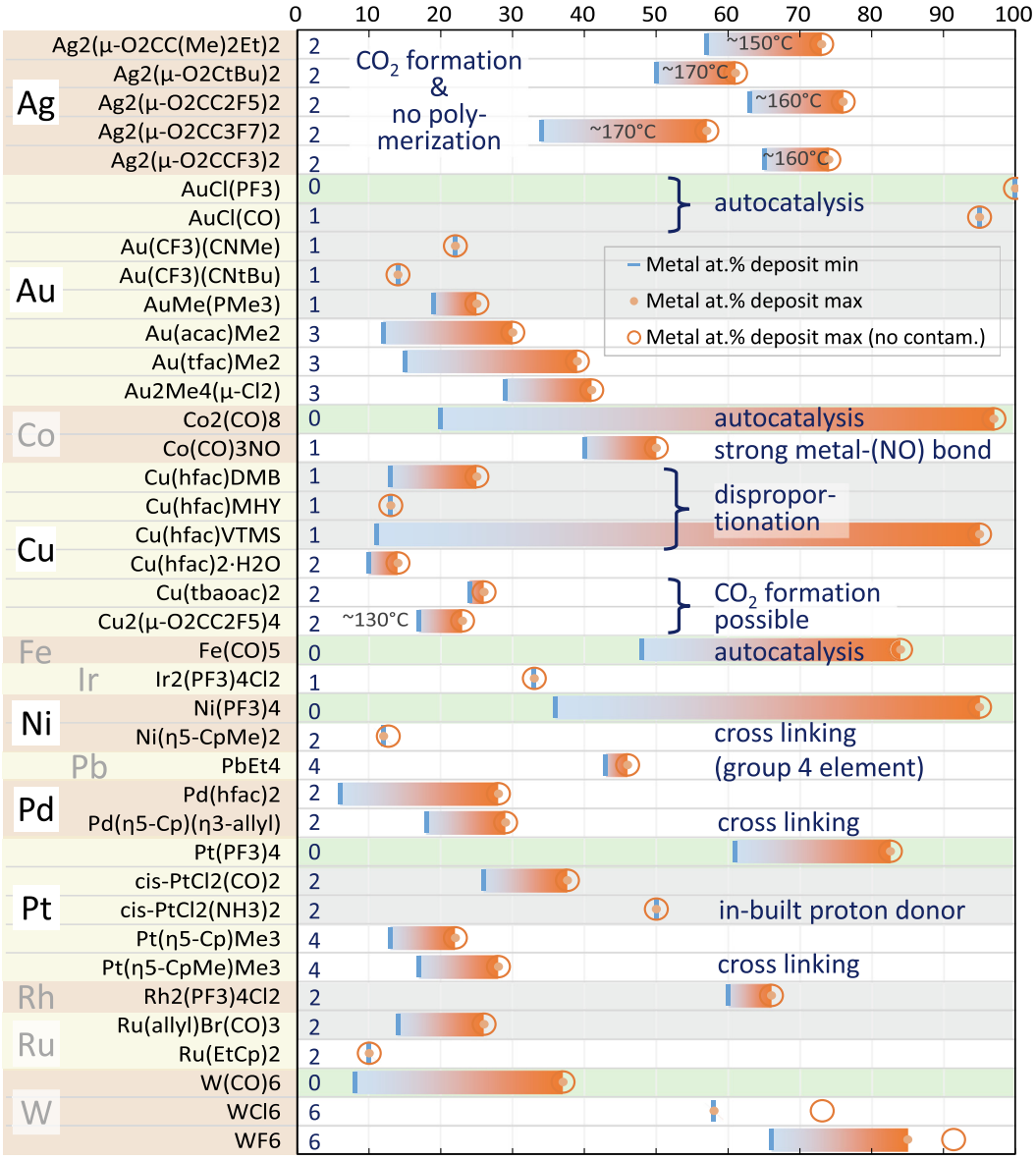

Fig. 5.12. FEBID precursors summarized according to the central metal atom with their metal content range (blue-orange bars). The metal oxidation state is noted along the bottom horizontal axis. Precursors are highlighted with ligands being all neutral (light green bars), mixed neutral + ionic (grey bars), or fully ionic (white). Specific FEBID conditions and precursor ligand peculiarities are noted. Note that the large ranges of FEBID metal content for the individual precursors found in literature point to the dominant role temperature and residual gas conditions can have in FEBID. For details compare to Fig. 5.1 and chapters 3 and 4.

(stable metal oxidation state) to define precursor design rules is tempting but probably not possible. From Fig. 5.12 it seems rather that various sets of mechanisms favour a certain ligand for a given metal. However, the same ligand does not provide high FEBID metal content for another metal. Compare for instance the metal contents for carbonyls of tungsten, iron, and cobalt; the chlorido precursor family with PF_3 for Au, Rh, and Ir; and the carboxylates of Ag and Cu in Fig. 5.12. Also the intuitive standard of using carbon-free and very small ligands for FEBID is seen to fail occasionally as general design pattern because silver carboxylates give high metal contents while $Ir_2(PF_3)_4(\mu\text{-}Cl)_2$ does not.

Having said this, we understand that Fig. 5.12 illustrates the wealth of metal contents obtained in FEBID where the fields of thermal and non-thermal (electron-induced) mechanisms interplay on various surfaces. Fig. 5.12 also shows the evidence that the parameter field of FEBID with respect to the mechanisms (i-vi) calls for further detailed investigations with the goal to achieve high metal contents for all metal elements in FEBID 3D nanoprinting.

6. Perspectives

Summarizing from the previous sections, the complexity of the FEBID process is challenging for high fidelity nanoprinting in combination with a contamination-free metallic material. The final deposit composition is a consequence of the local ecosystem of precursor, vacuum and/or reactive environment, further energy input as well as the balance between electron and precursor fluxes -all happening on a surface that is continuously irradiated and dynamically changing during the process. It seems that, there is a trade-off between purity and smooth surfaces and sidewalls of the deposit. Thermally unstable group 10 and 11 precursors often lead to high metal contents (cf. e.g. Sections 4.5.2 and 5.1.4) but on the other hand hamper reliable vertical growth of well-defined

geometries due to effects like Ostwald ripening [416]. Most of the impressive results on three-dimensional nanoprinting were achieved with cyclopentadienyl and β–diketonate ligands both of which have a strong tendency of cross-linking under electron beam impact. Here, the smooth carbonaceous matrix constitutes the backbone of the complex three-dimensional shapes in which the metallic grains are dispersed. An interesting exception is given by Co, Fe, and CoFe carbonyl precursors not discussed in this review. Here, high purities in the range of >90 at.% up to 100 at.% can be obtained for smooth 3D wire-frame structures [66] partly achieved for elevated substrate temperatures [417]. The high purity may be explained by the formation of surface bound intermediate species assembling to clusters that undergo a concerted reaction cascade under FEBID conditions including electron- and thermally induced decomposition [35]. But also autocatalytic reactions may play a role as observed in the case of $Co_2(CO)_8$ [418] under HV conditions and $Fe(CO)_5$ under UHV conditions [88,419], cf. Section 5.1.1.

Therefore, future developments in FEBID will have to pursue different routes depending on the targeted application. Beyond the established in-situ and post-purification strategies, such routes may include dynamical FEBID process optimization by pulse schemes (cf. Section 6.5), electron-enhanced CVD (cf. Section 6.4), 3D printing of FEBID scaffolds to be conformally coated by ALD (cf. Section 3.2.4), or electron-enhanced ALD (cf. Section 6.3). In parallel, precursor design may develop towards in-operando purification by reactive ligands (cf. Section 6.2) or the efficient use of water in the FEBID HV environment (cf. Section 6.1).

All these research lines profit from the valuable input of CVD and ALD as well as fundamental surface and gas phase studies to understand and to control the local chemistry that occurs during FEBID. The local energy input by electrons that is specific to FEBID, in combination with the typical HV environment, causes the extreme flexibility of the process along with its ease to implement it in conventional vacuum chambers of any scanning electron microscope. On the other hand, exactly the same specialities introduce a degree of complexity that can never be managed for all target materials and geometries at the same time but only for specific precursors under well-adapted process conditions.

6.1. Ultra high vacuum vs. high vacuum (UHV vs. HV)

Most scanning electron microscopes are conceived for HV background pressures in the 10^{-6} mbar range with best vacuum reaching the 10^{-7} mbar range. This translates to an impingement rate of residual gas molecules in the order of one monolayer per second or per ten seconds, respectively. The residual gas composition is typically composed of water taking 50 to 60% while the rest varies according to the maintenance and usage of the microscope and can usually contain volatile hydrocarbons, carbon oxide, oxygen, and the purge gas nitrogen. Since water is a dipolar molecule, it has a long residence time on surfaces and is a natural co-reaction partner in HV FEBID. As discussed in Section 5.3.2, it is a source of reactive atomic hydrogen and hydroxyl radicals upon electron irradiation, see Fig. 5.11. A prominent example of oxidation in HV conditions is nickel FEBID using the $Ni(CpMe)_2$ molecule, which resulted in nickel oxide although no oxygen is contained in the precursor, see Section 3.2.2. On the other hand, the density of residual water is low when approaching UHV. Below a background pressure of about $2{\cdot}10^{-7}$ mbar a transition from an adsorbed double layer of water to no adsorbed water was observed on a hydrophilic native oxide SiO_2:Si(100) surface at room temperature [420]. Hence protonation reactions to render ionic ligands more volatile (see Section 5.1) as well as oxidation of metal would be greatly suppressed. According to Barth et al., this transition pressure $2{\cdot}10^{-7}$ mbar serves as a threshold value between two regimes with only electron-induced precursor dissociation taking place below while above reaction channels involving water as co-reactant gain in importance [35]. Indeed, the latter is supported by comprehensive research using water as additional gas (cf. Section 5.3.2), however, the first claim deserves special attention as dissociative adsorption of the precursor may come into play (cf. Section 5.1.1).

UHV pressures in the range of 10^{-9} to 10^{-10} mbar translate to a proportionally decreased impingement rate of residual gas molecules to 3 or 0.3 monolayers per hour, respectively. This may trigger dissociative adsorption when precursors show (auto)catalytic reactions as the so-called poisoning of the surface is strongly reduced. Surface poisoning is known from CVD reactions in the context of accumulation of organic by-products of thermal reactions on the surface. For UHV conditions, it means that the clean catalytically active surface is neither passivated by co-deposited residual gas hydrocarbons nor by oxidation from the reactive hydroxyl radicals radicals formed from the residual gas upon electron irradiation. A very striking example for UHV is FEBID with $Fe(CO)_5$, which led to autocatalytic growth of metal nanocrystals even in the absence of electron irradiation and sole exposure to the gas flow after the formation of metallic nuclei [88].

6.2. In-operando purification

Being a single-step direct write process is one of the major benefits of FEBID. Delicate purification routines after deposition that certainly will induce geometrical modifications are therefore only the second-best choice to obtain purely metallic nanostructures. Ideally, the cleaning could be performed in-operando during growth.

The residual water in the vacuum chamber can be considered as one possible ingredient for high purity FEBID material, cf. Section 6.1. Hence, the introduction of co-reactants is a natural choice for in-operando purification. Oxidizing co-reactants proved successful for the deposition of noble metals, e.g. achieving pure gold deposition from $Au(tfac)Me_2$ either under water atmosphere in an environmental SEM [348] or upon water co-injection [347]. In the same manner reducing co-reactants like hydrogen or forming gas may be of interest not only for non-noble metal depositions. Hydrogen radicals were employed as post-deposition treatment on deposits from $Pt(\eta^5\text{-CpMe})Me_3$ [131] decreasing the carbon content from 81 at.% to 65 at.%. Up to now, no reducing reactants were reported in FEBID for in-operando purification to the best of our knowledge. Since ammonia releases the reducing agent hydrogen upon electron impact [259], it may be worth considering it as such a co-reactant.

In addition to the use of co-reactants, elevated substrate temperatures during deposition trigger further reactions. Precursors with cyclopentadienyl or β-diketonate ligands tend to polymerize. Thus, an increase in temperature will only improve the desorption of cleaved fragments while no modifications occur in already cross-linked ligands. In case of $Pt(\eta^5\text{-CpMe})Me_3$ this poses an upper limit on the achievable metal content without co-reactants of 35 at.%, see Section 3.2.2. For other precursors elevated temperatures can lead to dissociative adsorption and/or autocatalysis under UHV conditions (cf. Section 5.1.1) as well as thermally assisted electron-induced dissociation (cf. Section 5.2.3). Under HV conditions, the presence of the co-reactant water opens reaction channels that can enhance the desorption of ionic ligands by protonation but also oxidation of the metal by $OH^{\bullet}$ radicals formed by electron-induced ionization (cf. Section 5.3.2). Therefore, the achievable metal content can change drastically especially for some carbonyl and trifluorophosphine compounds depending on the respective deposition conditions as displayed in Fig. 5.1.

The most elegant approach to in-operando purification, however, relies on precursor design introducing reactive ligands. The

NH_3 ligand in cisplatin releases atomic hydrogen in two different reaction paths and enhances the desorption of the chlorine ligand as HCl. Further promising ligand candidates may feature the release of the thermodynamically stable CO_2 (cf. Section 5.2.2) or carry the oxidizing agent water (cf. Section 5.3.2) like $Cu(hfac)_2{\cdot}H_2O$. While FEBID experiments benefit from the dehydrated species to obtain better reproducibility, in principle the sublimation can be carried out such that the water is not released separately. Instead, the hydrated molecule can be transported into the gas phase [2].

6.3. Electron-enhanced ALD

Let us consider here the ALD of gallium nitride [421], boron nitride [422], silicon [423], and cobalt [424]. Growth of cobalt films at room temperature using sequential exposures of tricarbonylnitrosylcobalt(0) and low energy electrons, with electrons as co-reactants in UHV conditions was recently studied by the group of George [424]. The deposition temperatures used in electron-enhanced ALD (EE-ALD) are close to room temperature and thus considerably lower compared to CVD temperatures in the range of around 600 °C to 1100 °C (for Si and GaN), meaning that polymers or other heat sensitive substrates can be coated. Fig. 6.1a-b show the sequence for silicon deposition with disilane and electrons at 25–100 °C process temperature. The electrons needed a threshold energy of 25 eV and showed a maximum growth rate of 0.3 Å/cycle at 100 to 150 eV energy corresponding to dissociative chemisorption of silane (Si_2H_6) on silicon dangling bonds. Furthermore, both surface reactions showed self-limiting behaviour. The composition of the such deposited material contained Si:O:C as atomic ratio of 84:6:10. The carbon content was attributed to contamination by residual hydrocarbons in the chamber, which co-adsorbed on the dangling bonds. The oxygen probably originates from residual water. The purity compares well with UHV FEBID using silane and germane precursors [379,425]. The example in Fig. 6.1c shows electron-enhanced ALD of cobalt which was performed at room temperature with pulses of $Co(CO)_3NO$ and 75–200 eV electrons [424]. XPS composition measurements confirmed that all carbonyl ligands were desorbed while 13 % of the nitrosyl ligands were co-deposited, the remaining 87% ligands desorbed as well. Both ligands were detected during in-situ mass spectrometric measurements. The deposit's atomic ratio Co:O:N:C was about 52:42:7:0 indicating the complete removal of carbonyl ligands. The authors attributed the high oxygen content to ambient air exposure prior to composition measurements but did not exclude the oxidation via dissociated oxygen from the nitrosyl ligands. High-vacuum FEBID with $Co(CO)_3NO$ and keV energy electrons resulted in a metal content of about 80 at.% containing nitrogen as main impurity and carbon below 10 at.% [171,423].

Summarizing, the inclusion of non-thermal electron induced metal–ligand bond dissociation reactions into the ALD sequential co-reactant pulse scheme considerably expands the temperature window of self-limiting surface reactions towards room temperatures. Electron-enhanced ALD can thus enable metal coating of heat sensitive materials including as-deposited carbon-rich FEBID materials.

6.4. Electron-enhanced CVD

Boszo and Avouris [426,427] performed electron-enhanced CVD of ultra-thin films of amorphous hydrogenated silicon, silicon nitride, silicon dioxide, and silicon oxynitride ultra-thin films at −173°C. They used an UHV system to adsorb Si_2H_6, Si_2H_6-O_2, Si_2H_6–NO, and Si_2H_6-NH_3 layers and irradiated them with 0.3–1 keV electrons. The process pressures of disilane, oxygen, nitrogen monoxide, and ammonia were adjusted to about $1.3{\cdot}10^{-7}$ mbar and

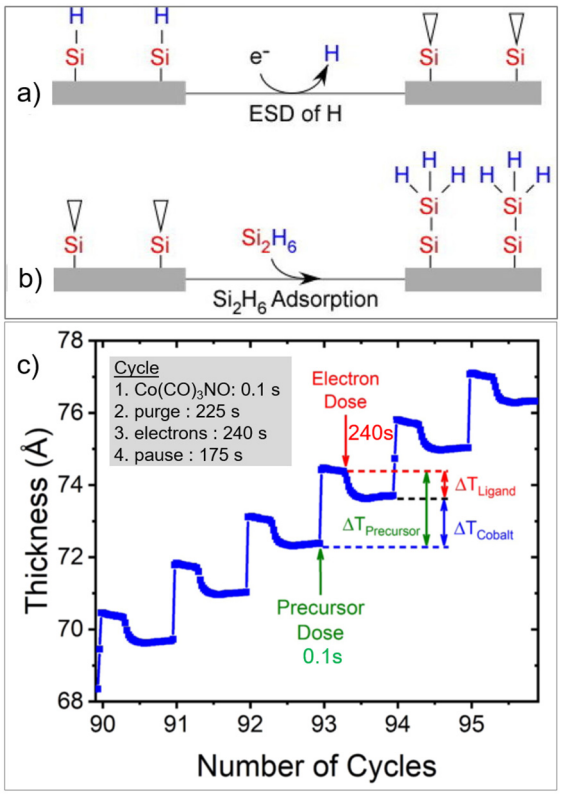

Fig. 6.1. Electron-enhanced ALD. a & b) Sequence for silicon deposition. The electrons dissociate the hydrogen from silicon and leave reactive dangling bonds. Adapted with permission from Sprenger et al. [423] copyright (2019) American Chemical Society. c) In-situ ellipsometry thickness measurements during cobalt deposition. Modified from Sobell et al. [424].

resulted in very small growth rates of about 0.02 monolayers per second. They pointed out that this process can be particularly useful in growing thin films, which under normal CVD conditions cannot be formed because of metal clustering.

Recently, Nadhom et al. [428] used free electrons in an argon plasma as reducing agent in CVD to deposit Fe, Co, and Ni from their corresponding metallocene precursors (MCp_2 with M = Fe, Co, and Ni). The best film metal contents so far were about 75 at.% Fe, 42 at.% Co, and 30 at.% Ni with sometimes large amounts of oxygen included; an element not contained in the precursor. This indicates that metal content improvement is possible by better vacuum control below their present base pressure of 0.06 mbar. Increasing the bias potential of the substrate from –40 V to +40 V resulted in metal contents almost linearily increasing from zero to their above mentioned maximum values. It is clear that the attraction of the number of electrons as well as their energy increases with positive substrate bias and still further increasing may result in even higher contents of metal. However, from the perspective of FEBID and condensed phase electron irradiation experiments discussed in Section 3.2, cyclopentadienyl ligands are very difficult to remove from the surface. The related metal carbonyls might be more beneficial in electron-enhanced CVD as they can result in relatively high metal contents, see Fig. 5.1.

When employing a focused electron beam in combination with the substrate bias, electron-enhanced CVD may be performed spatially selective, either for direct writing of high-purity metal structures or as post-coating routine for nanostructures already present. Here, a conformal growth may be achieved as long as the interaction volume of the electron extends over the entire nanostructure.

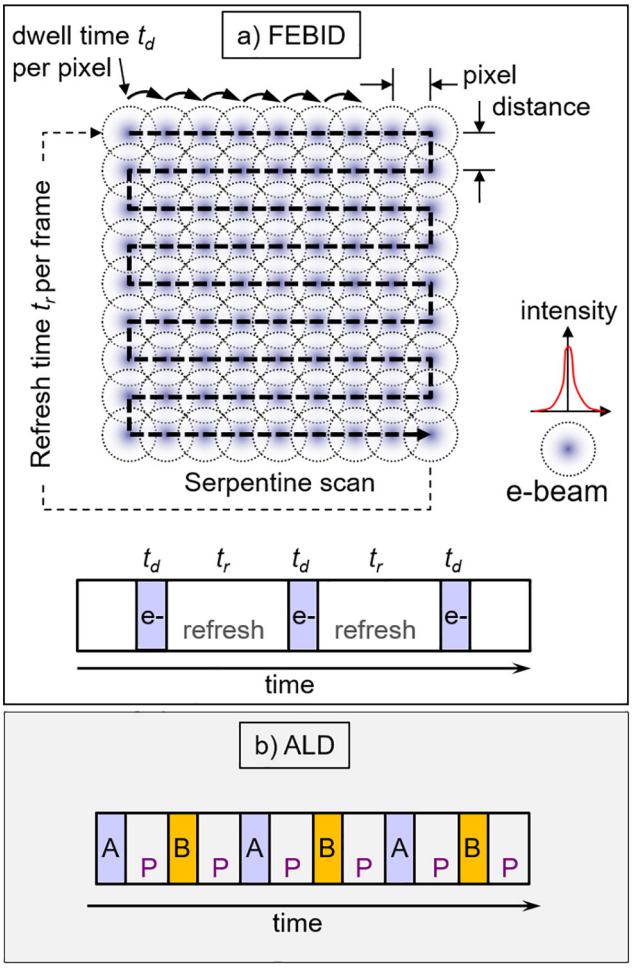

Fig. 6.2. a) Scheme of FEBID writing pattern for a square. The focused electron beam is moved in a raster by the SEM and entails an exposure (dwell) - refresh time pattern for the individual pixels. Note that the gas is typically not pulsed but continuously supplied in FEBID. b) ALD gas pulsing scheme. The two co-reactant precursors A and B are sequentially pulsed into the reactor and separated by purge gas pulses P to avoid gas reactions.

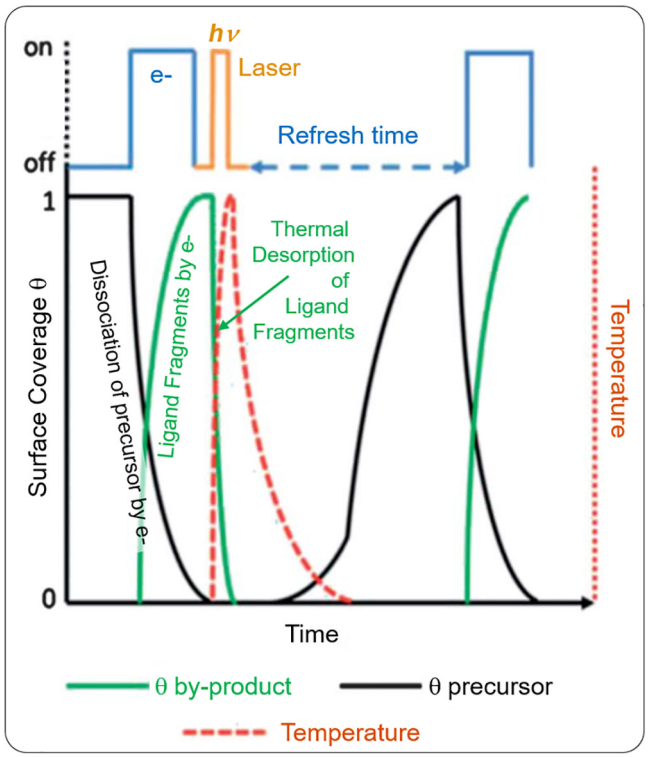

Fig. 6.3. Scheme of sequential FEB and laser pulses to dissociate precursor molecules and to remove the ligand fragments by thermal desorption, respectively. Modified from Roberts et al. [172]. Note that the precursor flow was continuous and not pulsed.

6.5. Pulsed FEBID

FEBID is inherently performed in a pulse mode when depositing areal or three-dimensional structures as the focused beam needs to be scanned over an area or must "print" between the different free-standing elements to keep them on the same height level [1]. Only straight cylindrical structures – coaxially grown into the focused electron beam, like for scanning probe tips or antennae – employ the continuous spot exposure without moving the beam. The scan pattern for a simple square deposit exemplifies the related exposure chronology for FEBID and is shown in Fig. 6.2a.

The time pulse scheme is less common in the FEBID community and rather the terms dwell time t_d and refresh time t_r per pixel are frequently used. During the dwell time the FEB dwells and irradiates on the pixel (the focus area of the beam), where it induces the local electron dissociation reactions. When it moves on to the next pixel, the previous pixel starts to refresh with new precursor molecules from the gas phase or by surface diffusion. There is an analogy to the ALD cycles shown in Fig. 6.2b, where the precursor pulses are separated in time. While in ALD the time scale is given by the completion of the self-limiting surface reactions and the complete purge of the gas molecules and reaction products to avoid gas phase reactions, the time scale in FEBID is given by the electron dissociation rate and the refreshment rate kinetics. In contrast to ALD, there is typically no pulsing of the gas molecules in FEBID – it is rather typically supplied continuously to refresh the dissociated adsorbate molecules with new ones from the gas phase. The refreshment time scale (i.e. adsorption time scale) is in the ten millisecond range, while the time scale for the electron dissociation reaction is in the microsecond and less time scale [1]. The time scale of a corresponding precursor "purge" as inherent to ALD would translate to the pump time, when the typical operating pressure with molecules of around 10^{-5} to 10^{-4} mbar reduces to the background pressure of around 10^{-6} mbar after closing the molecule supply. This is in the order of one to tens of seconds depending on chamber volume and (turbo) pump speed and could be performed without purge gas.

What has been largely overlooked so far in FEBID is that the ligand fragment surface kinetics may dominate the contamination level and thus the low metal content in the deposited material. This implies that the time scale of the electron exposure pulse as well as the refreshment rate with new molecules need to be adapted to the time scale of desorption of ligand fragments. When the electron pulse is too long and the refreshment rate too high then the ligand fragments will be co-deposited and embedded before they can desorb. FEBID proceeds at temperatures where practicable growth rates can be obtained by physisorption of the precursor molecules. However, as we discussed in Section 5.1, the ligand fragments can have stronger interaction with the surface due to their ionic character. This entails that these ligand fragments would need extra thermal energy to desorb efficiently. To meet these requirements, Roberts et al. [172] successfully proposed to use a sequence of FEB exposure and laser pulses to heat and cool the substrate rapidly in order to remove the ligand frag-

ments from the surface, and to allow for new arriving precursor molecules to adsorb see Fig. 6.3.

The heat pulse is constrained by the thermal decomposition temperature of the molecule, which should not be reached as then the local deposition by the electron beam will extend to the full heated area of the laser spot. Using the above electron & photon (heat) exposure scheme they were able to increase the platinum content in FEBID with Pt(η^5-Cp)Me_3 to 35 at.% see Section 3.2.2. Potentially, changing the continuous precursor supply to sequential (closed during the laser pulse) may still improve the metal content in such arrangements. Finally, of note is that integration of such heat pulses by lasers would also offer an additional parameter of (selective) control of surface reactions in ALD processes.

Author contributions

Overview of surface deposition techniques: I. Utke; evaluation of precursors and process performance: I. Utke, P. Swiderek, K. Höflich; introductory sections: J. Jurczyk, K. Madajska, P. Martinovic; FEBID related sections: K. Höflich and I. Utke; ALD related sections: I. Utke; CVD related sections to I.B. Szymańska, K. Madajska; surface science/gas phase related sections: P. Swiderek and I. B. Szymańska, and perspectives: I. Utke and K. Höflich.

Declaration of Competing Interest

The authors declare that they have no known competing financial interests or personal relationships that could have appeared to influence the work reported in this paper.

Acknowledgements

IU, JJ, and PS acknowledge that research was conducted with the financial support of the EU Horizon 2020 Marie Curie-Sklodowska Innovative Training Network "ELENA" (Low energy ELEctron driven chemistry for the advantage of emerging Nanofabrication methods, grant agreement No 722149). IU acknowledges funding from the Swiss National Science Foundation SNF project 200021E-164211. PS acknowledges funding from DFG project SW26/13-1,2 (Mechanisms of electron-induced reactions in focused electron beam induced deposition). KH acknowledges the financial support from DFG project "chiralFEBID" under grant no. HO 5461/3-1. IBSz, KM acknowledge the financial support of the Nicolaus Copernicus University in Toruń.

Appendix A. Supplementary data

Supplementary data to this article can be found online at https://doi.org/10.1016/j.ccr.2021.213851.

References

[1] I. Utke, P. Hoffmann, J. Melngailis, Gas-assisted focused electron beam and ion beam processing and fabrication, J. Vac. Sci. Technol. B. 26 (2008) 1197–1276, https://doi.org/10.1116/1.2955728.
[2] T.T. Kodas, M.J. Hampden-Smith, The Chemistry of Metal CVD, Wiley-VCH, Weinheim, Germany, 1994, https://doi.org/10.1002/9783527615858.
[3] A.C. Jones, M.L. Hitchman, Chemical Vapour Deposition: Precursors, Processes and Applications, Royal Society of Chemistry, Cambridge, UK, 2009. https://doi.org/10.1039/9781788010672-00001.
[4] A.L. Johnson, J.D. Parish, Recent developments in molecular precursors for atomic layer deposition, in: Organomet. Chem. Vol. 42, The Royal Society of Chemistry, 2018: pp. 1–53. https://doi.org/10.1039/9781788010672-00001.
[5] R.M.M. Thorman, T.P.P. Ragesh Kumar, D.H.H. Fairbrother, O. Ingólfsson, D. Howard Fairbrother, O. Ingólfsson, The role of low-energy electrons in focused electron beam induced deposition: four case studies of representative precursors, Beilstein J. Nanotechnol. 6 (2015) 1904–1926. https://doi.org/10.3762/bjnano.6.194.
[6] J.A. Spencer, S.G. Rosenberg, M. Barclay, Y.-C. Wu, L. McElwee-White, D.H. Fairbrother, Understanding the electron-stimulated surface reactions of organometallic complexes to enable design of precursors for electron beam-induced deposition, Appl. Phys. A Mater. Sci. Process. 117 (2014) 1631–1644, https://doi.org/10.1007/s00339-014-8570-5.
[7] W.G. Carden, H. Lu, J.A. Spencer, D.H. Fairbrother, L. McElwee-White, Mechanism-based design of precursors for focused electron beam-induced deposition, MRS Commun. 8 (2018) 343–357, https://doi.org/10.1557/mrc.2018.77.
[8] M. Allendorf, From Bunsen to VLSI: 150 Years of Growth in Chemical Vapor Deposition Technology, Electrochem. Soc. Interface. 7 (1998) 36–39, https://www.electrochem.org/dl/interface/spr/spr98/IF3-98-Pages36-39.pdf.
[9] S.P. Krumdiek, CVD Reactors and Delivery System Technology, in: A. C. Jones, M.L. Hitchman (Eds.), Chem. Vap. Depos. Precursors, Process. Appl., Royal Society of Chemistry, Cambridge, UK, 2009 https://doi.org/10.1039/9781847558794-00037.
[10] M. Reinke, E. Ponomarev, Y. Kuzminykh, P. Hoffmann, Combinatorial Characterization of TiO2 Chemical Vapor Deposition Utilizing Titanium Isopropoxide, ACS Comb. Sci. 17 (2015) 413–420, https://doi.org/10.1021/acscombsci.5b00040.
[11] R.L. Puurunen, A Short History of Atomic Layer Deposition: Tuomo Suntola's Atomic Layer Epitaxy, Chem. Vap. Depos. 20 (2014) 332–344, https://doi.org/10.1002/cvde.201402012.
[12] S.M. George, Atomic Layer Deposition: An Overview, Chem. Rev. 110 (2010) 111–131, https://doi.org/10.1021/cr900056b.
[13] R.L. Puurunen, Surface chemistry of atomic layer deposition: A case study for the trimethylaluminum/water process, J. Appl. Phys. 97 (2005) 121301, https://doi.org/10.1063/1.1940727.
[14] N. Pinna, M. Knez, Atomic Layer Deposition of Nanostructured Materials, Wiley-VCH Verlag GmbH & Co. KGaA, Weinheim, Germany, 2012. https://doi.org/10.1002/9783527639915.
[15] J. Bachmann, Atomic Layer Deposition in Energy Conversion Applications, Wiley-VCH Verlag GmbH & Co. KGaA, Weinheim, Germany, 2017. https://doi.org/10.1002/9783527694822.
[16] C. Marichy, M. Bechelany, N. Pinna, Atomic Layer Deposition of Nanostructured Materials for Energy and Environmental Applications, Adv. Mater. 24 (2012) 1017–1032, https://doi.org/10.1002/adma.201104129.
[17] M. Knez, K. Nielsch, L. Niinistö, Synthesis and Surface Engineering of Complex Nanostructures by Atomic Layer Deposition, Adv. Mater. 19 (2007) 3425–3438, https://doi.org/10.1002/adma.200700079.
[18] J.R. Bakke, K.L. Pickrahn, T.P. Brennan, S.F. Bent, Nanoengineering and interfacial engineering of photovoltaics by atomic layer deposition, Nanoscale. 3 (2011) 3482–3508, https://doi.org/10.1039/c1nr10349k.
[19] X. Meng, Atomic and molecular layer deposition in pursuing better batteries, J. Mater. Res. (2020) 1–24, https://doi.org/10.1557/jmr.2020.173.
[20] H.C.M. Knoops, M.E. Donders, M.C.M. van de Sanden, P.H.L. Notten, W.M.M. Kessels, Atomic layer deposition for nanostructured Li-ion batteries, J. Vac. Sci. Technol. A. 30 (2012) 010801, https://doi.org/10.1116/1.3660699.
[21] J.W. Elam, D. Routkevitch, P.P. Mardilovich, S.M. George, Conformal Coating on Ultrahigh-Aspect-Ratio Nanopores of Anodic Alumina by Atomic Layer Deposition, Chem. Mater. 15 (2003) 3507–3517, https://doi.org/10.1021/cm0303080.
[22] V. Cremers, R.L. Puurunen, J. Dendooven, Conformality in atomic layer deposition: Current status overview of analysis and modelling, Appl. Phys. Rev. 6 (2019) 021302, https://doi.org/10.1063/1.5060967.
[23] W. Szmyt, C. Guerra, C. Dransfeld, I. Utke, Solving the inverse Knudsen problem: gas diffusion in random fibrous media, J. Memb. Sci. 620 (2021) 118728, https://doi.org/10.1016/j.memsci.2020.118728.
[24] P. Poodt, D.C. Cameron, E. Dickey, S.M. George, V. Kuznetsov, G.N. Parsons, F. Roozeboom, G. Sundaram, A. Vermeer, Spatial atomic layer deposition: A route towards further industrialization of atomic layer deposition, J. Vac. Sci. Technol. A. 30 (2012) 010802, https://doi.org/10.1116/1.3670745.
[25] V. Miikkulainen, M. Leskelä, M. Ritala, R.L. Puurunen, Crystallinity of inorganic films grown by atomic layer deposition: Overview and general trends, J. Appl. Phys. 113 (2013) 021301, https://doi.org/10.1063/1.4757907.
[26] D.J.H. Emslie, P. Chadha, J.S. Price, Metal ALD and pulsed CVD: Fundamental reactions and links with solution chemistry, Coord. Chem. Rev. 257 (2013) 3282–3296, https://doi.org/10.1016/j.ccr.2013.07.010.
[27] D.J. Hagen, M.E. Pemble, M. Karppinen, Atomic layer deposition of metals: Precursors and film growth, Appl. Phys. Rev. 6 (2019) 041309, https://doi.org/10.1063/1.5087759.
[28] J.W. Maina, A. Merenda, M. Weber, J.M. Pringle, M. Bechelany, L. Hyde, L.F. Dumée, Atomic layer deposition of transition metal films and nanostructures for electronic and catalytic applications, Crit. Rev. Solid State Mater. Sci. (2020) 1–22, https://doi.org/10.1080/10408436.2020.1819200.
[29] S.D. Elliott, G. Dey, Y. Maimaiti, Classification of processes for the atomic layer deposition of metals based on mechanistic information from density functional theory calculations, J. Chem. Phys. 146 (2017) 052822, https://doi.org/10.1063/1.4975085.
[30] A.N. Broers, W.W. Molzen, J.J. Cuomo, N.D. Wittels, Electron-beam fabrication of 80Å metal structures, Appl. Phys. Lett. 29 (1976) 596–598, https://doi.org/10.1063/1.89155.
[31] W.F. van Dorp, B. van Someren, C.W. Hagen, P. Kruit, P.A. Crozier, Approaching the Resolution Limit of Nanometer-Scale Electron Beam-Induced Deposition, Nano Lett. 5 (2005) 1303–1307, https://doi.org/10.1021/nl050522i.

[32] O. Ingólfsson, Low-Energy Electrons Fundamentals and Applications, Jenny Stanford Publishing, New York, 2019, https://doi.org/10.1201/9780429058820.
[33] E. Böhler, J. Warneke, P. Swiderek, Control of chemical reactions and synthesis by low-energy electrons, Chem. Soc. Rev. 42 (2013) 9219–9231, https://doi.org/10.1039/c3cs60180c.
[34] M. Huth, F. Porrati, O.V. Dobrovolskiy, Focused electron beam induced deposition meets materials science, Microelectron. Eng. 185–186 (2018) 9–28, https://doi.org/10.1016/j.mee.2017.10.012.
[35] S. Barth, M. Huth, F. Jungwirth, Precursors for direct-write nanofabrication with electrons, J. Mater. Chem. C. 8 (2020) 15884–15919, https://doi.org/10.1039/D0TC03689G.
[36] A.C. Jones, M.L. Hitchman, Overview of Chemical Vapour Deposition, in: A.C. Jones, M.L. Hitchman (Eds.), Chem. Vap. Depos. Precursors, Process. Appl., Royal Society of Chemistry, Cambridge, UK, 2009 https://doi.org/10.1039/9781847558794-00001.
[37] T. Kääriäinen, D. Cameron, M.-L. Kääriäinen, A. Sherman, Fundamentals of Atomic Layer Deposition, in: At. Layer Depos, John Wiley & Sons, Inc, 2013, pp. 1–31, https://doi.org/10.1002/9781118747407.ch1.
[38] M. Toth, C. Lobo, V. Friedli, A. Szkudlarek, I. Utke, Continuum models of focused electron beam induced processing, Beilstein J. Nanotechnol. 6 (2015) 1518–1540, https://doi.org/10.3762/bjnano.6.157.
[39] J.D. Fowlkes, R. Winkler, B.B. Lewis, M.G. Stanford, H. Plank, P.D. Rack, Simulation-Guided 3D Nanomanufacturing via Focused Electron Beam Induced Deposition, ACS Nano. 10 (2016) 6163–6172, https://doi.org/10.1021/acsnano.6b02108.
[40] R. Winkler, B.B. Lewis, J.D. Fowlkes, P.D. Rack, H. Plank, High-Fidelity 3D-Nanoprinting via Focused Electron Beams: Growth Fundamentals, ACS Appl. Nano Mater. 1 (2018) 1014–1027, https://doi.org/10.1021/acsanm.8b00158.
[41] L. Skoric, D. Sanz-Hernández, F. Meng, C. Donnelly, S. Merino-Aceituno, A. Fernández-Pacheco, Layer-by-Layer Growth of Complex-Shaped Three-Dimensional Nanostructures with Focused Electron Beams, Nano Lett. 20 (2020) 184–191, https://doi.org/10.1021/acs.nanolett.9b03565.
[42] L. Keller, M. Huth, Pattern generation for direct-write three-dimensional nanoscale structures via focused electron beam induced deposition, Beilstein J. Nanotechnol. 9 (2018) 2581–2598, https://doi.org/10.3762/bjnano.9.240.
[43] R. Winkler, J.D. Fowlkes, P.D. Rack, H. Plank, 3D nanoprinting via focused electron beams, J. Appl. Phys. 125 (2019) 210901, https://doi.org/10.1063/1.5092372.
[44] A. Fernández-Pacheco, L. Skoric, J.M. De Teresa, J. Pablo-Navarro, M. Huth, O. V. Dobrovolskiy, Writing 3D Nanomagnets Using Focused Electron Beams, Materials (Basel). 13 (2020) 3774, https://doi.org/10.3390/ma13173774.
[45] I. Utke, J. Michler, R. Winkler, H. Plank, Mechanical Properties of 3D Nanostructures Obtained by Focused Electron/Ion Beam-Induced Deposition: A Review, Micromachines. 11 (2020) 397, https://doi.org/10.3390/mi11040397.
[46] A. Reiser, L. Koch, K.A. Dunn, T. Matsuura, F. Iwata, O. Fogel, Z. Kotler, N. Zhou, K. Charipar, A. Piqué, P. Rohner, D. Poulikakos, S. Lee, S.K. Seol, I. Utke, C. van Nisselroy, T. Zambelli, J.M. Wheeler, R. Spolenak, Metals by Micro-Scale Additive Manufacturing: Comparison of Microstructure and Mechanical Properties, Adv. Funct. Mater. 30 (2020) 1910491, https://doi.org/10.1002/adfm.201910491.
[47] F. De Angelis, M. Patrini, G. Das, I. Maksymov, M. Galli, L. Businaro, L.C. Andreani, E. Di Fabrizio, A hybrid plasmonic-photonic nanodevice for label-free detection of a few molecules, Nano Lett. 8 (2008) 2321–2327, https://doi.org/10.1021/nl801112e.
[48] F. De Angelis, G. Das, P. Candeloro, M. Patrini, M. Galli, A. Bek, M. Lazzarino, I. Maksymov, C. Liberale, L.C. Andreani, E. Di Fabrizio, Nanoscale chemical mapping using three-dimensional adiabatic compression of surface plasmon polaritons, Nat. Nanotechnol. 5 (2010) 67–72, https://doi.org/10.1038/nnano.2009.348.
[49] K. Höflich, M. Becker, G. Leuchs, S. Christiansen, Plasmonic dimer antennas for surface enhanced Raman scattering, Nanotechnology. 23 (2012), https://doi.org/10.1088/0957-4484/23/18/185303.
[50] C. Haverkamp, K. Höflich, S. Jäckle, A. Manzoni, S. Christiansen, Plasmonic gold helices for the visible range fabricated by oxygen plasma purification of electron beam induced deposits, Nanotechnology. 28 (2017) 055303, https://doi.org/10.1088/1361-6528/28/5/055303.
[51] P. Woźniak, I. De Leon, K. Höflich, C. Haverkamp, S. Christiansen, G. Leuchs, P. Banzer, Chiroptical response of a single plasmonic nanohelix, Opt. Express. 26 (2018) 19275, https://doi.org/10.1364/oe.26.019275.
[52] K. Höflich, T. Feichtner, E. Hansjürgen, C. Haverkamp, H. Kollmann, C. Lienau, M. Silies, Resonant behavior of a single plasmonic helix, Optica. 6 (2019) 1098, https://doi.org/10.1364/optica.6.001098.
[53] P. Woźniak, I. De Leon, K. Höflich, G. Leuchs, P. Banzer, Interaction of light carrying orbital angular momentum with a chiral dipolar scatterer, Optica. 6 (2019) 961–965, https://doi.org/10.1364/optica.6.000961.
[54] R. Winkler, F.-P. Schmidt, U. Haselmann, J.D. Fowlkes, B.B. Lewis, G. Kothleitner, P.D. Rack, H. Plank, Direct-Write 3D Nanoprinting of Plasmonic Structures, ACS Appl. Mater. Interfaces. 9 (2017) 8233–8240, https://doi.org/10.1021/acsami.6b13062.
[55] C.H. Schwalb, C. Grimm, M. Baranowski, R. Sachser, F. Porrati, H. Reith, P. Das, J. Müller, F. Völklein, A. Kaya, M. Huth, A Tunable Strain Sensor Using Nanogranular Metals, Sensors (Switzerland). 10 (2010) 9847–9856, https://doi.org/10.3390/s101109847.
[56] M. Dukic, M. Winhold, C.H. Schwalb, J.D. Adams, V. Stavrov, M. Huth, G.E. Fantner, Direct-write nanoscale printing of nanogranular tunnelling strain sensors for sub-micrometre cantilevers, Nat. Commun. 7 (2016) 12487, https://doi.org/10.1038/ncomms12487.
[57] I. Utke, P. Hoffmann, R. Berger, L. Scandella, High-resolution magnetic Co supertips grown by a focused electron beam, Appl. Phys. Lett. 80 (2002) 4792–4794, https://doi.org/10.1063/1.1489097.
[58] L.M. Belova, O. Hellwig, E. Dobisz, E. Dan Dahlberg, Rapid preparation of electron beam induced deposition Co magnetic force microscopy tips with 10 nm spatial resolution, Rev. Sci. Instrum. 83 (2012) 093711, https://doi.org/10.1063/1.4752225.
[59] H. Plank, R. Winkler, C.H. Schwalb, J. Hütner, J.D. Fowlkes, P.D. Rack, I. Utke, M. Huth, Focused electron beam-based 3D nanoprinting for scanning probe microscopy: A review, Micromachines. 11 (2020) 48, https://doi.org/10.3390/mi11010048.
[60] F. Kolb, K. Schmoltner, M. Huth, A. Hohenau, J. Krenn, A. Klug, E.J.W. List, H. Plank, Variable tunneling barriers in FEBID based PtC metal-matrix nanocomposites as a transducing element for humidity sensing, Nanotechnology. 24 (2013) 305501, https://doi.org/10.1088/0957-4484/24/30/305501.
[61] G. Arnold, R. Winkler, M. Stermitz, A. Orthacker, J.-H. Noh, J.D. Fowlkes, G. Kothleitner, M. Huth, P.D. Rack, H. Plank, Tunable 3D Nanoresonators for Gas-Sensing Applications, Adv. Funct. Mater. 28 (2018) 1707387, https://doi.org/10.1002/adfm.201707387.
[62] M. Gabureac, L. Bernau, I. Utke, G. Boero, Granular Co-C nano-Hall sensors by focused-beam-induced deposition, Nanotechnology 21 (2010) 115503, https://doi.org/10.1088/0957-4484/21/11/115503.
[63] M. Gavagnin, H.D. Wanzenboeck, S. Wachter, M.M. Shawrav, A. Persson, K. Gunnarsson, P. Svedlindh, M. Stöger-Pollach, E. Bertagnolli, Free-standing magnetic nanopillars for 3D nanomagnet logic, ACS Appl. Mater. Interfaces. 6 (2014) 20254–20260, https://doi.org/10.1021/am505785t.
[64] A. Fernández-Pacheco, R. Streubel, O. Fruchart, R. Hertel, P. Fischer, R.P. Cowburn, Three-dimensional nanomagnetism, Nat. Commun. 8 (2017), https://doi.org/10.1038/ncomms15756.
[65] J.M. De Teresa, A. Fernández-Pacheco, R. Córdoba, L. Serrano-Ramón, S. Sangiao, M.R. Ibarra, Review of magnetic nanostructures grown by focused electron beam induced deposition (FEBID), J. Phys. D. Appl. Phys. 49 (2016), https://doi.org/10.1088/0022-3727/49/24/243003.
[66] L. Keller, M.K.I. Al Mamoori, J. Pieper, C. Gspan, I. Stockem, C. Schröder, S. Barth, R. Winkler, H. Plank, M. Pohlit, J. Müller, M. Huth, Direct-write of free-form building blocks for artificial magnetic 3D lattices, Sci. Rep. 8 (2018) 6160, https://doi.org/10.1038/s41598-018-24431-x.
[67] O.V. Dobrovolskiy, R. Sachser, S.A. Bunyaev, D. Navas, V.M. Bevz, M. Zelent, W. Śmigaj, J. Rychły, M. Krawczyk, R.V. Vovk, M. Huth, G.N. Kakazei, Spin-Wave Phase Inverter upon a Single Nanodefect, ACS Appl. Mater. Interfaces. 11 (2019) 17654–17662, https://doi.org/10.1021/acsami.9b02717.
[68] G. Pakeltis, Z. Hu, A.G. Nixon, E. Mutunga, C.P. Anyanwu, C.A. West, J.C. Idrobo, H. Plank, D.J. Masiello, J.D. Fowlkes, P.D. Rack, Focused Electron Beam Induced Deposition Synthesis of 3D Photonic and Magnetic Nanoresonators, ACS Appl. Nano Mater. 2 (2019) 8075–8082, https://doi.org/10.1021/acsanm.9b02182.
[69] S. Sangiao, L. Morellón, M.R. Ibarra, J.M. De Teresa, Ferromagnet-superconductor nanocontacts grown by focused electron/ion beam techniques for current-in-plane Andreev Reflection measurements, Solid State Commun. 151 (2011) 37–41, https://doi.org/10.1016/j.ssc.2010.10.028.
[70] K. Makise, K. Mitsuishi, M. Shimojo, B. Shinozaki, Microstructural analysis and Transport Properties of MoO and MoC nanostructures prepared by focused electron beam-induced deposition, Sci. Rep. 4 (2014) 5740, https://doi.org/10.1038/srep05740.
[71] M. Winhold, P.M. Weirich, C.H. Schwalb, M. Huth, Superconductivity and metallic behavior in $Pb_xC_yO_\delta$ structures prepared by focused electron beam induced deposition, Appl. Phys. Lett. 105 (2014) 1–6, https://doi.org/10.1063/1.4898819.
[72] S. Sengupta, C. Li, C. Baumier, A. Kasumov, S. Guéron, H. Bouchiat, F. Fortuna, Superconducting nanowires by electron-beam-induced deposition, Appl. Phys. Lett. 106 (2015), https://doi.org/10.1063/1.4906269 042601.
[73] G. Di Prima, R. Sachser, P. Trompenaars, H. Mulders, M. Huth, Direct-write single electron transistors by focused electron beam induced deposition, Nano Futur. 3 (2019), https://doi.org/10.1088/2399-1984/ab151c 025001.
[74] M. Huth, F. Kolb, H. Plank, Dielectric sensing by charging energy modulation in a nano-granular metal, Appl. Phys. A Mater. Sci. Process. 117 (2014) 1689–1696, https://doi.org/10.1007/s00339-014-8631-9.
[75] K. Höflich, R. Bin Yang, A. Berger, G. Leuchs, S. Christiansen, The Direct Writing of Plasmonic Gold Nanostructures by Electron-Beam- Induced Deposition, Adv. Mater. 23 (2011) 2657–2661, https://doi.org/10.1002/adma.201004114.
[76] T. Bret, T. Hofmann, K. Edinger, Industrial perspective on focused electron beam-induced processes, Appl. Phys. A Mater. Sci. Process. 117 (2014) 1607–1614, https://doi.org/10.1007/s00339-014-8601-2.
[77] K. Edinger, K. Wolff, P. Spies, T. Luchs, H. Schneider, N. Auth, C.F. Hermanns, M. Waiblinger, Photomask repair using low energetic electrons, Proc. SPIE. 9635 (2015) 96351P-1-96351P–9, https://doi.org/10.1117/12.2207755.
[78] N. GmbH, nanotools, (2021), https://www.nanotools.com/products.
[79] T. Bret, Physico-chemical study of the focused electron beam induced deposition process, PhD Thesis EPFL Nr 3321, 2005.
[80] C. Haverkamp, PhD thesis, FU Berlin, 2017.
[81] I. Langmuir, The constitution and fundamental properties of solids and liquids. Part I. Solids, J. Am. Chem. Soc. 38 (1916) 2221–2295, https://doi.org/10.1021/ja02268a002.
[82] I. Langmuir, The adsorption of gases on plane surfaces of glass, mica and platinum, J. Am. Chem. Soc. 40 (1918) 1361–1403, https://doi.org/10.1021/ja02242a004.

[83] S. Brunauer, P.H. Emmett, E. Teller, Adsorption of Gases in Multimolecular Layers, J. Am. Chem. Soc. 60 (1938) 309–319, https://doi.org/10.1021/ja01269a023.
[84] D. Sanz-Hernández, A. Fernández-Pacheco, Modelling focused electron beam induced deposition beyond Langmuir adsorption, Beilstein J. Nanotechnol. 8 (2017) 2151–2161, https://doi.org/10.3762/bjnano.8.214.
[85] G.L. Vignoles, W. Ros, I. Szelengowicz, C. Germain, A Brownian motion algorithm for tow scale modeling of chemical vapor infiltration, Comput. Mater. Sci. 50 (2011) 1871–1878, https://doi.org/10.1016/j.commatsci.2011.01.031.
[86] R.R. Kunz, T.M. Mayer, Electron beam induced surface nucleation and low-temperature decomposition of metal carbonyls, J. Vac. Sci. Technol. B Microelectron. Nanom. Struct. 6 (1988) 1557. https://doi.org/10.1116/1.584214.
[87] M. Drost, F. Tu, F. Vollnhals, I. Szenti, J. Kiss, H. Marbach, On the Principles of Tweaking Nanostructure Fabrication via Focused Electron Beam Induced Processing Combined with Catalytic Growth Processes, Small Methods. 1 (2017) 1700095, https://doi.org/10.1002/smtd.201700095.
[88] M.M. Walz, M. Schirmer, F. Vollnhals, T. Lukasczyk, H.-P. Steinrück, H. Marbach, Electrons as "Invisible Ink": Fabrication of Nanostructures by Local Electron Beam Induced Activation of SiO_x, Angew. Chemie - Int. Ed. 49 (2010) 4669–4673, https://doi.org/10.1002/anie.201001308.
[89] H. Marbach, Electron beam induced surface activation: a method for the lithographic fabrication of nanostructures via catalytic processes, Appl. Phys. A Mater. Sci. Process. 117 (2014) 987–995, https://doi.org/10.1007/s00339-014-8578-x.
[90] G.N. Parsons, R.D. Clark, Area-Selective Deposition: Fundamentals, Applications, and Future Outlook, Chem. Mater. 32 (2020) 4920–4953, https://doi.org/10.1021/acs.chemmater.0c00722.
[91] S.J.C. Irvine, D. Lamb, Photo-assisted CVD, in: A.C. Jones, M.L. Hitchman (Eds.), Chem. Vap. Depos. Precursors, Process. Appl., Royal Society of Chemistry, Cambridge, UK, 2009 https://doi.org/10.1039/9781847558794-00477.
[92] D.E. Newbury, N.W.M. Ritchie, Performing elemental microanalysis with high accuracy and high precision by scanning electron microscopy/silicon drift detector energy-dispersive X-ray spectrometry (SEM/SDD-EDS), J. Mater. Sci. 50 (2015) 493–518, https://doi.org/10.1007/s10853-014-8685-2.
[93] C. Haverkamp, G. Sarau, M.N. Polyakov, I. Utke, M.V. Puydinger dos Santos, S. Christiansen, K. Höflich, A novel copper precursor for electron beam induced deposition, Beilstein J. Nanotechnol. 9 (2018) 1220–1227, https://doi.org/10.3762/bjnano.9.113.
[94] D. Spoddig, K. Schindler, P. Rödiger, J. Barzola-Quiquia, K. Fritsch, H. Mulders, P. Esquinazi, Transport properties and growth parameters of PdC and WC nanowires prepared in a dual-beam microscope, Nanotechnology. 18 (2007) 495202, https://doi.org/10.1088/0957-4484/18/49/495202.
[95] A. Folch, J. Tejada, C.H. Peters, M.S. Wrighton, Electron beam deposition of gold nanostructures in a reactive environment, Appl. Phys. Lett. 66 (1995) 2080–2082, https://doi.org/10.1063/1.113909.
[96] A. Folch, J. Servat, J. Esteve, High-vacuum versus "environmental" electron beam deposition, J. Vac. Sci. Technol. B. 14 (1996) 2609–2614, https://doi.org/10.1116/1.588994.
[97] K. Höflich, J. Jurczyk, Y. Zhang, M.V. Puydinger dos Santos, M. Götz, C. Guerra-Nuñez, J.P. Best, C. Kapusta, I. Utke, Direct Electron Beam Writing of Silver-Based Nanostructures, ACS Appl. Mater. Interfaces. 9 (2017) 24071–24077, https://doi.org/10.1021/acsami.7b04353.
[98] C. O'Regan, A. Lee, J.D. Holmes, N. Petkov, P. Trompenaars, H. Mulders, Electrical properties of platinum interconnects deposited by electron beam induced deposition of the carbon-free precursor, $Pt(PF_3)_4$, J. Vac. Sci. Technol. B. 31 (2013) 021807, https://doi.org/10.1116/1.4794343.
[99] J.H. Moore, P. Swiderek, S. Matejcik, M. Allan, Fundamentals of interactions of electrons with molecules, in: P. Russell, I. Utke, S. Moshkalev (Eds.), Nanofabrication Using Focus. Ion Electron Beams Princ. Appl., Oxford University Press, New York, 2012: p. 184.
[100] L.G. Christophorou, J.K. Olthoff, Fundamental electron interactions with plasma processing gases, 1st ed., Springer, Boston, 2004, https://doi.org/10.1007/978-1-4419-8971-0.
[101] D.H. Fairbrother, S.G. Rosenberg, C.W. Hagen, I. Utke, P. Swiderek, Focused electron beam-induced processing, in: O. Ingólfsson (Ed.), Low-Energy Electrons Fundam. Appl., Pan Stanford, 2019: p. 219 https://doi.org/10.1201/9780429058820.
[102] J.H. Moore, C.C. Davis, M.A. Coplan, Building Scientific Apparatus, 2nd ed., Westview Press, 1989.
[103] J.D. Wnuk, S.G. Rosenberg, J.M. Gorham, W.F. van Dorp, C.W. Hagen, D.H. Fairbrother, Electron beam deposition for nanofabrication: Insights from surface science, Surf. Sci. 605 (2011) 257–266, https://doi.org/10.1016/j.susc.2010.10.035.
[104] M. Rohdenburg, P. Martinović, K. Ahlenhoff, S. Koch, D. Emmrich, A. Gölzhäuser, P. Swiderek, Cisplatin as a Potential Platinum Focused Electron Beam Induced Deposition Precursor: NH_3 Ligands Enhance the Electron-Induced Removal of Chlorine, J. Phys. Chem. C. 123 (2019) 21774–21787, https://doi.org/10.1021/acs.jpcc.9b05756.
[105] K. Ahlenhoff, C. Preischl, P. Swiderek, H. Marbach, Electron Beam-Induced Surface Activation of Metal-Organic Framework HKUST-1: Unraveling the Underlying Chemistry, J. Phys. Chem. C. 122 (2018) 26658–26670, https://doi.org/10.1021/acs.jpcc.8b06226.
[106] F. Zaera, Mechanisms of surface reactions in thin solid film chemical deposition processes, Coord. Chem. Rev. 257 (2013) 3177–3191, https://doi.org/10.1016/j.ccr.2013.04.006.
[107] Z. Warneke, M. Rohdenburg, J. Warneke, J. Kopyra, P. Swiderek, Electron-driven and thermal chemistry during water-assisted purification of platinum nanomaterials generated by electron beam induced deposition, Beilstein J. Nanotechnol. 9 (2018) 77–90, https://doi.org/10.3762/bjnano.9.10.
[108] T.E. Madey, Electron- and Photon-Stimulated Desorption: Probes of Structure and Bonding at Surfaces, Science 234 (1986) 316–322. https://doi.org/10.1126/science.234.4774.316.
[109] S. Massey, A.D. Bass, L. Sanche, Role of Low-Energy Electrons (<35 eV) in the Degradation of $Fe(CO)_5$ for Focused Electron Beam Induced Deposition Applications: Study by Electron Stimulated Desorption of Negative and Positive Ions, J. Phys. Chem. C. 119 (2015) 12708–12719, https://doi.org/10.1021/acs.jpcc.5b02684.
[110] A. Priebe, I. Utke, L. Pethö, J. Michler, Application of a Gas-Injection System during the FIB-TOF-SIMS Analysis - Influence of Water Vapor and Fluorine Gas on Secondary Ion Signals and Sputtering Rates, Anal. Chem. 91 (2019) 11712–11722, https://doi.org/10.1021/acs.analchem.9b02287.
[111] J.A. Spencer, Y.-C. Wu, L. McElwee-White, D.H. Fairbrother, Electron Induced Surface Reactions of *cis*-$Pt(CO)_2Cl_2$: A Route to Focused Electron Beam Induced Deposition of Pure Pt Nanostructures, J. Am. Chem. Soc. 138 (2016) 9172–9182, https://doi.org/10.1021/jacs.6b04156.
[112] J.D. Wnuk, J.M. Gorham, S.G. Rosenberg, W.F. van Dorp, T.E. Madey, C.W. Hagen, D.H. Fairbrother, Electron beam irradiation of dimethyl-(acetylacetonate) gold(III) adsorbed onto solid substrates, J. Appl. Phys. 107 (2010) 054301, https://doi.org/10.1063/1.3295918.
[113] W.G. Carden, R.M. Thorman, I. Unlu, K.A. Abboud, D.H. Fairbrother, L. McElwee-White, Design, Synthesis, and Evaluation of CF_3AuCNR Precursors for Focused Electron Beam-Induced Deposition of Gold, ACS Appl. Mater. Interfaces. 11 (2019) 11976–11987, https://doi.org/10.1021/acsami.8b18368.
[114] J.D. Wnuk, J.M. Gorham, S.G. Rosenberg, T.E. Madey, C.W. Hagen, D.H. Fairbrother, Atomic radical abatement of organic impurities from electron beam deposited metallic structures, J. Vac. Sci. Technol. B. 28 (2010) 527–537, https://doi.org/10.1116/1.3378142.
[115] S. Wang, Y.-M. Sun, Q. Wang, J.M. White, Electron-beam induced initial growth of platinum films using $Pt(PF_3)_4$, J. Vac. Sci. Technol. B. 22 (2004) 1803–1806, https://doi.org/10.1116/1.1761266.
[116] K. Bernal Ramos, M.J. Saly, Y.J. Chabal, Precursor design and reaction mechanisms for the atomic layer deposition of metal films, Coord. Chem. Rev. 257 (2013) 3271–3281, https://doi.org/10.1016/j.ccr.2013.03.028.
[117] J.-R. Chen, W. Zhang, R.K. Nahm, M.A. DiFeo, J.R. Engstrom, Design and characterization of a microreactor for spatially confined atomic layer deposition and in situ UHV surface analysis, J. Vac. Sci. Technol. A. 35 (2017) 061604, https://doi.org/10.1116/1.4996553.
[118] https://www.atomiclimits.com/2018/07/28/in-situ-studies-of-ald-processes-reaction-mechanisms, 2018.
[119] K. Knapas, M. Ritala, In Situ Studies on Reaction Mechanisms in Atomic Layer Deposition, Critical Reviews in Solid State and Materials Sciences 38 (2013) 167–202, https://doi.org/10.1080/10408436.2012.693460.
[120] T. Kruck, Trifluorophosphine Complexes of Transition Metals, Angew. Chemie Int. Ed. English. 6 (1967) 53–67, https://doi.org/10.1002/anie.196700531.
[121] A. Perentes, G. Sinicco, G. Boero, B. Dwir, P. Hoffmann, Focused electron beam induced deposition of nickel, J. Vac. Sci. Technol. B Microelectron. Nanom. Struct. 25 (2007) 2228–2232, https://doi.org/10.1116/1.2794071.
[122] Y. Ohshita, M. Ishikawa, T. Kada, H. Machida, A. Ogura, Ni Thin Film Deposition from Tetrakistrifluorophosphine-Nickel, Jpn. J. Appl. Phys. 44 (2005) L315–L317, https://doi.org/10.1143/JJAP.44.L315.
[123] R.S. Nyholm, The stereochemistry and valence states of nickel, Chem. Rev. 53 (1953) 263–308, https://doi.org/10.1021/cr60165a004.
[124] I.D. Kharitonov, V.A. Mazgunova, V.A. Babain, A.I. Kostylev, A.O. Merkushkin, A.A. Shemukhin, Y.V. Balakshin, A.V. Kozhemyako, S.N. Kalmykov, E.P. Magomedbekov, A CVD Process for Producing Atomic Current Sources Based on ^{63}Ni, Radiochemistry. 60 (2018) 158–163, https://doi.org/10.1134/S1066362218020054.
[125] T. Kruck, K. Baur, Synthesis of Tetrakis(trifluorophosphine)platinum(0) and Tetrakis(trifluorophosphine)palladium(0), Angew. Chemie Int. Ed. 4 (1965) 521, https://doi.org/10.1002/anie.196505211.
[126] A.P.J.M. Botman, Towards high purity nanostructures from electron beam induced deposition of platinum, Technische Universiteit Delft, 2009.
[127] G. Wilkinson, The Preparation and Properties of Tetrakistribromophosphine Nickel and Tetrakistrifluorophosphine Nickel, J. Am. Chem. Soc. 73 (1951) 5501–5502, https://doi.org/10.1021/ja01155a566.
[128] M.J. Rand, Chemical Vapor Deposition of Thin-Film Platinum, J. Electrochem. Soc. 120 (1973) 686–693, https://doi.org/10.1149/1.2403534.
[129] J.D. Barry, M. Ervin, J. Molstad, A. Wickenden, T. Brintlinger, P. Hoffman, J. Meingailis, Electron beam induced deposition of low resistivity platinum from $Pt(PF_3)_4$, J. Vac. Sci. Technol. B. 24 (2006) 3165–3168, https://doi.org/10.1116/1.2395962.
[130] S.G. Rosenberg, K. Landheer, C.W. Hagen, D.H. Fairbrother, Substrate temperature and electron fluence effects on metallic films created by electron beam induced deposition, J. Vac. Sci. Technol. B. 30 (2012) 051805, https://doi.org/10.1116/1.4751281.
[131] A. Botman, M. Hesselberth, J.J.L. Mulders, Improving the conductivity of platinum-containing nano-structures created by electron-beam-induced

deposition, Microelectron. Eng. 85 (2008) 1139–1142, https://doi.org/10.1016/j.mee.2007.12.036.
[132] M.H. Ervin, D. Chang, B. Nichols, A. Wickenden, J. Barry, J. Melngailis, Annealing of electron beam induced deposits of platinum from $Pt(PF_3)_4$, J. Vac. Sci. Technol. B. 25 (2007) 2250–2254, https://doi.org/10.1116/1.2806978.
[133] M. Takeguchi, M. Shimojo, K. Furuya, Post-deposition processes for nanostructures formed by electron beam induced deposition with $Pt(PF_3)_4$ precursor, Appl. Phys. A Mater. Sci. Process. 93 (2008) 439–442, https://doi.org/10.1007/s00339-008-4851-1.
[134] A. Botman, C.W. Hagen, J. Li, B.L. Thiel, K.A. Dunn, J.J.L. Mulders, S. Randolph, M. Toth, Electron postgrowth irradiation of platinum-containing nanostructures grown by electron-beam-induced deposition from $Pt(PF_3)_4$, J. Vac. Sci. Technol. B. 27 (2009) 2759–2763, https://doi.org/10.1116/1.3253551.
[135] C. Elbadawi, M. Toth, C.J. Lobo, Pure Platinum Nanostructures Grown by Electron Beam Induced Deposition, ACS Appl. Mater. Interfaces. 5 (2013) 9372–9376, https://doi.org/10.1021/am403167d.
[136] S.J. Randolph, A. Botman, M. Toth, Deposition of highly porous nanocrystalline platinum on functionalized substrates through fluorine-induced decomposition of $Pt(PF_3)_4$ adsorbates, Part. Part. Syst. Charact. 30 (2013) 672–677, https://doi.org/10.1002/ppsc.201300036.
[137] M. Ishikawa, I. Muramoto, H. Machida, S. Imai, A. Ogura, Y. Ohshita, Chemical vapor deposition of NiSi using $Ni(PF_3)_4$ and Si_3H_8, Thin Solid Films. 515 (2007) 8246–8249, https://doi.org/10.1016/j.tsf.2007.02.051.
[138] J.F. Friedman, T.M. Miller, J.K. Friedman-Schaffer, A.A. Viggiano, G.K. Rekha, A. E. Stevens, Electron attachment to $Ni(PF_3)_4$ and $Pt(PF_3)_4$, J. Chem. Phys. 128 (2008) 104303, https://doi.org/10.1063/1.2831391.
[139] M. Allan, Electron scattering in $Pt(PF_3)_4$: Elastic scattering, vibrational, and electronic excitation, J. Chem. Phys. 134 (2011) 204309, https://doi.org/10.1063/1.3594206.
[140] O. May, D. Kubala, M. Allan, Dissociative electron attachment to $Pt(PF_3)_4$-a precursor for Focused Electron Beam Induced Processing (FEBIP), Phys. Chem. Chem. Phys. 14 (2012) 2979–2982, https://doi.org/10.1039/c2cp23268e.
[141] K. Landheer, S.G. Rosenberg, L. Bernau, P. Swiderek, I. Utke, C.W. Hagen, D.H. Fairbrother, Low-Energy Electron-Induced Decomposition and Reactions of Adsorbed Tetrakis(trifluorophosphine)platinum $[Pt(PF_3)_4]$, J. Phys. Chem. C. 115 (2011) 17452–17463, https://doi.org/10.1021/jp204189k.
[142] M. Zlatar, M. Allan, J. Fedor, Excited states of $Pt(PF_3)_4$ and their role in focused electron beam nanofabrication, J. Phys. Chem. C. 120 (2016) 10667–10674, https://doi.org/10.1021/acs.jpcc.6b02660.
[143] M. Ishikawa, T. Kada, H. Machida, Y. Ohshita, A. Ogura, Ni Precursor for Chemical Vapor Deposition of NiSi, Jpn. J. Appl. Phys. 43 (2004) 1833–1836, https://doi.org/10.1143/JJAP.43.1833.
[144] C. Mansilla, Y. Zondag, J.J.L. Mulders, P.H.F. Trompenaars, Comparison of Pd electron beam induced deposition using two precursors and an oxygen purification strategy, Nanotechnology. 28 (2017) 375302, https://doi.org/10.1088/1361-6528/aa79e8.
[145] Y. Tatsuno, T. Yoshida, S. Otsuka, N. Al-Salem, B.L. Shaw, (η3-Allyl)Palladium (II) Complexes, in: Robert J. Angelici (Ed.), Inorg. Synth. Reagents Transit. Met. Complex Organomet. Synth. Vol. 28, Inorganic Syntheses, Inc., 1990: pp. 343–345 https://doi.org/10.1002/9780470132593.ch88.
[146] A. Chemical, (η3-Allyl)(η5-cyclopentadienyl)palladium(II), 98%, (2021). http://www.aspirasci.com/3-allyl-5-cyclopentadienylpalladiumii-98 (accessed January 12, 2021).
[147] K.W. Egger, Cyclopentadienyl-metal complexes II. Mass spectrometric and gas phase kinetic studies on the thermal stability and the structure of $(CH_3)_3Pt$-π-C_5H_5, J. Organomet. Chem. 24 (1970) 501–506, https://doi.org/10.1016/S0022-328X(00)80295-8.
[148] D.A. Tolan, Y.K. Abdel-Monem, M.A. El-Nagar, Anti-tumor platinum (IV) complexes bearing the anti-inflammatory drug naproxen in the axial position, Appl. Organomet. Chem. 33 (2019) e4763, https://doi.org/10.1002/aoc.4763.
[149] Merck, Trimethyl(methylcyclopentadienyl)platinum(IV) 98%, (2021). https://www.sigmaaldrich.com/PL/pl/product/aldrich/645605?context=product (accessed September 29, 2020).
[150] M. Hiratani, T. Nabatame, Y. Matsui, K. Imagawa, S. Kimura, Platinum Film Growth by Chemical Vapor Deposition Based on Autocatalytic Oxidative Decomposition, J. Electrochem. Soc. 148 (2001) C524–C527, https://doi.org/10.1149/1.1381389.
[151] X. Jiang, S.F. Bent, Area-Selective Atomic Layer Deposition of Platinum on YSZ Substrates Using Microcontact Printed SAMs, J. Electrochem. Soc. 154 (2007) D648–D656, https://doi.org/10.1149/1.2789301.
[152] Z. Xue, H. Thridandam, H.D. Kaesz, R.F. Hicks, Organometallic Chemical Vapor Deposition of Platinum. Reaction Kinetics and Vapor Pressures of Precursors, Chem. Mater. 4 (1992) 162–166, https://doi.org/10.1021/cm00019a032.
[153] J.-C. Hierso, P. Serp, R. Feurer, P. Kalck, MOCVD of rhodium, palladium and platinum complexes on fluidized divided substrates: Novel process for one-step preparation of noble-metal catalysts, Appl. Organomet. Chem. 12 (1998) 161–172, https://doi.org/10.1002/(SICI)1099-0739(199803)12:3<161::AID-AOC689>3.0.CO;2-6.
[154] D.S. Saulys, A. Ermakov, E.L. Garfunkel, P.A. Dowben, Electron-beam-induced patterned deposition of allylcyclopentadienyl palladium using scanning tunneling microscopy, J. Appl. Phys. 76 (1994) 7639–7641, https://doi.org/10.1063/1.357935.
[155] M. Weber, H.W.P. Koops, M. Rudolph, J. Kretz, G. Schmidt, New compound quantum dot materials produced by electron-beam induced deposition, J. Vac. Sci. Technol. B. 13 (1995) 1364–1368, https://doi.org/10.1116/1.587854.
[156] L. Rotkina, J.F. Lin, J.P. Bird, Nonlinear current-voltage characteristics of Pt nanowires and nanowire transistors fabricated by electron-beam deposition, Appl. Phys. Lett. 83 (2003) 4426–4428, https://doi.org/10.1063/1.1629382.
[157] O. Yavas, C. Ochiai, M. Takai, Y.K. Park, C. Lehrer, S. Lipp, L. Frey, H. Ryssel, A. Hosono, S. Okuda, Field emitter array fabricated using focused ion and electron beam induced reaction, J. Vac. Sci. Technol. B. 18 (2000) 976–979, https://doi.org/10.1116/1.591310.
[158] A. Botman, J.J.L. Mulders, R. Weemaes, S. Mentink, Purification of platinum and gold structures after electron-beam-induced deposition, Nanotechnology. 17 (2006) 3779–3785, https://doi.org/10.1088/0957-4484/17/15/028.
[159] R.M. Langford, T.-X. Wang, D. Ozkaya, Reducing the resistivity of electron and ion beam assisted deposited Pt, Microelectron. Eng. 84 (2007) 784–788, https://doi.org/10.1016/j.mee.2007.01.055.
[160] F. Porrati, R. Sachser, C.H. Schwalb, A.S. Frangakis, M. Huth, Tuning the electrical conductivity of Pt-containing granular metals by postgrowth electron irradiation, J. Appl. Phys. 109 (2011) 063715, https://doi.org/10.1063/1.3559773.
[161] R. Sachser, F. Porrati, C.H. Schwalb, M. Huth, Universal Conductance Correction in a Tunable Strongly Coupled Nanogranular Metal, Phys. Rev. Lett. 107 (2011) 206803, https://doi.org/10.1103/PhysRevLett.107.206803.
[162] S. Mehendale, J.J.L. Mulders, P.H.F. Trompenaars, A new sequential EBID process for the creation of pure Pt structures from $MeCpPtMe_3$, Nanotechnology. 24 (2013) 145303, https://doi.org/10.1088/0957-4484/24/14/145303.
[163] B. Geier, C. Gspan, R. Winkler, R. Schmied, J.D. Fowlkes, H. Fitzek, S. Rauch, J. Rattenberger, P.D. Rack, H. Plank, Rapid and Highly Compact Purification for Focused Electron Beam Induced Deposits: A Low Temperature Approach Using Electron Stimulated H_2O Reactions, J. Phys. Chem. C. 118 (2014) 14009–14016, https://doi.org/10.1021/jp503442b.
[164] A.J. Morris, R.T. McGibbon, A.B. Bocarsly, Electrocatalytic carbon dioxide activation: the rate-determining step of pyridinium-catalyzed CO_2 reduction, ChemSusChem 4 (2011) 191–196. https://doi.org/10.1002/cssc.201000379.
[165] B.B. Lewis, R. Winkler, X. Sang, P.R. Pudasaini, M.G. Stanford, H. Plank, R.R. Unocic, J.D. Fowlkes, P.D. Rack, 3D Nanoprinting via laser-assisted electron beam induced deposition: growth kinetics, enhanced purity, and electrical resistivity, Beilstein J. Nanotechnol. 8 (2017) 801–812, https://doi.org/10.3762/bjnano.8.83.
[166] H. Plank, T. Haber, C. Gspan, G. Kothleitner, F. Hofer, Chemical tuning of PtC nanostructures fabricated via focused electron beam induced deposition, Nanotechnology. 24 (2013) 175305, https://doi.org/10.1088/0957-4484/24/17/175305.
[167] J.D. Fowlkes, R. Winkler, B.B. Lewis, A. Fernández-Pacheco, L. Skoric, D. Sanz-Hernández, M.G. Stanford, E. Mutunga, P.D. Rack, H. Plank, High-Fidelity 3D-Nanoprinting via Focused Electron Beams: Computer-Aided Design (3BID), ACS Appl. Nano Mater. 1 (2018) 1028–1041, https://doi.org/10.1021/acsanm.7b00342.
[168] H.W.P. Koops, A. Kaya, M. Weber, Fabrication and characterization of platinum nanocrystalline material grown by electron-beam induced deposition, J. Vac. Sci. Technol. B. 13 (1995) 2400–2403, https://doi.org/10.1116/1.588008.
[169] S. Frabboni, G.C. Gazzadi, A. Spessot, TEM study of annealed Pt nanostructures grown by electron beam-induced deposition, Phys. E Low-Dimensional Syst. Nanostruct. 37 (2007) 265–269, https://doi.org/10.1016/j.physe.2006.06.018.
[170] A. Botman, J.J.L. Mulders, C.W. Hagen, Creating pure nanostructures from electron-beam-induced deposition using purification techniques: A technology perspective, Nanotechnology. 20 (2009) 372001, https://doi.org/10.1088/0957-4484/20/37/372001.
[171] J.J.L. Mulders, L.M. Belova, A. Riazanova, Electron beam induced deposition at elevated temperatures: Compositional changes and purity improvement, Nanotechnology. 22 (2011) 055302, https://doi.org/10.1088/0957-4484/22/5/055302.
[172] N.A. Roberts, J.D. Fowlkes, G.A. Magel, P.D. Rack, Enhanced material purity and resolution via synchronized laser assisted electron beam induced deposition of platinum, Nanoscale. 5 (2013) 408–415, https://doi.org/10.1039/c2nr33014h.
[173] R.M. Langford, D. Ozkaya, J. Sheridan, R. Chater, Effects of Water Vapour on Electron and Ion Beam Deposited Platinum, Microsc. Microanal. 10 (2004) 1122–1123, https://doi.org/10.1017/S1431927604883417.
[174] E. Villamor, F. Casanova, P.H.F. Trompenaars, J.J.L. Mulders, Embedded purification for electron beam induced Pt deposition using $MeCpPtMe_3$, Nanotechnology. 26 (2015) 095303, https://doi.org/10.1088/0957-4484/26/9/095303.
[175] M.G. Stanford, B.B. Lewis, J.H. Noh, J.D. Fowlkes, N.A. Roberts, H. Plank, P.D. Rack, Purification of Nanoscale Electron-Beam-Induced Platinum Deposits via a Pulsed Laser-Induced Oxidation Reaction, ACS Appl. Mater. Interfaces. 6 (2014) 21256–21263, https://doi.org/10.1021/am506246z.
[176] H. Plank, G. Kothleitner, F. Hofer, S.G. Michelitsch, C. Gspan, A. Hohenau, J. Krenn, Optimization of postgrowth electron-beam curing for focused electron-beam-induced Pt deposits, J. Vac. Sci. Technol. B. 29 (2011) 051801, https://doi.org/10.1116/1.3622314.
[177] H. Plank, J.H. Noh, J.D. Fowlkes, K. Lester, B.B. Lewis, P.D. Rack, Electron-Beam-Assisted Oxygen Purification at Low Temperatures for Electron-Beam-Induced Pt Deposits: Towards Pure and High-Fidelity Nanostructures, ACS Appl. Mater. Interfaces. 6 (2014) 1018–1024, https://doi.org/10.1021/am4045458.
[178] B.B. Lewis, M.G. Stanford, J.D. Fowlkes, K. Lester, H. Plank, P.D. Rack, Electron-stimulated purification of platinum nanostructures grown via focused

electron beam induced deposition, Beilstein J. Nanotechnol. 6 (2015) 907–918, https://doi.org/10.3762/bjnano.6.94.
[179] J.D. Fowlkes, B. Geier, B.B. Lewis, P.D. Rack, M.G. Stanford, R. Winkler, H. Plank, Electron nanoprobe induced oxidation: a simulation of direct-write purification, Phys. Chem. Chem. Phys. 17 (2015) 18294–18304, https://doi.org/10.1039/c5cp01196e.
[180] R. Sachser, H. Reizh, D. Huzel, M. Winhold, M. Huth, Catalytic Purification of Directly Written Nanostructured Pt Microelectrodes, ACS Appl. Mater. Interfaces. 6 (2014) 15868–15874, https://doi.org/10.1021/am503407y.
[181] H. Wang, G. Wu, X.P. Cai, Y. Zhao, Z.F. Shi, J. Wang, X.C. Xia, X. Dong, B.L. Zhang, Y. Ma, G.T. Du, Effect of growth temperature on structure and optical characters of NiO films fabricated by PA-MOCVD, Vacuum. 86 (2012) 2044–2047, https://doi.org/10.1016/j.vacuum.2012.05.006.
[182] J.E. Gozum, D.M. Pollina, J.A. Jensen, G.S. Girolami, "Tailored" organometallics as precursors for the chemical vapor deposition of high-purity palladium and platinum thin films, J. Am. Chem. Soc. 110 (1988) 2688–2689, https://doi.org/10.1021/ja00216a073.
[183] J.-C. Hierso, C. Satto, R. Feurer, P. Kalck, Organometallic Chemical Vapor Deposition of Palladium under Very Mild Conditions of Temperature in the Presence of a Low Reactive Gas Partial Pressure, Chem. Mater. 8 (1996) 2481–2485, https://doi.org/10.1021/cm960106m.
[184] Y. Chen, H.D. Kaesz, H. Thridandam, R.F. Hicks, Low-temperature organometallic chemical vapor deposition of platinum, Appl. Phys. Lett. 53 (1988) 1591–1592, https://doi.org/10.1063/1.99921.
[185] Z. Xue, M. Jane Strouse, D.K. Shuh, C.B. Knobler, H.D. Kaesz, R.F. Hicks, R.S. Williams, Characterization of (Methylcyclopentadienyl) trimethylplatinum and Low-Temperature Organometallic Chemical Vapor Deposition of Platinum Metal, J. Am. Chem. Soc. 111 (1989) 8779–8784, https://doi.org/10.1021/ja00206a002.
[186] R. Kumar, S. Roy, M. Rashidi, R.J. Puddephatt, New precursors for chemical vapour deposition of platinum and the hydrogen effect on cvd, Polyhedron. 8 (1989) 551–553, https://doi.org/10.1016/S0277-5387(00)80758-5.
[187] J.-H. Kwon, S.-G. Yoon, Preparation of Pt thin films deposited by metalorganic chemical vapor deposition for ferroelectric thin films, Thin Solid Films. 303 (1997) 136–142, https://doi.org/10.1016/S0040-6090(97)00003-5.
[188] E. Feurer, H. Suhr, Thin palladium films prepared by metal-organic plasma-enhanced chemical vapour deposition, Thin Solid Films. 157 (1988) 81–86, https://doi.org/10.1016/0040-6090(88)90348-3.
[189] E. Feurer, S. Kraus, H. Suhr, Plasma chemical vapor deposition of thin platinum films, J. Vac. Sci. Technol. A 7 (1989) 2799–2802, https://doi.org/10.1116/1.576182.
[190] I.J.M. Erkens, M.A. Verheijen, H.C.M. Knoops, T.F. Landaluce, F. Roozeboom, W.M.M. Kessels, Plasma-Assisted Atomic Layer Deposition of PtO_x from (MeCp)$PtMe_3$ and O_2 Plasma, Chem. Vap. Depos. 20 (2014) 258–268, https://doi.org/10.1002/cvde.201407109.
[191] H.C.M. Knoops, A.J.M. Mackus, M.E. Donders, M.C.M. van de Sanden, P.H.L. Notten, W.M.M. Kessels, Remote Plasma ALD of Platinum and Platinum Oxide Films, Electrochem. Solid-State Lett. 12 (2009) G34–G36, https://doi.org/10.1149/1.3125876.
[192] J. Chae, H.-S. Park, S.-W. Kang, Atomic Layer Deposition of Nickel by the Reduction of Preformed Nickel Oxide, Electrochem. Solid-State Lett. 5 (2002) C64–C67, https://doi.org/10.1149/1.1475199.
[193] M. Daub, M. Knez, U. Goesele, K. Nielsch, Ferromagnetic nanotubes by atomic layer deposition in anodic alumina membranes, J. Appl. Phys. 101 (2007) 09J111, https://doi.org/10.1063/1.2712057.
[194] Q. Fang, Growth of platinum films by atomic layer deposition (ALD), White Pap. - Oxford Instruments. 44 (2009).
[195] H. Van Bui, F. Grillo, J.R. Van Ommen, Atomic and molecular layer deposition: off the beaten track, Chem. Commun. 53 (2017) 45–71, https://doi.org/10.1039/c6cc05568k.
[196] T. Aaltonen, M. Ritala, T. Sajavaara, J. Keinonen, M. Leskelä, Atomic Layer Deposition of Platinum Thin Films, Chem. Mater. 15 (2003) 1924–1928, https://doi.org/10.1021/cm021333t.
[197] A.J.M. Mackus, N. Leick, L. Baker, W.M.M. Kessels, Catalytic Combustion and Dehydrogenation Reactions during Atomic Layer Deposition of Platinum, Chem. Mater. 24 (2012) 1752–1761, https://doi.org/10.1021/cm203812v.
[198] M. Van Daele, C. Detavernier, J. Dendooven, Surface species during ALD of platinum observed with: In situ reflection IR spectroscopy, Phys. Chem. Chem. Phys. 20 (2018) 25343–25356, https://doi.org/10.1039/c8cp03585g.
[199] A.J.M. Mackus, D. Garcia-Alonso, H.C.M. Knoops, A.A. Bol, W.M.M. Kessels, Room-Temperature Atomic Layer Deposition of Platinum, Chem. Mater. 25 (2013) 1769–1774, https://doi.org/10.1021/cm400274n.
[200] F. Grillo, J.A. Moulijn, M.T. Kreutzer, J.R. van Ommen, Nanoparticle sintering in atomic layer deposition of supported catalysts: Kinetic modeling of the size distribution, Catal. Today. 316 (2018) 51–61, https://doi.org/10.1016/j.cattod.2018.02.020.
[201] J. Dendooven, R.K. Ramachandran, E. Solano, M. Kurttepeli, L. Geerts, G. Heremans, J. Rongé, M.M. Minjauw, T. Dobbelaere, K. Devloo-Casier, J.A. Martens, A. Vantomme, S. Bals, G. Portale, A. Coati, C. Detavernier, Independent tuning of size and coverage of supported Pt nanoparticles using atomic layer deposition, Nat. Commun. 8 (2017) 1074, https://doi.org/10.1038/s41467-017-01140-z.
[202] S.M. Geyer, R. Methaapanon, R. Johnson, S. Brennan, M.F. Toney, B. Clemens, S. Bent, Structural evolution of platinum thin films grown by atomic layer deposition, J. Appl. Phys. 116 (2014) 064905, https://doi.org/10.1063/1.4892104.
[203] A.J.M. Mackus, M.J. Weber, N.F.W. Thissen, D. Garcia-Alonso, R.H.J. Vervuurt, S. Assali, A.A. Bol, M.A. Verheijen, W.M.M. Kessels, Atomic layer deposition of Pd and Pt nanoparticles for catalysis: On the mechanisms of nanoparticle formation, Nanotechnology. 27 (2016) 34001, https://doi.org/10.1088/0957-4484/27/3/034001.
[204] F. Grillo, H. Van Bui, J.A. Moulijn, M.T. Kreutzer, J.R. van Ommen, Understanding and Controlling the Aggregative Growth of Platinum Nanoparticles in Atomic Layer Deposition: An Avenue to Size Selection, J. Phys. Chem. Lett. 8 (2017) 975–983, https://doi.org/10.1021/acs.jpclett.6b02978.
[205] G.T. Stauf, P.A. Dowben, K. Emrich, S. Barfuss, W. Hirschwald, N.M. Boag, Stability and Decomposition of Gaseous Allylcyclopentadienylpalladium, J. Phys. Chem. 93 (1989) 749–753, https://doi.org/10.1021/j100339a048.
[206] S. Engmann, M. Stano, Š. Matejčík, O. Ingólfsson, Gas phase low energy electron induced decomposition of the focused electron beam induced deposition (FEBID) precursor trimethyl (methylcyclopentadienyl) platinum(IV) (MeCpPtMe_3), Phys. Chem. Chem. Phys. 14 (2012) 14611–14618, https://doi.org/10.1039/c2cp42637d.
[207] A. Niklewski, T. Strunskus, G. Witte, C. Wöll, Metal-Organic Chemical Vapor Deposition of Palladium: Spectroscopic Study of Cyclopentadienyl-allyl-palladium Deposition on a Palladium Substrate, Chem. Mater. 17 (2005) 861–868, https://doi.org/10.1021/cm048798z.
[208] Q.-H. Wu, M. Gunia, T. Strunskus, G. Witte, M. Muhler, C. Wöll, Deposition of palladium from a Cylcopentadienyl-allyl-palladium Precursor on Si-Based Substrates with Various Pretreatments: The Role of Surface Si-OH and Si-H Species Studied by X-ray Photoelectron Spectroscopy, Chem. Vap. Depos. 11 (2005) 355–361, https://doi.org/10.1002/cvde.200506390.
[209] J.D. Wnuk, J.M. Gorham, S.G. Rosenberg, W.F. van Dorp, T.E. Madey, C.W. Hagen, D.H. Fairbrother, Electron Induced Surface Reactions of the Organometallic Precursor Trimethyl(methylcyclopentadienyl)platinum(IV), J. Phys. Chem. C. 113 (2009) 2487–2496, https://doi.org/10.1021/jp807824c.
[210] M.N. Hedhili, J.H. Bredehöft, P. Swiderek, Electron-Induced Reactions of MeCpPtMe_3 investigated by HREELS, J. Phys. Chem. C. 113 (2009) 13282–13286, https://doi.org/10.1021/jp810834r.
[211] C. Lien, H. Sun, X. Qin, F. Zaera, Platinum atomic layer deposition on metal substrates: A surface chemistry study, Surf. Sci. 677 (2018) 161–166, https://doi.org/10.1016/j.susc.2018.07.002.
[212] C. Lien, M. Konh, B. Chen, A.V. Teplyakov, F. Zaera, Gas-Phase Electron-Impact Activation of Atomic Layer Deposition (ALD) Precursors: MeCpPtMe_3, J. Phys. Chem. Lett. 9 (2018) 4602–4606, https://doi.org/10.1021/acs.jpclett.8b02125.
[213] B. Karasulu, R.H.J. Vervuurt, W.M.M. Kessels, A.A. Bol, Continuous and ultrathin platinum films on graphene using atomic layer deposition: A combined computational and experimental study, Nanoscale. 8 (2016) 19829–19845, https://doi.org/10.1039/c6nr07483a.
[214] Merck, Nickel(II) hexafluoroacetylacetonate hydrate, Mater. Saf. Data Sheet. (2021). https://us.vwr.com/assetsvc/asset/en_US/id/16490607/contents (accessed January 12, 2021).
[215] K. V. Katok, V.A. Tertykh, S.Y. Brichka, G.P. Prikhod'ko, Catalytic synthesis of carbon nanotubes over ordered mesoporous matrices, J. Therm. Anal. Calorim. 86 (2006) 109–114. https://doi.org/10.1007/s10973-006-7584-4.
[216] J.P. Murray, J.O. Hill, DSC determination of the sublimation enthalpy of tris(2,4-pentanedionato)cobalt(III) and bis(2,4-pentanedionato)-nickel(II) and -copper(II), Thermochim. Acta. 109 (1987) 383–390, https://doi.org/10.1016/0040-6031(87)80034-5.
[217] Y. Yu, Y. Liu, J. Wang, S. Qing, K. Yu, Catalyst Enhanced Chemical Vapor Deposition of Nickel on Polymer Surface, J. Wuhan Univ. Technol. Mater. Sci. Ed. 34 (2019) 293–298, https://doi.org/10.1007/s11595-019-2049-3.
[218] S.M. Pillai, T. G. L., R. M., Dimerization of ethylene catalyzed by β-diketonate complexes of cobalt and nickel, J. Mol. Catal. 58 (1990) 171–183.
[219] W.-C. GmbH, Process for preparing palladium(II)acetylacetonate, US3960909 (1976).
[220] A.R. Siedle, R.A. Newmark, L.H. Pignolet, Structure of Palladium Bis (hexafluoroacetylacetonate) and the Systematics of Its Acid-Base Chemistry, Inorg. Chem. 22 (1983) 2281–2286, https://doi.org/10.1021/ic00158a012.
[221] S. Okeya, S. Ooi, K. Matsumoto, Y. Nakamura, S. Kawaguchi, Bis(β-diketonato)-palladium(II) and -platinum(II) Complexes, Bull. Chem. Soc. Jpn. 54 (1981) 1085–1095, https://doi.org/10.1246/bcsj.54.1085.
[222] A.R. Siedle, R.A. Newmark, A.A. Kruger, L.H. Pignolet, 2:1 Lewis Base Adducts of Palladium Bis(hexafluoroacetylacetonate). Structure and β-Diketonate Exchange in (bpy)Pd($C_5HF_6O_2$)$_2$, Inorg. Chem. 20 (1981) 3399–3404, https://doi.org/10.1021/ic50224a049.
[223] J.J. Senkevich, G.R. Yang, T.M. Lu, T.S. Cale, C. Jezewski, W.A. Lanford, Phosphorus Atomic Layers Promoting the Chemisorption of Highly Polarizable Transition Metallorganics, Chem. Vap. Depos. 8 (2002) 189–192, https://doi.org/10.1002/1521-3862(20020903)8:5<189::AID-CVDE189>3.0.CO;2-Y.
[224] S. Voss, D. Zeng, S. Jeffery, K. King, Process for the preperation of platinum acetylacetonato complexes, EP20080022220 (2008). https://patents.google.com/patent/US7442820B1/en.
[225] N.B. Morozova, G.I. Zharkova, P.P. Semyannikov, S. V. Sysoev, I.K. Igumenov, N.E. Fedotova, N. V. Gelfond, Vapor pressure of precursors for CVD on the base of platinum group metals, J Phys. IV Fr. 11 (2001) Pr3-609-Pr3-616, https://doi.org/10.1051/jp4:2001377.
[226] S. Flanagan, E. Hall, W. Bowie, J.W. Fuhs, R. Logan, F. Maniei, A. Hunt, A design-of-experiments approach to modeling activity coefficients in solvent mixtures: A case study using platinum(II) acetylacetonate in mixtures of

acetone, cyclohexanol, 1,2,3,4-tetrahydronaphthalene and propylene carbonate, Green Chem. 7 (2005) 333–338, https://doi.org/10.1039/b418130a.
[227] Strem Chemicals, Platinum(II) hexafluoroacetylacetonate, 98% (99.9%-Pt), (2021). https://www.strem.com/catalog/v/78-1550/53/platinum_65353-51-7 (accessed September 29, 2020).
[228] G.I. Zharkova, P.A. Stabnikov, S.A. Sysoev, I.K. Igumenov, Volatility and crystal lattice energy of palladium(II) chelates, J. Struct. Chem. 46 (2005) 320–327, https://doi.org/10.1007/s10947-006-0047-8.
[229] I. Igumenov, MO CVD of Noble Metals, J. Phys. IV Colloq. 05 (1995) C5-489-C5-496. https://doi.org/10.1051/jphyscol:1995556.
[230] C. Garrido, H. van den Bergh, Temperature effect on photolytic deposition of platinum ohmic contacts and schottky diodes, Appl. Phys. A Solids Surfaces. 53 (1991) 265–272, https://doi.org/10.1007/BF00324263.
[231] E.W. Berg, J.T. Truemper, Vapor pressure-temperature data for various metal β-diketone chelates, Anal. Chim. Acta. 32 (1965) 245–252, https://doi.org/10.1016/S0003-2670(00)88930-8.
[232] D.R. Diercks, B.P. Gorman, J.J.L. Mulders, Electron Beam-Induced Deposition for Atom Probe Tomography Specimen Capping Layers, Microsc. Microanal. 23 (2017) 321–328, https://doi.org/10.1017/S1431927616011740.
[233] T. Maruyama, T. Tago, Nickel thin films prepared by chemical vapour deposition from nickel acetylacetonate, J. Mater. Sci. 28 (1993) 5345–5348, https://doi.org/10.1007/BF00570088.
[234] V. Cominos, A. Gavriilidis, Sublimation and deposition behaviour of palladium (II) acetylacetonate, Eur. Phys. J. AP. 15 (2001) 23–33, https://doi.org/10.1051/epjap:2001164.
[235] G.Y. Meng, L. Huang, M. Pan, C.S. Chen, D.K. Peng, Preparation and characterization of Pd and Pd-Ni alloy membranes on porous substrates by MOCVD with mixed metal β-diketone precursors, Mater. Res. Bull. 32 (1997) 385–395, https://doi.org/10.1016/S0025-5408(97)00005-6.
[236] V. Bhaskaran, M.J. Hampden-Smith, T.T. Kodas, Palladium Thin Films Grown by CVD from (1,1,1,5,5,5-Hexafluoro-2,4-pentanedionato) Palladium(II), Chem. Vap. Depos. 3 (1997) 281–286, https://doi.org/10.1002/cvde.19970030206.
[237] Z. Yuan, R.J. Puddephatt, Allyl(β-diketonato)palladium(II) Complexes as Precursors for Palladium Films, Adv. Mater. 6 (1994) 51–54, https://doi.org/10.1002/adma.19940060109.
[238] K. Daub, V.K. Wunder, R. Dittmeyer, CVD preparation of catalytic membranes for reduction of nitrates in water, Catal. Today. 67 (2001) 257–272, https://doi.org/10.1016/S0920-5861(01)00313-3.
[239] G. Malandrino, R. Lo Nigro, I.L. Fragalà, MOCVD of platinum (100)-oriented films on random hastelloy C276, Chem. Vap. Depos. 5 (1999) 59–61, https://doi.org/10.1002/(sici)1521-3862(199903)5:2<59::aid-cvde59>3.0.co;2-q.
[240] J.M. Lee, S.-K. Hong, C.S. Hwang, H.J. Kim, C.-G. Suk, Characterization of Pt Electrodes for Ferroelectric Thin Films Prepared by Metallorganic Chemical Vapor Deposition Using $Pt(CF_3COCHCOCF_3)_2$ and $(CH_3C_5H_4)Pt(CH_3)_3$, J. Korean Phys. Soc. 33 (1998) S148–S151. https://www.jkps.or.kr/journal/download_pdf.php?spage=148&volume=33&number=9(2).
[241] J.W. Elam, A. Zinovev, C.Y. Han, H.H. Wang, U. Welp, J.N. Hryn, M.J. Pellin, Atomic layer deposition of palladium films on Al_2O_3 surfaces, Thin Solid Films. 515 (2006) 1664–1673, https://doi.org/10.1016/j.tsf.2006.05.049.
[242] J.J. Senkevich, F. Tang, D. Rogers, J.T. Drotar, C. Jezewski, W.A. Lanford, G.-C. Wang, T.-M. Lu, Substrate-Independent Palladium Atomic Layer Deposition, Chem. Vap. Depos. 9 (2003) 258–264, https://doi.org/10.1002/cvde.200306246.
[243] G.A.T. Eyck, J.J. Senkevich, F. Tang, D. Liu, S. Pimanpang, T. Karaback, G.-C. Wang, T.-M. Lu, C. Jezewski, W.A. Lanford, Plasma-assisted Atomic Layer Deposition of Palladium, Chem. Vap. Depos. 11 (2005) 60–66, https://doi.org/10.1002/cvde.200306312.
[244] M. Utriainen, M. Kröger-Laukkanen, L.-S. Johansson, L. Niinistö, Studies of metallic thin film growth in an atomic layer epitaxy reactor using $M(acac)_2$ (M = Ni, Cu, Pt) precursors, Appl. Surf. Sci. 157 (2000) 151–158, https://doi.org/10.1016/S0169-4332(99)00562-0.
[245] J. Hämäläinen, E. Puukilainen, T. Sajavaara, M. Ritala, M. Leskelä, Low temperature atomic layer deposition of noble metals using ozone and molecular hydrogen as reactants, Thin Solid Films. 531 (2013) 243–250, https://doi.org/10.1016/j.tsf.2013.01.091.
[246] S.G. Rosenberg, M. Barclay, D.H. Fairbrother, Electron Induced Surface Reactions of Organometallic $Metal(hfac)_2$ Precursors and Deposit Purification, ACS Appl. Mater. Interfaces. 6 (2014) 8590–8601, https://doi.org/10.1021/am501457h.
[247] S. Engmann, B. Ómarsson, M. Lacko, M. Stano, Š. Matejčík, O. Ingólfsson, Dissociative electron attachment to hexafluoroacetylacetone and its bidentate metal complexes $M(hfac)_2$; M = Cu, Pd, J. Chem. Phys. 138 (2013) 234309, https://doi.org/10.1063/1.4810877.
[248] T. Weiss, J. Warneke, V. Zielasek, P. Swiderek, M. Bäumer, XPS study of thermal and electron-induced decomposition of Ni and Co acetylacetonate thin films for metal deposition, J. Vac. Sci. Technol. A Vacuum, Surfaces, Film. 34 (2016) 041515, https://doi.org/10.1116/1.4953469.
[249] G.O. Hunter, J.O. Lerach, T.R. Lockso, B.D. Leskiw, The gas-phase ligand exchange of copper and nickel acetylacetonate, hexafluoroacetylacetonate and trifluorotrimethylacetylacetonate complexes, Rapid Commun. Mass Spectrom. 24 (2010) 129–137, https://doi.org/10.1002/rcm.4370.
[250] E.L. Crane, Y. You, R.G. Nuzzo, G.S. Girolami, Mechanistic Studies of CVD Metallization Processes: Reactions of Rhodium and Platinum β-Diketonate Complexes on Copper Surfaces, J. Am. Chem. Soc. 122 (2000) 3422–3435, https://doi.org/10.1021/ja993653s.
[251] J. Kopyra, C. Koenig-Lehmann, I. Bald, E. Illenberger, A Single Slow Electron Triggers the Loss of Both Chlorine Atoms from the Anticancer Drug Cisplatin: Implications for Chemoradiation Therapy, Angew. Chemie - Int. Ed. 48 (2009) 7904–7907, https://doi.org/10.1002/anie.200903874.
[252] M. Juhász, S. Takahashi, T. Fujii, Temperature-resolved thermal analysis of cisplatin by evolved gas analysis-mass spectrometry, J. Anal. Appl. Pyrolysis. 91 (2011) 114–118, https://doi.org/10.1016/j.jaap.2011.01.009.
[253] J. Warneke, M. Rohdenburg, Y. Zhang, J. Orzagh, A. Vaz, I. Utke, J.T.M. De Hosson, W.F. Van Dorp, P. Swiderek, Role of NH_3 in the Electron-Induced Reactions of Adsorbed and Solid Cisplatin, J. Phys. Chem. C. 120 (2016) 4112–4120, https://doi.org/10.1021/acs.jpcc.5b12184.
[254] F. Ferreira Da Silva, R.M. Thorman, R. Bjornsson, H. Lu, L. Mcelwee-White, O. Ingólfsson, Dissociation of the FEBID precursor *cis*-$Pt(CO)_2Cl_2$ driven by low-energy electrons, Phys. Chem. Chem. Phys. 22 (2020) 6100–6108, https://doi.org/10.1039/c9cp06633k.
[255] S. Dasari, P. Bernard Tchounwou, Cisplatin in cancer therapy: Molecular mechanisms of action, Eur. J. Pharmacol. 740 (2014) 364–378, https://doi.org/10.1016/j.ejphar.2014.07.025.
[256] T.K. Kiffmeyer, C. Kube, S. Opiolka, K.G. Schmidt, G. Schöppe, P.J.M. Sessink, Vapour pressures, evaporation behaviour and airborne concentrations of hazardous drugs: implications for occupational safety, Pharm. J. 268 (2002) 331–337.
[257] J.A. Spencer, M. Barclay, M.J. Gallagher, R. Winkler, I. Unlu, Y.-C.C. Wu, H. Plank, L. McElwee-White, D.H. Fairbrother, Comparing postdeposition reactions of electrons and radicals with Pt nanostructures created by focused electron beam induced deposition, Beilstein J. Nanotechnol. 8 (2017) 2410–2424, https://doi.org/10.3762/bjnano.8.240.
[258] A. Mahgoub, H. Lu, R.M. Thorman, K. Preradovic, T. Jurca, L. McElwee-White, H. Fairbrother, C.W. Hagen, Electron beam-induced deposition of platinum from $Pt(CO)_2Cl_2$ and $Pt(CO)_2Br_2$, Beilstein J. Nanotechnol. 11 (2020) 1789–1800, https://doi.org/10.3762/bjnano.11.161.
[259] E. Böhler, J.H. Bredehöft, P. Swiderek, Low-energy electron-induced hydroamination reactions between different amines and olefins, J. Phys. Chem. C. 118 (2014) 6922–6933, https://doi.org/10.1021/jp501192v.
[260] B.D. Fahlman, A.R. Barron, Substituent effects on the volatility of metal β-diketonates, Adv. Mater. Opt. Electron. 10 (2000) 223–232, https://doi.org/10.1002/1099-0712(200005/10)10:3/5<223::AID-AMO411>3.0.CO;2-M.
[261] A. Devi, J. Goswami, R. Lakshmi, S.A. Shivashankar, S. Chandrasekaran, A novel Cu(II) chemical vapor deposition precursor: Synthesis, characterization, and chemical vapor deposition, J. Mater. Res. 13 (1998) 687–692, https://doi.org/10.1557/JMR.1998.0086.
[262] D.P. Graddon, The absorption spectra of complex salts-III cupric ethylacetoacetate, J. Inorg. Nucl. Chem. 14 (1960) 161–168, https://doi.org/10.1016/0022-1902(60)80253-9.
[263] A.G. Bunn, P.J. Carroll, B.B. Wayland, Coordination Polymers of Tetracyanoethylene with Metal Hexafluoroacetylacetonates : Formation and X-Ray Crystal Structures, Inorg. Chem. 31 (1992) 1297–1299, https://doi.org/10.1021/ic00033a031.
[264] Y. Pauleau, A.Y. Fasasi, Kinetics of Sublimation of Copper(II) Acetylacetonate Complex Used for Chemical Vapor Deposition of Copper Films, Chem. Mater. 3 (1991) 45–50, https://doi.org/10.1021/cm00013a015.
[265] E.W. Berg, J.T. Truemper, A study of the volatile characteristics of various metal β-diketone chelates, J. Phys. Chem. 64 (1960) 487–490, https://doi.org/10.1021/j100833a029.
[266] M.K. Chaudhuri, S.K. Dehury, S.S. Dhar, U. Bora, B.M. Choudary, L.K. Mannepalli, Process for making metal acetylacetonates - United States Patent, US7282573B2, 2007. https://patents.google.com/patent/US7282573B2.
[267] M. Widmer, Deposition Pyrolytique Induite par Laser de Microstructures en Cuivre a Partir de Precurseurs Volatils., EPFL, PhD thesis N° 1075, 1992.
[268] A. Jain, T.T. Kodas, T.S. Corbitt, M.J. Hampden-Smith, Chemical Vapor Deposition of Copper from (hfac)CuL (L = VTMS and 2-butyne) in the Presence of Water, Methanol, and Dimethyl Ether, Chem. Mater. 8 (1996) 1119–1127, https://doi.org/10.1021/cm950546y.
[269] R. Teghil, D. Ferro, L. Bencivenni, M. Pelino, A thermodynamic study of the sublimation processes of aluminium and copper acetylacetonates, Thermochim. Acta. 44 (1981) 213–222. https://doi.org/10.1016/0040-6031(81)80042-1.
[270] W.R. Wolf, R.E. Sievers, G.H. Brown, Vapor Pressure Measurements and Gas Chromatographic Studies of the Solution Thermodynamics of Metal β-Diketonates, Inorg. Chem. 11 (1972) 1995–2002, https://doi.org/10.1021/ic50115a003.
[271] D. Temple, A. Reisman, Chemical Vapor Deposition of Copper from Copper (II) Hexafluoroacetylacetonate, J. Electrochem. Soc. 136 (1989) 3525–3529, https://doi.org/10.1149/1.2096498.
[272] A. Luisier, I. Utke, T. Bret, F. Cicoira, R. Hauert, S.-W. Rhee, P. Doppelt, P. Hoffmann, Comparative Study of Cu Precursors for 3D Focused Electron Beam Induced Deposition, J. Electrochem. Soc. 151 (2004) C535–C537, https://doi.org/10.1149/1.1765680.
[273] A. Szkudlarek, A.R. Vaz, Y. Zhang, A. Rudkowski, C. Kapusta, R. Erni, S. Moshkalev, I. Utke, Formation of pure Cu nanocrystals upon post-growth annealing of Cu-C material obtained from focused electron beam induced deposition: comparison of different methods, Beilstein J. Nanotechnol. 6 (2015) 1508–1517, https://doi.org/10.3762/bjnano.6.156.
[274] M.V. Puydinger dos Santos, A. Szkudlarek, A. Rydosz, C. Guerra-Nuñez, F. Béron, K.R. Pirota, S. Moshkalev, J.A. Diniz, I. Utke, M.V.P. dos Santos, A.

Szkudlarek, A. Rydosz, C. Guerra-Nuñez, F. Béron, K.R. Pirota, S. Moshkalev, J. A. Diniz, I. Utke, Comparative study of post-growth annealing of $Cu(hfac)_2$, $Co_2(CO)_8$ and $Me_2Au(acac)$ metal precursors deposited by FEBID, Beilstein J. Nanotechnol. 9 (2018) 91–101, https://doi.org/10.3762/bjnano.9.11.
[275] H. Miyazoe, I. Utke, H. Kikuchi, S. Kiriu, V. Friedli, J. Michler, K. Terashima, Improving the metallic content of focused electron beam-induced deposits by a scanning electron microscope integrated hydrogen-argon microplasma generator, J. Vac. Sci. Technol. B. 28 (2010) 744–750, https://doi.org/10.1116/1.3449808.
[276] B. Lecohier, B. Calpini, J.-M. Philippoz, H. van den Bergh, D. Laub, P.A. Buffat, Copper Film Growth by Chemical Vapor Deposition: Electrical and Optical Measurements in Real Time, and Studies of Morphology, J. Electrochem. Soc. 140 (1993) 789–796, https://doi.org/10.1149/1.2056160.
[277] R.L. Van Hemert, L.B. Spendlove, R.E. Sievers, Vapor Deposition of Metals by Hydrogen Reduction of Metal Chelates, J. Electrochem. Soc. 112 (1965) 1123–1126, https://doi.org/10.1149/1.2423376.
[278] L.H. Dubois, P.M. Jeffries, G.. Girolami, Advanced Metallization for ULSZ Applications, in: V.V.S. Rana, R.V. Joshi, I. Ohdomari (Eds.), Adv. Met. ULSZ Appl., Materials Research Society, Pittsburgh, PA, 1992: pp. 375–381.
[279] A.E. Kaloyeros, A. Feng, J. Garhart, K.C. Brooks, S.K. Ghosh, A.N. Saxena, F. Luehrs, Low-Temperature Metal-Organic Chemical Vapor Deposition (LTMOCVD) of Device-Quality Copper Films for Microelectronic Applications, J. Electron. Mater. 19 (1990) 271–276, https://doi.org/10.1007/BF02733818.
[280] G. Ramaswamy, A.K. Raychaudhuri, J. Goswami, S.A. Shivashankar, Scanning tunneling microscope study of the morphology of chemical vapor deposited copper films and its correlation with resistivity, J. Appl. Phys. 82 (1997) 3797–3807, https://doi.org/10.1063/1.365742.
[281] J. Goswami, S.A. Shivashankar, G. Anathakrishna, Effects of reaction kinetics on the microstructure of chemical vapour deposited copper films: Experiment and simulation, Thin Solid Films. 305 (1997) 52–60, https://doi.org/10.1016/S0040-6090(97)00189-2.
[282] H. Li, E.T. Eisenbraun, A.E. Kaloyeros, Remote plasma chemical vapor deposition of copper for applications in microelectronics, J. Vac. Sci. Technol. B Microelectron. Nanom. Struct. 10 (1992) 1337. https://doi.org/10.1116/1.585865.
[283] C. Oehr, H. Suhr, Thin Copper Films by Plasma CVD Using Copper-Hexafluoro-Acetylacetonate, Appl. Phys. A Solids Surf. 45 (1988) 151–154, https://doi.org/10.1007/BF02565202.
[284] J. Pelletier, R. Pantel, J.C. Oberlin, Y. Pauleau, P. Gouy-Pailler, Preparation of copper thin films at ambient temperature by microwave plasma-enhanced chemical vapor deposition from the copper (II) acetylacetonate-argon-hydrogen system, J. Appl. Phys. 70 (1991) 3862–3866, https://doi.org/10.1063/1.349192.
[285] N. Awaya, Y. Arita, Plasma-Enhanced Chemical Vapor Deposition of Copper, Jpn. J. Appl. Phys. 30 (1991) 1813–1817, https://doi.org/10.1143/JJAP.30.1813.
[286] J. Huo, R. Solanki, J. McAndrew, Characteristics of copper films produced via atomic layer deposition, J. Mater. Res. 17 (2002) 2394–2398, https://doi.org/10.1557/JMR.2002.0350.
[287] R.P. Chaukulkar, N.F.W. Thissen, V.R. Rai, S. Agarwal, Low temperature hydrogen plasma-assisted atomic layer deposition of copper studied using in situ infrared reflection absorption spectroscopy, J. Vac. Sci. Technol. A. 32 (2014) 01A108, https://doi.org/10.1116/1.4831915.
[288] Unpublished experiments carried out in a home-built ALD reactor repeatedly resulted in a CVD process.
[289] T.S. Tripathi, M. Karppinen, Efficient Process for Direct Atomic Layer Deposition of Metallic Cu Thin Films Based on an Organic Reductant, Chem. Mater. 29 (2017) 1230–1235, https://doi.org/10.1021/acs.chemmater.6b04597.
[290] S.E. Stein, NIST Chemistry WebBook, NIST Standard Reference Database, in: P. J. Linstrom, W.G. Mallard (Eds.), National Institute of Standards and Technology, Gaithersburg, MD, 20899, 2013: p. Number 69.
[291] J. Kopyra, F. Rabilloud, H. Abdoul-Carime, Interaction of gas phase copper(II) acetylacetonate with slow electrons, Phys. Chem. Chem. Phys. 20 (2018) 7746–7753, https://doi.org/10.1039/c7cp08149a.
[292] M. Rohdenburg, H. Boeckers, C.R. Brewer, L. McElwee-White, P. Swiderek, Efficient NH_3-based process to remove chlorine from electron beam deposited ruthenium produced from $(\eta^3\text{-}C_3H_5)Ru(CO)_3Cl$, Sci. Rep. 10 (2020) 10901, https://doi.org/10.1038/s41598-020-67803-y.
[293] S.L. Cohen, M. Liehr, S. Kasi, Selectivity in copper chemical vapor deposition, Appl. Phys. Lett. 60 (1992) 1585–1587, https://doi.org/10.1063/1.107259.
[294] G.S. Girolami, P.M. Jeffries, L.H. Dubois, Mechanistic Studies of Copper Thin-Film Growth from CuI and CuII β-Diketonates, J. Am. Chem. Soc. 115 (1993) 1015–1024, https://doi.org/10.1021/ja00056a028.
[295] S.L. Cohen, M. Liehr, S. Kasi, Surface analysis studies of copper chemical vapor deposition from 1,5-cyclooctadiene-copper(I)-hexafluoroacetylacetonate, J. Vac. Sci. Technol. A. 10 (1992) 863–868, https://doi.org/10.1116/1.577685.
[296] Q. Ma, F. Zaera, deposition processes Chemistry of $Cu(acac)_2$ on Ni(110) and Cu(110) surfaces: Implications for atomic layer deposition processes, J. Vac. Sci. Technol. A. 31 (2013) 01A112. https://doi.org/10.1116/1.4763358.
[297] X. Hu, J. Schuster, S.E. Schulz, T. Gessner, Surface chemistry of copper metal and copper oxide atomic layer deposition from copper(II) acetylacetonate: a combined first-principles and reactive molecular dynamics study, Phys. Chem. Chem. Phys. 17 (2015) 26892–26902, https://doi.org/10.1039/c5cp03707g.
[298] Y. Duan, A.V. Teplyakov, Deposition of copper from Cu(I) and Cu(II) precursors onto HOPG surface: Role of surface defects and choice of a precursor, J. Chem. Phys. 146 (2017) 052814, https://doi.org/10.1063/1.4971287.
[299] P. Doppelt, Why is coordination chemistry stretching the limits of micro-electronics technology?, Coord Chem. Rev. 178–180 (1998) 1785–1809, https://doi.org/10.1016/s0010-8545(98)00087-3.
[300] A. Elements, Copper(I)/(II) Hexafluoro-2,4-Pentanedionate-Vinyltrimethylsilane Complex, (2021). https://www.americanelements.com/copper-i-ii-hexafluoro-2-4-pentanedionate-vinyltrimethylsilane-complex-139566-53-3.
[301] L. Pirolli, A.V. Teplyakov, Molecular view of copper deposition chemistry: (Hexafluoroacetylacetonate)Cu(vinyltrimethylsilane) on a Si(1 0 0)-2 × 1 surface, Surf. Sci. 600 (2006) 3313–3320, https://doi.org/10.1016/j.susc.2006.06.019.
[302] K.-K. Choi, S.G. Pyo, D.W. Lee, S.-W. Rhee, Metalorganic Chemical Vapor Deposition of Copper Using (Hexafluoroacetylacetonate)Cu(I)(3,3-dimethyl-1-butene) with a Liquid Delivery System, Jpn. J. Appl. Phys. 41 (2002) 2962–2968, https://doi.org/10.1143/jjap.41.2962.
[303] S.-W. Kang, S.-H. Han, S.-W. Rhee, (hfac)Cu(I)(MP) (hfac = hexafluoroacetylacetonate, MP = 4-methyl-1-pentene) and (hfac)Cu(I)(DMB) (DMB = 3,3-dimethyl-1-butene) for the chemical vapor deposition of copper film, Thin Solid Films. 350 (1999) 10–13, https://doi.org/10.1016/S0040-6090(99)00346-6.
[304] S.W. Rhee, S.W. Kang, S.H. Han, Property of HexafluoroacetylacetonateCu(I)(3,3-dimethyl-1-butene) as a Liquid Precursor for Chemical Vapor Deposition of Copper Films, Electrochem. Solid-State Lett. 3 (2000) 135–137, https://doi.org/10.1149/1.1390980.
[305] T.-Y. Chen, J. Vaissermann, E. Ruiz, J.P. Sénateur, P. Doppelt, 2-Methyl-1-hexen-3-yne Lewis Base Stabilized β-Diketonate Copper(I) Complexes: X-ray Structures, Theoretical Study, and Low-Temperature Chemical Vapor Deposition of Copper Metal, Chem. Mater. 13 (2001) 3993–4004, https://doi.org/10.1021/cm0012318.
[306] K.K. Choi, S.W. Rhee, Effect of the neutral ligand (L) on the characteristics of hexafluoroacetylacetonate (hfac)Cu(I)-L precursor and on the copper deposition process, Thin Solid Films. 409 (2002) 147–152, https://doi.org/10.1016/S0040-6090(02)00118-9.
[307] Y. Ochiai, J. Fujita, S. Matsui, Electron-beam-induced deposition of copper compound with low resistivity, J. Vac. Sci. Technol. B. 14 (1996) 3887–3891, https://doi.org/10.1116/1.588687.
[308] T. Bret, I. Utke, A. Bachmann, P. Hoffmann, In situ control of the focused-electron-beam-induced deposition process, Appl. Phys. Lett. 83 (2003) 4005–4007, https://doi.org/10.1063/1.1626261.
[309] T. Bret, I. Utke, C. Gaillard, P. Hoffmann, Periodic structure formation by focused electron-beam-induced deposition, J. Vac. Sci. Technol. B. 22 (2004) 2504–2510, https://doi.org/10.1116/1.1800356.
[310] I. Utke, A. Luisier, P. Hoffmann, D. Laub, P.A. Buffat, Focused-electron-beam-induced deposition of freestanding three-dimensional nanostructures of pure coalesced copper crystals, Appl. Phys. Lett. 81 (2002) 3245–3247, https://doi.org/10.1063/1.1517180.
[311] A.A. Martin, M. Toth, Cryogenic Electron Beam Induced Chemical Etching, ACS Appl. Mater. Interfaces. 6 (2014) 18457–18460, https://doi.org/10.1021/am506163w.
[312] M.G. Lassiter, P.D. Rack, Nanoscale electron beam induced etching: a continuum model that correlates the etch profile to the experimental parameters, Nanotechnology 19 (2008) 455306, https://doi.org/10.1088/0957-4484/19/45/455306.
[313] M.B. Naik, W.N. Gill, R.H. Wentorf, R.R. Reeves, CVD of copper using copper(I) and copper(II) β-diketonates, Thin Solid Films. 262 (1995) 60–66, https://doi.org/10.1016/0040-6090(95)05840-0.
[314] E.S. Choi, S.K. Park, H.H. Lee, Growth and Resistivity Behavior of Copper Film by Chemical Vapor Deposition, J. Electrochem. Soc. 143 (1996) 624–627, https://doi.org/10.1149/1.1836490.
[315] M. Joulaud, C. Angekort, P. Doppelt, T. Mourier, D. Mayer, Evaluation of (hfac)Cu(MHY) for Cu CVD, Microelectron. Eng. 64 (2002) 107–115, https://doi.org/10.1016/S0167-9317(02)00774-8.
[316] E. Szłyk, I. Szymańska, Studies of new volatile copper(I) complexes with triphenylphosphite and perfluorinated carboxylates, Polyhedron. 18 (1999) 2941–2948, https://doi.org/10.1016/S0277-5387(99)00199-0.
[317] P. Piszczek, I.B. Szymańska, E. Talik, J. Heimann, Deposition of thin copper layers using copper(II) carboxylate complexes with tert-butylamine as new CVD precursors, Chem. Vap. Depos. 19 (2013) 251–259, https://doi.org/10.1002/cvde.201207049.
[318] I. Szymańska, P. Piszczek, R. Szczęsny, E. Szłyk, Thermal and MS studies of silver(I) 2,2-dimethylbutyrate complexes with tertiary phosphines and their application for CVD of silver films, Polyhedron. 26 (2007) 2440–2448, https://doi.org/10.1016/j.poly.2006.12.028.
[319] R. Szczęsny, E. Szłyk, Thermal decomposition of some silver(I) carboxylates under nitrogen atmosphere, J. Therm. Anal. Calorim. 111 (2013) 1325–1330, https://doi.org/10.1007/s10973-012-2485-1.
[320] Merck, Silver heptafluorobutyrate, Safety Data Sheet, (2021). https://www.sigmaaldrich.com/PL/pl/product/aldrich/307424?context=product (accessed January 21, 2021).
[321] M. Hauptschein, A.V. Grosse, Perfluoroalkyl Halides Prepared from Silver Perfluoro-fatty Acid Salts. I. Perfluoroalkyl Iodides, J. Am. Chem. Soc. 73 (1951) 2461–2463, https://doi.org/10.1021/ja01150a016.
[322] E. Szłyk, P. Piszczek, A. Grodzicki, M. Chaberski, A. Goliński, J. Szatkowski, T. Błaszczyk, CVD of AgI Complexes with Tertiary Phosphines and Perfluorinated Carboxylates - A New Class of Silver Precursors, Chem. Vap. Depos. 7 (2001) 111–116, https://doi.org/10.1002/1521-3862(200105)7:3<111::AID-CVDE1113.0.CO;2-V.

[323] Merck, Silver trifluoroacetate, Safety Data Sheet, (2021). https://www.sigmaaldrich.com/PL/pl/product/aldrich/t62405?context=product.
[324] L. Berger, J. Jurczyk, K. Madajska, T.E.J. Edwards, I. Szymańska, P. Hoffmann, I. Utke, High-Purity Copper Structures from a Perfluorinated Copper Carboxylate Using Focused Electron Beam Induced Deposition and Post-Purification, ACS Appl. Electron. Mater. 2 (2020) 1989–1996, https://doi.org/10.1021/acsaelm.0c00282.
[325] J. Jurczyk, K. Madajska, L. Berger, L. Brockhuis, T.E.J. Edwards, K. Höflich, C. Kapusta, I. Szymańska, I. Utke, Ligand chain length study of silver carboxylates in focused electron beam induced deposition, Preprints. (2021) 2021010415, https://doi.org/10.20944/preprints202101.0415.v1.
[326] I.B. Szymańska, Gaseous phase studies of new copper(II) carboxylate complexes with tert-butylamine as potential precursors for chemical vapor deposition (CVD), Polyhedron. 50 (2013) 200–207, https://doi.org/10.1016/j.poly.2012.10.046.
[327] I.B. Szymańska, P. Piszczek, W. Bała, K. Bartkiewicz, E. Szłyk, Ag/Cu layers grown on Si(111) substrates by thermal inducted chemical vapor deposition, Surf. Coatings Technol. 201 (2007) 9015–9020, https://doi.org/10.1016/j.surfcoat.2007.04.111.
[328] J. Jurczyk, C. Glessi, K. Madajska, L. Berger, J.I.K. Nyrud, I. Szymańska, C. Kapusta, M. Tilset, I. Utke, Vacuum versus Ambient Pressure Inert Gas Thermogravimetry: A Study of Silver Carboxylates, J. Therm. Anal. Calorim. (2021). https://doi.org/10.1007/s10973-021-10616-6.
[329] L. Berger, K. Madajska, I.B. Szymanska, K. Höflich, M.N. Polyakov, J. Jurczyk, C. Guerra-Nuñez, I. Utke, Gas-assisted silver deposition with a focused electron beam, Beilstein J. Nanotechnol. 9 (2018) 224–232, https://doi.org/10.3762/bjnano.9.24.
[330] K. Höflich, J.M. Jurczyk, K. Madajska, M. Götz, L. Berger, C. Guerra-Nuñez, C. Haverkamp, I. Szymanska, I. Utke, Towards the third dimension in direct electron beam writing of silver, Beilstein J. Nanotechnol. 9 (2018) 842–849, https://doi.org/10.3762/bjnano.9.78.
[331] A. Grodzicki, I. Łakomska, P. Piszczek, I. Szymańska, E. Szłyk, Copper(I), silver (I) and gold(I) carboxylate complexes as precursors in chemical vapour deposition of thin metallic films, Coord. Chem. Rev. 249 (2005) 2232–2258, https://doi.org/10.1016/j.ccr.2005.05.026.
[332] M.J. Shapiro, W.J. Lackey, J.A. Hanigofsky, D.N. Hill, W.B. Carter, E.K. Barefield, Chemical vapor deposition of silver films for superconducting wire applications, J. Alloys Compd. 187 (1992) 331–349, https://doi.org/10.1016/0925-8388(92)90439-G.
[333] L. Sala, I.B. Szymańska, C. Dablemont, A. Lafosse, L. Amiaud, Response under low-energy electron irradiation of a thin film of a potential copper precursor for focused electron beam induced deposition (FEBID), Beilstein J. Nanotechnol. 9 (2018) 57–65, https://doi.org/10.3762/bjnano.9.8.
[334] M. Lacko, P. Papp, I.B. Szymańska, E. Szłyk, Š. Matejčík, Electron interaction with copper(II) carboxylate compounds, Beilstein J. Nanotechnol. 9 (2018) 384–398, https://doi.org/10.3762/bjnano.9.38.
[335] G.D. Roberts, W.V. Edward, The Mass Spectra of Some Silver Salts, Org. Mass Spectrom. 16 (1981) 546–550, https://doi.org/10.1002/oms.1210161209.
[336] T. Ohta, F. Cicoira, P. Doppelt, L. Beitone, P. Hoffmann, Static vapor pressure measurement of low volatility precursors for molecular vapor deposition below ambient temperature, Chem. Vap. Depos. 7 (2001) 33–37, https://doi.org/10.1002/1521-3862(200101)7:1<33::AID-CVDE33>3.0.CO;2-Y.
[337] S. Komiya, J.K. Kochi, Reversible Linkage Isomerisms of β-Diketonato Ligands. Oxygen-Bonded and Carbon-Bonded Structures in Gold(III) Acetylacetonate Complexes Induced by Phosphines, J. Am. Chem. Soc. 99 (1977) 3695–3704, https://doi.org/10.1021/ja00453a030.
[338] S. Chemicals, Dimethyl(acetylacetonate)gold(III), 98% (99.9%-Au), (2021). https://www.strem.com/catalog/v/79-1500/25/gold_14951-50-9.
[339] P.P. Semyannikov, B.L. Moroz, S.V. Trubin, G.I. Zharkova, P.A. Pyryaev, M.Y. Smirnov, V.I. Bukhtiyarov, Chemical Vapor Infiltration Method for Deposition of Gold Nanoparticles on Porous Alumina Supports, J. Struct. Chem. 47 (2006) 458–464, https://doi.org/10.1007/s10947-006-0323-7.
[340] H.W.P. Koops, R. Weiel, D.P. Kern, T.H. Baum, High-resolution electron-beam induced deposition, J. Vac. Sci. Technol. B. 6 (1988) 477–481, https://doi.org/10.1116/1.584045.
[341] H.W.P. Koops, J. Kretz, M. Rudolph, M. Weber, G. Dahm, K.L.K.L. Lee, Characterization and Application of Materials Grown by Electron-Beam-Induced Deposition, Jpn. J. Appl. Phys. 33 (1994) 7099–7107, https://doi.org/10.1143/JJAP.33.7099.
[342] H.W.P. Koops, C. Schössler, A. Kaya, M. Weber, Conductive dots, wires, and supertips for field electron emitters produced by electron-beam induced deposition on samples having increased temperature, J. Vac. Sci. Technol. B Microelectron. Nanom. Struct. 14 (1996) 4105, https://doi.org/10.1116/1.588600.
[343] I. Utke, M.G. Jenke, C. Röling, P.H. Thiesen, V. Iakovlev, A. Sirbu, A. Mereuta, A. Caliman, E. Kapon, Polarisation stabilisation of vertical cavity surface emitting lasers by minimally invasive focused electron beam triggered chemistry, Nanoscale. 3 (2011) 2718–2722, https://doi.org/10.1039/c1nr10047e.
[344] P.G. Blauner, Y. Butt, J.S. Ro, C.V. Thompson, J. Melngailis, Focused ion beam induced deposition of low-resistivity gold films, J. Vac. Sci. Technol. B. 7 (1989) 1816–1818, https://doi.org/10.1116/1.584465.
[345] S. Graells, R. Alcubilla, G. Badenes, R. Quidant, Growth of plasmonic gold nanostructures by electron beam induced deposition, Appl. Phys. Lett. 91 (2007) 121112, https://doi.org/10.1063/1.2786600.
[346] O. Sqalli, I. Utke, P. Hoffmann, F. Marquis-Weible, Gold elliptical nanoantennas as probes for near field optical microscopy, J. Appl. Phys. 92 (2002) 1078–1083, https://doi.org/10.1063/1.1487918.
[347] M.M. Shawrav, P. Taus, H.D. Wanzenboeck, M. Schinnerl, M. Stöger-Pollach, S. Schwarz, A. Steiger-Thirsfeld, E. Bertagnolli, Highly conductive and pure gold nanostructures grown by electron beam induced deposition, Sci. Rep. 6 (2016) 34003, https://doi.org/10.1038/srep34003.
[348] K. Mølhave, D.N. Madsen, A.M. Rasmussen, A. Carlsson, C.C. Appel, M. Brorson, C.J.H. Jacobsen, P. Bøggild, Solid Gold Nanostructures Fabricated by Electron Beam Deposition, Nano Lett. 3 (2003) 1499–1503, https://doi.org/10.1021/nl034528o.
[349] A.V. Riazanova, Y.G.M. Rikers, J.J.L. Mulders, L.M. Belova, Pattern Shape Control for Heat Treatment Purification of Electron-Beam-Induced Deposition of Gold from the $Me_2Au(acac)$ Precursor, Langmuir. 28 (2012) 6185–6191, https://doi.org/10.1021/la203599c.
[350] D. Belić, M.M. Shawrav, M. Gavagnin, M. Stöger-Pollach, H.D. Wanzenboeck, E. Bertagnolli, Direct-Write Deposition and Focused-Electron-Beam-Induced Purification of Gold Nanostructures, ACS Appl. Mater. Interfaces. 7 (2015) 2467–2479, https://doi.org/10.1021/am507327y.
[351] I. Utke, B. Dwir, K. Leifer, F. Cicoira, P. Doppelt, P. Hoffmann, E. Kapon, Electron beam induced deposition of metallic tips and wires for microelectronics applications, Microelectron. Eng. 53 (2000) 261–264, https://doi.org/10.1016/S0167-9317(00)00311-7.
[352] I. Utke, P. Hoffmann, B. Dwir, K. Leifer, E. Kapon, P. Doppelt, Focused electron beam induced deposition of gold, J. Vac. Sci. Technol. B Microelectron. Nanom. Struct. 18 (2000) 3168–3171, https://doi.org/10.1116/1.1319690.
[353] M.G. Jenke, D. Lerose, C. Niederberger, J. Michler, S. Christiansen, I. Utke, Toward local growth of individual nanowires on three-dimensional microstructures by using a minimally invasive catalyst templating method, Nano Lett. 11 (2011) 4213–4217, https://doi.org/10.1021/nl2021448.
[354] T.H. Baum, C.R. Jones, Laser chemical vapor deposition of gold, Appl. Phys. Lett. 47 (1985) 538–540, https://doi.org/10.1063/1.96119.
[355] T.H. Baum, C.R. Jones, Laser chemical vapor deposition of gold: Part II, J. Vac. Sci. Technol. B Microelectron. Nanom. Struct. 4 (1986) 1187–1191, https://doi.org/10.1116/1.583481.
[356] C.E. Larson, T.H. Baum, R.L. Jackson, Chemical Vapor Deposition of Gold, J. Electrochem. Soc. 134 (1987) 266, https://doi.org/10.1149/1.2100427.
[357] E. Feurer, H. Suhr, Preparation of Gold Films by Plasma-CVD, Appl. Phys. A Solids Surfaces. 44 (1987) 171–175, https://doi.org/10.1007/BF00626420.
[358] W. Fuß, M. Rühe, Chlor(trifluorphosphan)gold(I), eine einfache flüchtige Goldverbindung, Zeitschrift Für Naturforsch. B. 47 (1992) 591–593. https://doi.org/10.1515/znb-1992-0422.
[359] J.J.L. Mulders, J.M. Veerhoek, E.G.T. Bosch, P.H.F. Trompenaars, Fabrication of pure gold nanostructures by electron beam induced deposition with Au(CO)Cl precursor: deposition characteristics and primary beam scattering effects, J. Phys. D. Appl. Phys. 45 (2012) 475301, https://doi.org/10.1088/0022-3727/45/47/475301.
[360] E.M. Meyer, S. Gambarotta, F. Carlo, A. Chiesi-Villa, C. Guastini, Polynuclear Aryl Derivatives of Group 11 Metals: Synthesis, Solid State-Solution Structural Relationship, and Reactivity with Phosphines, Organometallics. 8 (1989) 1067–1079, https://doi.org/10.1021/om00106a031.
[361] W.F. van Dorp, X. Wu, J.J.L.L. Mulders, S. Harder, P. Rudolf, J.T.M. De Hosson, Gold Complexes for Focused-Electron-Beam-Induced Deposition, Langmuir. 30 (2014) 12097–12105, https://doi.org/10.1021/la502618t.
[362] W.G. Carden, J. Pedziwiatr, K.A. Abboud, L. McElwee-White, Halide Effects on the Sublimation Temperature of X-Au-L Complexes: Implications for Their Use as Precursors in Vapor Phase Deposition Methods, ACS Appl. Mater. Interfaces. 9 (2017) 40998–41005, https://doi.org/10.1021/acsami.7b12465.
[363] A. Gräfe, T. Kruck, Übergangsmetall-Trifluormethyl-Komplexe: Erste Trifluormethyl-Komplexe von Gold mit Fluorphosphan-Liganden, J. Organomet. Chem. 506 (1996) 31–35, https://doi.org/10.1016/0022-328X(95)05637-5.
[364] P.D. Tran, P. Doppelt, Gold CVD Using Trifluorophosphine Gold(I) Chloride Precursor and Its Toluene Solutions, J. Electrochem. Soc. 154 (2007) D520–D525, https://doi.org/10.1149/1.2766648.
[365] F. Calderazzo, D.B. Dell'Amico, Transition-Metal-Catalyzed Oxidation of Carbon Monoxide by Dichlorine To Produce Phosgene, Inorg. Chem. 21 (1982) 3639–3642. https://doi.org/10.1021/ic00140a011.
[366] A. Marashdeh, T. Tiesma, N.J.C. van Velzen, S. Harder, R.W.A. Havenith, J.T.M. De Hosson, W.F. van Dorp, The rational design of a Au(I) precursor for focused electron beam induced deposition, Beilstein J. Nanotechnol. 8 (2017) 2753–2765, https://doi.org/10.3762/bjnano.8.274.
[367] A. Haaland, J. Hougen, H.V. Volden, R.J. Puddephatt, The molecular structure of methyl(trimethylphosphine)gold(I) by gas electron diffraction, J. Organomet. Chem. 325 (1987) 311–315, https://doi.org/10.1016/0022-328X(87)80410-2.
[368] H. Schmidbaur, A. Shiotani, Darstellung komplexer Organogold-Verbindungen durch Liganden-Substitutionsreaktionen, Chem. Ber. 104 (1971) 2821–2830, https://doi.org/10.1002/cber.19711040921.
[369] M.B.E. Griffiths, Z.S. Dubrawski, G. Bačić, A. Japahuge, J.D. Masuda, T. Zeng, S. T. Barry, Controlling the Thermal Stability and Volatility of Organogold(I) Compounds for Vapor Deposition with Complementary Ligand Design, Eur. J. Inorg. Chem. (2019) 4927–4938, https://doi.org/10.1002/ejic.201901087.
[370] M. Mäkelä, Studies on Atomic Layer Deposition of Gold and Silver Thin Films, University of Helsinki, 2018. https://helda.helsinki.fi/handle/10138/235245.

[371] Chloro(dimethylsulfide)gold(I), https://www.americanelements.com/chloro-dimethylsulfide-gold-i-29892-37-3#section-properties (accessed September 29, 2020).
[372] T. Brintlinger, M.S. Fuhrer, J. Melngailis, I. Utke, T. Bret, A. Perentes, P. Hoffmann, M. Abourida, P. Doppelt, Electrodes for carbon nanotube devices by focused electron beam induced deposition of gold, J. Vac. Sci. Technol. B Microelectron. Nanom. Struct. 23 (2005) 3174, https://doi.org/10.1116/1.2130355.
[373] N.H. Dryden, J.G. Shapter, L.L. Coatsworth, P.R. Norton, R.J. Puddephatt, [CF_3Au(CNMe)] as a Precursor for CVD of Gold, Chem. Mater. 4 (1992) 979–981, https://doi.org/10.1021/cm00023a009.
[374] M.B.E. Griffiths, P.J. Pallister, D.J. Mandia, S.T. Barry, Atomic Layer Deposition of Gold Metal, Chem. Mater. 28 (2016) 44–46, https://doi.org/10.1021/acs.chemmater.5b04562.
[375] P.J. Pallister, S.T. Barry, Surface chemistry of group 11 atomic layer deposition precursors on silica using solid-state nuclear magnetic resonance spectroscopy, J. Chem. Phys. 146 (2017), https://doi.org/10.1063/1.4968021 052812.
[376] J. Kopyra, F. Rabilloud, P. Wierzbicka, H. Abdoul-Carime, Energy-Selective Decomposition of Organometallic Compounds by Slow Electrons: The Case of Chloro(dimethyl sulfide)gold(I), J. Phys. Chem. A 125 (2021) 966–972, https://doi.org/10.1021/acs.jpca.0c09988.
[377] M. Winhold, C.H. Schwalb, F. Porrati, R. Sachser, A.S. Frangakis, B. Kämpken, A. Terfort, N. Auner, M. Huth, Binary Pt-Si nanostructures prepared by focused electron-beam-induced deposition, ACS Nano. 5 (2011) 9675–9681, https://doi.org/10.1021/nn203134a.
[378] F. Porrati, B. Kämpken, A. Terfort, M. Huth, Fabrication and electrical transport properties of binary Co-Si nanostructures prepared by focused electron beam-induced deposition, J. Appl. Phys. 113 (2013), https://doi.org/10.1063/1.4790320.
[379] S. Ketharanathan, R. Sharma, P.A. Crozier, J. Drucker, Electron beam induced deposition of pure, nanoscale Ge, J. Vac. Sci. Technol. B Microelectron. Nanom. Struct. 24 (2006) 678–681, https://doi.org/10.1116/1.2178372.
[380] J. Bishop, C.J. Lobo, A. Martin, M. Ford, M. Phillips, M. Toth, Role of activated chemisorption in gas-mediated electron beam induced deposition, Phys. Rev. Lett. 109 (2012) 146103, https://doi.org/10.1103/PhysRevLett.109.146103.
[381] J.D. Ferguson, E.R. Smith, A.W. Weimer, S.M. George, ALD of SiO_2 at Room Temperature Using TEOS and H_2O with NH_3 as the Catalyst, J. Electrochem. Soc. 151 (2004) G528–G535, https://doi.org/10.1149/1.1768548.
[382] A. Perentes, P. Hoffmann, Focused Electron Beam Induced Deposition of Si-Based Materials From SiO_xC_y to Stoichiometric SiO_2: Chemical Compositions, Chemical-Etch Rates, and Deep Ultraviolet Optical Transmissions, Chem. Vap. Depos. 13 (2007) 176–184, https://doi.org/10.1002/cvde.200606583.
[383] A. Perentes, A. Bachmann, M. Leutenegger, I. Utke, C. Sandu, P. Hoffmann, Focused electron beam induced deposition of a periodic transparent nano-optic pattern, Microelectron. Eng. 73–74 (2004) 412–416, https://doi.org/10.1016/S0167-9317(04)00146-7.
[384] I. Utke, J. Michler, P. Gasser, C. Santschi, D. Laub, M. Canton, P.A. Buffat, C. Jiao, P. Hoffmann, Cross Section Investigations of Compositions and Sub-Structures of Tips Obtained by Focused Electron Beam Induced Deposition, Adv. Eng. Mater. 7 (2005) 323–331, https://doi.org/10.1002/adem.200500061.
[385] G. Hochleitner, H.D. Wanzenboeck, E. Bertagnolli, Electron beam induced deposition of iron nanostructures, J. Vac. Sci. Technol. B Microelectron. Nanom. Struct. 26 (2008) 939–944, https://doi.org/10.1116/1.2907781.
[386] W.F. Edgell, W.E. Wilson, R. Summitt, The infrared spectrum and vibrational assignment for $Fe(CO)_5$. Bonding considerations, Spectrochim. Acta. 19 (1963) 863–872, https://doi.org/10.1016/0371-1951(63)80173-3.
[387] O. González-Blanco, V. Branchadell, Density functional study of the Fe–CO bond dissociation energies of $Fe(CO)_5$, J. Chem. Phys. 110 (1999) 778–783, https://doi.org/10.1063/1.478045.
[388] F. Vollnhals, M. Drost, F. Tu, E. Carrasco, A. Späth, R.H. Fink, H.P. Steinrück, H. Marbach, Electron-beam induced deposition and autocatalytic decomposition of $Co(CO)_3NO$, Beilstein J. Nanotechnol. 5 (2014) 1175–1185, https://doi.org/10.3762/bjnano.5.129.
[389] M. Reinke, Y. Kuzminykh, P. Hoffmann, Surface Reaction Kinetics of Titanium Isopropoxide and Water in Atomic Layer Deposition, J. Phys. Chem. C. 120 (2016) 4337–4344, https://doi.org/10.1021/acs.jpcc.5b10529.
[390] M. Reinke, Y. Kuzminykh, F. Eltes, S. Abel, T. LaGrange, A. Neels, J. Fompeyrine, P. Hoffmann, Low Temperature Epitaxial Barium Titanate Thin Film Growth in High Vacuum CVD, Adv. Mater. Interfaces. 4 (2017) 1700116, https://doi.org/10.1002/admi.201700116.
[391] M. Junige, M. Löffler, M. Geidel, M. Albert, J.W. Bartha, E. Zschech, B. Rellinghaus, W.F.V. Dorp, Area-selective atomic layer deposition of Ru on electron-beam-written Pt(C) patterns versus SiO_2 substratum, Nanotechnology. 28 (2017) 395301, https://doi.org/10.1088/1361-6528/aa8844.
[392] X. Tang, L.A. Francis, P. Simonis, M. Haslinger, R. Delamare, O. Deschaume, D. Flandre, P. Defrance, A.M. Jonas, J.P. Vigneron, J.P. Raskin, Room temperature atomic layer deposition of Al_2O_3 and replication of butterfly wings for photovoltaic application, J. Vac. Sci. Technol. A Vacuum, Surfaces, Film. 30 (2012) 01A146, https://doi.org/10.1116/1.3669521.
[393] T. Nam, J.-M. Kim, M.-K. Kim, H. Kim, W.-H. Kim, Low-temperature Atomic Layer Deposition of TiO_2, Al_2O_3, and ZnO Thin Films, J. Korean Phys. Soc. 59 (2011) 452–457, https://doi.org/10.3938/jkps.59.452.
[394] D.L. Pugmire, C.M. Woodbridge, S. Root, M.A. Langell, Nickelocene adsorption on single-crystal surfaces, J. Vac. Sci. Technol. A Vacuum, Surfaces, Film. 17 (1999) 1581–1586, https://doi.org/10.1116/1.581854.
[395] K.W. Kolasinski, Surface Science: Foundations of Catalysis and Nanoscience, Third Edit, John Wiley & Sons, Ltd, 15 (2012), https://doi.org/10.1002/9781119941798.
[396] M. Drost, F. Tu, L. Berger, C. Preischl, W. Zhou, H. Gliemann, C. Wöll, H. Marbach, Surface-Anchored Metal-Organic Frameworks as Versatile Resists for Gas-Assisted E-Beam Lithography: Fabrication of Sub-10 Nanometer Structures, ACS Nano. 12 (2018) 3825–3835, https://doi.org/10.1021/acsnano.8b01071.
[397] K. Muthukumar, H.O. Jeschke, R. Valentí, E. Begun, J. Schwenk, F. Porrati, M. Huth, Spontaneous dissociation of $Co_2(CO)_8$ and autocatalytic growth of Co on SiO2: A combined experimental and theoretical investigation, Beilstein J. Nanotechnol. 3 (2012) 546–555, https://doi.org/10.3762/bjnano.3.63.
[398] K. Muthukumar, H.O. Jeschke, R. Valentí, Dynamics and fragmentation mechanism of $(C_5H_4CH_3)Pt(CH_3)_3$ on SiO_2 surfaces, Beilstein J. Nanotechnol. 9 (2018) 711–720, https://doi.org/10.3762/bjnano.9.66.
[399] K. Muthukumar, R. Valentí, H.O. Jeschke, Dynamics of tungsten hexacarbonyl, dicobalt octacarbonyl, and their fragments adsorbed on silica surfaces, J. Chem. Phys. 140 (2014) 184706, https://doi.org/10.1063/1.4873584.
[400] G. Bor, Metal carbonyl clusters: thermodynamics of their formation and stability. Some novel results on cobalt, rhodium, ruthenium, and mixed Clusters, Pure Appl. Chem. 58 (1986) 543–552, https://doi.org/10.1351/pac198658040543.
[401] T. Hamann, A. Edtbauer, F. Ferreira da Silva, S. Denifl, P. Scheier, P. Swiderek, Dissociative electron attachment to gas-phase formamide, Phys. Chem. Chem. Phys. 13 (2011) 12305–12313, https://doi.org/10.1039/c1cp20833k.
[402] S.G. Lias, J.E. Bartmess, J.F. Liebman, J.L. Holmes, R.D. Levin, W.G. Mallard, Ion Energetics Data, in: P.J. Linstrom, W.G. Mallard (Eds.), NIST Chem. WebBook, NIST Stand. Ref. Database Number 69, National Institute of Standards and Technology, Gaithersburg MD, 20899, 2008. https://doi.org/10.18434/T4D303.
[403] K. Ahlenhoff, S. Koch, D. Emmrich, R. Dalpke, A. Gölzhäuser, P. Swiderek, Electron-induced chemistry of surface-grown coordination polymers with different linker anions, Phys. Chem. Chem. Phys. 21 (2019) 2351–2364, https://doi.org/10.1039/c8cp07028h.
[404] Inorganic Compounds: Physical and Thermochemical Data, (n.d.). http://www2.ucdsb.on.ca/tiss/stretton/database/inorganic_thermo.htm.
[405] I. Bald, J. Langer, P. Tegeder, O. Ingólfsson, From isolated molecules through clusters and condensates to the building blocks of life A short tribute to Prof. Eugen Illenberger's work in the field of negative ion chemistry, Int. J. Mass Spectrom. 277 (2008) 4–25. https://doi.org/10.1016/j.ijms.2008.06.013.
[406] R.R. Ford, Carbon Monoxide Adsorption on the Transition Metals, Adv. Catal. 21 (1970) 51–150, https://doi.org/10.1016/S0360-0564(08)60564-7.
[407] Q. Ma, F. Zaera, Chemistry of Cu(acac)2 on Ni(110) and Cu(110) surfaces: Implications for atomic layer deposition processes, J. Vac. Sci. Technol. A Vacuum, Surfaces, Film. 31 (2013) 01A112, https://doi.org/10.1116/1.4763358.
[408] J. Warneke, W.F. Van Dorp, P. Rudolf, M. Stano, P. Papp, Š. Matejčík, T. Borrmann, P. Swiderek, Acetone and the precursor ligand acetylacetone: Distinctly different electron beam induced decomposition?, Phys Chem. Chem. Phys. 17 (2015) 1204–1216, https://doi.org/10.1039/c4cp04239e.
[409] A. Turchanin, A. Gölzhäuser, Carbon Nanomembranes, Adv. Mater. 28 (2016) 6075–6103, https://doi.org/10.1002/adma.201506058.
[410] J.H. Noh, M.G. Stanford, B.B. Lewis, J.D. Fowlkes, H. Plank, P.D. Rack, Nanoscale electron beam-induced deposition and purification of ruthenium for extreme ultraviolet lithography mask repair, Appl. Phys. A Mater. Sci. Process. 117 (2014) 1705–1713, https://doi.org/10.1007/s00339-014-8745-0.
[411] Y. Li, Y.N. Kim, E.J. Lee, W.P. Cai, S.O. Cho, Synthesis of silver nanoparticles by electron irradiation of silver acetate, Nucl. Instruments Methods Phys. Res. Sect. B Beam Interact. with Mater. Atoms. 251 (2006) 425–428, https://doi.org/10.1016/j.nimb.2006.06.019.
[412] Y. Itikawa, N. Mason, Cross sections for electron collisions with water molecules, J. Phys. Chem. Ref. Data. 34 (2005) 1–22, https://doi.org/10.1063/1.1799251.
[413] J.-S. Yoon, M.-Y. Song, J.-M. Han, S.H. Hwang, W.-S. Chang, B. Lee, Y. Itikawa, Cross sections for electron collisions with hydrogen molecules, J. Phys. Chem. Ref. Data. 37 (2008) 913–931, https://doi.org/10.1063/1.2838023.
[414] B.C. Garrett, D.A. Dixon, D.M. Camaioni, D.M. Chipman, M.A. Johnson, C.D. Jonah, G.A. Kimmel, J.H. Miller, T.N. Rescigno, P.J. Rossky, S.S. Xantheas, S.D. Colson, A. H. Laufer, D. Ray, P.F. Barbara, D.M. Bartels, K.H. Becker, K.H. Bowen, S.E. Bradforth, I. Carmichael, J.V. Coe, L.R. Corrales, J.P. Cowin, M. Dupuis, K.B. Eisenthal, J.A. Franz, M.S. Gutowski, K.D. Jordan, B.D. Kay, J.A. LaVerne, S.V. Lymar, T.E. Madey, C.W. McCurdy, D. Meisel, S. Mukamel, A.R. Nilsson, T.M. Orlando, N.G. Petrik, S.M. Pimblott, J.R. Rustad, G.K. Schenter, S.J. Singer, A. Tokmakoff, L.S. Wang, C. Wittig, T.S. Zwier, Role of water in electron-initiated processes and radical chemistry: Issues and scientific advances, Chem. Rev. 105 (2005) 355–389, https://doi.org/10.1021/cr030453x.
[415] F. Schmidt, P. Swiderek, J.H. Bredehöft, Formation of Formic Acid, Formaldehyde, and Carbon Dioxide by Electron-Induced Chemistry in Ices of Water and Carbon Monoxide, ACS Earth Sp. Chem. 3 (2019) 1974–1986, https://doi.org/10.1021/acsearthspacechem.9b00168.
[416] C. Granqvist, R. Buhrman, Size distributions for supported metal catalysts: Coalescence growth versus ostwald ripening, J. Catal. 42 (1976) 477–479, https://doi.org/10.1016/0021-9517(76)90125-1.
[417] R. Córdoba, J. Sesé, J.M.M. De Teresa, M.R.R. Ibarra, R. Cordoba, J. Sese, High-purity cobalt nanostructures grown by focused-electron-beam-induced deposition at low current, Microelectron. Eng. 87 (2010) 1550–1553, https://doi.org/10.1016/j.mee.2009.11.027.

[418] R. Córdoba, J. Sesé, M.R. Ibarra, J.M. De Teresa, Autocatalytic growth of Co on pure Co surfaces using $Co_2(CO)_8$ precursor, Appl. Surf. Sci. 263 (2012) 242–246, https://doi.org/10.1016/j.apsusc.2012.09.037.
[419] T. Lukasczyk, M. Schirmer, H.P. Steinrück, H. Marbach, Electron-beam-induced deposition in ultrahigh vacuum: Lithographic fabrication of clean iron nanostructures, Small. 4 (2008) 841–846, https://doi.org/10.1002/smll.200701095.
[420] A. Opitz, M. Scherge, S.I.U. Ahmed, J.A. Schaefer, A comparative investigation of thickness measurements of ultra-thin water films by scanning probe techniques, J. Appl. Phys. 101 (2007) 064310, https://doi.org/10.1063/1.2712155.
[421] J.K. Sprenger, A.S. Cavanagh, H. Sun, K.J. Wahl, A. Roshko, S.M. George, Electron Enhanced Growth of Crystalline Gallium Nitride Thin Films at Room Temperature and 100 °C Using Sequential Surface Reactions, Chem. Mater. 28 (2016) 5282–5294, https://doi.org/10.1021/acs.chemmater.6b00676.
[422] J. Sprenger K., H. Sun, A.S. Cavanagh, A. Roshko, P.T. Blanchard, S.M. George, Electron-Enhanced Atomic Layer Deposition of Boron Nitride Thin Films at Room Temperature and 100 °C, The Journal of Physical Chemistry C 122 (2018) 9455–9464, https://doi.org/10.1021/acs.jpcc.8b00796.
[423] J.K. Sprenger, H. Sun, A.S. Cavanagh, S.M. George, Electron-enhanced atomic layer deposition of silicon thin films at room temperature, J. Vac. Sci. Technol. A Vacuum, Surfaces, Film. 36 (2018) 01A118, https://doi.org/10.1116/1.5006696.
[424] Z.C. Sobell, A.S. Cavanagh, S.M. George, Growth of cobalt films at room temperature using sequential exposures of cobalt tricarbonyl nitrosyl and low energy electrons, J. Vac. Sci. Technol. A. 37 (2019) 060906, https://doi.org/10.1116/1.5113711.
[425] F. Hirose, H. Sakamoto, Low-temperature Si selective epitaxial growth using electron-beam-induced reaction, Jpn. J. Appl. Phys. 34 (1995) 5904–5907, https://doi.org/10.1143/JJAP.34.5904.
[426] F. Bozso, P. Avouris, Electronic Excitation-Induced Surface Chemistry and Electron-Beam-Assisted Chemical Vapor Deposition, MRS Online Proc. Libr. 158 (1989) 201–209, https://doi.org/10.1557/PROC-158-201.
[427] F. Bozso, P. Avouris, Electron-induced chemical vapor deposition by reactions induced in adsorbed molecular layers, Appl. Phys. Lett. 53 (1988) 1095–1097, https://doi.org/10.1063/1.100655.
[428] H. Nadhom, D. Lundin, P. Rouf, H. Pedersen, Chemical vapor deposition of metallic films using plasma electrons as reducing agents, J. Vac. Sci. Technol. A. 38 (2020) 033402, https://doi.org/10.1116/1.5142850.